TECHNISCHE UNIVERSITÄT DRESDEN

Faculty of Environmental Sciences

Forest Biomass and Land Cover Change Assessment of the Margalla Hills National Park in Pakistan Using a Remote Sensing Based Approach

Doctoral dissertation for obtaining the degree of:

Doctor rerum naturalium (Dr. rer. nat.)

<u>Submitted by</u>:

Mohammad Qasim,

M.Sc. Tropical Forestry

Born on 28.05.1982, in Karachi, Pakistan.

<u>Reviewers</u>:

Prof. Dr. habil. Elmar Csaplovics, Chair of Remote Sensing, Faculty of Environmental Sciences, Technische Universität Dresden.

Prof. Dr. habil. Michael Köhl, Institute of Wood Science, Faculty of Mathematics, Informatics and Natural Sciences, Universität Hamburg.

Prof. Dr. habil. Marcus Nüsser, Südasien-Institut, Abteilung Geographie, Universität Heidelberg.

Date of Defence: 18.03.2022

Submitted: July 2022, Dresden.

Declaration of conformity

I hereby confirm the accordance of this copy with the original dissertation on the topic:

"Forest Biomass and Land Cover Change Assessment of the Margalla Hills National Park in Pakistan Using a Remote Sensing Based Approach"

Dresden, 07.2022.

…………………………………………

Place, Date

…………………………………………

Signature

Declaration

I hereby declare that this thesis entitled "**Forest Biomass and Land Cover Change Assessment of the Margalla Hills National Park in Pakistan Using a Remote Sensing Based Approach**" submitted to the Faculty of Environmental Sciences, Technical University of Dresden, is my work and, it contains no materials previously published or written by another person and has not been previously submitted or accepted elsewhere to any other university or institute for the award of any other degree.

Mohammad Qasim

Dresden, Germany
07.2022.

Acknowledgments

I would like to express my sincerest thanks to Prof. Dr. habil. Elmar Csaplovics, Chair of Remote Sensing, Institute of Photogrammetry and Remote Sensing, Faculty of Environmental Sciences, Technische Universität (TU) Dresden for his kind support, guidance, and supervision throughout this Ph.D. journey. I would like to extend my sincere gratitude to Prof. Dr. habil. Michael Köhl, Faculty of Mathematics, Informatics and Natural Sciences, Department Biology, Universität Hamburg for his precious time and valuable suggestions for the improvement of my dissertation. I am also very thankful to Prof. Dr. habil. Marcus Nüsser, Abteilungsleiter, Südasien-Institut, Abteilung Geographie, Universität Heidelberg for valuable suggestions and insights that helped in improving my dissertation. I am grateful to Prof. Dr. Marieke van der Maaten-Theunissen, Chair of Forest Growth and Woody Biomass Production, Institute of Forest Growth and Forest Computer Sciences, Faculty of Environmental Sciences, TU Dresden for the timely provision of field measuring instruments and for personally demonstrating their use and sharing the manuals for use.

I would like to thank DAAD for the scholarship which made my stay possible here at the Chair of Remote Sensing of TU Dresden for pursuing my Ph.D. Without this financial support, the completion of a Ph.D. would have been a distant reality for me.

I would like to thank my colleagues and friends at the Chair of Remote Sensing, TU Dresden; Mike Salazar Villegas, Daniala Limache de la Faunte, Dr. rer. nat. Babatunde Adeniyi Osunmadewa, Christopher Marrs, Dr. Milena Markovic, Dr. rer. nat. Marion Pause and Anke Hahn, for the interesting and stimulating discussions and memorable times at the Chair of Remote Sensing, TU Dresden.

I would like to thank the staff of the Islamabad Wildlife Management Board for their support during the field expeditions. I am grateful to Mr. Rab Nawaz, Senior Director, WWF-Pakistan, Islamabad office, for providing the expensive instruments for conducting the field inventories. I am thankful to Mr. Muhammad Waseem, Manager

Table of Contents:

List of Tables:

List of Figures:

List of Acronyms

AFOLU	Agriculture, Forestry and Other Land Use
AGB	Aboveground Biomass
AGC	Aboveground Carbon
AJK	Azad Jammu and Kashmir
ALOS-2	Advance Land Observing Satellite-2
ANN	Artificial Neural Network
ANR	Assisted Natural Regeneration
ARTMAP	Adaptive Resonance Theory-Supervised Predictive Mapping
ASM	Angular Second Moment
a.s.l.	Above Sea Level
AVHRR	Advanced Very High Resolution Radiometer
BAU	Business as Usual
BEF	Biomass Expansion Factor
BGB	Belowground Biomass
BGC	Belowground Carbon
BoA	Bottom-of-Atmosphere
CART	Classification and Regression Tree
CBD	Convention on Biodiversity
CDA	Capital Development Authority
cm	centimetre
CO_2	Carbon Dioxide
CPEC	China Pakistan Economic Corridor
CRS	Coordinate Reference System
dB	decibels
DBH	Diameter at breast height
DEM	Digital Elevation Model
DOD	Department of Defense
DOS	Dark Object Subtraction
DT	Decision Tree
EC	European Commission
ECV	Essential Climate Variable
EOSAT	Earth Observation Satellite Company
EPSG	European Petroleum Survey Group

EROS	Earth Resources Observation and Science
ERTS	Earth Resource Technology Satellite
ESA	European Space Agency
ETM+	Enhanced Thematic Mapper Plus
EVI	Enhanced Vegetation Index
EW	Extra-Wide Swath
FAO	Food and Agriculture Organization
Fig.	Figure
GEDI	Global Ecosystem Dynamics Investigation
GHG	Greenhouse Gas
GHz	Gigahertz
GIS	Geographic Information System
GLCM	Gray Level Co-occurrence Matrix
GMES	Global Monitoring for Environment and Security
GPS	Global Positioning System
GRASS	Geographic Resources Analysis Support System
GRD	Ground Range Detection
Gt	Gigatonne
Hectare	ha
ICESat-2	Ice Cloud and Land Elevation Satellite-2
IPCC	Intergovernmental Panel on Climate Change
IRS	Indian Remote-Sensing Satellite
ISODATA	Iterative Self-Organizing Data Analysis
ISRO	Indian Space Research Organization
IUCN	International Union for Conservation of Nature
IW	Interferometric Wide swath
IWMB	Islamabad Wildlife Management Board
kg	Kilogram
KPK	Khyber Pakhtunkhwa
LC	Land Cover
LCC	Land Cover Change
LCCD	Land Cover Change Detection
LFCC	Low Forest Cover Country
LiDAR	Light Detection and Ranging

LISS	Linear Imaging Self-Scanning Sensor
LU	Land Use
m	meter
MD	Mahalanobis Distance
MDA	Mean Decrease Accuracy
MDC	Minimum Distance Classifier
MDG	Mean Decrease Gini
Mg	Megagram
MHNP	Margalla Hills National Park
MLC	Maximum Likelihood Classifier
MLP	Multilayer Perception
MLR	Multi Linear Regression
mm	millimetre
MODIS	Moderate Resolution Imaging Spectroradiometer
MSI	Multispectral Imager
MSS	Multispectral Scanner
NASA	National Aeronautics and Space Administration
NDVI	Normalized Difference Vegetation Index
NIR	Near Infrared
NISAR	NASA-ISRO SAR
nm	nanometer
NOAA	National Oceanic and Atmospheric Administration
North	N
OLI	Operational Land Imager
OOB	Out-of-Bag
PALSAR-2	Phased-Array L-band Synthetic Aperture Radar – 2
PNG	Portable Network Graphics
ppm	parts per million
RBF	Radial Basis Function
REDD+	Reducing Emissions from Deforestation and Forest Degradation and the Role of Conservation of Forest Carbon, Sustainable Management of Forests and Enhancement of Forest Carbon Stocks
RF	Random Forest

RGB	Red Green Blue
RMSE	Root Mean Square Error
ROC	Rate of Change
S1	Sentinel-1
S2	Sentinel-2
SAM	Spectral Angle Mapper
SAR	Synthetic Aperture Radar
SBEF	Sub-tropical Broadleaved Evergreen Forest
SCP	Semi-Automatic Classification Plugin
SCPF	Sub-tropical Chir Pine Forest
sd	Standard Deviation
SGB	Stochastic Gradient Boosting
SM	Strip Map
SNAP	Sentinel Application Platform
SOC	Soil organic carbon
SR	Stepwise Regression (Backward Elimination)
SRTM	Shuttle Radar Topography Mission
SVM	Support Vector Machine
SWIR	Short Wave Infrared
TanDEM-X	TerraSAR-X add-on for Digital Elevation Measurements
TIRS	Thermal Infrared Sensor
TM	Thematic Mapper
ToA	Top-of-Atmosphere
UN	United Nations
USGS	United States Geological Survey
UTM	Universal Transverse Mercator
VHF	Very High Frequency
VIF	Variance Inflation Factor
VIs	Vegetation Indices
WD	Wood Density
WGS	World Geodetic System
WV	Wave
WWF-P	World Wide Fund for Nature-Pakistan

Abstract

Context: Climate change is one of the greatest threats recently, of which the developing countries are facing most of the brunt. In the fight against climate change, forests can play an important role, since they hold a substantial amount of terrestrial carbon and can therefore affect the global carbon cycle. Forests are also an essential source of livelihood for a remarkably high proportion of people worldwide and a harbor for rich global biodiversity. Forests are however facing high deforestation rates. Deforestation is regarded as the most widespread process of land cover change (LCC), which is the conversion of one land cover type to the other land cover type. Most of this deforestation occurs in developing countries. Agricultural expansion has been reported as the most significant widespread driver of deforestation in Asia, Africa, and Latin America. This deforestation is altering the balance of forest carbon stocks and threatening biodiversity. Pakistan is also a low forest cover country and faces high deforestation rates at the same time, due to the high reliance of local communities on forests. Moreover, it is also the most adversely affected by climate change. Agricultural expansion and population growth have been regarded as the most common drivers of deforestation in Pakistan. Financial incentives such as 'Reducing Emissions from Deforestation and Forest Degradation, and the Role of Conservation of Forest Carbon, Sustainable Management of Forests and Enhancement of Forest Carbon Stocks' (REDD+) offer hope for developing countries for not only halting deforestation but also alleviating poverty. However, such initiatives require the estimation of biomass and carbon stocks of the forest ecosystems. Therefore, it becomes necessary that the biomass and carbon potentials of the forests are explored, as well as the LCCs are investigated for identifying the deforestation and forest degradation hit areas. Based on the aforementioned, the following research objectives/sub-objectives were investigated in the MHNP, which is adjoined with the capital city of Pakistan, Islamabad; **A)** Forest Biomass and Carbon Stock Assessment of Margalla Hills National Park (MHNP) **A.1)** Aboveground Biomass (AGB) and Aboveground Carbon (AGC) assessment of the Sub-tropical Chir Pine Forest (SCPF) and Sub-tropical Broadleaved Evergreen Forest (SBEF) using Field Inventorying Techniques **A.2)** Exploring linear regression relationship between Sentinel-1 (S1) and Sentinel-2 (S2)

satellite data with the AGB of SCPF and SBEF **A.3)** AGB estimation combining remote sensing and machine learning approach **B)** LC Classification and Land Cover Change Detection (LCCD) of MHNP for the time-period between 1999 and 2019 **B.1)** LC Classification for the years 1999, 2009 and 2019 using Machine Learning Algorithm **B.2)** LCCD of MHNP between 1999 to 2019.

Research Objective A) Forest Biomass and Carbon Stock Assessment of MHNP;

Materials and Methods: For the field inventorying, stratified random sampling was adopted. The field sampling was conducted from March 2019 to June 2019. There were 46 circular sampling plots, of 17.84 m radius, laid in SCPF and 31 circular plots were laid in SBEF. The diameter at breast height (DBH) of trees above 5 cm was recorded using DBH tape. The heights of the trees were recorded using a Vertex IV instrument. The following variables were calculated using prescribed equations; quadratic mean diameter (cm), volume (m^3), basal area (m^2), density, AGB (Mg), and AGC (Mg C). For AGC, a conversion factor of 0.5 was used. All the variables were scaled up to the hectares. Regression analysis was performed for exploring the linear relationships between the variables. In the case of a non-linear relationship, power regression was used. The Coefficient of Determination (R^2) was used for assessing the strengths of the statistical relationships between the variables. Means and standard deviations were calculated for the variables. For normality distribution of the data, *Shapiro-Wilk Test* was performed. *Wilcoxon Rank Sum Test* was used for the non-linear data for exploring the statistical differences between the two variables. Spearman correlation coefficients were also investigated between the two variables. A significance level of 0.5 was used for the statistical tests. The statistical analyses were performed in the RStudio software.

In the case of remote sensing, S2 Level-1C (for August 19, 2019) and S1 C-band SAR data were used in this study. For S2, band 2, band 3, band 4, and band 8 were downloaded using QGIS software. The S2 Level-1C are radiometrically and geometrically corrected products. The ToA reflectance for Sentinel-2 data was converted to BoA reflectance, using the Dark Object Subtraction (DOS) method, by employing the DOS1 algorithm of the SCP of the QGIS software. For S1,

Interferometric Wide Swath (IW) Ground Range Detection (GRD) Level-1 data, in dual polarization (VV+VH), was downloaded on August 24, 2019, from (https://scihub.copernicus.eu/). Pre-processing was performed in the SNAP software. Pre-processing steps involved; *Apply Orbit File*, *Thermal Noise Removal*, *Border Noise Removal*, *Calibration*, *Speckle Filtering*, *Radiometric Terrain Flattening*, *Range Doppler Terrain Correction.* S2 and S1 images were imported into the RStudio Software, and the study sites were extracted for further processing and analysis. Vegetation Indices VIs; Normalized Difference Vegetation Index (NDVI) and Enhanced Vegetation Index (EVI), from the S2 site image, were calculated using QGIS software. The Grey Level Co-occurrence Matrix (GLCM) technique was used for texture analysis. Three GLCM metrics; Entropy, Angular Second Moment (ASM), and Contrast, were calculated for both the S1 and S2 site images using QGIS software. The statistics for mean, maximum, standard deviation, and minimum for VIs, VV Polarization (from S1 site image) and VH Polarization (from S1 site image), and texture indices for S1 and S2 site images were computed using QGIS software. Overall, 16 predictor sets each for both forest types, SCPF and SBEF were formed. In total, there were 70 variables, for each forest type, which were used in this study. Two machine learning algorithms, Random Forest (RF) and Support Vector Machine (SVM), and Stepwise Regression-Backward Elimination (SR) were used for exploring the best model for the AGB mapping of the two forest types of the study area. For RF, 'randomForest' and 'caret' packages were used and for SVM, 'e1071 package' was used. The root mean square error (RMSE) and Coefficient of Determination (R^2) were used for the selection of the best model, with higher preference given to RMSE. RStudio was used for the analysis and spatial map prediction was performed using the 'raster' package of R. Final AGB maps were prepared in the QGIS software.

Results: The SCPF recorded a mean AGC of 73.36 ± 32.55 Mg C ha^{-1} and the SBEF recorded a mean AGC of 16.88 ± 25.81 Mg C ha^{-1}. A significant statistical difference was recorded between the mean AGC of the two forests (*W = 43, p < 0.05*). Mean AGB for SCPF was recorded as 146.73 ± 65.11 Mg ha^{-1}, while for SBEF it was 33.77 ± 51.63 Mg ha^{-1}. Again, a significant statistical difference was recorded between the mean AGB of the two forests (*W = 43, p < 0.05*). The DBH interval 35-40 cm for SCPF recorded the highest number of stems, 114, forming 17.81% of the

total stems of the SCPF. The DBH interval 10-15 cm contained the highest number of stems, 167, for SBEF. This interval formed 37.70% of the total stems of the SBEF. *Pinus roxburghii* had the highest contribution of the AGC (Mg C ha^{-1}) to the SCPF with 98.85% of the total. *Eucalyptus camaldulensis* had the highest AGC (Mg C ha^{-1}) contribution, with 33.65% of the total, for SBEF. The NDVI of MHNP ranged between -0.34 and 0.80. The EVI of MHNP ranged from -0.11 to 0.89. Linear regression analysis had shown weak statistical associations between the NDVI and the AGB of the two forests. Weak statistical associations were also recorded for the EVI and the AGB of the two forests. The VH and VV Polarizations from the two forests also showed weak statistical associations with the AGB of the two forests. RF was found to be the better algorithm for SCPF for AGB estimation. The final RF model was recorded for the predictor set 'S1 and VIs' having six variables. The RF model had an RMSE of 52.46 Mg ha^{-1} and an R^2 value of 0.31. The predicted AGB map for SCPF using the RF model recorded values ranging from 94.55 Mg ha^{-1}to 283.77 Mg ha^{-1}. A significant statistical association (R^2= 0.89) was recorded between the predicted and observed AGB of the SCPF. SVM was recorded as the best algorithm for the SBEF. The final model of SVM was recorded for the predictor set 'S1 and S2 Texture' containing nine variables. The RMSE for the final SVM model was recorded as 32.59 Mg ha^{-1} and the R^2 value was 0.21. The predicted AGB map for SBEF using the SVM model recorded values ranging from 9.67 Mg ha^{-1} to 30.92 Mg ha^{-1}. The predicted and observed AGB for SBEF recorded moderate statistical association (R^2= 0.4).

Research Objective B) LC Classification and LCCD of MHNP for the time-period between 1999 and 2019;

Materials and Methods: Three Landsat images i.e., Landsat-5 Thematic Mapper (TM) image (for April 28, 2009), Landsat 7 Enhanced Thematic Mapper Plus (ETM+) image (for July 14, 1999), and Landsat-8 Operational Land Imager (OLI) image (for April 8, 2019) were downloaded using QGIS software. These are Level-1 Tier-1 products that are geometrically and radiometrically corrected. The atmospheric correction was performed, using the DOS method, employing the DOS1 algorithm of the SCP of the QGIS software. Site areas were extracted from the Landsat images using RStudio. Seven land cover classes were identified which included i.e.,

Agricultural Land, Barren Land, SCPF, SBEF, Grassland, Settlements, and Water Body. These classes were identified using natural color composites, NIR composites, high-resolution imagery available from Google Earth, field visits, and experts' knowledge from the site area. The polygon-shaped selection was used for the collection of training samples. QGIS was used for this process. Overall, 105 polygons were created using a stratified random sampling approach. The polygons were saved as a shapefile and the shapefile was imported to RStudio for further analysis. The sample size of 272 pixels was used for avoiding the misbalance between training samples using the down-sampling approach. Supervised classification was performed using the RF algorithm in the RStudio. The 'randomForest' package was used for the LC classification using the RF algorithm. The raster files were imported in QGIS software and respective LC maps for the years 1999, 2009, and 2019 were developed. For the accuracy assessment, a field visit was conducted from March 2019 to June 2019 and 50 samples for each land cover class, except for the water body, were collected. The water body was not accessible thus 10 samples were collected from it using high-resolution imagery from Google Earth. Overall, there were 310 reference samples, which were collected using the stratified random sampling approach. The samples were saved as a shapefile which was imported to the RStudio for the accuracy assessments. The 'raster' package of R was used for this purpose. The accuracy measures i.e., overall accuracy, kappa coefficient, user's accuracy, and producer's accuracy were used. A confusion matrix for each LC classification was also generated. For change detection, a post-classification comparison method was employed, using QGIS software, for assessing the changes in the LC classes for time-periods i.e., 1999-2009, 2009-2019, and 1999-2019. The LCC in percentages and annual change rates in ha for LC classes were also calculated.

Results: For LC classifications, the SBEF had the highest cover percentages amongst all the land cover classes, which were 40.90%, 40.11%, and 43.21% for the years 1999, 2009, and 2019, respectively. Overall accuracies of 94.83%, 96.77%, and 97.09% were recorded for the years 1999, 2009, and 2019, respectively. Kappa coefficients of 0.93, 0.96, and 0.96 were recorded for the years 1999, 2009, and 2019, respectively. The highest decrease for the time-period 2009-2019 was

recorded for SCPF which was 14.99%. The overall highest increase, for the time-period 1999-2019, was recorded for agricultural land which was 130.62%.

Overall Conclusion: SCPF had a higher mean AGB and mean AGC compared to the SBEF. The difference can be attributed to the larger sizes of the trees in the SCPF compared to the SBEF. It may also be attributed to the species composition since pines have been reported to have more carbon stocks compared to broadleaved species. *Pinus roxburghii* and *Eucalyptus camaldulensis* recorded the highest AGC, compared to other tree species, for the SCPF and SBEF, respectively. The unimodal DBH distributions of the two forests hinted toward the undue pressures on these forests in the form of deforestation and forest degradation. NDVI and EVI for the two forests showed weak statistical associations with the AGB of the two forests. VH and VV polarizations also showed weak statistical associations with the AGB of the two forests. RF was recorded as a better algorithm for SCPF and SVM was recorded as a better algorithm for the SBEF. SBEF recorded the highest LC amongst all the land cover classes for the years 1999, 2009, and 2019. The highest decrease was recorded for SCPF for the time-period 2009-2019. Agricultural land had the highest increase amongst all the LC classes for the overall period from 1999-2019. Comparison with other studies had shown both the forests had lower AGB and AGC, which may be also lower in terms of their actual potential.

It is recommended that findings from this study should be adopted by Islamabad Wildlife Management Board (IWMB) and incorporated into the sustainable management plans for the MHNP. The design of REDD+ projects should be initiated by IWMB in cooperation with various national and international organizations. Research methodologies from this study should be adopted and included in future monitoring and research studies, related to forest biomass/carbon and LCCs, of the MHNP. Local communities should be involved in the conservation strategies and plans of the MHNP. The site and species-specific allometric equations should be developed for future AGB/AGC studies in MHNP.

1. Introduction:

1.1. Importance of Forest Biomass and Carbon:

Climate change is one of the greatest threats of recent times (Soutter and Mõttus, 2020); (Hilbig et al., 2013); (Poškus and Žukauskienė, 2017). It is defined as the shift in the climate patterns, which is mainly caused by Greenhouse Gas (GHG) emissions (Fawzy et al., 2020). CO_2 has mainly received widespread attention, among other GHG emissions, due to its increasing levels which have resulted in increasing temperatures, shifting precipitation patterns and unpredictable extreme events, etc. (Reichstein et al., 2013). The CO_2 concentration has risen from approximately 277 parts per million (ppm) in 1750, which was the beginning of the Industrial Era, to 409.85 ± 0.1 ppm in 2019 (Joos and Spahni, 2008); (Dlugokencky and Tans, 2020). Anthropogenic activities are the most responsible for causing this climate change (Xi-Liu and Qing-Xian, 2018). The severity of climate change can be seen in the fact that the average temperature over land for the period 2006-2015 was 1.53°C higher than the period 1850-1900 and also 0.66°C higher than the equivalent global mean temperature change (IPCC, 2019). Deforestation and forest degradation have led to an increase in GHG emissions from 490 ± 180 Gt CO_2 in 1970 to 680 ± 300 Gt CO_2 in 2010 (IPCC, 2007a). In addition, of the total anthropogenic GHG emissions from 2007-2016, almost 23% have come from Agriculture, Forestry, and Other Land Use (AFOLU) (IPCC, 2019). The anthropogenic use influences at various intensities about 60-85% of forests and 70-90% of other natural ecosystems (IPCC, 2019).

Forests are spread over 31% of the earth's surface, which makes up 4.06 billion hectares (ha) of the land surface (FAO, 2020a). Fig. 1 shows the global distribution and proportion of the forest area by climatic domain where the tropical domain forms the highest percentage of forest area with 45%, followed by boreal with 27%, temperate with 16%, and sub-tropical with 11%. Forest ecosystems are considered the main carbon pool in terrestrial ecosystems (Gower, 2003). They account for 80% of terrestrial carbon and also play an essential role in climate change mitigation (Liu

1

et al., 2017); (Chen et al., 2018). The mean forest carbon for the globe stands at 75 Mg C ha^{-1} (Rojas Montaño et al., 2017). The estimated annual carbon sequestration by forests is 2-4 gigatons (Qureshi et al., 2012). Forests, therefore, greatly affect the global carbon cycle which is related to the greenhouse effect (Costanza et al., 1998); (Li et al., 2020). Forests are also an essential source of income and livelihood for 1.6 billion people in the world and can significantly affect human lives (Mukul et al., 2020); (Liu et al., 2007). They also provide a range of ecosystem services as well as harbor immensely rich biodiversity (Brockerhoff et al., 2017).
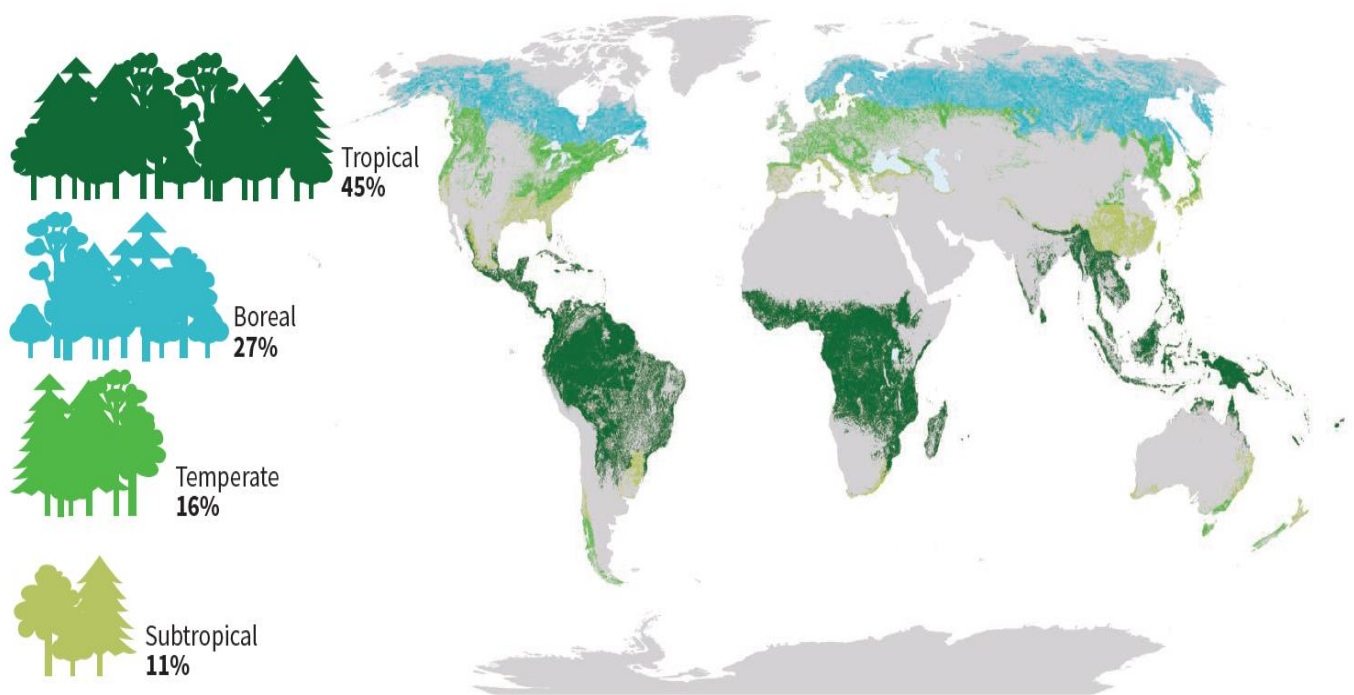
Fig. 1: Proportion and Distribution of Global Forest Area by Climatic Domain (FAO, 2020b)

The forest biomass is an important indicator that can be used for assessing the forest carbon status since carbon forms half of the dry weight of a tree (Vicharnakorn et al., 2014); (Bi et al., 2004); (Köhl et al., 2006); (Brown, 1997). The AFOLU offers one of the largest potentials for GHG emissions reduction through reduced deforestation and forest degradation, amounting to 0.4–5.8 Gt CO_2-eq per year (IPCC, 2019). However, according to the fourth assessment report of the Intergovernmental Panel on Climate Change (IPCC) (IPCC, 2007a), there is a limited

amount of information available regarding forest biomass and carbon status at both national and regional levels. For limiting warming to 1.5°C or 2°C, large-scale implementation of mitigation response options would require afforestation/reforestation activities over large areas (IPCC, 2019). The United Nations Framework Convention on Climate Change (UNFCCC) has also recognized the Aboveground Biomass (AGB) as an Essential Climate Variable (ECV) (Omar et al., 2017). ECVs are the physical, biological, and chemical variables or groups of variables that critically affect the earth's climate (Bojinski et al., 2014). The '*reducing emissions from deforestation and forest degradation and the role of conservation of forest carbon, sustainable management of forests and enhancement of forest carbon stocks*' (REDD+) is also a result-based financial incentive for developing countries for countering deforestation (Maraseni et al., 2014); (Köhl et al., 2020b) since 98% of the deforestation is occurring in developing countries (FAO, 2020a). REDD+ is also one of the cheapest climate mitigation options for tackling climate change (Golub et al., 2018). However, such global initiatives require quantification of forest biomass and carbon (Gibbs et al., 2007); (Koch, 2010); (Campbell, 2009).

AGB, generally, accounts for 70% to 90% of total forest biomass and is considered one of the most important carbon pools of forest ecosystems (Cairns et al., 1997); (Chen et al., 2018). Additionally, the disturbances such as forest fires, logging, and land use change, directly affect the AGB which results in a higher contribution to the carbon fluxes from this particular pool compared to the other carbon pools (Issa et al., 2020). AGB is usually measured in the metric tons of dry matter per hectare (e.g. t ha^{-1} or Mg ha^{-1}) or in metric tons of carbon per hectare (e.g. t C ha^{-1} or Mg C ha^{-1}) (Rodríguez-Veiga et al., 2017); (Omar et al., 2017). Forest biomass generally is the total sum of living mass present above and below the ground including trunks, leaves, branches, roots, etc. (Chandola, 2014). These are the following carbon pools generally found in forest ecosystems; AGB, Belowground Biomass (BGB), deadwood, litter, and soil organic carbon (SOC) (Buchholz et al., 2014). AGB includes all living biomass above the soil including stems, shrubs, stumps, branches, barks, seeds, and foliage (FAO, 2010). BGB includes all the living biomass of the roots, of which, fine roots less than 2 mm are excluded because it's hard to distinguish them from the soil organic matter and litter (FAO, 2010). Deadwood is

3

comprised of all non-woody biomass that is not contained in the litter, either standing, lying on the ground, or in the soil and it also includes wood that is lying on the surface, dead roots and stumps that are larger than or equal to 10 cm in diameter or any other diameter that is used by the country (FAO, 2010). Litter includes all non-living wood biomass, above the mineral or organic soil, with a diameter less than the minimum diameter for the lying Deadwood (e.g. 10 cm) (FAO, 2010). SOC includes organic carbon in mineral and organic soils (including peats) for a specified depth chosen by the country and that is consistently applied through the time series (FAO, 2010). Fig. 2 shows the proportion of different carbon pools, with SOC the highest with 45%, followed by AGB and BGB (here collectively shown as living biomass) with 44%.
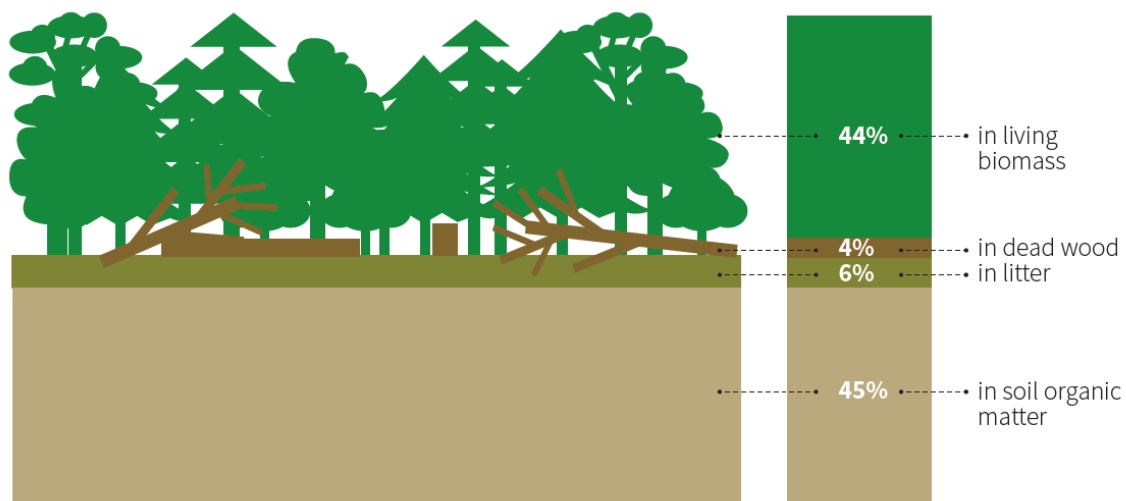
Fig. 2: Proportion of Carbon Stock in Forest Carbon Pools (FAO, 2020b)

Pakistan's forest area is 4.6%, according to the (FAO, 2020a). It is a low forest cover country (LFCC) (Aftab and Hickey, 2010). Forest per capita in Pakistan is only 0.03 compared to the global average of 1 ha (Ali et al., 2020). Despite this, Pakistan has faced one of the highest deforestation rates of 0.94% annually (from 2010-2020) in the world (FAO, 2020a). In Pakistan, there is a high reliance of local communities on the forestry resources living in and around the forests (Hussain et al., 2019); (Ali et al., 2005); (Shahbaz et al., 2007). For instance, 60% of the Himalayan Forests in

4

Pakistan have been destroyed due to the marginalized socio-economic conditions of the communities, rapidly growing population, and lack of substitute fuel (Gairola et al., 2008); (Lindner et al., 2010); (Pokhriyal et al., 2010). According to an estimate, 20% of the world population depends on forestry resources for meeting their essential livelihood means, which further signifies the importance of forestry resources (Cheng et al., 2019). Vedeld et al. (2007) also estimated that 22 percent of the average household income of the 19 developing countries has come from forest resources. Moreover, forest resources have contributed 10-12% to the average household income in Asia (Mukul et al., 2016). Pakistan is also one of the developing countries which are most affected by the adverse effects of climate change (Khan et al., 2020). This is despite Pakistan's contribution is only a meager 0.8% to the world's GHG emissions (Sajid, 2020); (Hussain et al., 2019b). The climate change effects on Pakistan over the last decade have been in the form of increasing floods, high temperatures, extreme water scarcities, increasing droughts, and increasing diseases and pests (Smit and Skinner, 2002). Pakistan was ranked overall as the 29th most vulnerable country to climate change in 2009-2011, similarly, it was placed 16th in 2010-2011, 12th in 2012, and 8th in 2015 (Abid et al., 2016); (Khan et al., 2020). The severe droughts that occurred from 1999 to 2003 and floods in 2010, 2011, 2012, and 2014 exacerbated the risky situation arising from climate change in Pakistan (Abid et al., 2016). The climate change situation has caused environmental destruction which has resulted in the loss of over $9.6 billion, since 2010, to the economy of Pakistan (Lin and Raza, 2019). Pakistan has also recognized the importance of the forestry sector for mitigating climate change (Hussain et al., 2019a); (Lin and Ahmad, 2016).

Protected areas are considered key management tools for the conservation of biodiversity and for avoiding deforestation, hence also contributing to the conservation of forest carbon stocks (Geldmann et al., 2013). The International Union for Conservation of Nature (IUCN) has defined a protected area as "*a clearly defined geographical space, recognized, dedicated and managed, through legal or other effective means, to achieve the long-term conservation of nature with associated ecosystem services and cultural values*" (Dudley, 2008). The protected areas have expanded from a mere 8.5% of land and inland waters in 2004 to 14.7%

in 2015 (Lewis et al., 2019). The effectively managed protected areas would generally improve biodiversity and ecosystem services (Adams et al., 2019); (Lanzas et al., 2019). Due to this, the Aichi Biodiversity Target 11 of the Strategic Plan for Biodiversity 2011–2020 has called for Parties to the Convention on Biological Diversity (CBD) for conserving at least 17% of terrestrial and inland water areas, and 10% of coastal and marine areas, especially areas of particular importance for biodiversity and ecosystem services, as protected areas by 2020 (Li et al., 2020). The protected areas are, however, faced with anthropogenic pressures which can result in increased deforestation, especially in developing areas (Islam et al., 2018); (Islam et al., 2019); (Jones et al., 2018); (Spracklen et al., 2015). National Park, which is a category II of protected areas, is a *"Large natural or near-natural areas protecting large-scale ecological processes with characteristic species and ecosystems, which also have environmentally and culturally compatible spiritual, scientific, educational, recreational and visitor opportunity"* (Dudley, 2008). There are 28 National Parks in Pakistan and overall protected areas (different categories including National Parks) cover 10.4% of the total land area of Pakistan (Khan, 2003).

1.2. Forest Biomass Measurements using Forest Inventory and Remotely Sensed Parameters:

AGB can only be measured directly and accurately through destructive sampling (Wilkes et al., 2018). This is however laborious, expensive, impractical, and rarely adopted (Ketterings et al., 2001); (Dumitrașcu et al., 2020). Destructive sampling is also not recommended for places where there is threatened flora and fauna (Kumar and Mutanga, 2017). Non-destructive methods include the use of allometric equations for the estimation of AGB (Rodríguez-Veiga et al., 2017); (Debastiani et al., 2019). The allometric equations are statistical models based on the forest inventory data such as diameter at breast height (DBH), height, wood density, and forest type (Chave et al., 2004). The forest inventory data is one of the most reliable sources for carbon estimation globally (Zhao et al., 2019). The choice of the allometric equation is, however, critical, where an inconsiderate selection of the equation may lead to errors of up to 79% (Clark et al., 2001). For reduction in

6

uncertainties in AGB estimation, site and species-specific allometric equations have been emphasized (Soares and Schaeffer-Novelli, 2005). In Pakistan, however, there is a lack of allometric equations for local tree species for AGB estimation (Ismail et al., 2018). The other non-destructive method, involving forest inventorying data, includes the use of the Biomass Expansion Factors (BEF) and Wood Density (WD) to convert the tree volume to the AGB (Asrat et al., 2020); (Hossain et al., 2020); (Sun et al., 2020); (Lu et al., 2016). BEF is unit less and is defined as *"the ratio of oven-dried tree biomass to either the commercial or stem oven-dried biomass including bark"* (Schepaschenko et al., 2018); (IPCC, 2003). The BEF accounts for the non-merchantable/non-commercial portions of the tree (Njana, 2017). The value for the BEF mainly depends on the tree species and tree age (Koch, 2010). The non-destructive methods, involving forest inventorying data, however, are not feasible for large-scale areas (Kumar and Mutanga, 2017); (Dumitrașcu et al., 2020); (Fassnacht et al., 2014); (Ghosh and Behera, 2018).

Due to mainly the advantage to cover larger spatial areas, remote sensing-based approaches, combined with the field inventorying data, are preferred for the AGB estimations (Goetz et al., 2009); (Issa et al., 2020); (Dang et al., 2019). Remote sensing methods are also lesser time-consuming (Vashum and Jayakumar, 2012); (Issa et al., 2020). Remote sensing methods, therefore, are considered the most popular methods for AGB estimation (Lu et al., 2016). The United Nations collaborative programme on REDD (UN-REDD) has also advocated for the inclusion of remote sensing methods in national forest monitoring systems of the countries due to their effectiveness (Dang et al., 2019). There are mainly three categories of sensors involved in remote sensing methods; 1) passive sensors 2) active sensors such as Radio Detection and Ranging (Radar) 3) Light Detection and Ranging (LiDAR) (which is also an active sensor) (Issa et al., 2020); (Li et al., 2020); (Rodríguez-Veiga et al., 2017); (Su et al., 2016); (Shao and Zhang, 2016); (Kumar et al., 2015). All three categories have their advantages and disadvantages (Issa et al., 2020).

Passive sensors/optical remote sensing have been used widely by numerous researchers for AGB estimation (Kumar and Mutanga, 2017); (Thenkabail et al.,

2004); (Hyde et al., 2006); (Foody et al., 2003); (Sun et al., 2002); (Rahman et al., 2005); (Zheng et al., 2004); (Basuki et al., 2013); (Kajisa et al., 2009); (Muukkonen and Heiskanen, 2005); (Li et al., 2008); (Calvão and Palmeirim, 2004); (Dong et al., 2003). These have been commonly employed for AGB estimation because of high correlations between the spectral bands and/or vegetation indices (VIs) with the AGB (Zhao et al., 2016); (Sinha et al., 2015). Passive sensors utilize the energy from the sun and cannot operate without sunlight (Indirabai et al., 2019). The spatial resolutions for the passive sensors vary from less than one meter to hundreds of meters (Kumar and Mutanga, 2017). The signals obtained by the passive sensors are sensitive to the forest canopy structure (Gibbs et al., 2007); (Foody et al., 2001). The passive sensors have been available and operating for a very long time and provide rich data archives (Rodríguez-Veiga et al., 2017); (Issa et al., 2020); (Beamish et al., 2020); (Gómez et al., 2016). For instance, Landsat and the National Oceanic and Atmospheric Administration (NOAA) Advanced Very High Resolution Radiometer (AVHRR) missions have been operating for the last 40 years and more (Rodríguez-Veiga et al., 2017); (Lu, 2006). The other advantage is that high to coarse resolution imageries from the passive sensors can be obtained for free or low cost (Rodríguez-Veiga et al., 2017); (Issa et al., 2020). The main drawback of the passive sensors is that they are obscured by the presence of the cloud cover which becomes especially challenging for tropical forests (Rodríguez-Veiga et al., 2017); (Kumar et al., 2019). Some of the passive sensors include; Coarse Spatial Resolution (> 100 m): Moderate Resolution Imaging Spectroradiometer (MODIS), AVHRR, Meteosat and SPOT Vegetation; Medium Spatial Resolution (10-100 m): Sentinel-2 (S2), Thematic Mapper (TM), Enhanced Thematic Mapper Plus (ETM+), Operational Land Imager (OLI) and SPOT; Fine/High Spatial Resolution (< 5m): QuickBird, WorldView-2 and IKONOS (Issa et al., 2020).

Radar can acquire satellite data irrespective of cloud covers, weather, and light conditions (Lu, 2006). Being an active sensor, Radar has its source of illumination and does not depend on sunlight like the optical remote sensing sensors (Chan and Koo, 2008); (Flores-Anderson et al., 2019). Some other characteristics of the Radar sensors include; Penetration through the vegetation, soil, and to a certain degree in dry snow; Sensitivity to the following: surface roughness, dielectric properties and

moisture, wave polarization and frequency; and volumetric analysis (Sinha et al., 2015). The dielectric properties are an essential component of a material that describes its interaction with an electrical field (McDonald et al., 2002); (Ashish and Kurtadikar, 2017). Synthetic Aperture Radar (SAR) is a technique/system of a Radar that uses signal processing for improving the spatial resolution beyond the limitation of physical antenna aperture (Curlander and McDonough, 1991). SAR uses the forward motion of an actual antenna for synthesizing a very long antenna which allows the use of longer microwave wavelengths and obtaining good spatial resolutions with reasonable-sized antenna structures (Chan and Koo, 2008). The energy utilized by the SAR for remote sensing falls in the electromagnetic microwave domain which ranges from 1 mm to 1 m in wavelengths or 0.3–300 GHz in terms of frequency (Konings et al., 2019). The most common microwave bands used in SAR remote sensing include X-band (2.4-3.8 cm wavelength), C-band (3.8-7.5 cm wavelength), L-band (15-30 cm wavelength) and some experiments have also used S-band (7.5-15 cm), P-band (30-100 cm wavelength) and Very High Frequency (VHF) band (> 1 m wavelength) (Ackermann, 2015); (Hanes, 2014); (Flores-Anderson et al., 2019). In SAR, the reflection of the energy from the objects back to the sensor is termed a backscatter and the earth features that interact with the transmitted energy are termed scatterers (Köhl et al., 2006). SAR systems are generally used in forest monitoring (Köhl et al., 2006); (Flores-Anderson et al., 2019). The longer wavelengths have a deeper penetration into the forest canopy and have a better correlation with the AGB (Woodhouse, 2006); (Jensen, 2009); (Sun et al., 2002). AGB can be retrieved from radar using regression and inversion models (Hanes, 2014). Various researchers have shown that the use of SAR sensors for estimating AGB holds potential (Berninger et al., 2018); (Wijaya, 2009); (Debastiani et al., 2019); (Hamdan et al., 2014); (Ghosh and Behera, 2018); (Huuva et al., 2020); (Schlund and Davidson, 2018).

Polarization of the electromagnetic waves, which is also an important parameter for the SAR data, refers to the orientation of the electric field intensity (Ackermann, 2015). The SAR sensors generally emit signals in horizontal (H) or vertical (V) polarizations (Sinha et al., 2015). The four general polarization combinations for SAR sensors include; 1) HH: the emitted signal has horizontal polarization and the

received backscatter also has horizontal polarization 2) HV: the emitted signal has horizontal polarization and the received backscatter has vertical polarization 3) VH: the emitted microwave signal has a vertical polarization and the received backscatter energy has a horizontal polarization 4) VV: the emitted signal has a vertical polarization and the received signal will also be in vertical polarization (Ghasemi et al., 2011). HH and VV are co - or like polarized and HV and VH are cross-polarized signals (Jensen, 2009). Similarly, based on the transmit-receive microwave polarizations, the SAR sensors can be categorized into; 1) Single-Polarization: same polarization is used for transmitting and receiving the signal 2) Cross-Polarization: different polarization is used for transmitting and receiving the signal 3) Dual-Polarization: the signal is transmitted in one polarization and received in two polarizations simultaneously (e.g. HH and HV) 4) Quad-Polarization: all four polarization combinations are used for transmitting and receiving the signals (Flores-Anderson et al., 2019); (Gaber et al., 2017). The cross-polarized microwave signals are more sensitive to the AGB (Sinha et al., 2015). Sentinel-1 (S1), Advance Land Observing Satellite (ALOS)-2, RADARSAT 2, RADARSAT constellation mission, TerraSAR-X, TerraSAR-X add-on for Digital Elevation Measurements (TanDEM-X), etc. are some of the SAR satellite missions. Some of the limitations of SAR sensors include the saturation problem, expensive satellite datasets, data processing difficulties, and complex interactions with the forests (Sinha et al., 2015).

LiDAR is a relatively new technology that has been used in AGB estimation (Kumar and Mutanga, 2017). It is an active-ranging technology that uses the shorter wavelength of near-infrared laser light (e.g. 1040 nm) and records its backscatter from the target object (Jensen, 2009); (Sun and Liu, 2019). It can effectively provide the forest canopy with a 3-Dimensional structure which can be further used for extraction of forest height and other biophysical parameters (Issa et al., 2020); (Sun and Liu, 2019); (Shan and Toth, 2008); (Vosselman and Maas, 2010). LiDAR systems can be mounted on aircraft, terrestrial platforms, and satellites (Maltamo et al., 2014). Various researchers have demonstrated a high degree of precision by using high-resolution LiDAR for AGB estimation (Bortolot and Wynne, 2005); (Thomas et al., 2006); (Nelson et al., 2007); (Lu et al., 2020); (Salum et al., 2020); (Saarela et al., 2020). The National Aeronautics and Space Administration's (NASA)

Global Ecosystem Dynamics Investigation (GEDI) and NASA's Ice Cloud and land Elevation Satellite (ICESat-2) are two such examples of LiDAR systems mounted on satellite platforms (Duncanson et al., 2020). The GEDI, however, is the first space-borne LiDAR mission that is specifically designed for vertical forest structures (Dubayah et al., 2020). The major drawback associated with LiDAR is that it is very costly, which makes it difficult particularly for developing countries to acquire LiDAR data and sensors for AGB estimation (Hernández-Stefanoni et al., 2020); (Issa et al., 2020). Nonetheless, despite various drawbacks, passive/optical, active/SAR/microwave and LiDAR techniques still have attracted scientific interest in the estimation of the AGB (Sinha et al., 2015). Fig. 3 shows the comparative penetration, through the forest canopy, of the three widely used remotely sensed techniques for AGB estimation.
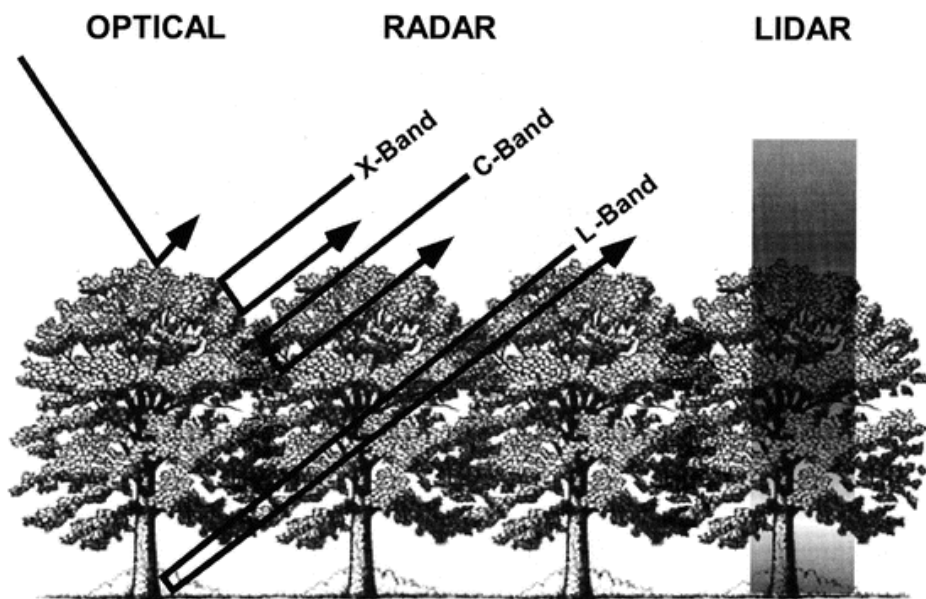
Fig. 3: Comparative Penetration of three Remote Sensing Techniques in the Forest Canopy (Pancel and Köhl, 2016).

1.3. Parametric and Non-Parametric Based Algorithms:

The linear, quadratic, exponential and logarithmic regression equations have been the most common regression equations which have been used for the AGB

estimation using field inventory parameters (Husch et al., 2002); (Ghosh and Behera, 2018). Parametric approaches/models such as linear regression, non-linear regression, multiple linear regression (MLR), etc. have also been the most common approach adopted for the estimation of AGB using remote sensing parameters (Lu et al., 2016); (Skowronski et al., 2014); (Kumar et al., 2013); (Li et al., 2019); (He et al., 2013). In these approaches, in case of the remote sensing, the first empirical relationship between AGB and remote sensing parameters is established and subsequently, this relationship is applied to the pixels of the image (Song, 2013); (Heiskanen, 2006). The parametric approaches are easy to implement, however, they require fulfilling assumptions like normal distribution of the data and absence of multicollinearity (Song, 2013); (Rodriguez-Galiano et al., 2012); (Breiman, 2001a). Parametric models also do not gauge the complex and non-linear relationship between the forest variables and remote sensing parameters (Li et al., 2019); (Zhu and Liu, 2015); (Ghosh and Behera, 2018). Non-parametric methods are highly powerful methods that can handle complex and non-linear problems (Breiman, 2001b); (Li et al., 2020). Non-parametric methods also do not depend on the distribution of the data (Ghosh and Behera, 2018); (Mutanga et al., 2012); (Rodriguez-Galiano et al., 2012). The use of non-parametric (which are often called machine learning algorithms) models have gained popularity and have been preferred over parametric-based algorithms for AGB estimation (Lu et al., 2016). Various studies have utilized non-parametric machine learning-based algorithms for the estimation of AGB using remote sensing parameters (Lu et al., 2016); (Jafari et al., 2020); (Li et al., 2020); (Ghosh and Behera, 2018); (Dang et al., 2019); (Deb et al., 2020).

The Random Forest (RF) and Support Vector Machine (SVM) algorithms, therefore, have also been used in this study owing to their wide use in estimating AGB by combining remote sensing parameters and field inventory data (Deb et al., 2020); (Opelele et al., 2021); (Yadav et al., 2021); (Liu et al., 2020); (Purohit et al., 2021); (López-Serrano et al., 2020); (Schuh et al., 2020); (Qiu et al., 2020). The RF and SVM algorithms assist in the interpretation and structuring of the models with the selected parameters (Breiman, 2001b); (Biau and Scornet, 2016).

1.4. Land Use/Land Cover Change and Classification:

Land use (LU) and land cover (LC) are two concepts that are often used interchangeably (Mishra et al., 2020). LC is the biophysical characteristics of the surface of the earth that includes vegetation distribution, water, soil, and other land features and land use is how the land has been utilized by humans (Liping et al., 2018).

LC can be directly observed using both fields as well as remote sensing images but LU may not be easily recognized and often requires ancillary information such as socio-economic data (Verburg et al., 2009). LU/LC has been identified as one of the major determining factors influencing global change with impacts on ecosystems and climate change (Foley et al., 2005); (Verburg et al., 2009).

LU/LC Change (LCC) is the conversion of LU/LC types into different LU/LC types (Pielke et al., 2011). Erb (2012) has identified two aspects of LU/LCC; i) Changes in LC: as already mentioned, conversion of LU/LC to another type, either expansion or contraction ii) Changes in LU/LC intensity: it is the intensity with which a LU/LC is utilized, however, changes in the intensity may not necessarily result in a change of an LC but may cause ecological changes. LCCs have occurred on vast areas of the earth's surface (Galicia and García-Romero, 2007). An increase in population and advances in technologies that have resulted in rapid economic development have been considered to put mainly the LC category of forests under stress, especially in developing countries (Meli Fokeng et al., 2020); (Pielke et al., 2011). For instance, the world population continues to increase at an alarming rate and is expected to reach 9.7 billion in 2050, and 11.2 billion by the turn of the century (UN, 2015). Geist and Lambin (2002) have distinguished LCC causes into; i) Proximate causes: human activities/immediate actions originating at local levels directly impacting LCs such as agricultural expansion etc. ii) Underlying causes: social processes that strengthen the proximate causes which may operate at a local level or may influence from national or global level such as in the form of population growth and agricultural policies etc.

The human-induced changes in LC have also altered the carbon fluxes of the terrestrial ecosystems (Li et al., 2018); (Clerici et al., 2014) and have contributed in a significant manner to the global CO_2 emissions (IPCC, 2014). The irrational use of land seriously degrades its original carbon stock potential (Lal, 2008). Deforestation is considered an essential and most widespread process of LCC (Lambin et al., 2001); (Lambin et al., 2003); (Rodríguez-Veiga et al., 2020). The IPCC has also emphasized that the conversion of forests to other LC types should be referred to as deforestation (Hu et al., 2019). Deforestation historically has been responsible for a large part of human-induced GHG emissions globally (IPCC, 2007b). It has been considered a global problem and is predicted to continue at an alarming rate in the future as well (Foley et al., 2005); (d'Annunzio et al., 2015). The most common drivers of deforestation in Asia have been classified as logging, agricultural expansion, urbanization, mining, and grazing (Hosonuma et al., 2012). Agricultural expansion, however, has been described as the largest cause of deforestation, ranging from 70% to 90 %, in Asia, Africa, and Latin America, according to various estimates (Nepstad et al., 2008); (Gutiérrez-Vélez et al., 2011); (Hosonuma et al., 2012). Williams et al. (2021) have also projected that 87.7% of the terrestrial vertebrate species will lose their habitat due to an increase in agricultural expansion by 2050.

Pakistan recorded a population of 208 million in 2017, which makes an annual growth rate of 2.4% compared to the previous census held in 1998 (Goujon et al., 2020). The growth rate is twice the average rate of South Asian countries, which is 1.2%, and if nothing changes Pakistan will double its population in 29 years compared to the South Asian countries which will need 58 years for doing so (Goujon et al., 2020). The increase in population at alarming rates in Pakistan has led to the rise in urbanization (Khan et al., 2021). According to an estimate, about 93% of global urbanization is occurring in developing countries alone (Natasha et al., 2020). There has also been a substantial increase in the agricultural area followed by the huge investments made by the government in Pakistan over the several decades (Ahmad, 2001). This has made the agricultural sector to be the largest contributor to the economy of Pakistan constituting 24% of its GDP and employing

14

almost half of its population (Aziz, 2021); (Ali et al., 2020); (Rehman Zia et al., 2020). Generally, population expansion combined with economic development, therefore, has been responsible for extensive LCC in Pakistan (Aziz, 2021). Agricultural expansion and population growth have been more specifically noted as the most common drivers of deforestation in Pakistan since deforestation is the most common form of LCC as already mentioned (Lodhi et al., 1998); (Nüsser, 2000); (Qasim et al., 2011); (Shehzad et al., 2014), followed by timber extraction, poverty, administrative reform, poor management, human-induced fires and road construction (Qamer et al., 2012); (Ali et al., 2005); (Ullah et al., 2021). For a healthy economy, 25% of the land surface has been recommended to be covered with forests, but as already mentioned, Pakistan is classified as an LFCC (FAO, 2012). Furthermore, there is no national-level LU/LC policy existing in Pakistan (Aziz, 2021). It is also feared that the megaprojects, which are considered to be at the core of socio-economic development in Pakistan such as the China-Pakistan Economic Corridor (CPEC) etc. to further aggravate LCC because of the absence of appropriate LU/LC policy at a national level for specifically addressing the ensuing issues (Samie et al., 2017). CPEC is an initiative started by China that focuses on the construction of railways, highways, optical fiber, oil and gas pipelines, etc. in Pakistan (Chen et al., 2017).

LC and LCC mapping are considered crucial steps for sustainable development planning considering their direct effects on ecosystem processes (Mei et al., 2016). Furthermore, analysis of LCC based on long-term satellite data is useful for understanding the patterns in LCC and can provide important information for policymakers (Hu et al., 2019). Remote sensing has been extensively used in LCC mapping at local and global scales (Yin et al., 2018); (Clark et al., 2012). A boom in the use of remote sensing in the recent decade can also be noticed further by the arrival of advanced sensors along with the open access data policy (Pouliot et al., 2014). Generally, few studies have focused on LCC in Pakistan in the past (Samie et al., 2017). However, it has been changing over time concerning its increasing importance. For instance, Chen et al. (2017) investigated the influence of LCC on the carbon stocks of the terrestrial ecosystems in Pakistan, using Landsat 5 TM data, and reported the decrease in future carbon stocks due to the business as usual (BAU) scenario. Gilani et al. (2020) studied the LCC in the capital city of Islamabad

that have occurred over four decades from 1976 to 2016, using Landsat 3 Multispectral Scanner (MSS), Landsat 5 TM, Landsat 7 ETM+ and Landsat 8 OLI data, and highlighted the increase in settlements and decrease in forest cover during this period. (Khan et al., 2020) also investigated the LCC in Islamabad from 1993 to 2018, using Landsat 5 TM and Landsat 8 OLI/Thermal Infrared Sensor (TIRS) data, with a major impact on the land surface temperature and reported an increase in impervious surfaces and decrease in forest cover increasing temperatures. Mannan et al. (2019a) investigated the LCC from 1998 to 2018, using Landsat 5 TM and Landsat 8 OLI data, and its impacts on the forest carbon stocks for the foothills of the Himalayan mountains of Pakistan and reported a decrease in forest carbon stocks and increase in agricultural lands and settlements. Tariq et al. (2021) investigated the LCC from 2000 to 2015 for the Fateh Jang, Attock District, Pakistan, using Landsat 7 ETM+ and Landsat 8 OLI/TIRS data, and reported a decrease in the vegetation area anan d increase in the settlements. Mazhar and Fadia (2019) studied the LCC from 1999 to 2019 for the city of Gujranwala, Pakistan, using Landsat 5 TM, Landsat 7 ETM+ and Landsat 8 OLI, and reported the decrease in vegetation and increase in settlements.

There are generally three types of pixel-based remote sensing image classification techniques; supervised unsupervised and hybrid classification (Li et al., 2014). Unsupervised classification is the computer-automated pixel-based classification that does not require prior knowledge of the study area and includes the following techniques i.e. K-means and Iterative Self-Organizing Data Analysis (ISODATA) etc. (Li et al., 2014). The hybrid classification involves the combination of supervised and unsupervised classifications (Kantakumar and Neelamsetti, 2015). In the supervised classification, the user selects respective training sets for the classification of different LC classes based on prior experience and knowledge of the respective area (Mather and Tso, 2016). Supervised classification is the most frequently used technique for image classification (Richards and Jia, 2006); (Mather and Tso, 2016). The supervised classification techniques include RF, spectral angle mapper (SAM), SVM, decision tree (DT), multilayer perceptron (MLP), maximum likelihood classifier (MLC), etc. (Ma et al., 2019); (Shih et al., 2019). The use of supervised machine learning algorithms in LC classifications has recently gained considerable

momentum (Talukdar et al., 2020a); (Maxwell et al., 2018). The machine learning algorithms i.e. RF, SVM, etc. have been outperforming the traditional statistical classifiers i.e. minimum distance classifier (MDC), MLC, etc. in terms of accuracy and reliable results, particularly in case of abundant data (Shih et al., 2019); (Schneider, 2012); (Pal and Mather, 2005). Numerous studies have been carried out which have used machine learning algorithms for the LC classifications (Talukdar et al., 2020b); (Zhang et al., 2019); (Teluguntla et al., 2018); (Pal, 2005). RF has particularly gained popularity for LC classifications due to its easy use and high accuracy (Pal, 2005); (Belgiu and Drăguţ, 2016); (Talukdar et al., 2020a). RF is also insensitive to noise or overtraining, which shows its ability to handle irregular data (Breiman, 2001b). RF is more robust than the single decision tree and easier to implement compared to other advanced algorithms such as SVM (Chan and Paelinckx, 2008); (Breiman, 2001b).

1.5. Research Objectives:

Based on the aforementioned, the following research objectives/sub-objectives were investigated in the study area, Margalla Hills National Park (MHNP);

A. Forest Biomass and Carbon Stock Assessment of MHNP.

A.1. AGB and AGC assessment of the Sub-tropical Chir Pine Forest (SCPF) and Sub-tropical Broadleaved Evergreen Forest (SBEF) using Field Inventorying Techniques.

A.2. Exploring linear regression relationship between S1 and S2 satellite data with the AGB of SCPF and SBEF.

A.3. AGB estimation combining remote sensing and machine learning approach.

B. LC Classification and Land Cover Change Detection (LCCD) of MHNP for the time-period between 1999 and 2019.

B.1. LC Classification for the years 1999, 2009, and 2019 using Machine Learning Algorithm

B.2. LCCD of MHNP between 1999 to 2019

2. Study Area:

The MHNP is spread over an area of 17,386 ha (Mannan et al., 2018). It is situated between 73°7'3.32" E, 33°41'59.61" N and 73°1'34.07" E, 33°45'2.87" N (WWF-Pakistan, 2009). The elevation of the MHNP is between 1,347 to 3,907 feet. The MHNP consists of three zones i.e., Margallah hills, Shakar Parian, and Rawal Lake. The Margallah hills Zone, however, forms most of the MHNP and is the extension of the Himalayan range. The MHNP has a rough topography with some steep slopes and various gullies.
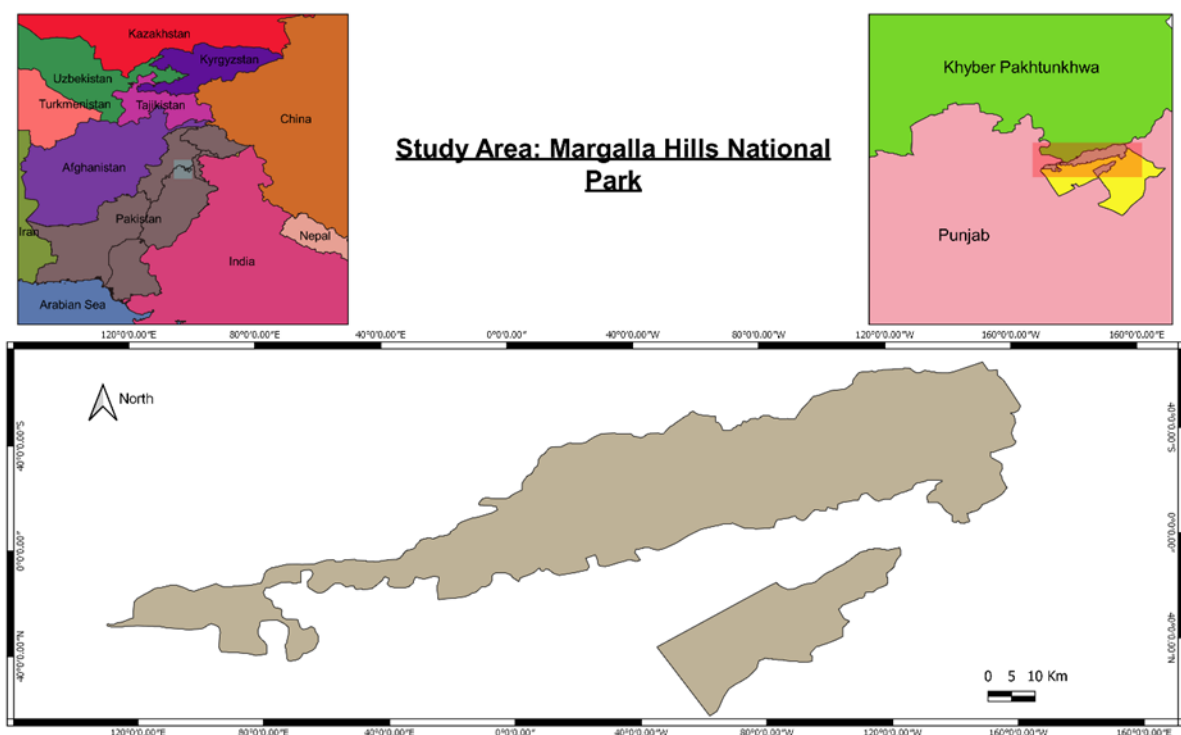
Fig. 4: Overview of the Study Area

According to Fig. 4, it can be seen that the MHNP is adjoined with the Federal Capital City of Pakistan, Islamabad, highlighted in yellow (Rawal Lake and Shakar Parian are located within the city and the Margalla Hills are located to the north of the city), and it is also extended to the Khyber Pakhtunkhwa Province. The MHNP was declared as a National Park on 27 April 1980 under Section 21(1) of the Islamabad Wildlife (Protection, Conservation, and Management) Ordinance, 1979 (Himalayan Wildlife Foundation, 2007). Before 1960, much of the area was classified

as a 'Reserve Forest'. Later, however, the area was declared a 'Wildlife Sanctuary' under the West Pakistan Wildlife Protection Ordinance, 1959 (Himalayan Wildlife Foundation, 2007).

There are 27 villages located within the boundaries of the MHNP. Agriculture is the mainstay for the subsistence of the people (Akbar, 2012). The climate of the area is subtropical semi-arid. The MHNP lies in the monsoon belt, and it experiences two rainy seasons: Winter rains from January to March, whereas summer rains from July to September. For the winter season, the temperature ranges from 1-15 °C, and for summer the temperature between 20-40 °C can be recorded. Specifically, MHNP has five seasons which are i.e., winter (December-February), spring (March-April), summer (May-June), monsoon (July-September), and autumn (November) (Anwar and Chapman, 2000). The average annual rainfall is 1,000 mm (Himalayan Wildlife Foundation, 2007). The soil of MHNP is mainly composed of limestone (Butt et al., 2015).

The flora of the MHNP includes 101 families, 548 genera, and 608 species (Akbar, 2012). The MHNP is composed of two types of forests i.e. SBEF and SCPF (Mannan et al., 2018).

The SCPF is predominantly located above the 900 m elevations (Himalayan Wildlife Foundation, 2007). The SCPF is mainly characterized by the *Pinus roxbughii* Sarg., which forms the main canopy. A heavy needle fall of the *Pinus roxburghii* occurs in May every year forming a thick carpet, which causes forest fires in this forest, due to the presence of resins in the needles (Gupta et al., 2020). Forest fires mainly occur due to human activities (Himalayan Wildlife Foundation, 2007). The understorey, which is mainly in the form of shrubs, is sparse. The shrub species include i.e., *Myrsine Africana* L., *Woodfordia fruticosa* (L.) Kurz, *Berberis lyceum* Royle etc. The grasses include i.e., *Themeda sp.* and *Heteropogon contortus* (L.), etc. The soil is light sandy, of moderate fertility, and has low pH values. Other areas in Pakistan where this forest is found include Murree Hills, Swat, Shinkiar,i etc. (Nizami, 2010).

The SBEF is classified as an arid forest and usually is composed of branchy trees, which vary from complete closure due to favorable conditions to scattered trees or shrubs on the drier sites (Sheikh, 1993). These are low forests with species that are mostly thorny and are often with evergreen leaves (Sheikh, 1993). The larger trees can be seen in valleys where deep soil and adequate water are available. Generally, these forests are encountered by noticeable erosion and are characterized by gullies and deep ravines, which makes the rocks and boulders common features to observe. A good amount of grasses and herbs, as understorey vegetation, may also develop during the monsoon season with the availability of water (Himalayan Wildlife Foundation, 2007). Some of the tree species include *Acacia modesta* Wall., *Cassia fistula* L., *Bauhinia variegate* L., and *Grewia optiva* J. R. Drumm. Ex Burret etc. The shrubs include the *Dodonaea viscose* (L.) Jacq., *Carissa opaca* Stapf ex Haines and *Justicia adhatoda* L. etc. The grasses include i.e., *Chrysopogon serrulatus* Trin., *Bothriochloa pertusa* (L.) A. Camus, and *Pennisetum orientale* L.C. Rich. etc. (Himalayan Wildlife Foundation, 2007). The soil is usually dry and shallow (Nizami, 2010). In other areas in Pakistan, these forests are generally found in Kala Chitta Mountains (Kherimurat), salt ranges, Malakand Agency, Parachinar, Loralai, Sohawa, etc. (Nizami, 2010).

The *Broussonetia papyrifera* (L.) L'Her. ex Vent. is the major invasive tree species, which is found at lower elevations, particularly in the plain areas of the MHNP (Malik and Husain, 2007). The fauna of the MHNP is also diverse. The wildlife species found here include Leopard (*Panthera pardus*), Rhesus Monkey (*Macaca mullata*), Barking Deer (*Muntiacus muntjak*), Grey Goral (*Naemorhedus goral*), Wild Boar (*Sus scrofa*), Asiatic Jackal (*Canis aureus*), Indian Crested Porcupine (*Hystrix indica*) and Indian Pangolin (*Manis crassicaudata*). There are also various birds of prey, game birds, reptiles, and butterflies found in the MHNP.

3. Materials and Methods:

3.1. Forest Biomass and Carbon Stock Assessment of MHNP:

3.1.1. Field Inventorying for Forest Biomass and Carbon Estimation:

3.1.1.1. Stratified Random Sampling:

Sampling in forestry offers various advantages over full enumeration such as cost-effectiveness, greater speed, and improved accuracy (Jin and Yang, 2020); (Jayaraman, 1999). The small sample sizes, thus, may lead to reduced errors such as those relating to field workers making mistakes in taking measurements and recording the data, errors related to the instruments, and/or during field inventory and data analysis (Jayaraman, 1999).

Generally, there exist two sampling approaches i.e. subjective and probability samplings (FAO, 2015). Subjective sampling utilizes personal experience and judgment for the selection of the sampling units which would represent the entire population. However, the subjective sampling approach may not accurately characterize the entire population which needs to be sampled (FAO, 2015). Probability sampling on another hand depends on the theory of probability for the selection of sampling units representing the entire population, which also means that the sampling units from the entire population would have an equal chance of selection. Some of the probability sampling approaches include simple random sampling, stratified sampling, systematic sampling, stratified random sampling, etc. (Jin and Yang, 2020).
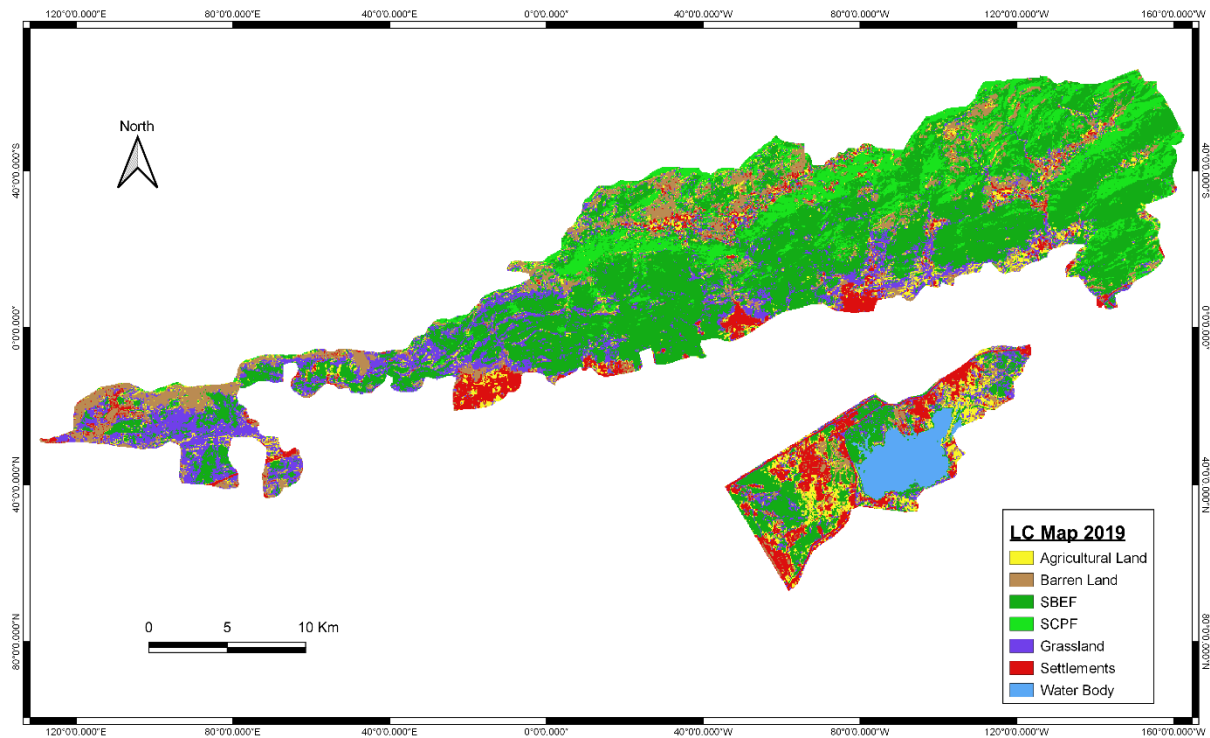
Fig. 5: LC Map for MHNP for the year 2019

Stratified random sampling was adopted for this research. In stratified random sampling the entire population, for example, the forest is broken down into different strata of familiar attributes and characteristics and randomly the samples are taken in each stratum. The advantages of stratified random sampling include the easier organization of the work and reduced bias and increased precision (FAO, 2015). In general, it also helps in decreasing the cost of field sampling. In the case of this research, the MHNP was first divided into two forest types i.e., SCPF and SBEF, and then respective samples were laid randomly in each of the forests. Overall, there were 46 sampling plots, which were laid in SCPF, and 31 sampling plots were laid in SBEF of the MHNP. The sampling was conducted mainly in the accessible areas of the MHNP. The limitations of the financial and personnel resources were also the essential factors that governed the overall sampling in the MHNP. Fig. 5 shows the LC Map for MHNP for the year 2019.

3.1.1.2. Plot Shape:

There can be different plot shapes that can be selected for sampling such as square, rectangle, circle, etc. The circular plots, however, are advantageous because they can be easily laid out, requiring only one control point, and easier management in hilly areas (Vries, 1986); (FAO, 2015). For this study, therefore, the sampling plots with a circular shape having a 17.84 m radius, which forms a 0.1 ha area each, were used (Pearson et al., 2005). Generally, in forestry for sampling purposes, the plots are selected with sizes ranging from 0.01 to 0.1 ha (West, 2009).

3.1.1.3. Data Collection (Measurement of Forest Variables):

The DBHs of all the trees above 5 cm were measured in the sampling plots, with the help of a DBH tape, at a height of 1.3 m above the ground level (Laar and Akça, 2007). The DBH tape was wrapped around a tree and the respective reading was noted, in cm, on the data collection form, attached as Annexure 1. DBH is the most common variable which is measured in forest inventories because it can easily be correlated to other variables (West, 2009). For younger trees, if a suitable height is not reached, this DBH can be measured at heights of 0.1-0.3 m (West, 2009). Overall, there were 640 trees sampled from the SCPF and 443 trees sampled from the SBEF of the MHNP. The sampling was conducted from March 2019 to June 2019. The GIS coordinates were also recorded from the center of the plots. While measuring the DBH of the trees, extreme care was shown towards the location of the recording of the DBHs. The scheme, which was adopted for measuring the DBHs of various straight, leaning, and forking trees, etc. during this study can be seen in Fig. 6. The local staff of the Islamabad Wildlife Management Board (IWMB) of the MHNP helped in the identification of various tree species. All the vernacular and scientific names of all the sampled trees were noted down on the data collection form. The IWMB is the legal custodian of the MHNP and is responsible for the protection and management of the MHNP.
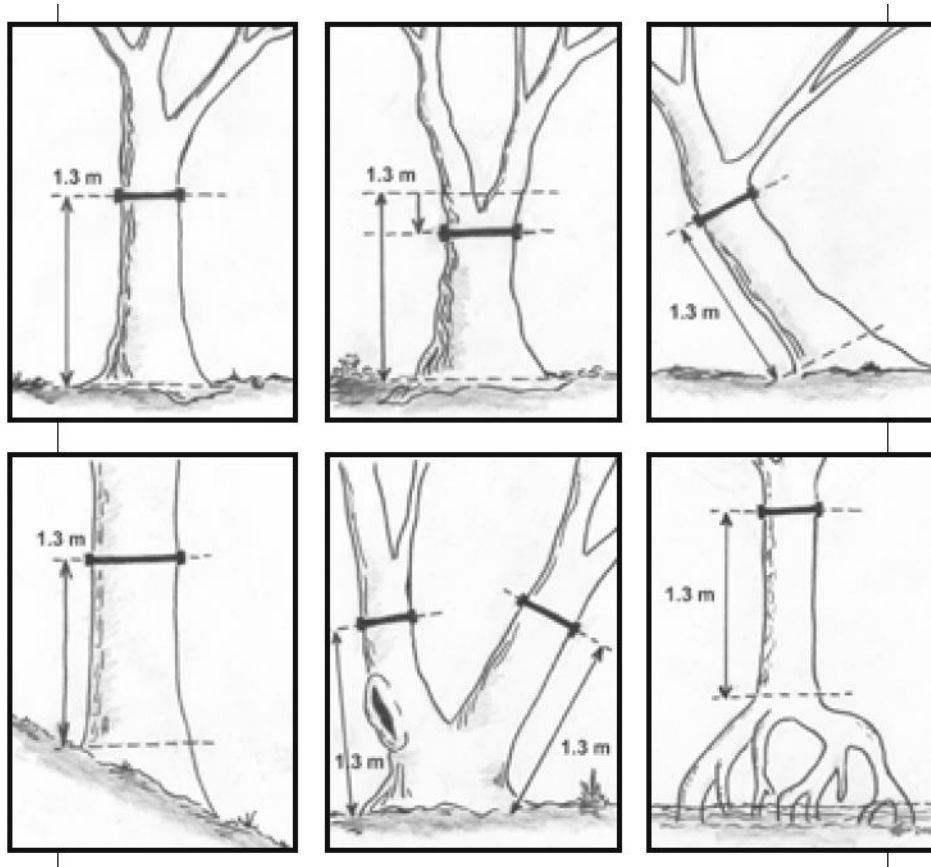
Fig. 6: DBH measurement locations' for trees (Pearson et al., 2005)

The heights of all 640 trees sampled from the SCPF and 443 trees sampled from the SBEF of the MHNP were measured. In each sampling plot, the heights of all the trees were measured and recorded in the data collection form. Height is also another attribute in forestry-related assignments or exercises that can be measured directly. There can be different types of heights i.e. tree height, bole height, merchantable height, etc. which can be measured in forestry inventories, therefore, utmost care should be given to the appropriate selection of the terminology especially corresponding to the objectives of the forest inventory assignment (Köhl et al., 2006). For this research tree height was used, which is defined as the vertical distance between the base of the tree and the tip of the tree (Köhl et al., 2006). Fig. 7 also shows the height of a single tree (Laar and Akça, 2007). The tree height measurement in the forests is generally a difficult, costly, and time-consuming task (Wang et al., 2019); (Næsset and Økland, 2002). All the heights during this study

25

were also measured by a single observer, the researcher himself (Hunter et al., 2013).
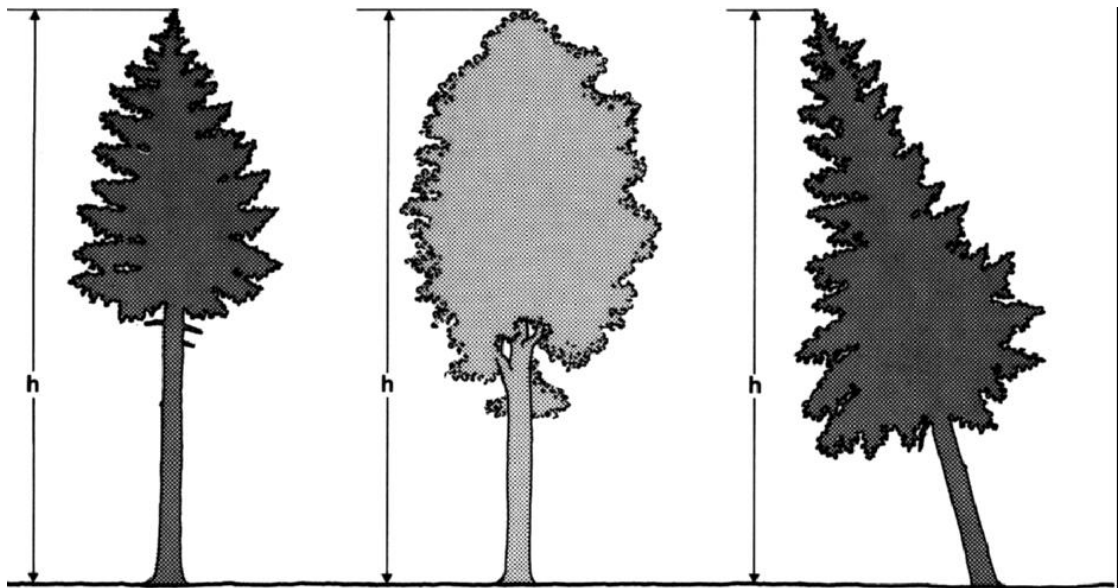
Fig. 7: Height of a Tree (Laar and Akça, 2007)

The Vertex IV instrument, along with its transponder, was used for the estimation of tree height. It uses ultrasound technology for the estimation of height, and is easy to use and precise (Velázquez-Martí et al., 2013); (Pariyar and Mandal, 2019). The location of the sampling plots which were laid in the SCPF and the SBEF at the MHNP for the forest inventorying can be seen in Fig. 8. The pictures from the MHNP can be found in Annexure 2.
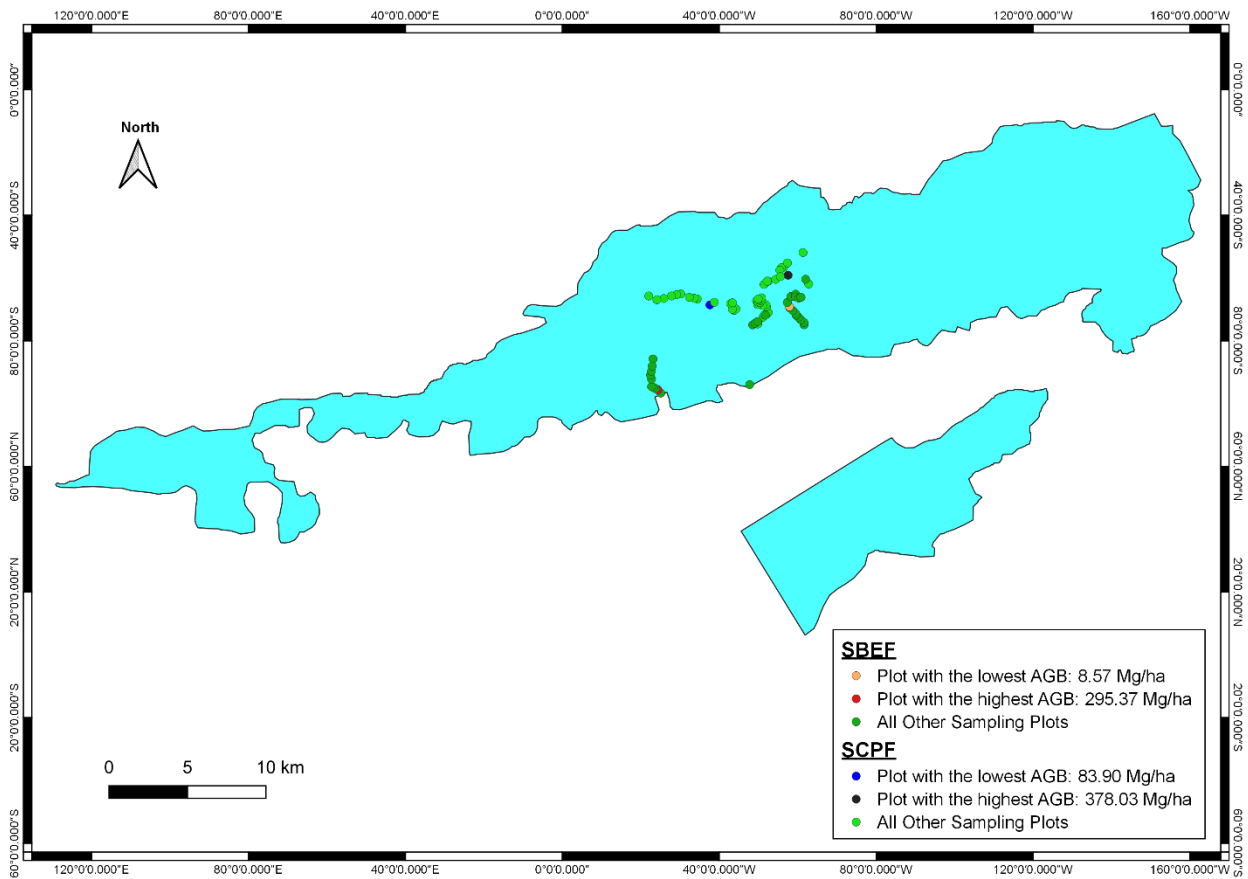
Fig. 8: Sampling Plots at the Two Forests of the MHNP

3.1.2. Satellite Remote Sensing:

3.1.2.1. S2 Data Acquisition and Processing:

The European Commission's (EC) Copernicus program, which was called the Global Monitoring for Environment and Security (GMES), started back in 1998 (Szantoi and Strobl, 2019). The program has a space component managed by the European Space Agency (ESA) which is responsible for the Copernicus Sentinel satellite constellations (Szantoi and Strobl, 2019). The S2 mission of the Copernicus program has become operational in October 2017 and it provides free access to satellite images (Corbane et al., 2020).

The S2 constellation mission has two satellites, the first is S2A which was launched on June 23, 2015, and the second satellite is the S2B, which got launched on March 7, 2017 (Wang et al., 2019). The S2 constellation has a high revisit time of 5 days. Their Multispectral Imager (MSI) collects data in 13 spectral bands and it uses push-broom technology by using a field of view of 290 km. The data produced by the S2 constellation can be found in three spatial resolutions of 10 m, 20m, and 60 m. The mission operates in a sun-synchronous orbit at an altitude of 786 km. The S2 data have been utilized in various vegetation-related studies (Mura et al., 2018). The details of the various spectral bands of S2 can be found in Table 1 (Lamquin et al., 2019).

Table 1: Spectral Bands of S2

Sr. No.	Band	Central Wavelength (nm)	Resolution (m)
1	Band 1 - Coastal aerosol	443	60
2	Band 2– Blue	490	10
3	Band 3 – Green	560	10
4	Band 4 – Red	665	10
5	Band 5 – Vegetation Red Edge	705	20
6	Band 6 – Vegetation Red Edge	740	20
7	Band 7 – Vegetation Red Edge	783	20
8	Band 8 – NIR	842	10
9	Band 8A – Narrow NIR	865	20
10	Band 9 – Water Vapour	945	60
11	Band 10 – Short Wave Infrared (SWIR) – Cirrus	1375	60
12	Band 11 – SWIR	1610	20
13	Band 12 – SWIR	2190	20

Two images of S2 were downloaded for this study because there was no single image representing the entire area i.e. the first image was for August 19, 2019, with a cloud cover of 0.4 percent, and the second image was also for the same date, August 19, 2019, with a 0.05 percent of cloud cover. For this study, the images, which were closest to the date of the forest inventory, were considered (Wessel et al., 2018). The Semi-Automatic Classification Plugin (SCP) (Congedo, 2016) of the QGIS (QGIS Development Team, 2020) was used for downloading the imageries (Gemusse et al., 2018). Band 2, band 3, band 4, and band 8 were used for taking advantage of the higher resolution of 10 m and to ensure consistency and to assure that there is no loss of information (Pandit et al., 2018). The product level of the images used was Level-1C. This product S2 Level-1C already includes the radiometric and geometric corrections (Pandžic et al., 2016). The S2 Level-1C products also contain the Top-of-Atmosphere (ToA) reflectance, which is needed to be converted to the Bottom-of-Atmosphere (BoA) reflectance for obtaining the surface characteristics (Estévez et al., 2020). The conversion to BoA reflectance was done using the Dark Object Subtraction method (DOS) which was developed by Chavez (1996). The DOS1 algorithm of the SCP of the QGIS software, developed by Congedo (2016), was used for the DOS method for conversion of the image into BoA reflectance (Gemusse et al., 2018); (Pandit et al., 2020).

The pre-processed S2 images were imported into the RStudio software (RStudio Team, 2020). The 'raster package' was loaded in the RStudio software (Hijmans and Ettan, 2012). The 'raster package' provides important functions for handling and importing raster layers (Kamusoko, 2019). The 'raster()' function was used for loading each band (band 2, band 3, band 4, and band 8) from each image as a single raster layer. The bands for each image were stacked using 'stack()', which is used for reading separate files (Kamusoko, 2019). The stacked files/images were converted into brick files/images using the 'brick()' function, which reads multiple layers from one file and has a better processing time compared to the 'stack()' function (Hijmans, 2017). Both the bricked images were mosaicked/merged using the 'merge()' function of the base package of R (R Core Team, 2020). Image mosaicking is the process where two or more images with overlapping areas are merged into a single image with an undistinguishable seamline (Burt and Adelson,

1983). Mosaicking is considered an important task in image processing in remote sensing (Li et al., 2015); (Li et al., 2019).

The sub-setting (clipping) of the image was conducted by using the shapefile of the study area, which reduces the processing time of the images since the study area forms only a small portion of the image. For this purpose, the 'shapefile()' function was used for importing the shapefile, and the 'crop()' and 'mask()' functions were used for cropping and clipping the image to the corresponding size of the study area. All three functions belong to the raster package of R. Fig. 70 shows the first image i.e., with four bands i.e., band 2 (B02), band 3 (B03), band 4 (B04), and band 8 (B08) (Annexure 1). Fig. 71 shows the second image with the same four bands (Annexure 1). Fig. 72 shows the merged S2 image (Annexure 1). Fig. 73 shows the clipped image of the study area (Annexure 1). The images were then converted to natural color composite and near-infrared (NIR) composite. Fig. 74 shows the natural color composite of the S2 image for the study area and Fig. 75 shows the NIR composite of the S2 image of the study area (Annexure 1). The methodological workflow for the AGB estimation and mapping can be seen in Fig. 11. The S2 raster image of the study area was saved and imported to QGIS software for the calculation and mapping of vegetation indices.

3.1.2.2. S1 Data Acquisition and Processing:

The S1 mission is the European Radar Observatory for the Copernicus joint initiative of the EC and the ESA. Copernicus was previously known as GMES, as already mentioned earlier. It is an initiative by Europe for providing information services related to the environment and security.

The S1 mission carries two satellites that are 180° apart (Crabbe et al., 2021). It contains a constellation of two identical satellites, S1A and S1B, which have been launched separately. The satellites are equipped with the C-Band SAR instrument which is operating at a center frequency of 5.405 GHz (Crabbe et al., 2021). The mission follows a sun-synchronous orbit which is at a height of 693 km (Huang et al., 2018). It includes four imaging modes i.e. Strip Map (SM), Interferometric Wide

swath (IW), Extra-Wide Swath (EW), and Wave (WV), having different resolutions (that is down to 5 m) and a coverage of up to 400 km with a capability of dual polarization (HH+HV, VV+VH) (Chang and Shoshany, 2016). Each mode is intended for use in different applications. The revisit time is 12 days for both satellites (Gao, 2019). The mission provides free data to the public for use.

A dual polarization (VV+VH), S1 IW Ground Range Detection (GRD) Level-1 scene was downloaded from the ESA Copernicus Open Access Hub (https://scihub.copernicus.eu/). The C-Band SAR product was downloaded for the date of August 24, 2019. The IW mode of acquisition has a 250 km swath width at a spatial resolution of 5 x 20 m spatial resolution (Single Look) and an incidence angle between 29.1° and 46.0° (Laurin et al., 2018). The IW mode of acquisition is suitable for land surface studies (Geudtner et al., 2013).

For the pre-processing of the downloaded S1 GRD scene, the workflow proposed by Filipponi (2019) was used. The pre-processing was conducted in the Sentinel Application Platform (SNAP) software version 8.0 of the ESA (SNAP, 2020). At first, a subset of the image was created after which the pre-processing steps were carried out. The steps involved for pre-processing were; *Apply Orbit File*, *Thermal Noise Removal*, *Border Noise Removal*, *Calibration*, *Speckle Filtering*, *Radiometric Terrain Flattening,* and *Range Doppler Terrain Correction.*

The 'Calibration' step converts the pixel values to the radiometrically calibrated backscatter (Filipponi, 2019). At this stage, the sigma nought ($\sigma°$) was converted to the beta nought (ß°), as for the 'Radiometric Terrain Flattening', the SNAP requires the beta nought (ß°) (Nuthammachot et al., 2020). Afterward, for reducing the salt and pepper effect, speckle filtering was done using the Multi-temporal Speckle Filter (Nuthammachot et al., 2020). For this purpose, the gamma map filter of a 5 x 5 pixel window was used because of its previous successful use in forested regions (Lopes et al., 1993).

The 'Radiometric Terrain Flattening' was applied since the study area was hilly and there would be a decline in the backscatter due to the double bounce scattering

mechanism (Folkesson et al., 2009). The 'Radiometric Terrain Flattening' thus reduces this relief influence on the backscatter coefficient (Nuthammachot et al., 2020). The 'Radiometric Terrain Flattening' was applied which converted the beta nought (ß°) to the Gamma nought (**γ**°) (Small, 2011). Subsequently, the 'Range Doppler Terrain Correction' was applied by using the Digital Elevation Model (DEM) that is derived from the Shuttle Radar Topography Mission (SRTM) 3 sec v.4 (Huang et al., 2018). In the same step, the image was projected to the coordinate system of Universal Transverse Mercator(UTM) zone 43N and it was also resampled to the 10 m spatial resolution (Nuthammachot et al., 2020). The backscatter coefficient σ° was converted to the decibels (dB) using logarithmic transformation (Filipponi, 2019); (Wang et al., 2019). The mathematical expression for this conversion is (Equation 1) (ESA, 2021);

$$\sigma°(dB) = 10 log 10 \sigma° \qquad\qquad (1)$$

where σ°(dB) is the normalized radar cross section and σ° is the backscatter for a specific polarization.

The Non-linear Median Filter (3 x 3) was applied for visual enhancement of the images (Dhruv et al., 2017). The shape file of the study area was imported into the SNAP software. The respective images with VH and VV Polarizations were clipped to the size of the study area and were saved as GeoTiff raster images. These raster images with VH and VV Polarizations were imported to the RStudio for obtaining the images in respective PNG formats. Fig. 9 shows the VH Polarization and Fig. 10 shows the VV Polarization of the study area. As can be seen in Fig. 9, the backscatter coefficient tσ° expressed in dB, ranges from -49.29 dB to 16.06 dB, with -49.29 dB being the lowest and the 16.06 dB being the highest. Similarly, Fig.10 shows the backscatter coefficient σ° (dB) from, the minimum of -42.48 dB to the maximum of 25.29 dB.
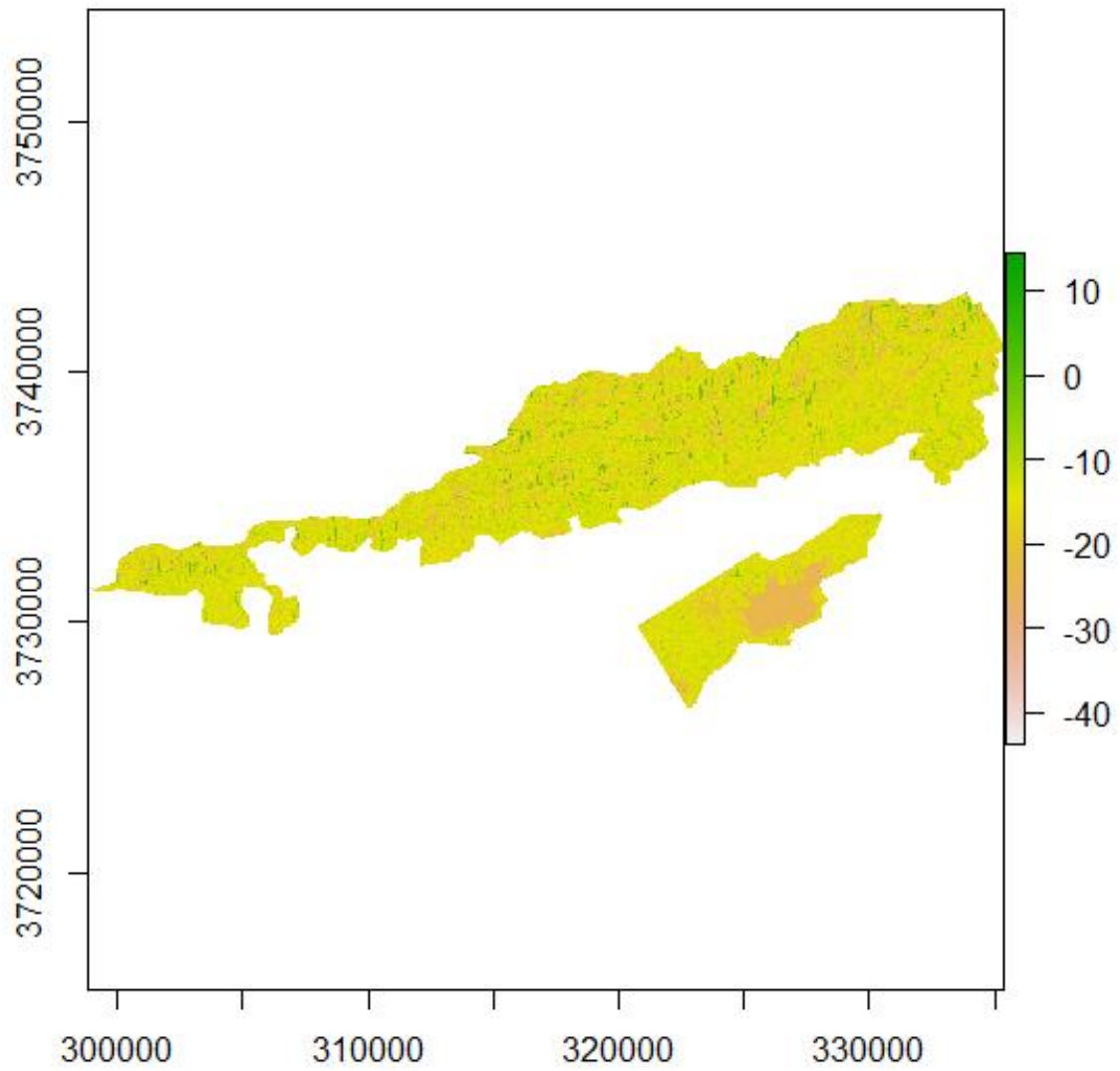
Fig. 9: VH Polarization from the Study Area
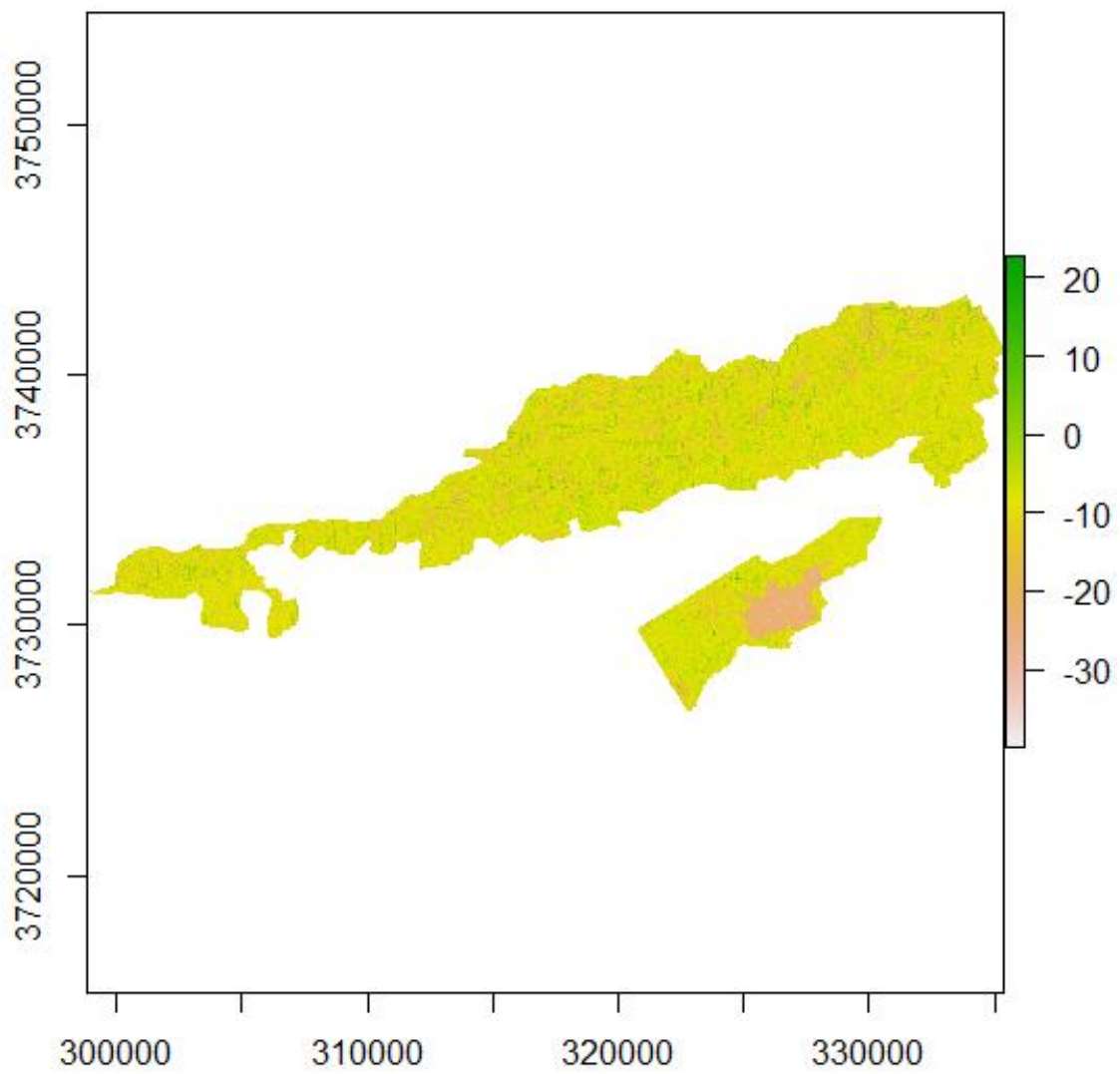
Fig. 10: VV Polarization of the Study Area
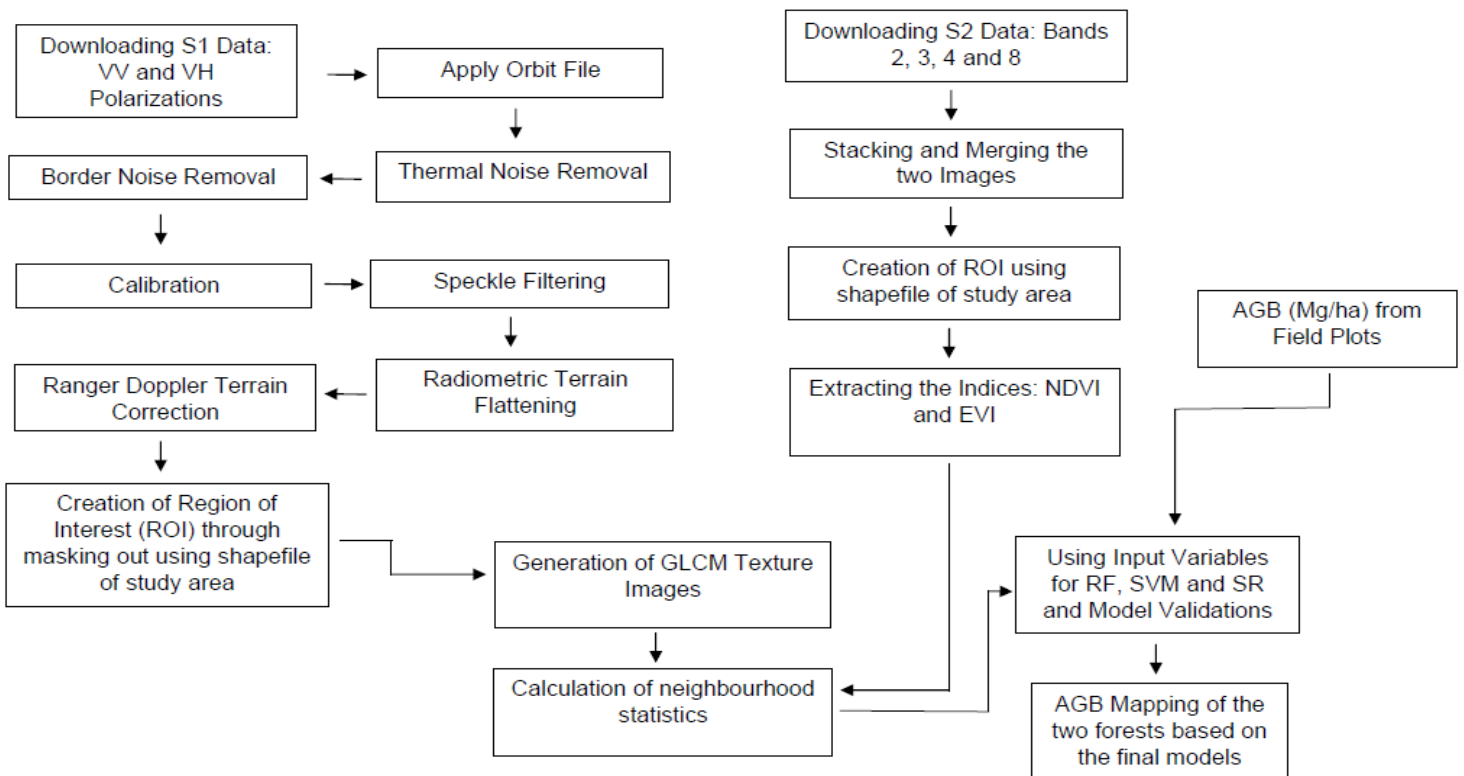
Fig. 11: Methodological workflow for AGB Estimation and Mapping

3.1.2.3.   Extraction of Variables from Satellite Data:

3.1.2.3.1. VIs:

VIs are the combination of different spectral bands in visible and near-infrared regions of the electromagnetic spectrum (Viña et al., 2011). These VIs are a simple way to extract information regarding vegetation characteristics from a large set of remote sensing data (Govaerts et al., 1999). They are a useful measure for determining the vigor and productivity of the vegetation (Steven et al., 2003). VIs have also been used for AGB estimation and have also demonstrated significant statistical relationships (Nagler et al., 2004). Some of the causes for this relationship include chlorophyll, water content, canopy structure, leaf angle, density, etc. (Taddeo et al., 2019). Several types of VIs exist which can be categorized into broadband and

narrowband (Agapiou et al., 2012). Abdou et al. (1995), for instance, reviewed around 35 VIs for their study. Similarly, Agapiou et al.(2012) reported 71 different VIs in their study.

For this research, the Normalized Difference Vegetation Index (NDVI) and Enhanced Vegetation Index (EVI) are used because of their relatively higher use due to significant correlations with the AGB (Guerini Filho et al., 2020).

3.1.2.3.1.1. NDVI:

NDVI is one of the most preferred indices for comparing vegetation and non-vegetation areas (Pandey et al., 2019b). Since the healthier and greener vegetation absorbs more visible light and reflects a higher infrared light compared to the unhealthy and sparse vegetation, therefore this characteristic is utilized by the NDVI for indicating these differences and changes (Silvia et al., 2019). The NIR zone is (0,75 – 1,3 μm) and the red zone is (0,62 – 0,75 μ m) within the electromagnetic spectrum (Silvia et al., 2019). The red portion of the visible light is absorbed by the leaves due to the presence of the chlorophyll and the NIR portion is reflected which also depends on the leaf and canopy structures (Buchhorn et al., 2016). The NDVI ranges from -1 to +1. The negative values portray water bodies, the values which are slightly above 0 represent bare grounds, values which are between 0.2 and 0.8 are representative of the spread and sparse vegetation and the values greater than 0.8 portrays greener vegetation and the values which are close to 1 are representatives of lush forests (Silvia et al., 2019). The formula for the NDVI is as follows (Equation 2) (Tucker, 1979);

$$\textbf{NDVI} = (NIR\text{-}RED)/(NIR\text{+}RED) \qquad (2)$$

The NDVI for the study area was calculated using QGIS software. S2 image for the study area was imported to the QGIS software and the raster calculator was used for writing the equation of the NDVI (Equation 1). After the calculation, the respective raster was saved for further analysis, and, using the layout manager of the QGIS software, an NDVI map was prepared (Fig. 47).

3.1.2.3.1.2. EVI:

EVI is also one of the most used indices mainly because of its simplicity, availability, and its utility in various kinds of ecosystems (Garroutte et al., 2016). EVI is also a ratio that contains the red and NIR bands of the electromagnetic spectrum which are correlated to the 'greenness' of the vegetation canopy (Garroutte et al., 2016). Amongst the two vegetation indices, NDVI and EVI, the EVI is more sensitive to the canopy structure, while NDVI is more sensitive to the chlorophyll (Gao et al., 2000). Both of these indices complement each other in vegetation-related studies (Huete et al., 2002). The value of the EVI also ranges from -1 to 1. The following formula was used for the EVI (Equation 3) (Huete et al., 2002);

$$\textbf{EVI} = 2.5(NIR-RED)/(NIR +6\times RED-7.5\times Blue+1) \qquad (3)$$

The EVI for the study area was calculated using QGIS software. S2 image for the study area was imported and the raster calculator was used for writing the equation for the EVI (Equation 2). The raster was saved for further use and, using the layout manager of the QGIS software, and EVI map was prepared (Fig. 51).

3.1.2.3.2. Grey Level Co-occurrence Matrix (GLCM):

The GLCM technique was used for texture analysis (Haralick et al., 1973). GLCM is a two-dimensional dependence matrix that takes into account the spatial relationship between the neighbouring pixels (Thakare and Patil, 2014). Three GLCM metrices were calculated for this study, for both the S2 and S1 data. These included Entropy, Angular Second Moment (ASM), and Contrast. The '*r.texture*' geo-algorithm of the Geographic Resources Analysis Support System (GRASS) plugin (GRASS Development Team, 2020) in the QGIS software was used for the calculation of the GLCM metrices, with the size of the pixel moving window of 3 x 3. *Entropy* measures the degree of disorder in the image (Ouma and Tateishi, 2015). *ASM* measures the textural uniformity of an image and is also called 'Energy' (Ouma and Tateishi,

2015). *Contrast* measures the amount of local variations in the image (Wang et al., 2010). The Entropy, ASM, and Contrast have also produced strong correlations with the AGB (Eckert, 2012); (Kuplich et al., 2003). The formulae for the three metrices, Entropy, ASM, and Contrast, are as follows (Equations 4, 5, and 6, respectively);

$$\mathbf{Entropy}_{\Delta x \Delta y} = -\sum_{i}\sum_{j} P(i,j)_{\Delta x \Delta y} \log P(i,j)_{\Delta x \Delta y} \qquad (4)$$

$$\mathbf{ASM}_{\Delta x \Delta y} = \sum_{i}\sum_{j} P(i,j)^2_{\Delta x \Delta y} \qquad (5)$$

$$\mathbf{Contrast}_{\Delta x \Delta y} = \sum_{i}\sum_{j} (i-j)^2_{\Delta x \Delta y} P(i,j)_{\Delta x \Delta y} \qquad (6)$$

Here above in the formulae, each element $P(i,j)_{\Delta x \Delta y}$ represents the relative frequency with which the two neighbouring pixels occur which are separated by the distance of Δx columns and Δy lines (Soares et al., 1997).

3.1.2.3.3. Extraction of Neighbourhood Statistics and Setting Up of the Predictor Sets for the Algorithms:

The GIS coordinates were recorded from the center of the sampling plots, using Garmin's handheld Global Positioning System (GPS) receiver, as already mentioned earlier. Since, it is common to have an error of 8-10 m in GPS-related surveys, a 15 m buffer was created around each point (Ghosh and Behera, 2018); (Carreiras et al., 2013). The main sources of the error have been described as the multipath propagation of GPS signals and tree canopies that block these signals (Zheng et al., 2005). The statistics for mean, maximum, standard deviation, and minimum for vegetation indices, VV and VH polarizations, and texture indices for S1 and S2 data inside the buffer were computed using QGIS software (Ghosh and Behera, 2018). Overall, there were 16 predictor sets and a total of 70 variables that were used in this

study; details of each predictor set along with their respective input variables can be seen in Table 2. These predictor sets were evaluated for both the forest types, SCPF and SBEF of the MHNP.

Table 2: Predictor Sets for the Algorithms

Sr. No.	Predictor Set	Input Variables
1	Bands	Band 2 (Blue), Band 3 (Green), Band 4 (Red), Band 8 (NIR)
2	Bands and S1	Band 2, Band 3, Band 4, Band 8, S1_VV, S1_VV_max, S1_VV_min, S1_VV_sd, S1_VV_avg, S1_VH, S1_VH_max, S1_VH_min, S1_VH_sd, S1_VH_avg
3	Bands and S1 Texture	Band 2, Band 3, Band 4, Band 8, S1_asm_VH, S1_asm_max_VH, S1_asm_min_VH, S1_asm_avg_VH, S1_asm_sd_VH, S1_ent_VH, S1_ent_max_VH, S1_ent_min_VH, S1_ent_avg_VH, S1_ent_sd_VH, S1_con_VH, S1_con_max_VH, S1_con_min_VH, S1_con_avg_VH, S1_con_sd_VH,S1_asm_VV, S1_asm_max_VV, S1_VV_asm_min_VV, S1_asm_avg_VV, S1_asm_sd_VV, S1_ent_VV, S1_ent_max_VV, S1_VV_ent_min_VV, S1_ent_avg_VV, S1_ent_sd_VV, S1_con_VV, S1_con_max_VV, S1_con_min_VV, S1_con_avg_VV, S1_con_sd_VV
4	Bands and S2 Texture	Band 2, Band 3, Band 4, Band 8, S2_asm, S2_asm_max, S2_asm_min, S2_asm_avg, S2_asm_sd, S2_ent, S2_ent_max, S2_ent_min, S2_ent_avg, S2_ent_sd, S2_con, S2_con_max, S2_con_min, S2_con_avg, S2_con_sd
5	Bands and VIs	Band 2, Band 3, Band 4, Band 8, NDVI, NDVI_max, NDVI_min, NDVI_avg, NDVI_sd, EVI, EVI_max, EVI_min, EVI_avg, EVI_sd
6	S1	S1_VV, S1_VV_max, S1_VV_min, S1_VV_sd, S1_VV_avg, S1_VH, S1_VH_max, S1_VH_min, S1_VH_sd, S1_VH_avg
7	S1 and S1 Texture	S1_VV, S1_VV_max, S1_VV_min, S1_VV_sd, S1_VV_avg, S1_VH, S1_VH_max, S1_VH_min, S1_VH_sd,

		S1_VH_avg, S1_asm_VH, S1_asm_max_VH, S1_asm_min_VH, S1_asm_avg_VH, S1_asm_sd_VH, S1_ent_VH, S1_ent_max_VH, S1_ent_min_VH, S1_ent_avg_VH, S1_ent_sd_VH, S1_con_VH, S1_con_max_VH, S1_con_min_VH, S1_con_avg_VH, S1_con_sd_VH, S1_asm_VV, S1_asm_max_VV, S1_VV_asm_min_VV, S1_asm_avg_VV, S1_asm_sd_VV, S1_ent_VV, S1_ent_max_VV, S1_VV_ent_min_VV, S1_ent_avg_VV, S1_ent_sd_VV, S1_con_VV, S1_con_max_VV, S1_con_min_VV, S1_con_avg_VV, S1_con_sd_VV
8	S1 and S2 Texture	S1_VV, S1_VV_max, S1_VV_min, S1_VV_sd, S1_VV_avg, S1_VH, S1_VH_max, S1_VH_min, S1_VH_sd, S1_VH_avg, S2_asm_max, S2_asm_min, S2_asm_avg, S2_asm_sd, S2_ent, S2_ent_max, S2_ent_min, S2_ent_avg, S2_ent_sd, S2_con, S2_con_max, S2_con_min, S2_con_avg, S2_con_sd
9	S1 and VIs	S1_VV, S1_VV_max, S1_VV_min, S1_VV_sd, S1_VV_avg, S1_VH, S1_VH_max, S1_VH_min, S1_VH_sd, S1_VH_avg, NDVI, NDVI_max, NDVI_min, NDVI_avg, NDVI_sd, EVI, EVI_max, EVI_min, EVI_avg, EVI_sd
10	S1 Texture	S1_asm_VH, S1_asm_max_VH, S1_asm_min_VH, S1_asm_avg_VH, S1_asm_sd_VH, S1_ent_VH, S1_ent_max_VH, S1_ent_min_VH, S1_ent_avg_VH, S1_ent_sd_VH, S1_con_VH, S1_con_max_VH, S1_con_min_VH, S1_con_avg_VH, S1_con_sd_VH, S1_asm_VV, S1_asm_max_VV, S1_VV_asm_min_VV, S1_asm_avg_VV, S1_asm_sd_VV, S1_ent_VV, S1_ent_max_VV, S1_VV_ent_min_VV, S1_ent_avg_VV, S1_ent_sd_VV, S1_con_VV, S1_con_max_VV, S1_con_min_VV, S1_con_avg_VV, S1_con_sd_VV
11	S1 Texture and S2 Texture	S1_asm_VH, S1_asm_max_VH, S1_asm_min_VH, S1_asm_avg_VH, S1_asm_sd_VH, S1_ent_VH, S1_ent_max_VH, S1_ent_min_VH,

		S1_ent_avg_VH, S1_ent_sd_VH, S1_con_VH, S1_con_max_VH, S1_con_min_VH, S1_con_avg_VH, S1_con_sd_VH, S1_asm_VV, S1_asm_max_VV, S1_VV_asm_min_VV, S1_asm_avg_VV, S1_asm_sd_VV, S1_ent_VV, S1_ent_max_VV, S1_VV_ent_min_VV, S1_ent_avg_VV, S1_ent_sd_VV, S1_con_VV, S1_con_max_VV, S1_con_min_VV, S1_con_avg_VV, S1_con_sd_VV, S2_asm_max, S2_asm_min, S2_asm_avg, S2_asm_sd, S2_ent, S2_ent_max, S2_ent_min, S2_ent_avg, S2_ent_sd, S2_con, S2_con_max, S2_con_min, S2_con_avg, S2_con_sd
12	S1 Texture and VIs	S1_asm_VH, S1_asm_max_VH, S1_asm_min_VH, S1_asm_avg_VH, S1_asm_sd_VH, S1_ent_VH, S1_ent_max_VH, S1_ent_min_VH, S1_ent_avg_VH, S1_ent_sd_VH, S1_con_VH, S1_con_max_VH, S1_con_min_VH, S1_con_avg_VH, S1_con_sd_VH, S1_asm_VV, S1_asm_max_VV, S1_VV_asm_min_VV, S1_asm_avg_VV, S1_asm_sd_VV, S1_ent_VV, S1_ent_max_VV, S1_VV_ent_min_VV, S1_ent_avg_VV, S1_ent_sd_VV, S1_con_VV, S1_con_max_VV, S1_con_min_VV, S1_con_avg_VV, S1_con_sd_VV, NDVI, NDVI_max, NDVI_min, NDVI_avg, NDVI_sd, EVI, EVI_max, EVI_min, EVI_avg, EVI_sd
13	S2 Texture	S2_asm_max, S2_asm_min, S2_asm_avg, S2_asm_sd, S2_ent, S2_ent_max, S2_ent_min, S2_ent_avg, S2_ent_sd, S2_con, S2_con_max, S2_con_min, S2_con_avg, S2_con_sd
14	S2 Texture and VIs	S2_asm_max, S2_asm_min, S2_asm_avg, S2_asm_sd, S2_ent, S2_ent_max, S2_ent_min, S2_ent_avg, S2_ent_sd, S2_con, S2_con_max, S2_con_min, S2_con_avg, S2_con_sd, NDVI, NDVI_max, NDVI_min, NDVI_avg, NDVI_sd, EVI, EVI_max, EVI_min, EVI_avg, EVI_sd
15	Vis	NDVI, NDVI_max, NDVI_min, NDVI_avg, NDVI_sd, EVI, EVI_max, EVI_min,

		EVI_avg, EVI_sd
16	All	Band 2, Band 3, Band 4, Band 8, NDVI, NDVI_max, NDVI_min, NDVI_avg, NDVI_sd, EVI, EVI_max, EVI_min, EVI_avg, EVI_sd, S2_asm, S2_asm_max, S2_asm_min, S2_asm_avg, S2_asm_sd, S2_ent, S2_ent_max, S2_ent_min, S2_ent_avg, S2_ent_sd, S2_con, S2_con_max, S2_con_min, S2_con_avg, S2_con_sd,S1_VV, S1_VV_max, S1_VV_min, S1_VV_sd, S1_VV_avg, S1_VH, S1_VH_max, S1_VH_min, S1_VH_sd, S1_VH_avg, S1_VH_asm, S1_asm_VH, S1_asm_max_VH, S1_asm_min_VH, S1_asm_avg_VH, S1_asm_sd_VH, S1_ent_VH, S1_ent_max_VH, S1_ent_min_VH, S1_ent_avg_VH, S1_ent_sd_VH, S1_con_VH, S1_con_max_VH, S1_con_min_VH, S1_con_avg_VH, S1_con_sd_VH, S1_asm_VV, S1_asm_max_VV, S1_VV_asm_min_VV, S1_asm_avg_VV, S1_asm_sd_VV, S1_ent_VV, S1_ent_max_VV, S1_VV_ent_min_VV, S1_ent_avg_VV, S1_ent_sd_VV, S1_con_VV, S1_con_max_VV, S1_con_min_VV, S1_con_avg_VV, S1_con_sd_VV

Note= Entropy (ent), Contrast (con), ASM (asm), maximum (max), minimum (min), sd (standard deviation), average (avg).

3.1.3. Data Analysis:

3.1.3.1. Data Analysis of the Field Parameters:

3.1.3.1.1. Quadratic Mean Diameter:

The quadratic mean diameter for each plot was computed as follows (Equation 7) (Iles and Wilson, 1977);

$$\text{Mean DBH} = \sqrt{\frac{d_i{}^2}{n}} \qquad\qquad (7)$$

The quadratic mean diameter is considered more useful than the average of DBHs because it is more closely related to the volume (West, 2009). For this research, quadratic mean diameter was referred to as the mean DBH.

3.1.3.1.2. Volume:

The tree volume was recorded using the following formula (Equation 8) (Philip, 1994);

Volume of a tree (m³) = $(\pi / 4) \times \text{DBH}^2 \times \text{H} \times \text{FF}$ $\qquad$ (8)

Whereas,

       H = Height of a tree

       FF = Form Factor

The volume of a tree is considered one of the most important variables in forestry because of commercial reasons and it can also be related easily to other forestry variables (West, 2009).

The form factor of a tree is defined as "*the stem volume which is expressed as the proportion of the cylinder volume of the same height which has diameter equal to the stem diameter at the selected reference point*" (Laar and Akça, 2007). For this research, a form factor of 0.45 was used for *Pinus roxburghii*, and for broadleaved species, a form factor of 0.59 was used as suggested by Gray (1956).

3.1.3.1.3. Basal Area:

The stand basal area is defined as the sum of the cross-sectional area of the stems at breast height and expressed per unit of ground area (West, 2009). The basal area was calculated by using the following formula (Equation 9) (Köhl et al., 2006);

$$\textbf{Basal Area}\ (\textbf{m}^2) = \frac{(\text{DBH})^2 \times \pi}{4} \qquad (9)$$

It is also an important variable used in forestry because it is often correlated with the tree volume and it also increases with the age of the trees and it can vary with the number of trees located in the stand (West, 2009).

3.1.3.1.4. Density:

The density is the number of trees per unit area (West, 2009). The density is considered an important variable because it helps in describing the developmental stages of a forest stand (West, 2009).

3.1.3.1.5. AGB:

Initially, the AGB was calculated as follows (Equation 10) (Brown et al., 1999); (Pandey et al., 2019b);

$$\textbf{AGB (Kg)} = \text{Volume (m}^3) \times \text{Wood Density (Kgm}^{-3}) \times \text{BEF} \qquad (10)$$

Whereas,

BEF = Biomass Expansion Factor

The 'Wood Density' is defined as "*the amount of actual wood substance which is present in a unit volume of wood*" (Zobel and Jett, 1995). It is considered an essential variable for AGB calculations (Fearnside, 1997). Following 'Wood

44

Densities' were sourced, for different tree species, from various published resources (Table 3);

Table 3: Wood Densities of Trees Species

Sr. No.	Species	Wood Density (g cm^{-3})	Sources
1	*Pinus roxburghii* Sarg.	0.49	(Sheikh et al., 2009)
2	*Bombax ceiba* L.	0.33	(Brown, 1997)
3	*Bauhinia variegata* L.	0.67	(Brown, 1997)
4	*Eucalyptus camaldulensis* Dehnh.	0.681	(Awan et al., 2012)
5	*Ficus palmata subsp. virgata* Forssk.	0.39	(Brown, 1997)
6	*Acacia modesta* Wall.	0.809	(Awan et al., 2012)
7	*Grewia optiva* J. R. Drumm. ex Burret	0.68	(Ranot and Sharma, 2013)
8	*Mallotus philippensis (Lam.) Muell. Arg.*	0.64	(Brown, 1997)
9	*Cassia fistula* L.	0.71	(Brown, 1997)
10	*Broussonetia papyrifera* (L.) L'Herit ex Vent.	0.507	(Ayarkwa et al., 2011)
11	*Celtis australis* L.	0.44	(Sheikh et al., 2011)
12	*Albizia lebbeck* (L.) Benth	0.55	(Brown, 1997)
13	*Ziziphus mauritiana* Lam.	0.76	(Brown, 1997)
14	*Ficus benghalensis* L.	0.39	(Brown, 1997)
15	*Flacourtia indica* (Burm. f.) Merr.	0.55	(Jothivel, 2016)

The wood densities ranged from 0.33 g cm^{-3} to 0.809 g cm^{-3}.

The BEF converts the tree volume into the AGB (Brown, 1997). The BEF of 1.51 was used for *Pinus roxburghii* and 1.59 was used for all other broadleaved tree species which were encountered during the sampling process (Haripriya, 2000).

The 'AGB (Kg)' was converted to 'AGB Mg (megagram)' by dividing the former by 1000.

3.1.3.1.6. AGC (Mg):

The 'AGB' was converted to 'Aboveground Carbon (AGC)' by using the carbon conversion factor of 0.5 (Köhl et al., 2020a).

3.1.3.1.7. Scaling Up to the Hectare:

The abovementioned variables i.e. Volume (m^3), Basal Area (m^2), Density, AGB (Mg), and AGC (Mg C) were scaled up to ha by dividing the variables by 0.1 (Torres et al., 2020).

3.1.3.1.8. Statistical Analysis:

Regression analysis was performed to see the linear relationship between the two variables. Power regression was used in case of a non-linear relationship between the two variables. Power regression has been widely applied in AGB modeling for coping with the non-linearity of the statistical relationships (Tetemke et al., 2019). The Coefficient of Determination (R^2) was used for assessing the strength of the statistical linear relationship between the two variables. It is a useful measure for assessing the statistical linear strength between the two variables (Pham et al., 2020). It has also been a common measure that has been used in AGB estimation studies (Hamdan et al., 2014). The evaluation of the strengths of the R^2 was based on the following; 1) 0.19 (weak) 2) 0.33 (moderate) and 3) 0.67 (substantial/significant) (Chin, 1998). The negative sign implies the negative statistical relationship between the two variables.

Means and standard deviations were calculated for the variables (mean ±sd). The data was checked for the normality distribution, for which *Shapiro-Wilk Test* was used. Since the data were not normally distributed, the *Wilcoxon Rank Sum Test* was used for probing the statistical difference between the two variables. The Spearman correlation coefficient (r_s), which is a nonparametric measure, was used for the correlation analysis of the two variables since the data was not normally distributed. For the Spearman correlation coefficient, which ranges between -1 to 1, the interpretation was done following Ratner, (2009); 1) 0 - no relationship 2) +1 (perfect positive linear relationship) 3) -1 (perfect negative relationship) 4) 0-0.3 (weak positive linear relationship) and -0.3-0 (weak negative relationship) 5) 0.3-0.7 (moderate positive linear relationship) and -0.3 - -0.7 (moderate negative linear relationship) 6) 0.7-1 (strong positive linear relationship) and -0.7 - -1 (strong negative linear relationship). A significance level of 0.05 was used for all the statistical tests and analysis. The statistical analysis was performed in RStudio, and the respective graphs were generated.

3.1.3.2. Data Analysis of the Satellite Remotely Sensed Parameters used for Estimation of AGB:

3.1.3.2.1. RF:

RF is a non-parametric machine learning algorithm that is used for both i.e. classification and regression (Fawagreh et al., 2014). It had been successfully used in the AGB estimation studies combined with remote sensing techniques (Pandit et al., 2018); (Chrysafis et al., 2017); (Dhanda et al., 2017); (Mutanga et al., 2012); (Pham and Brabyn, 2017); (Dang et al., 2019). It was developed by Breiman (2001b) and it uses the ensemble learning method for classification and regression (Fawagreh et al., 2014). The results from the ensemble models will be better, in most cases, compared to the results from the individual models (Dahinden and Guyon, 2011). Categorical data tend to produce classifications and continuous data are used for the regressions when using the RF algorithm (Youssef et al., 2016); (Horning, 2010). The response variables can be predicted as an average of all decision trees in case of a continuous variable classification or as a model vote among all decision

trees in case of a categorical classification (Mellor et al., 2015). Advantages of RF include; 1) higher accuracy 2) robustness to outliers and noise 3) computation speed 4) estimation of the importance of predictor variables (Cutler et al., 2007); (Rodriguez-Galiano et al., 2012). Also, a large number of predictor variables can be used in the case of RF (Breiman, 2001b). In the RF algorithm, the decision trees to the maximum extent are generated without pruning and for this case, two third of the training data is selected randomly using bootstrapping (where the data is re-sampled many times with replacement) (Pandit et al., 2018). This process strengthens the flexibility for the final prediction by aggregating the predictions which occurred across various individual trees (Pandit et al., 2018). The remaining one-third, which is the rest of the data, is used as the validation samples for estimating the model errors (Prasad et al., 2006). This remaining data, which is also not seen by the model, is known as the OOB data (out-of-bag) (Pandit et al., 2018). The RF algorithm requires two parameters 1) *mtry*; the number of predictor variables used for data splitting at each node of the decision tree 2) *ntree*; the total number of the trees used in the model (Pandit et al., 2020)

The 'randomForest' (Liaw and Wiener, 2002), 'caret' (Kuhn, 2008), and 'raster' packages (Hijmans and Ettan, 2012) were used in the RStudio statistical software (Millard and Richardson, 2015); (Ghosh and Behera, 2018). For the regression, the default value of 500 for *ntree* and 1/3 for *mtry* were used in the RF models (Pandit et al., 2018). The 'caret' package of the R was used for the identification of the most important variables in a model (Dang et al., 2019). The optimal number of variables is important for the improved accuracies of the models (Pham and Brabyn, 2017). It also increases the predictive power of the variables and results in easier interpretations (Gregorutti et al., 2017). Generally, a validation dataset is set aside from the overall dataset for evaluating the predictive performance of the model (Ghosh and Behera, 2018). However, in this research, since the dataset was small, a 5-fold cross-validation approach was used (Carreiras et al., 2013); (Ghosh and Behera, 2018).

3.1.3.2.2. SVM:

The SVM is a high-complexity classifier that has been widely used for classification and regression problems (Clevers et al., 2007). The SVM algorithm was developed by Vapnik (2000) and is a supervised learning technique that is based on statistical learning theory. In regression cases, the SVM utilizes the principle of structural risk minimization for optimizing performance and generalization (Axelsson et al., 2013). The SVM focuses on the training samples which are closest to the boundary between the classes in feature space (Pal and Foody, 2012). These samples are called Support Vectors (Maxwell et al., 2018). The SVM aims to find an optimal boundary that could maximize the separation (also known as margin) between the Support Vectors (Maxwell et al., 2018). Originally, the SVMs were designed for the identification of a linear class boundary, which is also called a hyperplane, but this limitation was addressed by projecting the feature space in a higher dimension (Maxwell et al., 2018). The projection to the higher dimensionality is also called the kernel trick (Maxwell et al., 2018). See also Fig. 12.
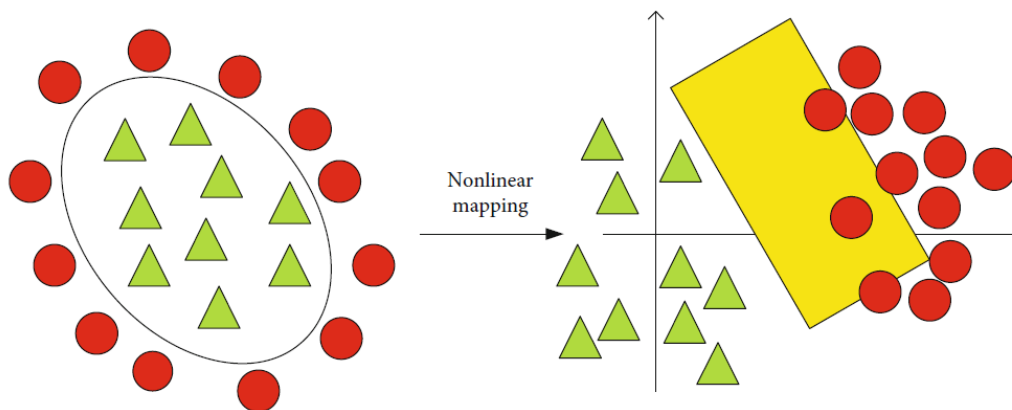
Fig. 12: Kernel function support vector machine diagram (Lv and Wang, 2020)

There are four common kernels used in SVM which include linear kernel function, polynomial kernel function, radial basis function (RBF), and sigmoid kernel function (Guo et al., 2012). In this study, the RBF was used due to its small computation cost, high prediction accuracy, and relatively good stability (Zhang et al., 2020). RBF had

also been used in previous AGB estimation studies (Pham et al., 2020); (Navarro et al., 2019); (Vafaei et al., 2018). For the SVM model, two parameters are often required i.e., 1) the regularization parameter C and the kernel width (γ) (Vafaei et al., 2018). The 'C' is the penalty parameter, which distinguishes the balance between the training error and the generalization error (Xue, 2015). The kernel width 'γ' is the width parameter of the RBF function (Zhang et al., 2020). The 'e1071' package (Meyer and Wien, 2017) was used for the implementation of the SVM in the RStudio. A similar, 5-fold cross-validation approach was used, which was described above for the RF model since the dataset was small. The variable selection was also carried out similarly to the RF model by using the 'caret' package in RStudio software.

3.1.3.2.3. Stepwise Regression:

Stepwise regression (SR) was adopted for this research. SR is a type of MLR analysis. It is usually opted for the selection of the most significant predictor variables in a model, keeping in view the importance of optimal parsimony (Breiman, 1995). There are three approaches to stepwise regression i.e. 1) Forward Selection, 2) Backward Elimination and 3) Mixed Selection (James et al., 2013); (Wang et al., 2016).

In 'Forward Selection', the model is empty first but then the variable most significant and which helps in improving the model is added. The process reiterates until the final set of most significant variables is added to the final model. The process is based on a pre-defined criterion. In 'Backward Elimination', the model starts with the full set of predictor variables. Then one by one, the variables which are not of any significance for the model are removed. This approach is also based on a pre-defined criterion. The 'Mixed Selection or Bidirectional Elimination', whereas is a combination of the abovementioned two approaches, 'Forward Selection' and 'Backward Elimination'.

In this research, the 'Backward Elimination' approach of the SR was used. The approach has been widely adopted in AGB estimation using remote sensing parameters (Li et al., 2008). The normality distribution of the data was checked using

the *Shapiro-Wilk Test* (He et al., 2013). The Spearman correlation coefficient of the variables was calculated using the RStudio software (Domingo et al., 2017). The logarithmic transformation of the data was also performed, where necessary (Means et al., 1999). The collinearity was assessed using the variance inflation factor (VIF). The variables having VIF above 10 were removed (He et al., 2013). Moreover, it was also ensured that the models met the basic assumptions of linear regression (Domingo et al., 2017). The 'caret' package was again used for the implementation of the 5-cross validation approach.

3.1.3.2.4. Model Validation and AGB Mapping:

The root mean square error (RMSE) and the R^2 were used for assessing the performance and strength of a model. The RMSE is widely used for assessing the differences between the values which are predicted by the model and the values which are actually measured (Zhu and Liu, 2015). The smaller RMSE implies a higher accuracy (Zhu and Liu, 2015). The RMSE is given as (Equation 11);

$$\text{RMSE} = \sqrt{\frac{\sum_{i=1}^{n}(y_i - \hat{y}_i)^2}{n}} \qquad (11)$$

Where y_i is the measured AGB in the field and $\hat{y}_i$ is the predicted AGB and n is the total number of the plots.

R^2 was also used for evaluating the linear relationship between the observed AGB and the predicted AGB by the final models from the two machine learning algorithms, RF and SVM, and from the SR (Zhu and Liu, 2015). The main weightage for the selection of the model, however, between the two metrices, RMSE and R^2, was given to the RMSE.

The final models for the two forest types, SCPF and SBEF, were selected for the AGB mapping based on the model evaluations. The 'raster' package of R was used for the spatial prediction of the AGB for both the forest types. The 'predict()' function

51

was used for this purpose, for which the raster object and the finalized models were provided as inputs. The AGB rasters for SBEF and SCPF were saved for further processing. The raster of the LC classification using Landsat 8 Operational Land Imager OLI and RF algorithm for the year 2019 was first converted to polygon/shapefile (the detailed process of the LC classification can be found in the method's section of the second objective of this study i.e., 3.2) and then SBEF and SCPF were extracted from this shapefile and converted to separate rasters, with a spatial resolution of 10 x 10 m, using QGIS software. The AGB rasters were then subtracted from the rasters of the respective forest types obtained as LC classification using Landsat 8 OLI image for the year 2019 and RF algorithm (Richardson et al., 2017). The maps were prepared using the final AGB rasters of the two forests. For this purpose, the 'layout manager' of the QGIS software was used. The LC classification derived from Landsat 8 OLI image, using RF algorithm, for the year 2019 also coincided with the field inventorying period.

3.2. LC Classification and LCCD of MHNP for the time-period between 1999 and 2019:

3.2.1. Landsat Data Acquisition and Processing:

The Landsat satellite programme initially called as Earth Resource Technology Satellite (ERTS) programme, was launched back in 1972 by NASA and United States Geological Survey (USGS) (Wulder et al., 2019). The Landsat satellite programme represents the record for the longest-running terrestrial satellite programme (Zhu et al., 2019). The Landsat archive has been held at USGS Earth Resources Observation and Science (EROS) Centre and contains more than 5.6 million acquisitions that have been sensed by the Landsat series satellites from Landsat-1 to the Landsat-8 satellite (Dwyer et al., 2018). The free and open policy has been adopted by USGS since 2008, which has resulted in a substantial surge in the use of the Landsat satellite data (Roy et al., 2014); (Wulder et al., 2012); (Wulder et al., 2019). The use of Landsat satellite data has been so extensive, that even global forest mapping was performed using Landsat data from 2000 to 2012, which revealed a forest loss of 1.5 million Km^2 (Hansen et al., 2013). Landsat satellite data, over the years, have demonstrated the capacity and ability for land cover mapping and monitoring of biophysical parameters and properties of the land surfaces (Hansen and Loveland, 2012); (Wulder et al., 2012). Landsat satellite data have also been used as a key input by the UN-REDD Programme, which was launched in 2008, for supporting the forest cover and carbon stocks measurement, reporting, and verification in developing countries (GOFC-GOLD, 2016). Fig. 13 provides a glimpse of the history and future satellite programme associated with the Landsat series mission.

Three Landsat satellite images, Landsat-5 TM image (Date: April 28, 2009), Landsat-7 ETM+ image (Date: July 14, 1999), and Landsat-8 OLI image (Date: April 8, 2019) were downloaded from the SCP, developed by Congedo (2016), using QGIS software. Table 4 provides the bands, their respective wavelengths, and spatial resolutions for the sensors: Landsat 5 TM, Landsat 7 ETM+, and Landsat 8 OLI/TIRS.
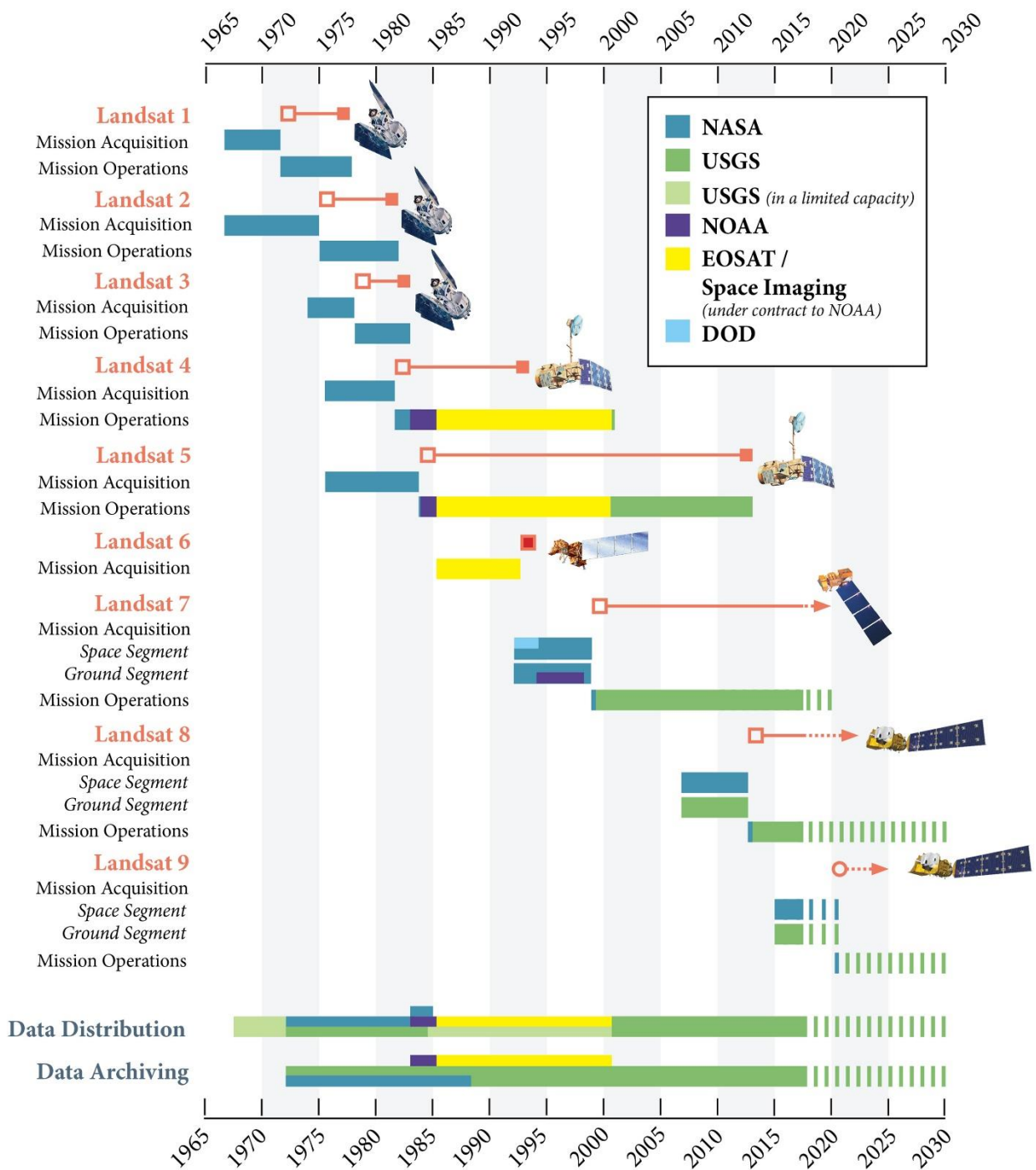
Fig. 13: Landsat series mission and history (Source: NASA/Landsat Legacy Project Team and American Society for Photogrammetry and Remote Sensing) (Wulder et al., 2019). DOD stands for Department of Defense and EOSAT stands for Earth Observation Satellite Company.

Table 4: Bands and pixel size information for the Landsat satellites and sensors

Landsat Sensors	Landsat 5 TM	Landsat 7 ETM+	Landsat 8 OLI/TIRS	Pixel Size (m)
Coastal Aerosol			B1 (0.43–0.45)	30
Blue	B1(0.45-0.52)	B1 (0.45–0.52)	B2 (0.45–0.51)	30
Green	B2 (0.52–0.60)	B2 (0.52–0.60)	B3 (0.53–0.59)	30
Red	B3 (0.63–0.69)	B3 (0.63–0.69)	B4 (0.64–0.67)	30
NIR	B4 (0.76–0.90)	B4 (0.77–0.90)	B5 (0.85–0.88)	30
Short Wave Infrared (SWIR) 1	B5 (1.55–1.75)	B5 (1.55–1.75)	B6 (1.57–1.65)	30
SWIR 2	B7 (2.08–2.35)	B7 (2.09–2.35)	B7 (2.11–2.29)	30
Thermal	B6 (10.40–12.50)	B6 (10.40–12.50)	B10 (10.60–11.19) B11 (11.50–12.51)	120 (TM), 60 (ETM+), 100 (TIRS)
Panchromatic			B8 (0.50–0.68)	15
Cirrus			B9 (1.36–1.38)	30

Note: B stands for the band. The empty space shows the absence of that band from the respective sensor. The wavelengths in parenthesis are in micrometers (µm). Cited from (Young et al., 2017).

The Landsat-5 was launched on March 1, 1984, with TM and Multi-Spectral Scanner (MSS) sensors on board (Chen et al., 2019). It has a repeat cycle of 16 days. The satellite was decommissioned on June 5, 2013 (Zhang and Roy, 2016). It has been recognized as the longest-serving satellite providing high-quality satellite data for about 29 years (Liu et al., 2017). Landsat 7 with an ETM+ sensor was launched on April 15, 1999, and is still operational (Goward et al., 2001). Landsat 8 was launched on February 11, 2013, with an OLI sensor and TIRS on board (Wang et al., 2017). It went operational on May 30, 2013 (Wulder et al., 2016). Both Landsat 7 and Landsat 8 also have a 16-day repeat cycle.

From the downloaded Landsat-5 TM and Landsat 7 ETM+ images, band 6, which is the thermal band, was excluded and from the Landsat 8 OLI image, bands 1, 8, 9, 10, and 11 were excluded (Table 5). The downloaded images were cloud-free (Table

5). The Landsat images were downloaded for the period coinciding with the field work which spanned from March 2019 to June 2019 and also for a similar seasonal period (spring-summer) to avoid seasonal variations (Fernández-Landa et al., 2016).

Table 5: Satellite data used in this study

Date	Satellite Imagery	Cloud Cover (%)	Paths and Rows	Bands Used	Spatial Resolution (m)
July 14, 1999	Landsat 7 ETM+	0	150-037	1,2,3,4,5,7	30
April 28, 2009	Landsat 5 TM	0	150-037	1,2,3,4,5,7	30
April 8, 2019	Landsat 8 OLI	0	150-037	2,3,4,5,6,7	30

All the three downloaded Landsat images, Landsat 7 ETM+, Landsat 5 TM and Landsat 8 OLI, were Level-1 Tier 1 Landsat products. The Level-1 Tier-1 products are high-quality satellite products and are already geometrically and radiometrically corrected (Dwyer et al., 2018); (USGS, 2019). Therefore, the downloaded Landsat images were not accounted for geometric and radiometric corrections. The atmospheric correction was performed using DOSmethod (Arjasakusuma et al., 2018); (Arekhi et al., 2019), employing the DOS1 algorithm of SCP of the QGIS software developed by Congedo (2016). The methodological workflow for this part of the study is presented in Fig. 14.
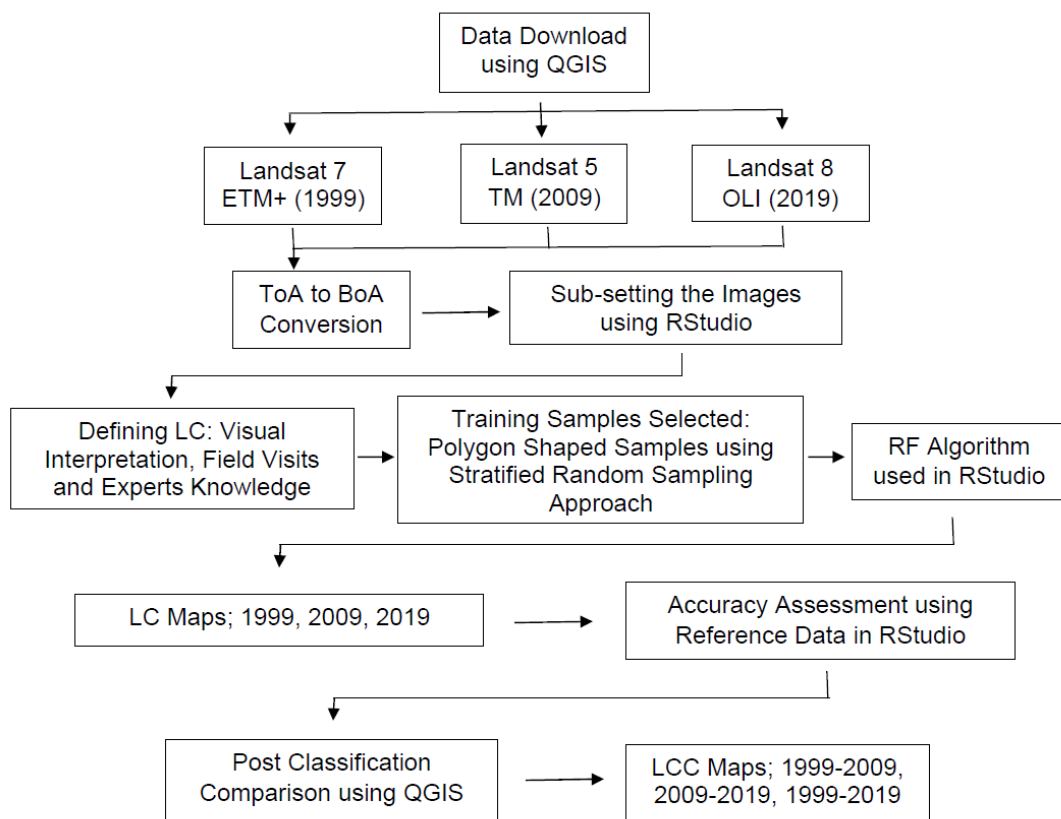
Fig. 14: Methodological Workflow for LC Mapping and LCCD

The pre-processed Landsat images were loaded in the RStudio software. The 'raster' package (Hijmans and Ettan, 2012) was employed for importing, stacking, bricking, and sub-setting (clipping) the images by using the following functions: raster()', 'stack()', 'brick()', 'crop()', 'mask()' and 'shapefile()'. The bands and clipped images for Landsat 7 ETM+ can be seen in Fig. 76 and Fig. 77, respectively (Annexure 1). The bands and clipped images for Landsat 5 TM can be seen in Fig. 80 and Fig. 81, respectively (Annexure 1). The bands and clipped images for Landsat 8 OLI can be seen in Fig. 84 and Fig. 85, respectively (Annexure 1). The images were converted to natural colour composite and NIR composite for classification purposes. The natural colour composites and NIR composites of Landsat 7 ETM+, Landsat 5 TM, and Landsat 8 OLI images of the study area can be

found in Fig. 78, Fig. 79, Fig. 82, Fig. 83, Fig. 86, and Fig. 87, respectively (Annexure 1).

3.2.2. Definition of LC Classes and the Sampling Procedure:

The visual interpretation was used by utilizing the natural colour composites, NIR composites, and high-resolution imagery available from Google Earth, along with the field visits and experts' knowledge from the site area for delineation of the land cover classes and the selection of training samples (Jin et al., 2018); (Ge et al., 2020); (Phan et al., 2020); (Mohajane et al., 2018). There were seven classes identified in the study area which include agricultural land, barren land, SBEF, SCPF, grassland, settlements, and water body. The description of the classes is provided in Table 6.

Table 6: Description of LC Classes

Sr. No.	Class	Description
1	Agricultural Land	Areas covered with agricultural fields.
2	Barren Land	Areas covered with barren fields and rocks.
3	SBEF	Area covered with SBEF.
4	SCPF	Area covered with SCPF.
5	Grassland	Area covered by grasses and sparse shrubs.
6	Settlements	Built up areas in the form of houses, building infrastructures, and roads.
7	Water Body	Permanent Lake i.e., Rawal Lake.

For collecting training samples, different collection strategies such as single pixel selection, seeding, and polygon-shaped selection are available (Chen and Stow, 2002). The polygon-shaped selection was used in this study (Chen and Stow, 2002); (Feng et al., 2015); (Phan et al., 2020). The 'New Shapefile Layer' tool in QGIS software was used for creating polygons. There were overall 105 polygons created with a stratified random sampling approach (i.e., 15 in SBEF, 14 in SCPF, 36 in settlements, 18 in barren land, 17 in agricultural land, and 5 in water body). The

settlements due to their wider spread had a higher number of polygons. The number of pixels between each LC class differed due to the different sizes of the polygons (Thanh Noi and Kappas, 2018). Table 7 shows the total number of pixels for each LC class collected through the different polygons. The polygons were saved into a new shapefile for further analysis in RStudio software. The SBEF had the highest number of pixels because it was the most dominant class.

Table 7: Pixels for LC Classes

Land Cover Classes	Agricultural Land	Barren Land	SBEF	SCPF	Grassland	Settlements	Water Body
Number of Pixels	272	1463	38909	512	982	1699	1323

The training sample imbalance can affect the classification by overfitting the majority class and the class with the lower numbers can be underrepresented (Breiman, 2001b); (He and Garcia, 2009); (Maxwell et al., 2018). The methods such as down-sampling the majority class or duplicating the minority class samples can be helpful against the over-fitting problem (Sun et al., 2007). The sample size of 272 pixels, therefore, was used, employing a down-sampling approach, as a training sample for all the land cover classes for avoiding the imbalance. Thanh Noi and Kappas (2018) reported that training samples with pixels more than 250/class improved the classification accuracy.

3.2.3. Supervised Classification using RF Algorithm:

RF is an ensemble, as mentioned earlier, which involves many independent individual decision trees; a decision tree is also called classification and regression tree (CART) (Feng et al., 2015). The final output of the RF is calculated based on all the decision trees involved, which is also illustrated in Fig. 15. As already explained in one of the previous sections, the bootstrap strategy selects 2/3 of the data randomly with a replacement for building each decision tree (Breiman, 2001b), and the 1/3 of this data is left out, known as the out-of-bag (OOB) data, which is used for cross-validation for evaluating the classification accuracy of the RF, also yielding the OOB error (Breiman, 2001b); (Feng et al., 2015). The OOB error hence is often used

for the assessment of the performance of RF in terms of its prediction (Janitza and Hornung, 2018). RF can be defined by the following equation (Equation 12) (Breiman, 2001b);

$$\{h(x, \theta_k), k = 1,2 \ldots i \ldots\} \qquad (12)$$

Whereas,

h= RF classifier,

x= Input Variable,

$\{\theta_k\}$ = Independently Identically Distributed Random Predictor Variables used for Generating each CART tree

RF algorithm also has default indices for calculating the importance of the variables used in classification problems which are Mean Decrease Accuracy (MDA) and Mean Decrease Gini (MDG) (Han et al., 2016). MDA measures the difference between the OOB error which results from data obtained from random permutations of different variables and the OOB error which results from the original data set, while the MDG is the measure of the reduction of the Gini impurity metric by a variable in a particular class (Breiman, 2001b). The larger the values for MDA and MDG, the more important the variable is (Han et al., 2016). The Gini impurity indicates the probability of misclassification and is a very popular criterion for selecting attributes during the construction of decision trees. It can, however, only be used for the categorical variables.
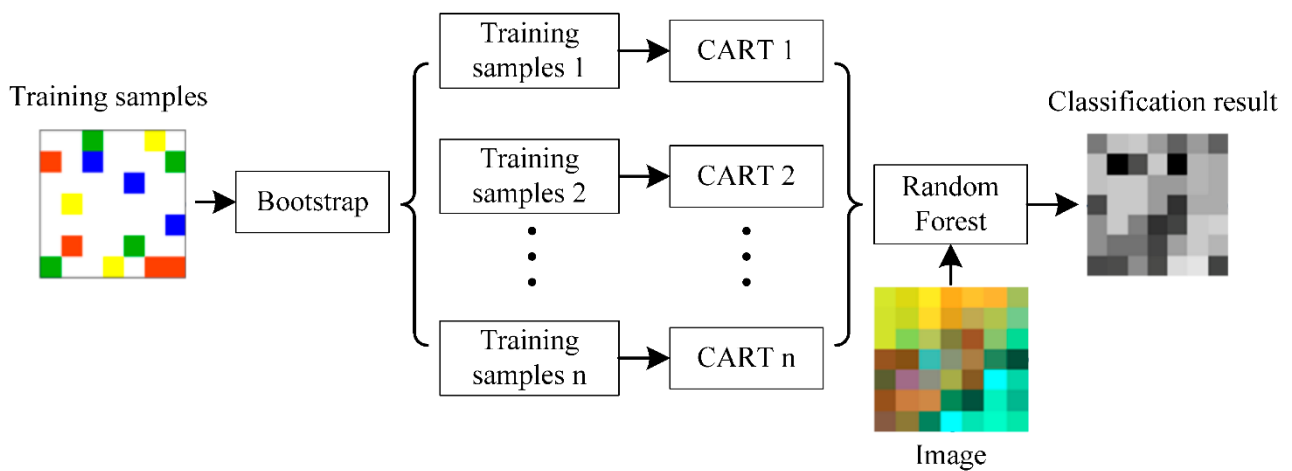
Fig. 15: Schematic Diagram for Image Classification Using Random Forest Algorithm (Feng et al., 2015)

As explained earlier, the RF algorithm requires only two primary parameters, *mtry* which is the number of randomly selected predictors as candidates at each split, and *ntree* which is the number of decision trees to be generated (Belgiu and Drăguţ, 2016). In this research, the *ntree* value of 250 was used after Feng et al. (2015) stated that with *ntree* = 200 desired accuracy results for RF can be achieved.

The shapefile of the training samples in polygon shapes was imported into RStudio software. The 'extract()' function of the raster package was used for extracting raster values for the respective land cover classes, from bricked file image (having multiple layers combined in one file) of the study area and shapefile with the training samples as inputs. The 'randomForest' package was used for performing the RF algorithm (Liaw and Wiener, 2002). The 'rep()' function of the base package of R was employed for down-sampling. The 'tuneRF ()' function of the 'randomForest' package was then used to train the model and for identification of the best value for *mtry* for which the OOB error is the smallest (Janitza and Hornung, 2018). This function also used the raster values extracted from the 'extract()' function as a data frame and the same sample size derived from 'rep()' employing the down-sampling technique. The

61

'predict()' function of the raster package was then used for spatial prediction of the land cover classes with the trained RF model and the bricked file image of the site area as inputs. The final classifications (for each year i.e., 1999, 2009, and 2019) were then saved as a raster file and opened in the QGIS software for developing land cover maps for each year, respectively. The 'varImpPlot()' function of the 'randomForest' package of R was used for identifying the important variables. Mainly, the R script was adapted from (Freie Universität Berlin, 2020).

3.2.4. Accuracy Assessment:

The accuracy assessment helps in identifying the differences between the land cover classification and the reference data (Negassa et al., 2020); (Disperati and Virdis, 2015); (Tsutsumida and Comber, 2015); (Pouliot et al., 2014). For the appropriate selection of the sample size of the reference data, no benchmark exists that is universally accepted (Gedefaw et al., 2020). Lillesand et al. (2015) however have suggested a minimum of 50 samples for each land cover class. Because of this, a field visit was conducted from March 2019 to June 2019 and 50 samples for each land cover class were collected, except for the water body (Lake). The water body was not accessible therefore only 10 samples were collected from it using high-resolution imagery from Google Earth. Overall, there were 310 reference samples collected using a stratified random sampling approach (Twisa and Buchroithner, 2019). The GIS coordinates of the reference samples were entered in the Microsoft Excel spreadsheet and were imported to the QGIS software. The shapefile for the reference samples was saved in the projected Coordinate Reference System (CRS); European Petroleum Survey Group (EPSG): 32643 –World Geodetic System (WGS) 84 / Universal Transverse Mercator (UTM) zone 43 North (N). The shapefile was imported in RStudio for the accuracy assessments. The 'raster' package (Hijmans and Ettan, 2012) was used for this purpose.

The accuracy measures, such as overall accuracy, kappa coefficient, user's and producer's accuracies were calculated in this study, and a confusion matrix (or error matrix) for each land cover classification i.e., 1999, 2009, and 2019 were generated (Congalton, 1991); (Gedefaw et al., 2020); (Foody, 2002). A confusion matrix is also

considered a standard way for presenting the accuracy assessment and characterizing the performance of the classification method utilized (Story and Congalton, 1986); (Rees, 1999).

Producer's accuracy, associated with the omission error, measures the number of pixels classified to an LC class to which they truly belong (Verma et al., 2020); (Zeferino et al., 2020) and hence reflects the accuracy from map maker's (the producer) point of view (Negassa et al., 2020). It is described as the accurate classification of the number of the reference sample sites divided by the total number of the reference sample sites for that class (Equation 13) (Negassa et al., 2020);

Producer′s Accuracy

$$= \frac{\text{Total number of pixels in a category}}{\text{Total number of pixels of that category derived from the reference data (i.e., row total)}} \quad (13)$$

User's accuracy, associated with the commission error, measures the number of pixels classified in an LC class but actually belonging to another LC class (Verma et al., 2020) and hence provides the accuracy on the other hand from the point of the map user (Negassa et al., 2020). User's accuracy is thus the total number of correct classifications per particular class divided by the row total (Equation 14) (Negassa et al., 2020);

User′s Accuracy

$$= \frac{\text{Total number of pixels in a category}}{\text{Total number of pixels of that category derived from the reference data (i.e., column total)}} \quad (14)$$

Overall accuracy calculates the measure of the accuracy of the entire classified image (Equation 15) (Negassa et al., 2020). The overall accuracy of at least 85% has been recommended by various researchers (Mohajane et al., 2018); (Foody, 2002); (Thomlinson et al., 1999).

$$\textbf{Overall Accuracy} = \frac{\text{Sum of the diagonal elements}}{\text{Total number of accuracy sites pixels (column total)}} \quad (15)$$

The kappa coefficient is a measure of agreement between the land cover classification and the respective reference data (Mishra et al., 2020). The kappa coefficient generally ranges between-1 to 1, but it usually falls between 0 to 1 (Wongpakaran et al., 2013). Five levels of accuracy for the kappa coefficient were used in this study; higher than 0.85 (excellent), 0.70 to 0.85 (very good), 0.55 to 0.70 (good), 0.4-0.55 (fair), lower than 0.4 (poor or very poor) (Monserud and Leemans, 1992).

The equation used for the calculation of the kappa statistics is as follows (Equation 16);

$$K = \frac{N \sum_{i=1}^{X} X_{ii} - \sum_{i=1}^{r}(X_{i+} \times X_{+i})}{N^2 - \sum_{i=1}^{r}(X_{i+} \times X_{+i})} \tag{16}$$

where N stands for the total number of samples in the matrix, r is the number of rows in the matrix, X_{ii} is the number in row i and column i, X_{+i} is the total for row i, and X_{i+} corresponds to the total for column i.

3.2.5. LCCD:

Change detection is "*the process of identifying differences in the state of an object or phenomenon by observing it at different times*" (Singh, 1989). There have been various change detection methods that have been developed in the last few decades such as image differencing, post-classification comparison, vegetation index differencing and principal component analysis, etc. (Lu et al., 2004). A post-classification comparison is a common approach used for change detection (Lu et al., 2004); (Mei et al., 2016); (Henchiri et al., 2020). The post-classification comparison, thus, was used in this study for the analysis of the land cover changes between different time-periods (Mishra et al., 2020); (Fernández-Landa et al., 2016). It involves a change matrix that provides essential information regarding the changes in the LC in different time-periods. Using the SCP (Congedo, 2016), the post-classification change/LCC matrix was generated for the three time periods: 1999 to 2009, 2009 to 2019, and 1999 to 2019 (Gedefaw et al., 2020). The area changes in

hectares and percentage changes for each LC for all three periods were calculated (Kindu et al., 2016); (Gashaw et al., 2018). The annual change rates in ha were also calculated for each LC (Tilahun et al., 2017).

The LCC % was calculated by the following equation (Equation 17) (Garai and Narayana, 2018);

$$\text{LCC\%} = \frac{\text{Present LC Area} - \text{Previous LC Area}}{\text{Previous LC Area}} \times 100 \qquad (17)$$

The Rate of Change (ROC) was calculated using the following equation (Equation 18) (MohanRajan et al., 2020);

$$ROC\ (ha/yr) = \frac{T_2 - T_1}{T_i} \qquad (18)$$

where T_1 is the area (ha) of LC for the initial time-period 1; T_2 is the area (ha) of LC for the final time-period 2; T_i is the time interval between the T_1 and T_2 in years (yr).

4. Results:

4.1. Forest Biomass and Carbon Stock Assessment of MHNP:

4.1.1. Structural Characteristics of the two Forests of the MHNP:

As demonstrated in Table 8, the mean AGC for SCPF was 73.36 ± 32.55 Mg C ha^{-1} and the mean AGC for SBEF was 16.88 ± 25.81 Mg C ha^{-1}. There was a significant difference recorded between the mean AGC of the two forests ($W = 43, p < 0.05$).

Table 8: Structural characteristics of forests of MHNP

Forests	Mean AGC (Mg Cha^{-1})	Mean AGB (Mg ha^{-1})	Mean Tree Volume (m^3 ha^{-1})	Mean Basal Area (m^2 ha^{-1})	Mean Density per hectare	Mean DBH (cm)	Mean Tree Height (m)
SCPF	73.36 ± 32.55	146.73 ± 65.11	198.75 ± 87.76	14.48 ± 4.80	139.13 ± 22.88	36.37 ± 6.51	27.34 ± 3.67
SBEF	16.88 ± 25.81	33.77 ± 51.63	37.82 ± 50.38	4.28 ± 3.43	142.90 ± 32.37	18.64 ± 6.03	10.62 ± 1.99
Combined	50.62 ± 40.84	101.25 ± 81.68	133.96 ± 108.96	10.37 ± 6.60	140.64 ± 26.96	29.23 ± 10.77	20.61 ± 8.81

The mean AGB for SCPF was recorded as 146.73 ± 65.11 Mg ha^{-1}, whereas the mean AGB for SBEF was recorded as 33.77 ± 51.63 Mg ha^{-1}. There was a significant difference recorded between the AGB of the two forests ($W = 43, p < 0.05$).

The mean tree volume for the SCPF was recorded as 198.75 ± 87.76 m^3 ha^{-1} and for SBEF, it was recorded as 37.82 ± 50.38 m^3 ha^{-1}. There was a significant difference recorded between the tree volume of the two forests ($W = 38, p < 0.05$).

The mean basal area for the SCPF was 14.48 ± 4.80 m^2 ha^{-1} and the mean basal area for SBEF was recorded as 4.28 ± 3.43 m^2 ha^{-1}. There was a significant difference recorded between the tree basal area of the two forests ($W = 68, p < 0.05$).

The mean density per ha for the SCPF was 139.13 ± 22.88 and the mean density per ha for SBEF was 142.90 ± 32.37. There was no significant difference recorded between the tree densities per ha of the two forests ($W = 723.5, p > 0.05$).

The mean DBH for the SCPF was 36.37 ± 6.51 cm and the mean DBH for the SBEF was 18.64 ± 6.03 cm. There was a significant difference recorded between the mean DBHs of the two forests ($W = 58, p < 0.05$).

The mean tree height for the SCPF was 27.34 ± 3.67 m and the mean tree height for the SBEF was 10.62 ± 1.99 m. There was a significant difference recorded between the mean tree heights of the two forests ($W = 0, p < 0.05$).

Spearman correlation coefficients were calculated between the AGB and other structural characteristics of the SCPF (Table 9). Strong positive and significant correlations were recorded between AGB and AGC, volume, basal area, mean DBH, and mean tree height.

Table 9: Spearman correlation coefficients for SCPF (*n*=46)

Variables	AGC (Mg Cha^{-1})	Volume (m^{3}ha^{-1})	Basal Area (m^{2}ha^{-1})	Mean DBH (cm)	Mean Tree Height (m)
AGB (Mgha^{-1})	1*	0.99*	0.94*	0.91*	0.75*
AGC (Mg Cha^{-1})		0.99*	0.94*	0.91*	0.75*
Volume (m^{3}ha^{-1})			0.94*	0.91*	0.75*
Basal Area (m^{2}ha^{-1})				0.87*	0.59*
Mean DBH (cm)					0.71*

*Correlation is significant at the 0.05 level.

Spearman correlation coefficients were calculated between AGB and other structural characteristics of the SBEF (Table 10). Strong positive and significant correlations were recorded between AGB and AGC, volume, basal area, mean DBH, and mean tree height.

Table 10: Spearman correlation coefficients for the SBEF (*n*=31)

Variables	AGC (Mg Cha^{-1})	Volume (m^{3}ha^{-1})	Basal Area (m^{2}ha^{-1})	Mean DBH (cm)	Mean Tree Height (m)
AGB (Mgha^{-1})	1*	0.95*	0.89*	0.87*	0.68*
AGC (Mg Cha^{-1})		0.95*	0.89*	0.87*	0.68*
Volume (m^{3}ha^{-1})			0.93*	0.90*	0.70*
Basal Area (m^{2}ha^{-1})				0.89*	0.52*
Mean DBH (cm)					0.64*

*Correlation is significant at the 0.05 level.

The DBH interval with the highest number of stems was recorded as 35-40 cm for the SCPF, as can be seen in Fig.16. It is followed by the DBH interval of 25-30 cm and the DBH interval of 20-25 cm. The total number of 114 stems was recorded in the DBH interval class 35-40 cm, which formed 17.81% of the total stems of the SCPF. Overall, there were 640 stems recorded for the SCPF. The DBH interval 25-30 cm recorded 107 stems, which formed 16.72% of the total stems, and for DBH interval 20-25 cm, 85 stems were recorded, forming 13.28% of the total stems of the SCPF. The maximum DBH was recorded as 67 cm, for *Pinus roxburghii*, and the minimum DBH as 10 cm, also for *Pinus roxburghii*, for the SCPF.
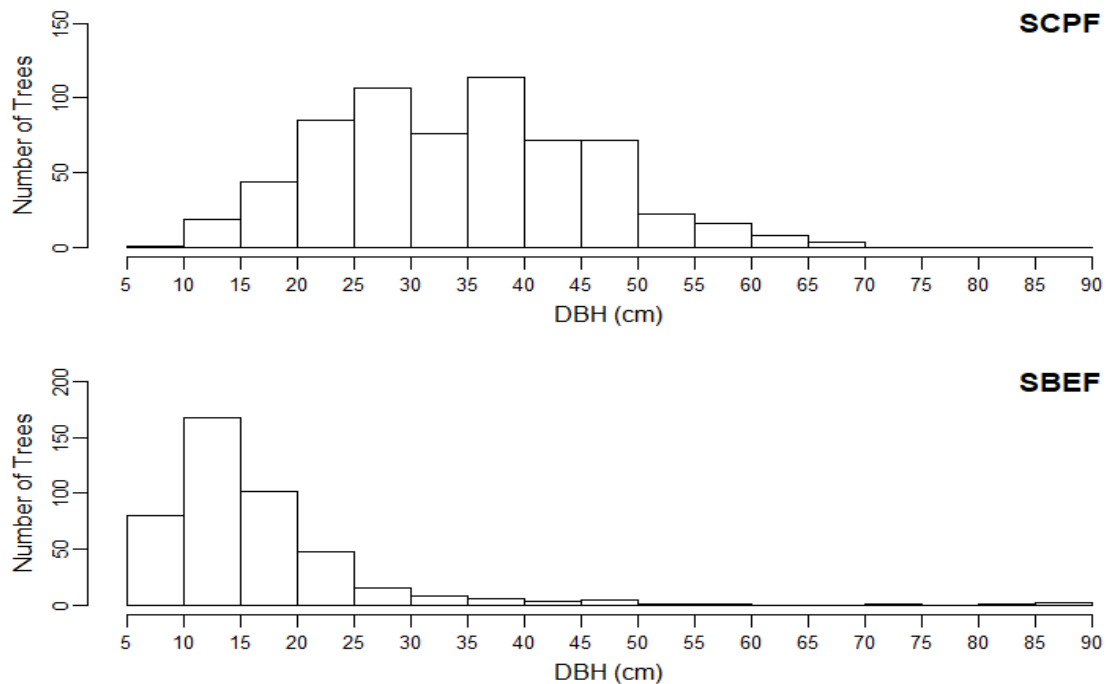
Fig. 16: DBH Distribution of the Two Forests of the MHNP

68

For SBEF, the DBH interval of 10-15 cm contained the highest number of stems, as demonstrated in Fig. 16. It included 167 stems, which formed 37.70% of the total stems of the SBEF. There were overall 443 stems recorded for the SBEF. The DBH interval 15-20 cm recorded the second highest number of trees with 102 trees, constituting 23.02% of the total number of trees. The DBH interval of 5-10 cm formed the interval with the third highest number of trees of 80, constituting 18.06% of the total stems. The highest DBH was recorded as 87 cm for *Ficus palmata subsp. virgata* and the lowest DBH was recorded as 5.5 cm for *Grewia optiva* for the SBEF.

As demonstrated in Fig.17, the height interval class 21-24 m contained the highest number of stems of 117, which forms 18.28% of the total stems of the SCPF. The class interval 24-27 m formed the second highest interval class with 114 stems, constituting 17.81% of all the stems. The class interval 27-30 m formed the third highest class interval with 102 stems, which made 15.94% of the total stems of the SCPF. The highest height was 41.7 m (*Pinus roxburghii*) and the lowest height was10 m (*Bauhinia variegata*) for the SCPF.

The height class intervals, 6-9 m, and 9-12 m contained the highest number of stems in the SBEF, as can be seen in Fig. 17. Both the intervals contained 163 stems each, which formed 36.79% of the total stems of the SBEF. The height class interval of 12-15 m contained the second highest number of stems after the two interval classes mentioned above. The 12-15 m interval class contained 41 stems which formed 9.26% of the total stems. The *Bombax cieba* was the tallest tree with 37.7 m height and *Acacia modesta* was recorded with the lowest height of 4.5 m for the SBEF.

The height distributions of the SCPF and the SBEF also show that there are no distinct strata for both forests.
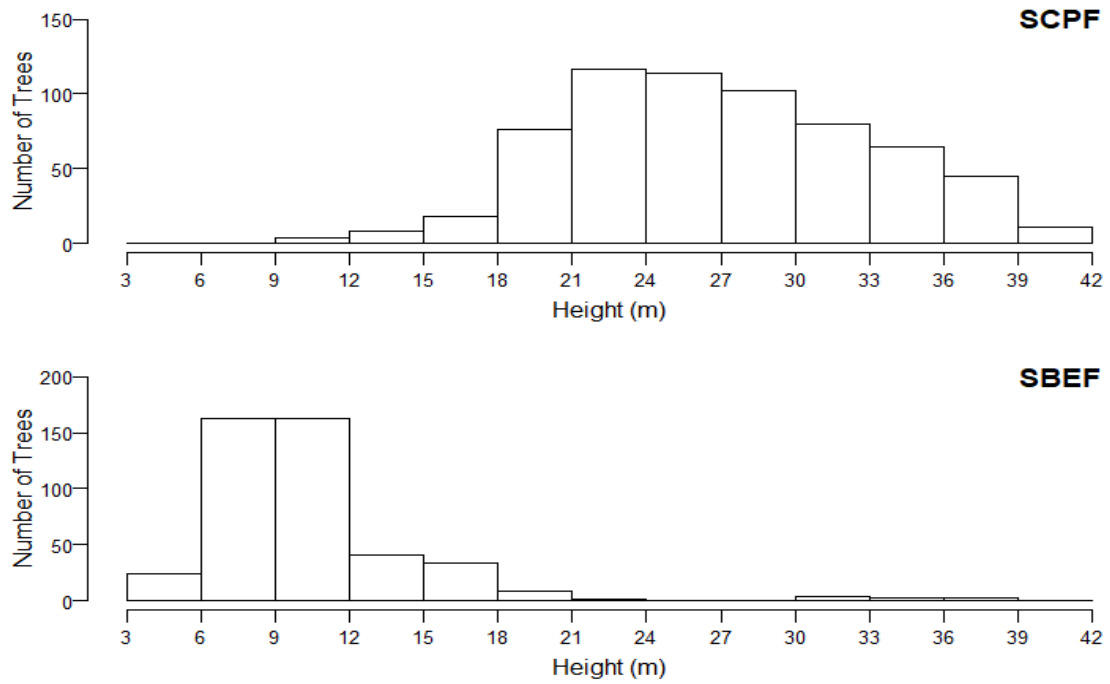
Fig. 17: Height Distribution of Two Forests of the MHNP

The AGB (Mg ha^{-1}) of the SCPF increases with the increasing mean DBH (cm) and mean tree height as shown in the 3D graph (Fig. 18).

The AGB (Mg ha^{-1}) of the SBEF has shown an erratic pattern against the mean DBH (cm) and the mean tree height (m) as can be seen in the 3D graph (Fig. 19).
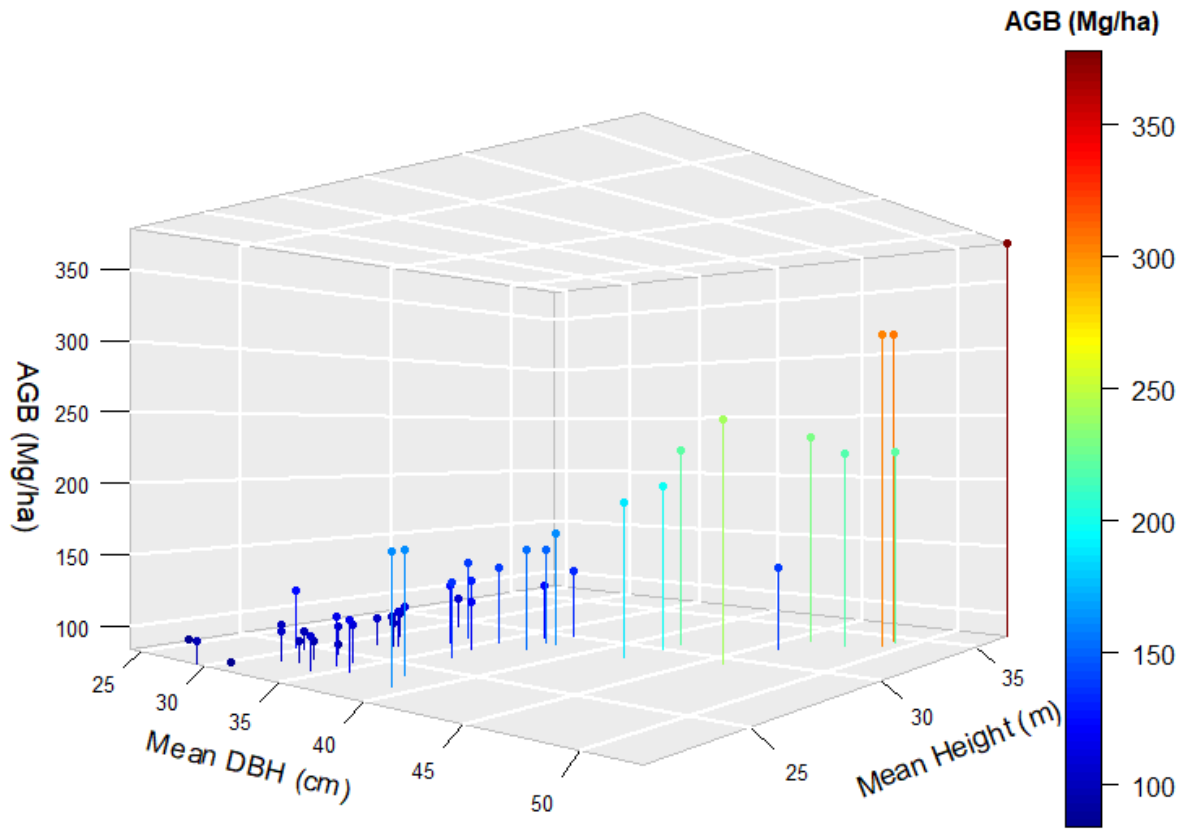
Fig. 18: AGB (Mg ha^{-1}) of SCPF against the Mean DBH (cm) and the Mean Height (m)
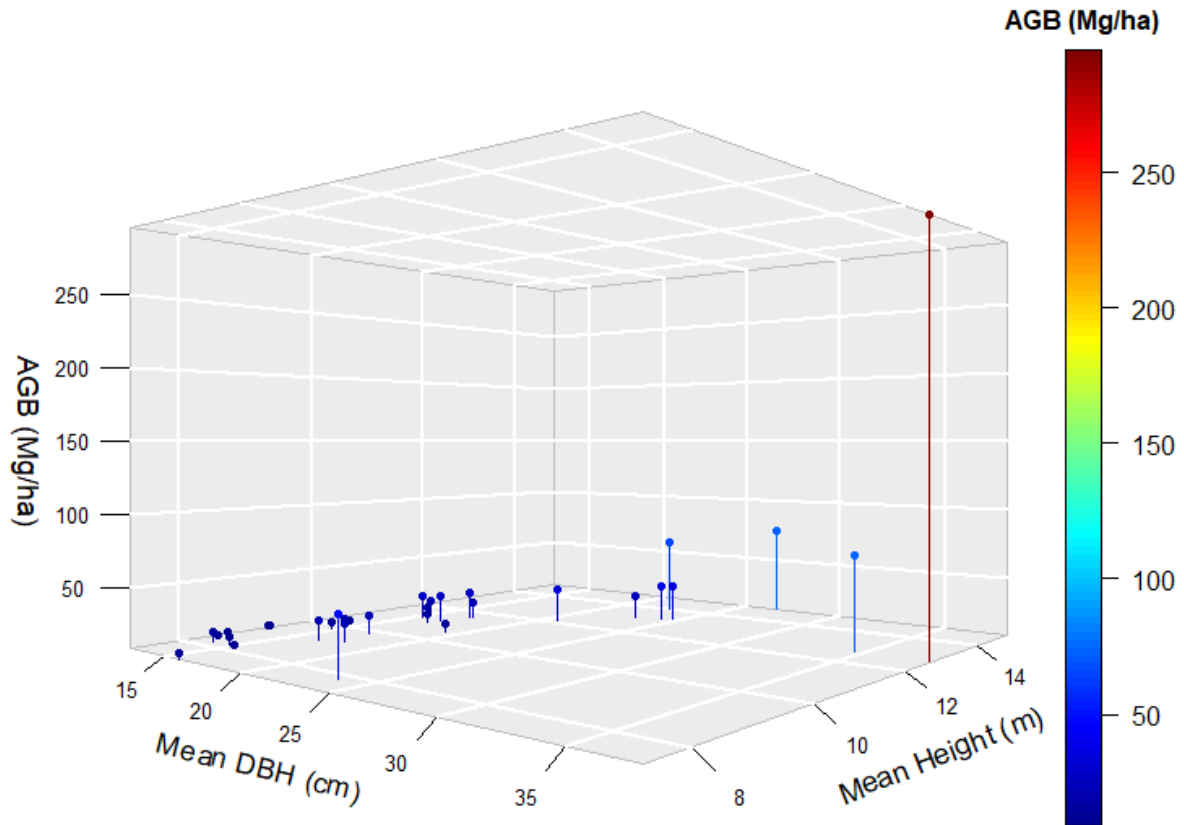
Fig. 19: AGB (Mg ha^{-1}) of SBEF against the Mean DBH (cm) and the Mean Height (m)

As demonstrated in Table 11, the *Pinus roxburghii* contributed the highest percentage of 98.85%, which constitutes a total AGC of 3336.13 Mg C ha^{-1}, from the overall total AGC of 3374.80 Mg C ha^{-1} for the SCPF. The *Bombax cieba* formed 0.81%, with 27.01 Mg C ha^{-1}, and the *Bauhinia variegata* contributed 0.34%, with 11.64 Mg C ha^{-1}, to the total AGC of the SCPF of MHNP.

Table 11: AGC contribution of different trees species in SCPF

Sr. No.	Species	Total AGC (Mg C ha^{-1})	AGC Percentage (%)
1	*Pinus roxburghii* Sarg.	3336.13	98.85
2	*Bombax ceiba* L.	27.01	0.81
3	*Bauhinia variegata* L.	11.66	0.34
Total		3374.80	100

For the SBEF, *Eucalyptus camaldulensis* formed the highest contribution of 33.65%, with 176.14 Mg C ha^{-1}, in the total AGC, as shown in Table 12. The *Ficus palmate subsp. virgata* and the *Bauhinia variegata* formed the second and third highest contributions with 94.24 Mg C ha^{-1}, 18%, and 73.35 Mg C ha^{-1}, 14.01%, respectively, in the total AGC of the SBEF of the MHNP. Similarly, the *Acacia modesta*, *Bombax ceiba*, and *Grewia optiva* followed with 42.29 Mg C ha^{-1} (8.08%), 36.94 Mg C ha^{-1} (7.06%), and 30.84 Mg C ha^{-1} (5.89%). The lowest contributions were recorded from the *Ficus benghalensis* with 0.7%, constituting 3.67 Mg C ha^{-1}, and the *Flacourtia indica*, with 0.1%, forming 0.51 Mg C ha^{-1}, of the total AGC of the SBEF of the MHNP.

Table 12: AGC contribution of different trees species in SBEF

Sr. No.	Species	Total AGC (Mg C ha^{-1})	AGC Percentage (%)
1	*Eucalyptus camaldulensis* Dehnh.	176.14	33.65
2	*Ficus palmata subsp. virgata* Forssk.	94.24	18
3	*Bauhinia variegate* L.	73.35	14.01
4	*Acacia modesta* Wall.	42.29	8.08
5	*Bombax ceiba* L.	36.94	7.06
6	*Grewia optiva* J. R. Drumm. ex Burret	30.84	5.89
7	*Mallotus philippensis* (Lam.) Muell. Arg.	20.78	3.97
8	*Cassia fistula* L.	10.99	2.1
9	*Broussonetia papyrifera* (L.) L'Herit ex Vent.	9.86	1.88
10	*Celtis australis* L.	9.29	1.77
11	*Albizia lebbeck* (L.) Benth	8.44	1.61

12	*Ziziphus mauritiana* Lam.	6.14	1.17
13	*Ficus benghalensis* L.	3.67	0.7
14	*Flacourtia indica* (Burm. f.) Merr.	0.51	0.1
Total		523.47	100

The highest AGC was recorded for plot no. 45, which was 189.01 Mg C ha^{-1}, for the SCPF, as demonstrated in Fig. 20. The plot no. 45 formed 5.06% of the total AGC of the SCPF. The highest AGC for plot no. 45 is attributed to the high DBH range which varied from 40-62.5 cm and the greater heights ranging from 28-40.1 m. Plot no. 16 recorded the second highest AGC of 153.90 Mg C ha^{-1} for SCPF. The lowest AGC for SCPF was recorded for plot no. 33, which was 41.95 Mg C ha^{-1}.

For SBEF, plot no. 19 recorded the highest AGC of 147.68 Mg C ha^{-1} (Fig. 20). Plot no. 19 formed 28.21% of the total AGC of the SBEF. The DBH range for Plot no. 19 was from 9-86 cm and the height ranged from 6.6-33 m, which contributed to the higher AGC in this plot. The *Eucalyptus camaldulensis* was also sampled from this plot which was the reason for higher DBHs and heights from this plot. Plot no. 31 was recorded with the second highest AGC of 36.85 Mg C ha^{-1} for the SBEF. Plot no. 9 of the SBEF recorded the lowest AGC of 4.28 Mg C ha^{-1}.
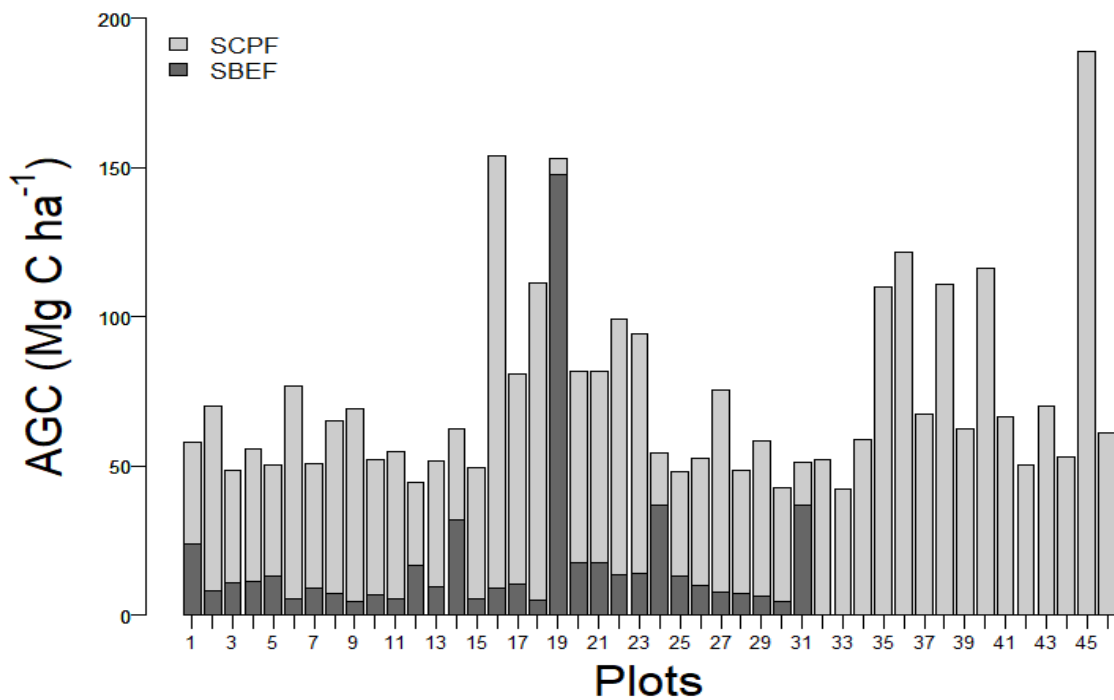
Fig. 20: AGC Distribution of the Two Forests of the MHNP

4.1.2. Regression and Correlation Analysis of *Pinus roxburghii*:

The regression analysis between DBH (predictor variable) and height (outcome variable) of the *Pinus roxburghii* had shown a significant association (R^2 = 0.74), where 74% of the variation in height is explained by the predictor variable, DBH, as evident from the Fig. 21. The relationship between the two variables is also statistically significant ($p < 0.05$). The linear regression equation obtained is the following; *y=11.55+0.45x*. The analysis included 612 sampled trees of *Pinus roxburghii*. Spearman correlation coefficient of 0.85 was recorded for the DBH and height variables, which shows a strong positive linear relationship between the two.

Fig. 21: DBH-Height Regression of *Pinus roxburghii*

The regression analysis between basal area (predictor variable) and volume (outcome variable) of the *Pinus roxburghii* had shown a significant association ($R^2 = 0.96$), which shows that 96% of the variation in volume is explained by the predictor variable, basal area, as demonstrated in Fig. 22. A significant statistical relationship was also revealed ($p < 0.05$) between the two variables. The total number of observations used for the analysis was 46. The linear regression equation of '*y=58.96+17.87x*' was obtained from the analysis. Spearman correlation coefficient of 0.94 was recorded for the basal area and volume variables, which shows a strong positive linear relationship between the two.

Fig. 22: Basal Area-Volume Regression of *Pinus roxburghii*

As demonstrated in Fig. 23, a non-linear relationship was revealed between the two variables, DBH (predictor variable) and AGB (outcome variable). This non-linear relationship was in the form of a power curve. A significant association was revealed between the two variables, AGB (outcome variable) and DBH (predictor variable) (R^2 = 0.98). The value of the coefficient of determination, R^2, shows that 98% of the variation in AGB is explained by the DBH. A significant statistical relationship was also revealed between the two variables (p < 0.05). The power regression equation of '*y=0.0007 * x$^{2.62}$*' was obtained from the analysis. A total number of 612 observations, for each variable, were used. Spearman correlation coefficient of 0.99 was recorded for the DBH and AGB, which shows a strong positive linear relationship between the two variables.

$$y = 0.0007 * x^{2.62}$$
$$R^2 = (0.98)$$
$$p < 0.05$$
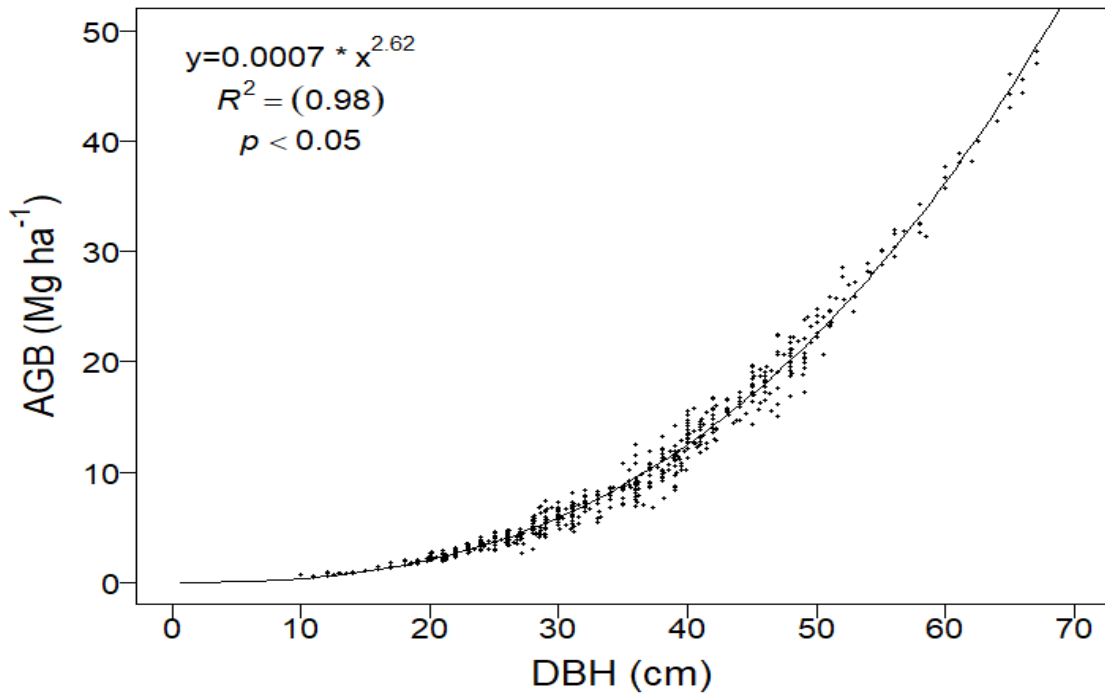
Fig. 23: DBH-AGB Power Regression of *Pinus roxburghii*

4.1.3. Regression and Correlation Analysis of *Bauhinia variegata*:

The regression analysis between the DBH (predictor variable) and height (outcome variable) of the *Bauhinia variegata* revealed a moderate association (R^2 = 0.36) (Fig. 24). Statistically, however, a significant relationship was revealed ($p < 0.05$). The linear regression equation of '*y=5.60+0.25x*' was obtained from the analysis. A total number of 141 observations, for each variable, were used. Spearman correlation coefficient of 0.66 was recorded for the DBH and height, which shows a moderate positive linear relationship between the two variables.
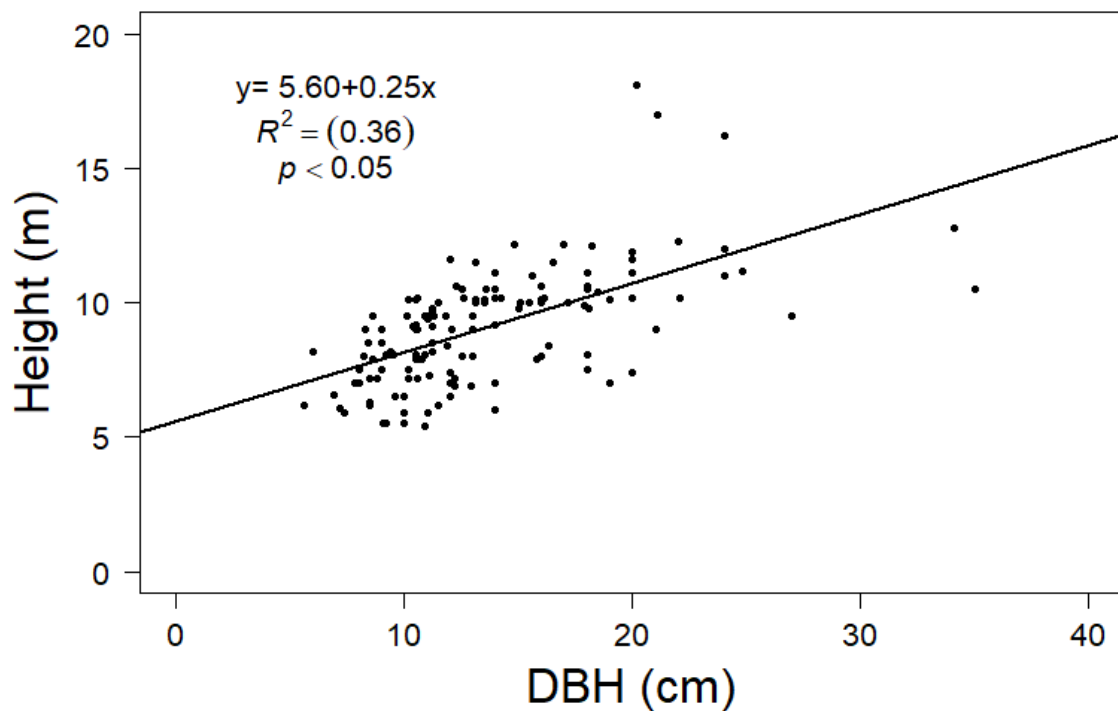
Fig. 24: DBH-Height Regression of *Bauhinia variegata*

According to Fig. 25, the regression analysis between the basal area (predictor variable) and volume (outcome variable) of the *Bauhinia variegata* revealed a significant association between the two variables (R^2 = 0.92); the value of the coefficient of determination, R^2, shows that 92% of the variation in the volume is explained by the predictor variable, basal area. A significant statistical relation was also revealed between the basal area and volume ($p < 0.05$). A total number of 20 observations, for each variable, was used for the regression analysis. The linear regression equation of '*y=0.07+5.86x*' was obtained from the analysis. Spearman correlation coefficient of 0.97 was recorded for the basal area and volume of the *Bauhinia variegata*, which shows a strong positive linear relationship between the two variables.
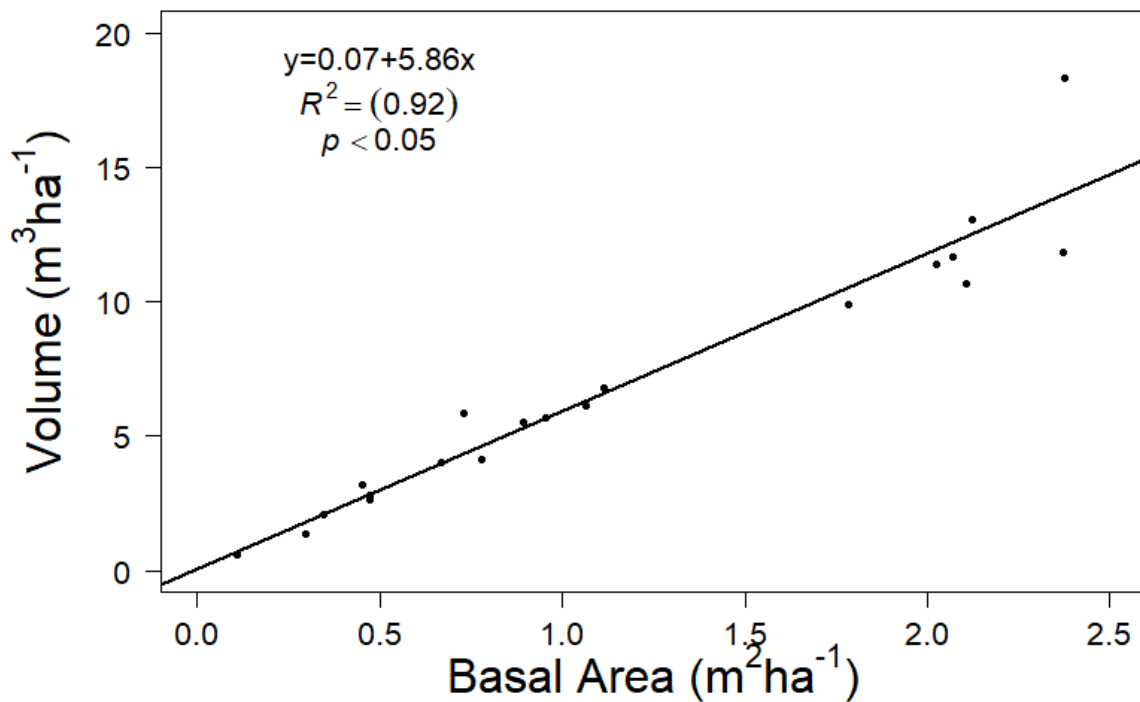
Fig. 25: Basal Area-Volume Regression of *Bauhinia variegata*

A non-liner relationship, in the form of power regression, was revealed between the DBH (predictor variable) and the AGB (outcome variable) of the *Bauhinia variegata,* according to Fig. 26. A significant association was revealed between the two variables (R^2 = 0.93), which shows that 93% of the variation in AGB can be explained by the DBH. A significant statistical relationship was also revealed between the two variables (p < 0.05). A total number of 141 observations, for each variable, were used for the regression analysis. The power regression equation of '*y=0.002 * x²·²¹*' was obtained from the analysis. Spearman correlation coefficient of 0.97 was recorded for the DBH and AGB, which shows a strong positive linear relationship between the two variables.
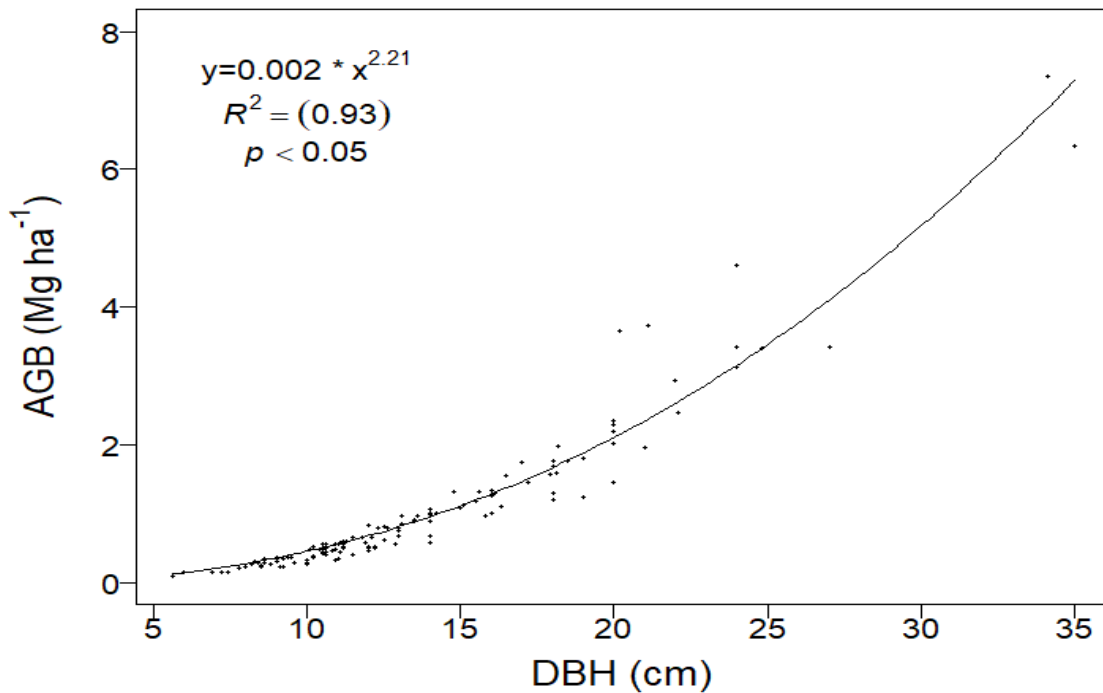
Fig. 26: DBH-Tree Biomass Power Regression of *Bauhinia variegata*

4.1.4. Regression and Correlation Analysis of *Grewia optiva*:

According to Fig. 27, the regression analysis between DBH (predictor variable) and height (outcome variable) of the *Grewia optiva* revealed a moderate association (R^2 = 0.42). A significant statistical relationship had been revealed between the two variables ($p < 0.05$). The linear regression equation of '*y=4.69+0.33x*' was obtained from the analysis. A total number of 71 observations, for each variable, were used for the regression analysis. Spearman correlation coefficient of 0.64 was recorded for the DBH and height, which shows a moderate positive linear relationship between the two variables.
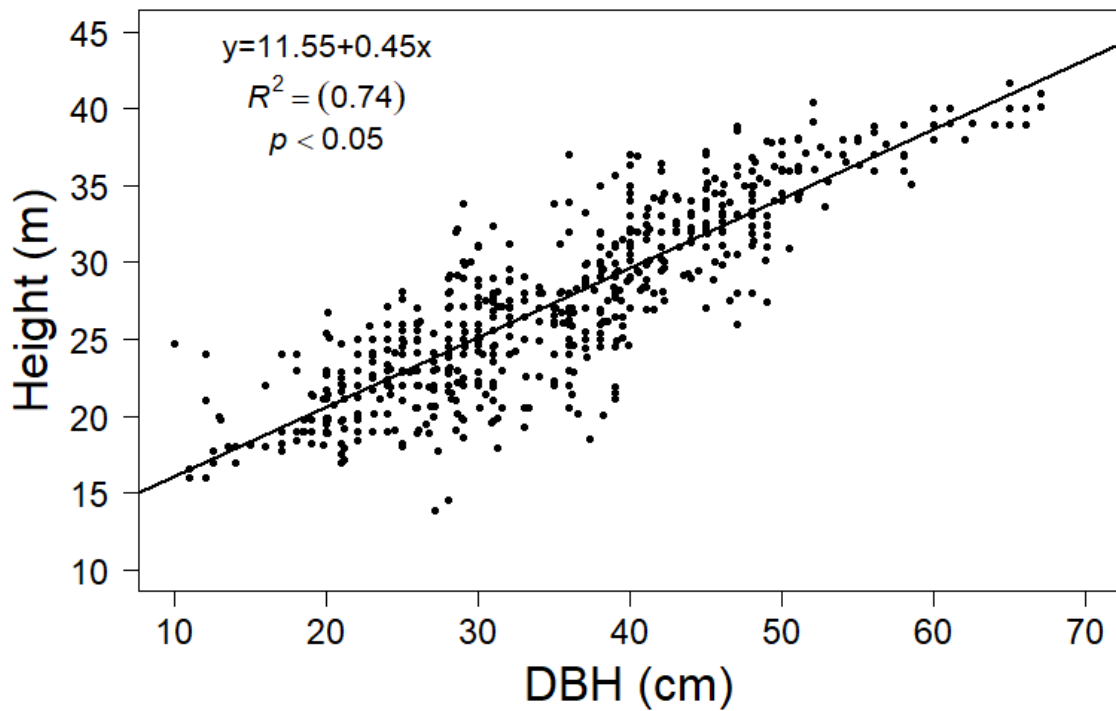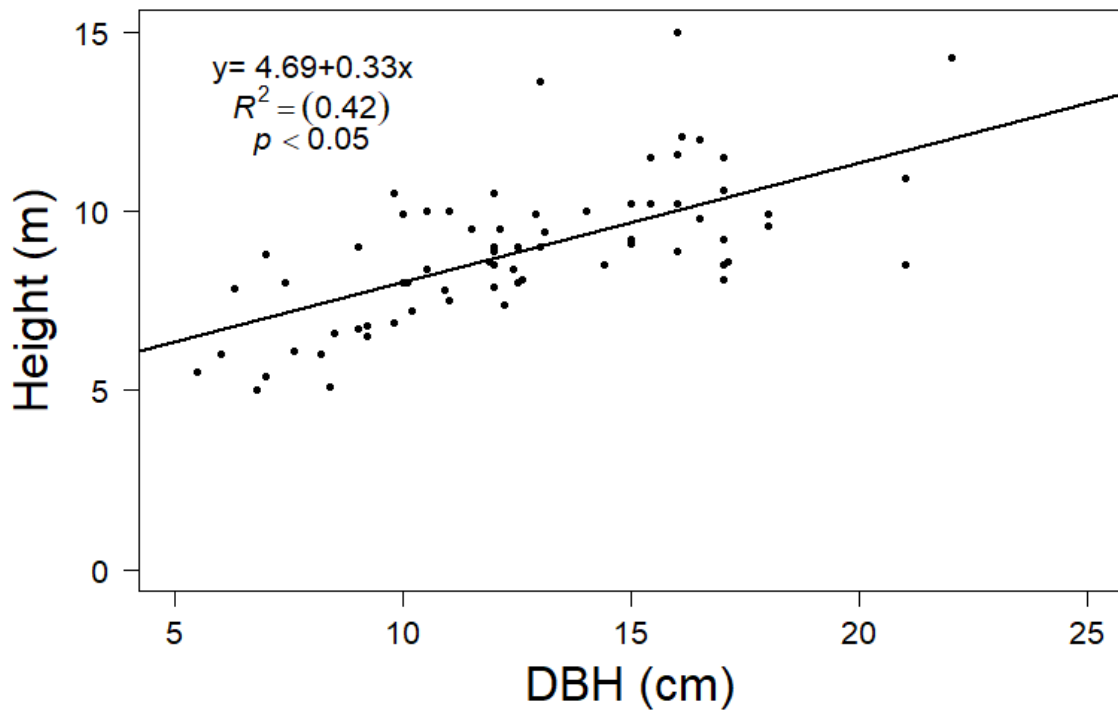
Fig. 27: DBH-Height Regression of *Grewia optiva*

According to Fig. 28, the regression analysis between the basal area (predictor variable) and volume (outcome variable) of the *Grewia optiva* revealed a significant association between the two variables (R^2 = 0.97); the value of the coefficient of determination, R^2, shows that 97% of the variation in the volume is explained by the predictor variable, basal area. A significant statistical relation was also revealed between the two variables (p < 0.05). A total number of 12 observations, for each variable, were used for the regression analysis. The linear regression equation of '*y=0.20+5.95x*' was obtained from the analysis. Spearman correlation coefficient of 0.97 was recorded for the basal area and volume of the *Grewia optiva*, which shows a strong positive linear relationship between the two variables.
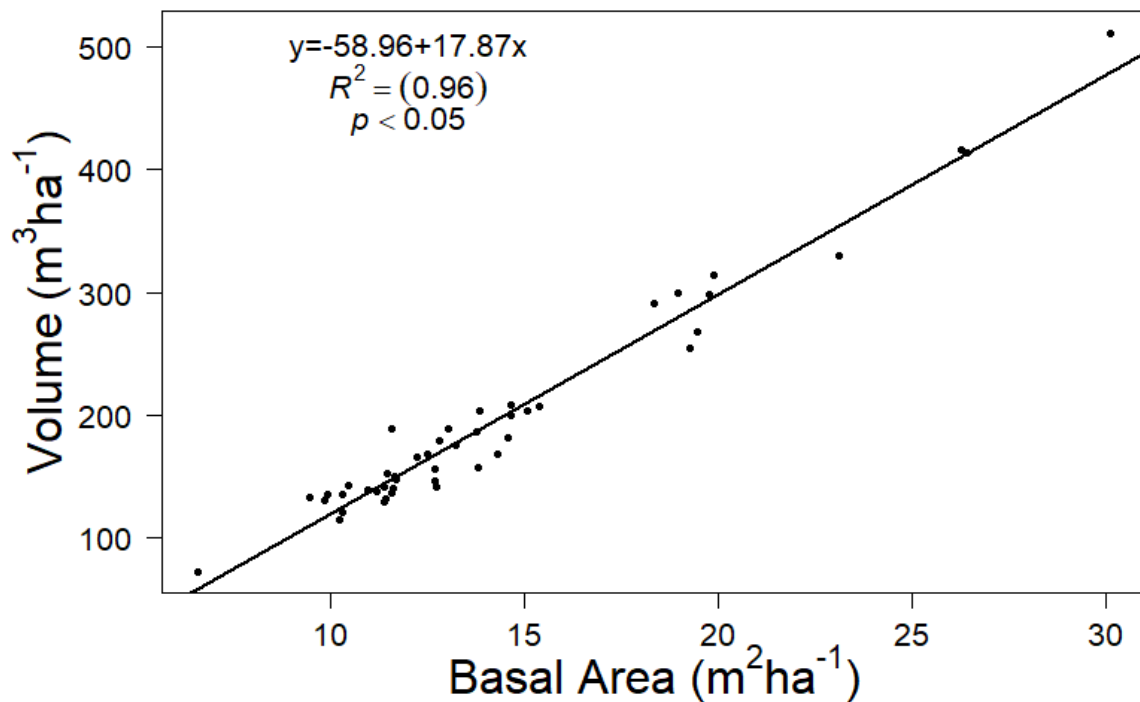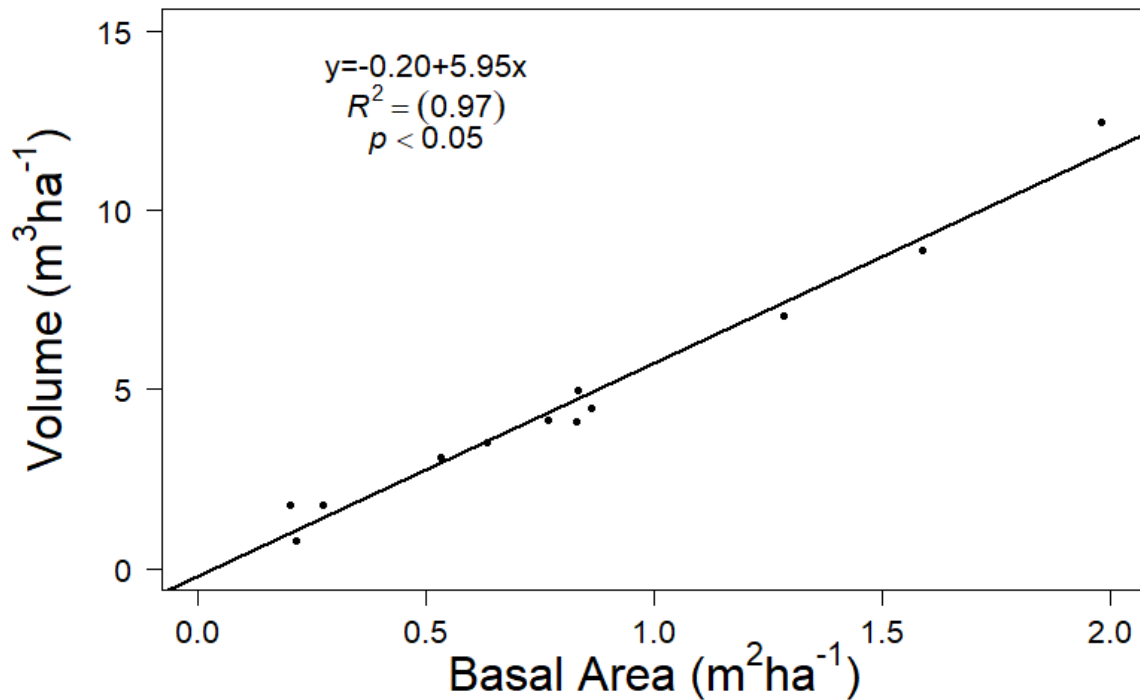
Fig. 28: Basal Area-Volume Regression of *Grewia optiva*

A non-linear relationship was recorded for the DBH (predictor variable) and the AGB (outcome variable) of the *Grewia optiva,* which can be seen in Fig. 29. This non-linear relationship was in the form of power regression. A moderate association was revealed between the two variables (R^2 = 0.59), which shows that 59% of the variation in AGB is explained by the DBH, which is the outcome variable. A significant statistical relationship was also revealed between the two variables ($p <$ 0.05). A total number of 71 observations, for each variable, was used for the regression analysis. The power regression equation of '*y=0.002 * x$^{2.33}$*' was obtained from the analysis. Spearman correlation coefficient of 0.97 was recorded for the DBH and AGB, which shows a strong positive linear relationship between the two variables.
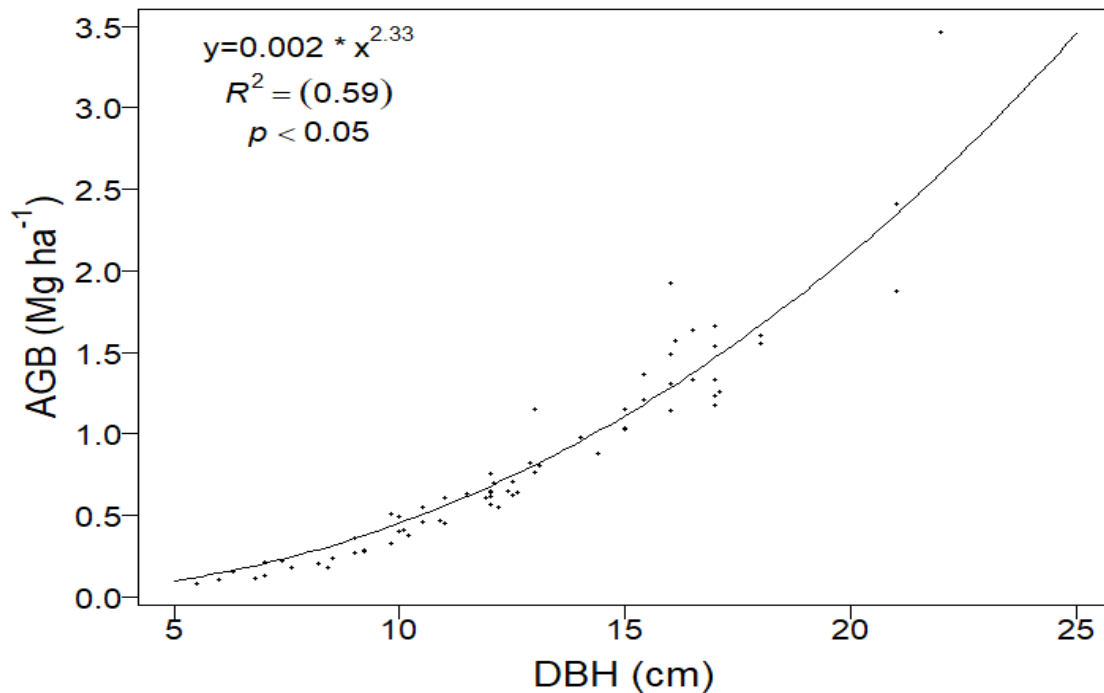
Fig. 29: DBH-AGB Power Regression of *Grewia optiva*

4.1.5. Indices estimation and regression analysis of AGB-Indices of the MHNP:

According to Fig. 30, the NDVI ranged from -0.34 to 0.80. The minimum NDVI value was recorded as -0.34 and the highest value was recorded as 0.80. The mean NDVI for the MHNP was recorded as 0.60 ± 0.19. The NDVI distribution of the MHNP is left-skewed (Fig. 31). The highest values of NDVI were recorded in the class interval 0.6-0.8 which was 69.82%, followed by 0.4-0.6 which was recorded as 21.22% (Table 13).
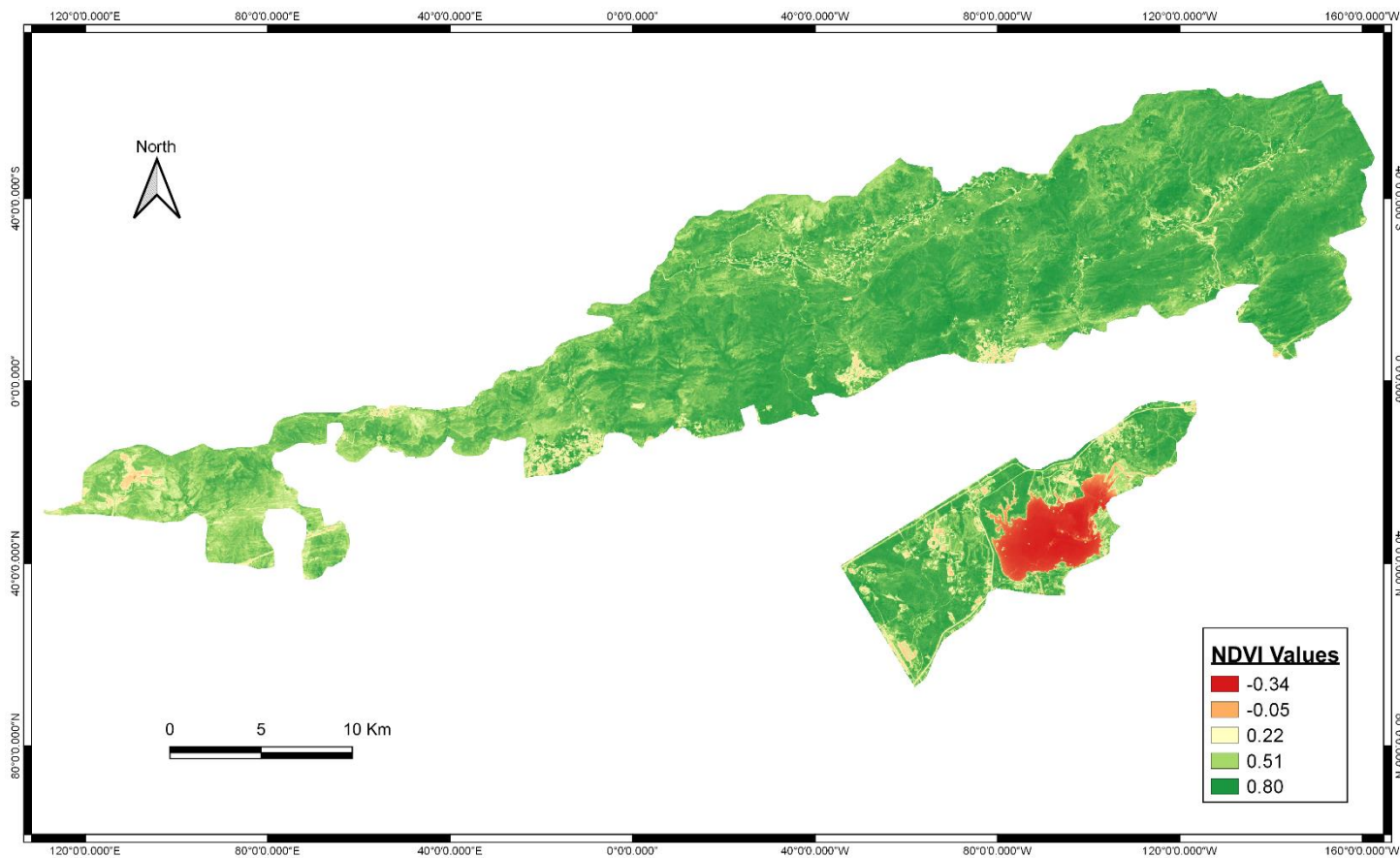
Fig. 30: NDVI Estimation of MHNP
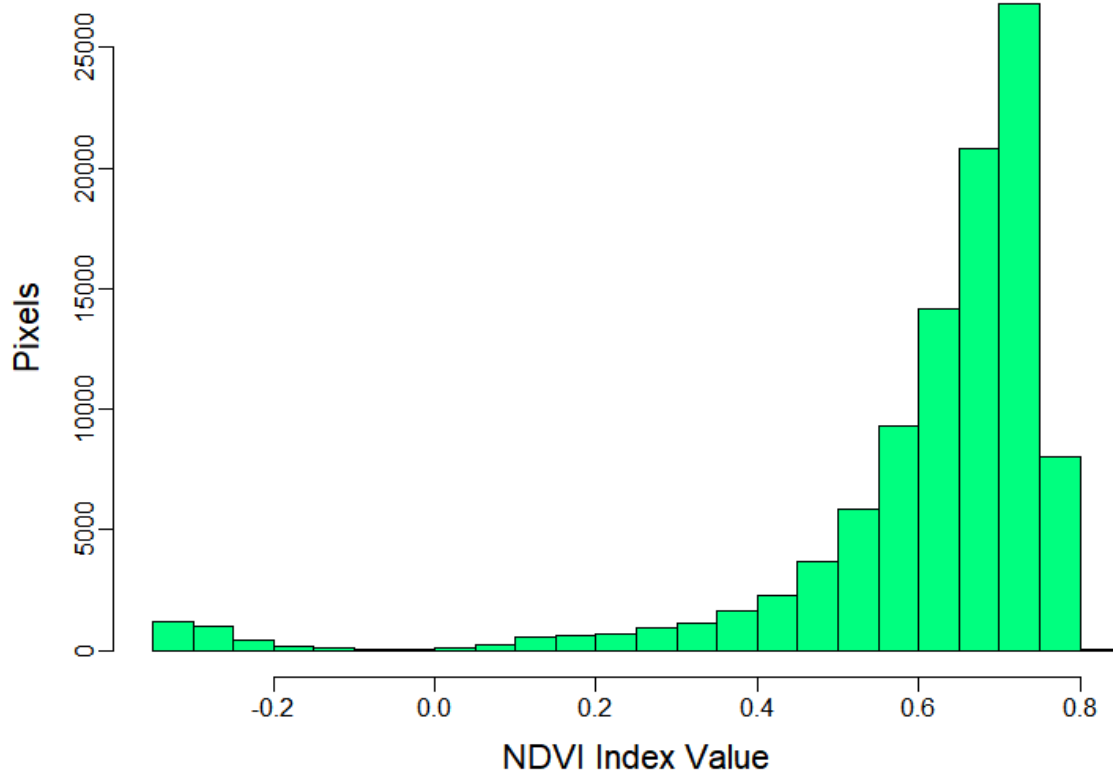
Fig. 31: NDVI Distribution of MHNP

Table 13: NDVI Percentage by Class Interval

Sr. No.	NDVI Index Class Interval	Percentage of Total Pixels
1	-0.4 - -0.2	2.53
2	-0.2 – 0	0.49
3	0 – 0.2	1.56
4	0.2 – 0.4	4.35
5	0.4 – 0.6	21.22
6	0.6 – 0.8	69.82

As demonstrated in Fig. 32, the regression analysis between the NDVI (predictor variable) and the AGB (outcome variable) had shown a weak association between the two variables (R^2 = 0.009). There was no significant statistical relationship observed between the two variables of NDVI and the AGB of the SCPF ($p > 0.05$). There were 46 observations used for each of the variables for the regression analysis. The linear regression equation of '*y=77.24+108.05x*' was obtained from the analysis.
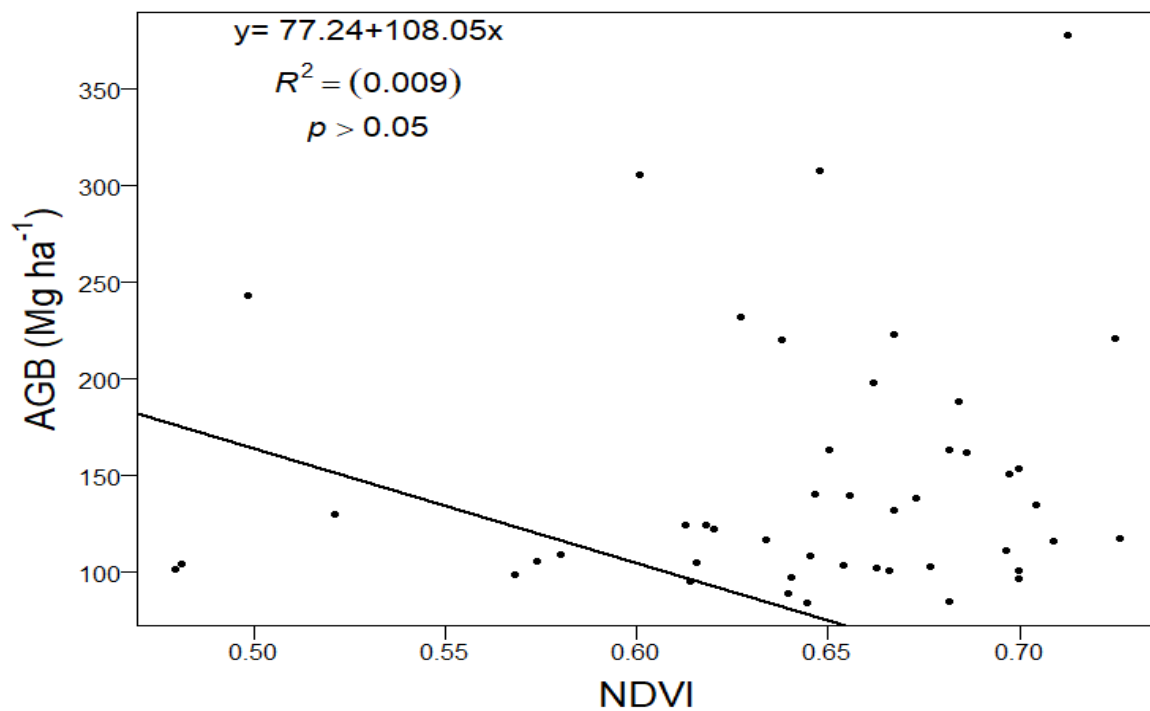
Fig. 32: NDVI-AGB Regression of SCPF

According to Fig. 33, the regression analysis between the NDVI (predictor variable) and AGB (outcome variable) for the SBEF at the MHNP had shown a weak association between the two variables (R^2 = 0.13). However, a significant statistical relation was revealed between the two variables ($p < 0.05$). There were 31 observations used for each of the variables for the regression analysis. The linear regression equation of '$y=462.1-595.8x$' was obtained from the analysis.

$$y= 462.1-595.8x$$
$$R^2 = (0.13)$$
$$p < 0.05$$
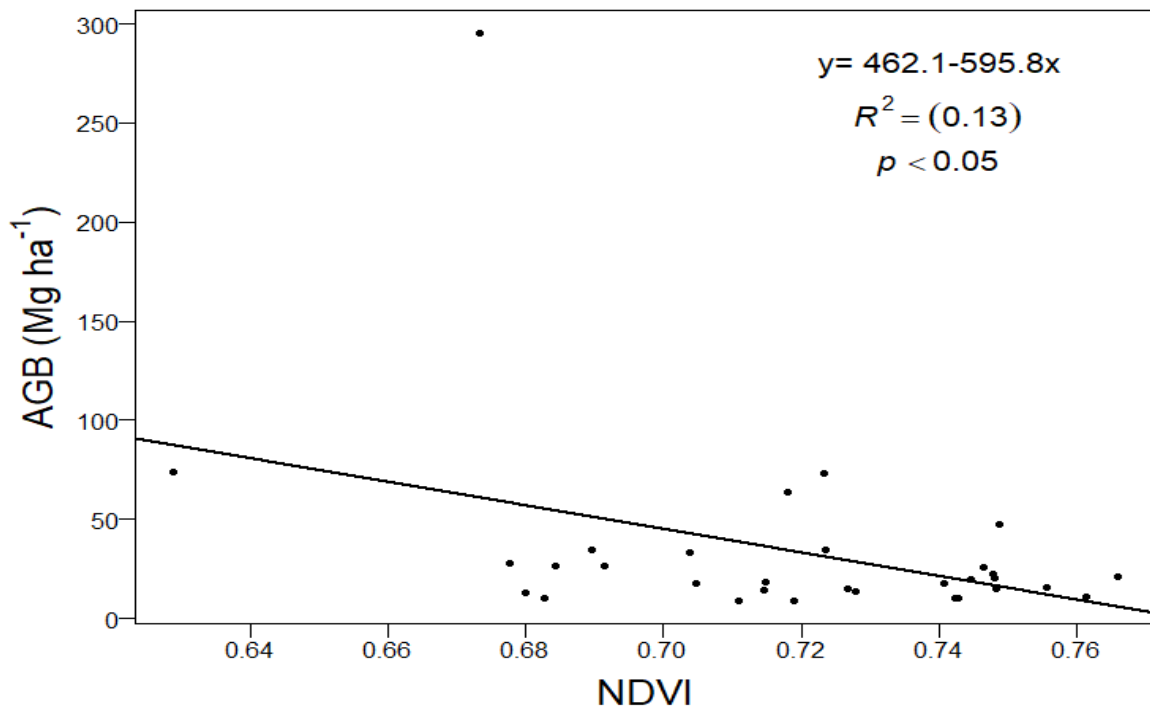
Fig. 33: NDVI-AGB Regression of SBEF

According to Fig. 34, the EVI values have ranged from -0.11 to 0.89. The minimum EVI was recorded as -0.11 and the highest EVI was recorded as 0.89. The mean value for EVI for the MHNP was recorded as 0.45 ± 0.16. The EVI shows a bimodal type of distribution for MHNP (Fig. 35). The highest percentage of EVI values was

recorded for the interval 0.4-0.6 which was 54.19%, followed by 0.2-0.4 which recorded 23.004% of the total values (Table 14).
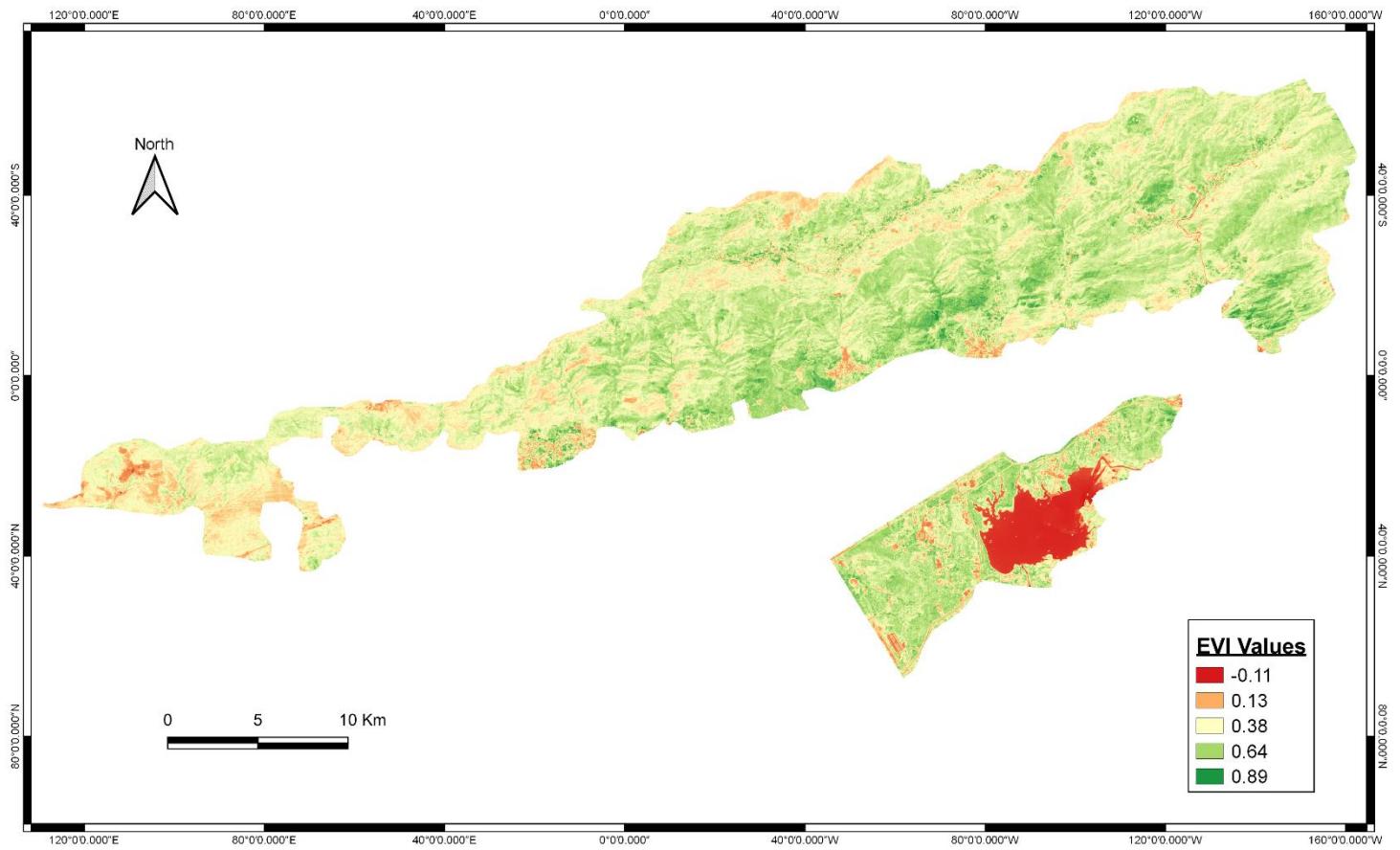
Fig. 34: EVI Estimation of MHNP
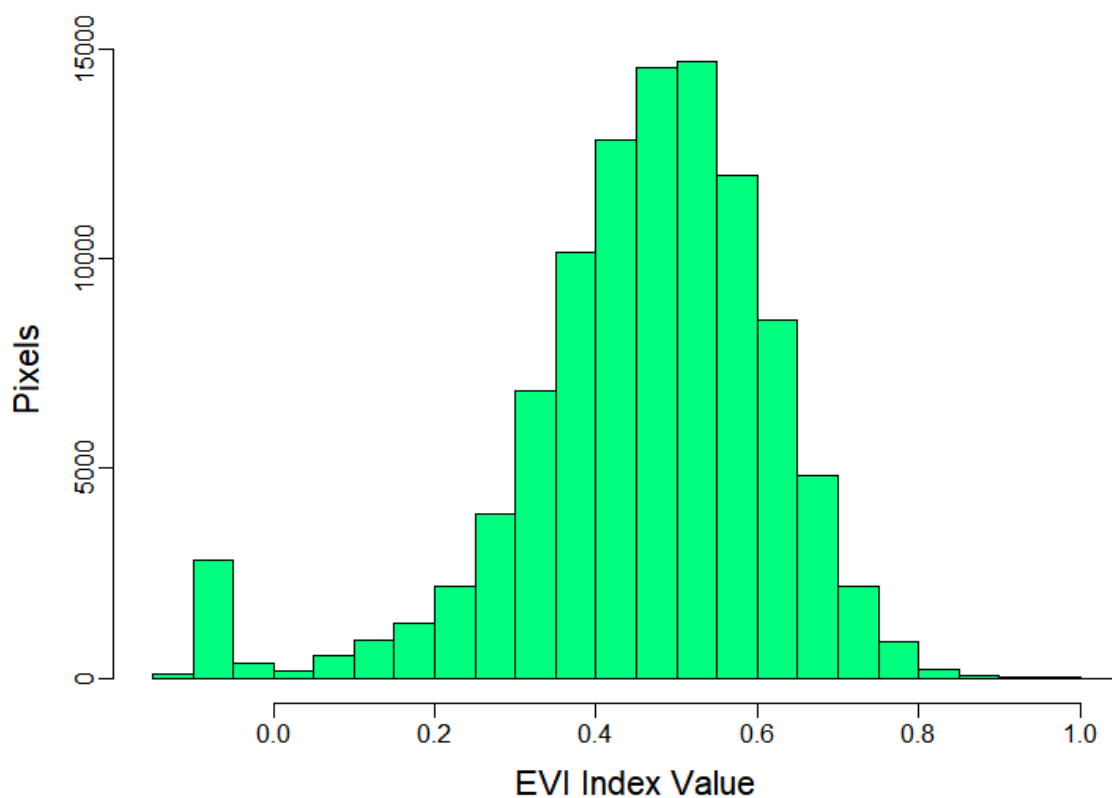
Fig. 35: EVI Distribution of MHNP

Table 14: EVI Percentage by Class Interval

Sr. No.	EVI Index Class Interval	Percentage of Total Pixels
1	-0.15 – 0	3.05
2	0 - 0.2	2.77
3	0.2-0.4	23.004
4	0.4-0.6	54.19
5	0.6-0.8	16.73
6	0.8-1	0.24

According to Fig. 36, the regression analysis between the EVI (predictor variable) and AGB (outcome variable) of the SCPF of MHNP had shown a weak association (R^2= 0.0002). Statistically, no significant relation was also revealed between the two variables ($p > 0.05$). There were 46 observations that were used for each of the variables for performing the regression analysis. The linear regression equation obtained from the analysis was, '*y=141.65+12.23x*'.
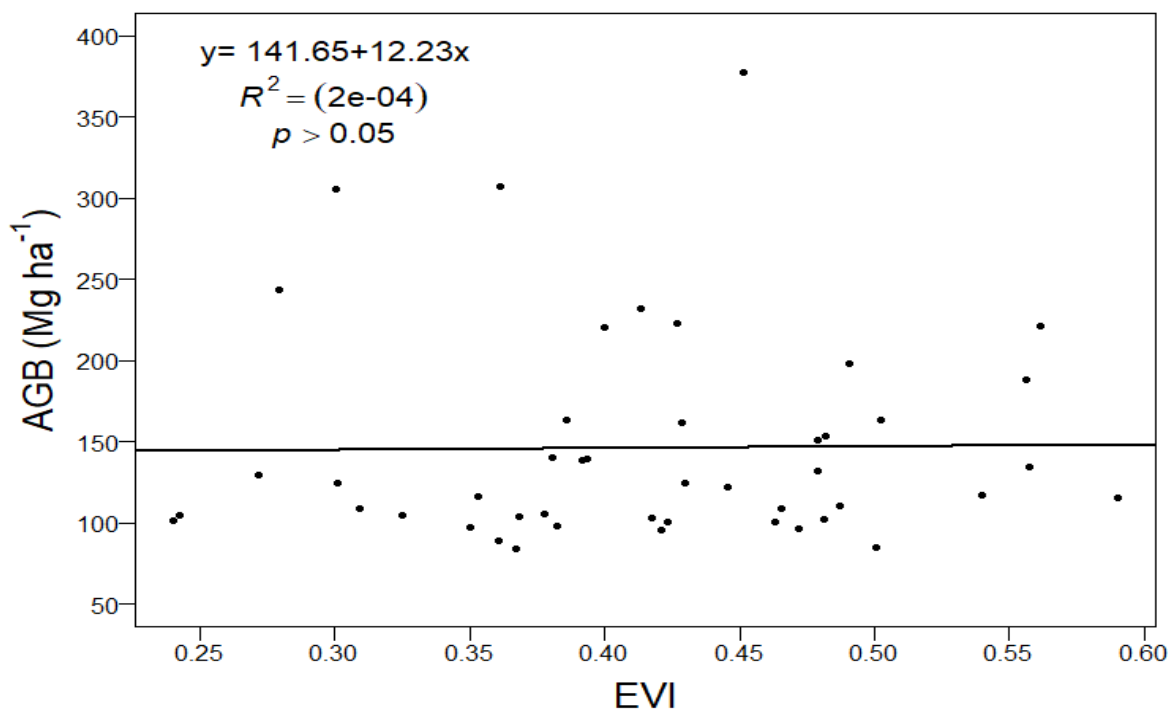
Fig. 36: EVI-AGB Regression of SCPF

According to Fig. 37, the regression analysis between the EVI (predictor variable) and AGB (outcome variable) for the SBEF of the MHNP had shown a weak association between (R^2 = 0.09). There was also no significant statistical relation revealed between the two variables ($p > 0.05$). There were 31 observations used for each of the variables for the regression analysis. The linear regression equation of '*y=136.48-186.13x*' was obtained from the analysis.
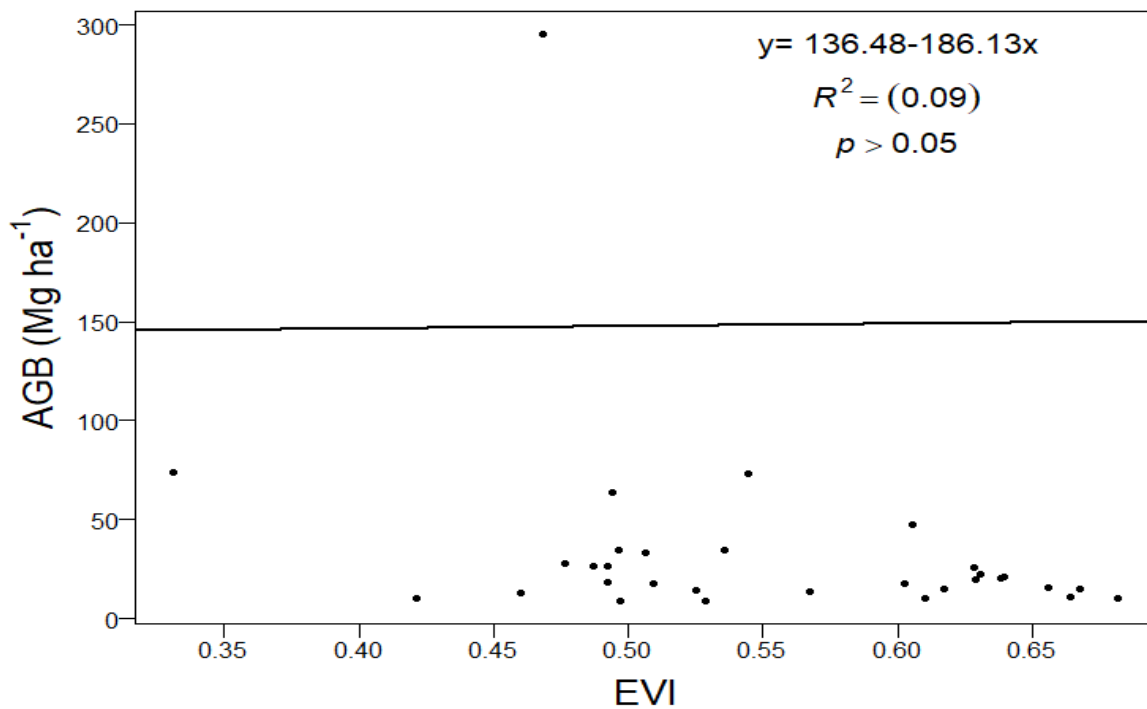
Fig. 37: EVI-AGB Regression of SBEF

4.1.6. Regression Analysis of VH and VV Polarizations with AGBof the two Forests:

The linear regression analysis between the VH Polarization (predictor variable) and the AGB (outcome variable) of the SCPF has revealed a weak association (R^2 = 0.07) (Fig. 38). There was no significant statistical relationship recorded between the two variables (p > 0.05). The linear regression equation for these two variables was recorded as '$y=7.527-8.538x$'.
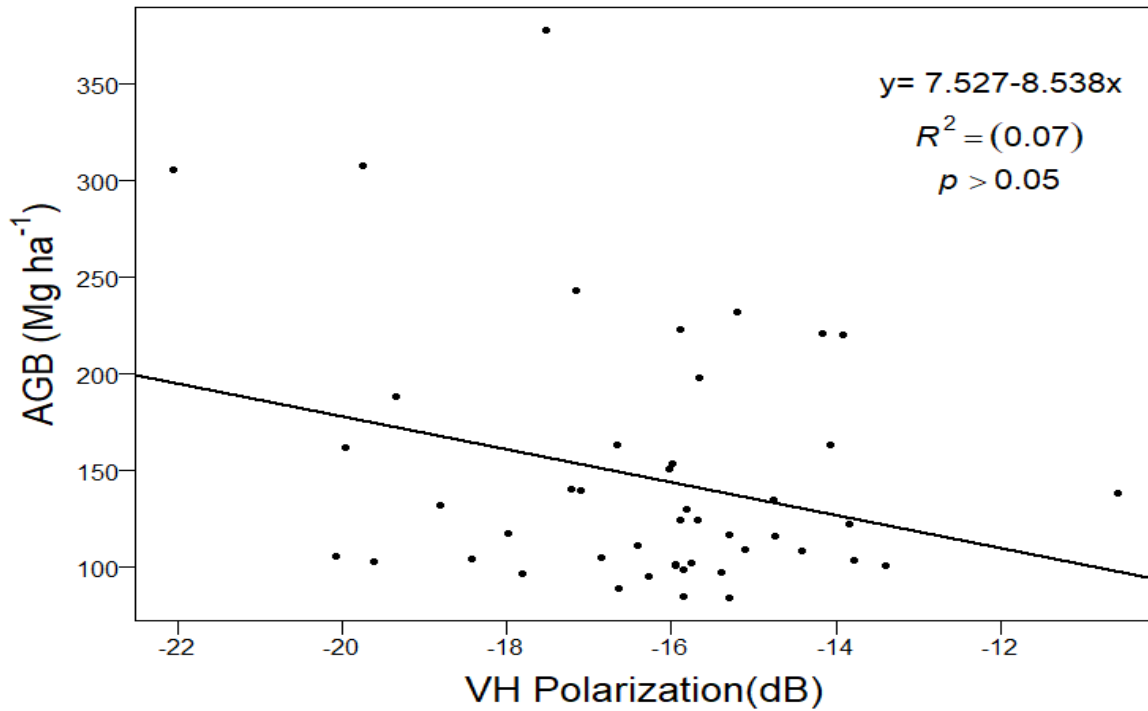
Fig. 38: VH Polarization-AGB Regression of SCPF

The linear regression analysis between the VV Polarization (predictor variable) and AGB (outcome variable) of the SCPF has revealed a weak association ($R^2 = 0.01$) (Fig. 39). There was no significant statistical relationship recorded between the two variables ($p > 0.05$). The linear regression equation for these two variables was recorded as '$y=108.953-3.711x$'.
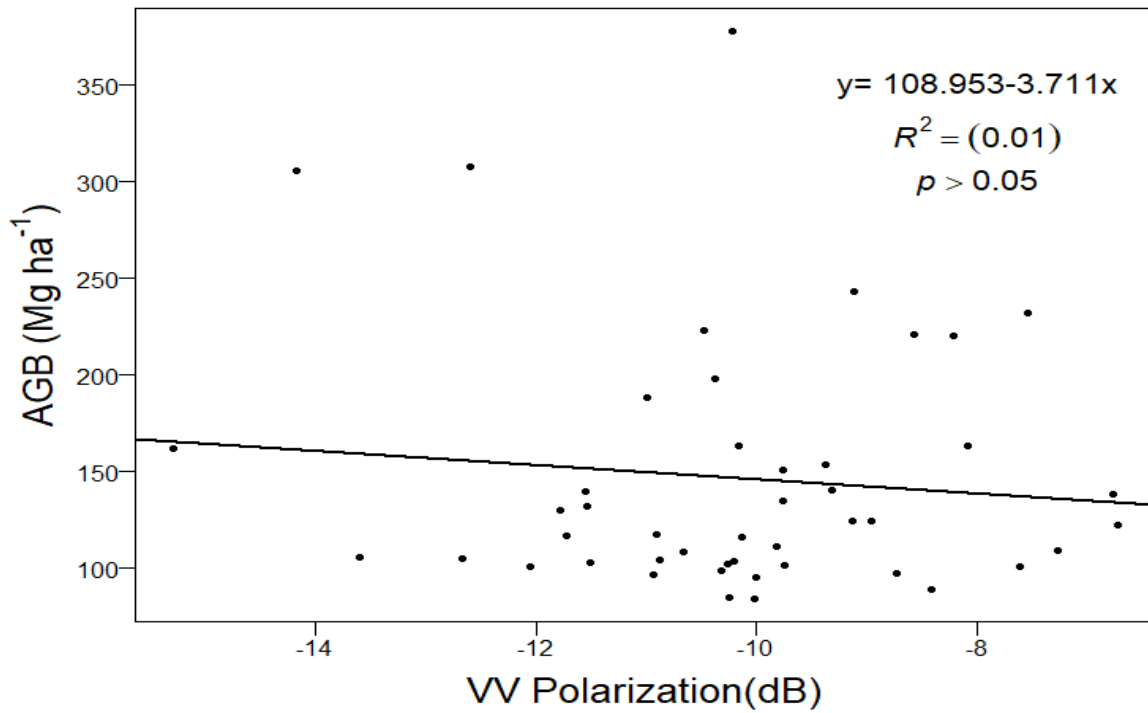
Fig. 39: VV Polarization-AGB Regression of SCPF

As shown in Fig. 40, the linear regression analysis between the VH Polarization (predictor variable) and AGB (outcome variable) of the SBEF has revealed a weak association between (R^2 = 0.001). There was no significant statistical relationship recorded between the two variables ($p > 0.05$). The linear regression equation for these two variables was recorded as '*y=44.28+0.69x*'.

94
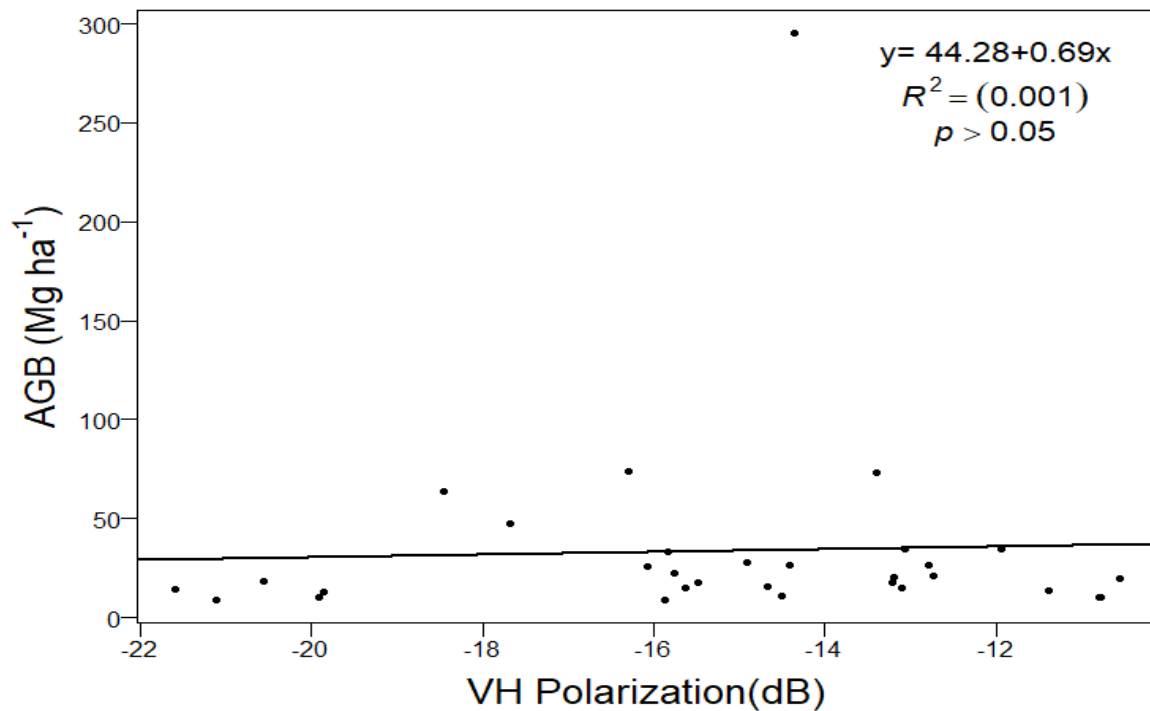
Fig. 40: VH Polarization-AGB Regression of the SBEF

As shown in Fig. 41, a weak linear regression association has been revealed between the VV Polarization (predictor variable) and AGB (outcome variable) of the SBEF (R^2 = 0.01). There was no statistically significant relationship recorded between the two variables ($p > 0.05$). The linear regression equation for these two variables was recorded as '*y=17.209-1.876x*'.
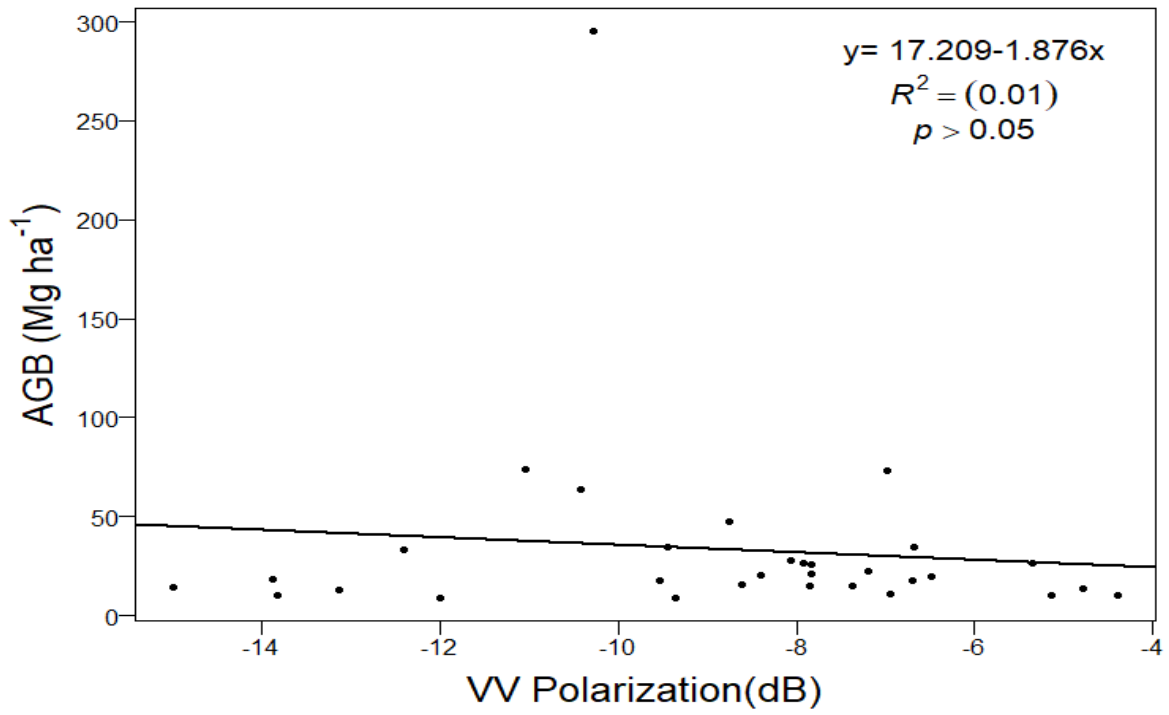
Fig. 41: VV Polarization-AGB Regression of the SBEF

4.1.7. Correlations, Model Evaluations and AGB Mapping of SCPF:

Fig. 42 shows the correlation of the 17 top remotely sensed parameters with the AGB of the SCPF. For this purpose, Spearman correlation coefficient was used. The highest moderate positive correlations were recorded for the following variables: S1_VH_sd (r_s: 0.4; $p< 0.05$), S1_VV_sd (r_s: 0.38; $p< 0.05$), S1_ent_min_VV (r_s: 0.36; $p< 0.05$), S1_ent_avg_VV (r_s: 0.31; $p< 0.05$), S1_VV_max (r_s: 0.31; $p< 0.05$). The rest of the variables showed weak positive and negative correlations with AGB of SCPF.
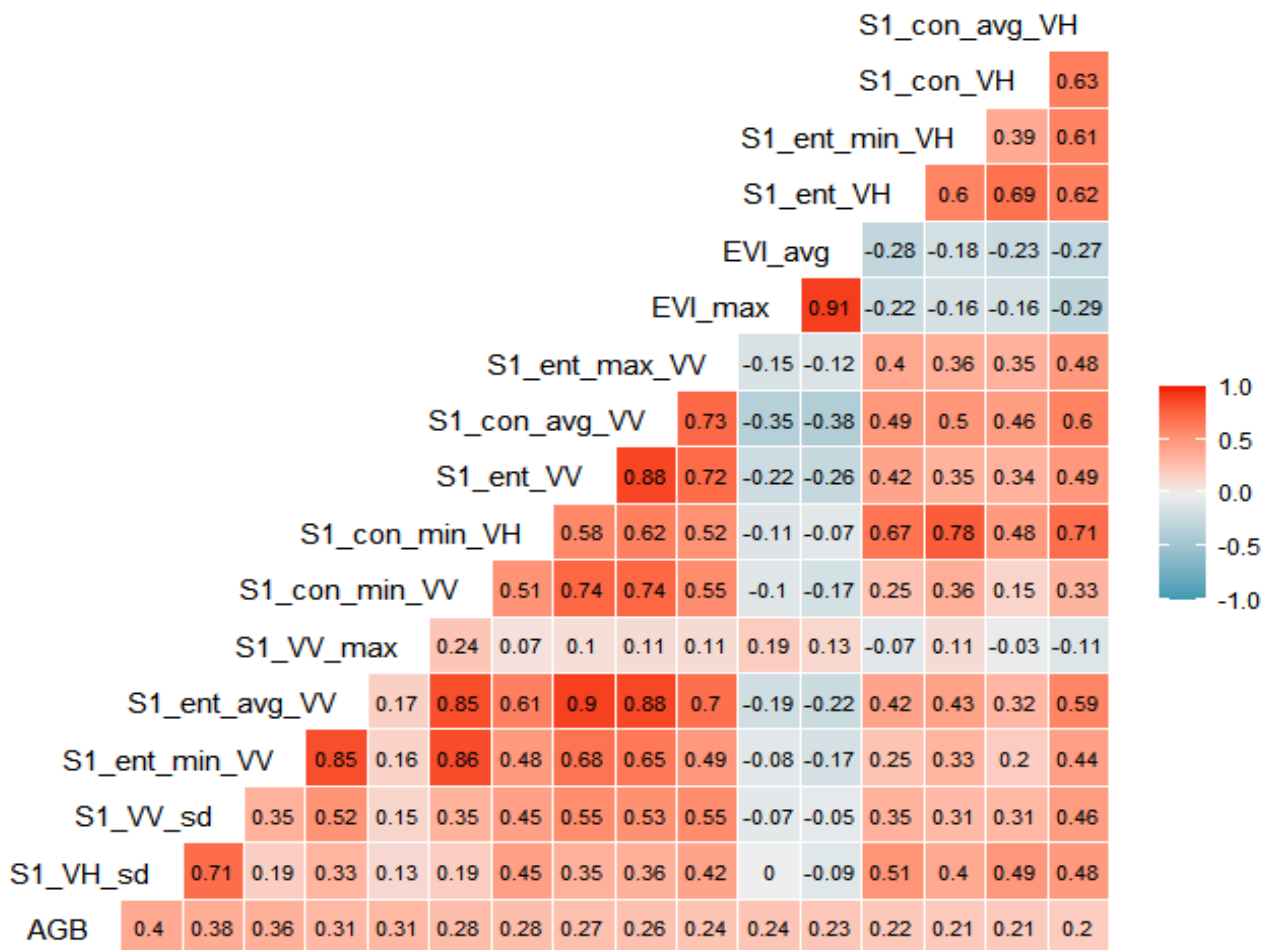
Fig. 42: Correlation between the remotely sensed variables and AGB of SCPF

Table 15 shows the model evaluations of the SCPF. Sixteen predictor sets were used for the evaluation of the two machine learning algorithms, RF and SVM, and the SR. The predictor set of 'S1 and VIs' resulted in producing the best model by using the RF algorithm. The model had the lowest RMSE of 52.46 Mg ha^{-1} and the R^2 value of 0.31. The range of the RF models varied from the lowest RMSE of 52.46 Mg ha^{-1} to the highest RMSE of 72.17 Mg ha^{-1}. The highest RMSE of the RF algorithm belonged to the predictor set of 'Bands and S1 Texture', which also had an R^2 value of 0.09. For the SVM, the predictor set with the lowest RMSE of 59.72 Mg ha^{-1} and the R^2 value of 0.18 was also recorded as the 'S1 and VIs'. The highest RMSE for the SVM was recorded for the predictor set 'VIs' which had an RMSE of 69.07 Mg ha^{-1} and the R^2 value of 0.10. For SR, the predictor set of 'S1 and VIs' again produced the lowest RMSE of 59.29 Mg ha^{-1} and R^2 value of 0.10. The highest RMSE for SR was recorded for the predictor set 'Bands and S2 Texture', which was 73.96 Mg ha^{-1} and the R^2 value was 0.08. The results have shown that all three, RF, SVM, and SR, had the same predictor set of 'S1 and VIs' which produced the lowest RMSE.

Table 15: Model Evaluations of the SCPF

Predictor Variable Sets	RF		SVM		SR	
	RMSE (Mg ha^{-1})	R^2	RMSE (Mg ha^{-1})	R^2	RMSE (Mg ha^{-1})	R^2
Bands	71.77	0.06	63.52	0.07	66.66	0.07
Bands and S1	55.47	0.32	60.06	0.18	65.11	0.08
Bands and S1 Texture	72.17	0.09	65.71	0.06	64.51	0.08
Bands and S2 Texture	68.69	0.14	66.95	0.23	73.96	0.08
Bands and VIs	67.21	0.03	65.44	0.05	61.96	0.18
S1	63.36	0.33	60.39	0.18	62.71	0.12
S1 and S1	57.22	0.21	64.29	0.17	70.04	0.11

Texture						
S1 and S2 Texture	58.48	0.24	63.01	0.12	63.98	0.09
S1 and Vis	52.46	0.31	59.72	0.18	59.29	0.10
S1 Texture	64.62	0.03	68.98	0.14	73.23	0.19
S1 Texture and S2 Texture	68.67	0.09	61.93	0.13	66.06	0.09
S1 Texture and Vis	67.52	0.11	66.57	0.10	68.01	0.04
S2 Texture	63.74	0.04	61.95	0.19	71.74	0.05
S2 Texture and Vis	68.96	0.06	66.21	0.08	69.16	0.04
Vis	68.02	0.05	69.07	0.10	60.84	0.16
All	58.44	0.21	65.38	0.06	67.61	0.06

The final model of the best predictor set 'S1 and VIs', using the RF algorithm, included the top six variables of all the variables. The variable ranking can be seen in Fig. 43, where the higher number, on a scale of 0 to 100, indicates the higher importance of a variable in the model. Through an iterative process, all those variables which did not contribute to improving the model were removed gradually. This led eventually to a model with only the top six variables (i.e., S1_VV_sd, S1_VV_min, S1_VH_avg, S1_VH_sd, S1_VV_avg, S1_VV_max) which provided the best result. The process started with a total of 20 variables and was reduced to the top six variables with the best RMSE. As already mentioned, the final RF model with the top six variables had the RMSE of 52.46 Mg ha^{-1}and the R^2 value of 0.31, which is also shown in Table 15. The final RF model of the predictor set 'S1 and VIs' with the six variables was further used for the AGB mapping of the SCPF of the MHNP.
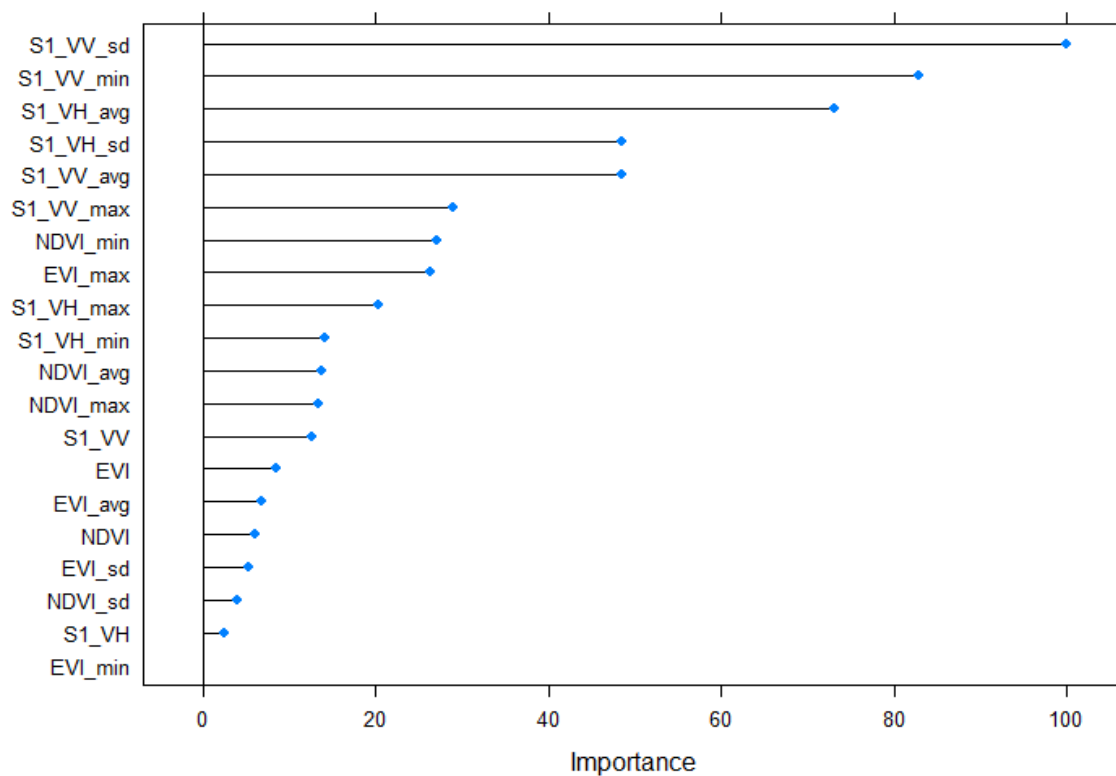
Fig. 43: Ranking of the Variables of the Predictor Set 'S1 and VIs' using RF algorithm

Fig. 44 shows the AGB map of the SCPF of MHNP. The map was produced using the RF model of the predictor set 'S1 and VIs' with six final variables. According to the map, the AGB has ranged from 94.55 Mg ha^{-1} to 283.77 Mg ha^{-1}. The lowest AGB was recorded as 94.55 Mg ha^{-1} and the highest as 283.77 Mg ha^{-1}. The mean value for the AGB was recorded as 163.57 ± 49.18 Mg ha^{-1}.
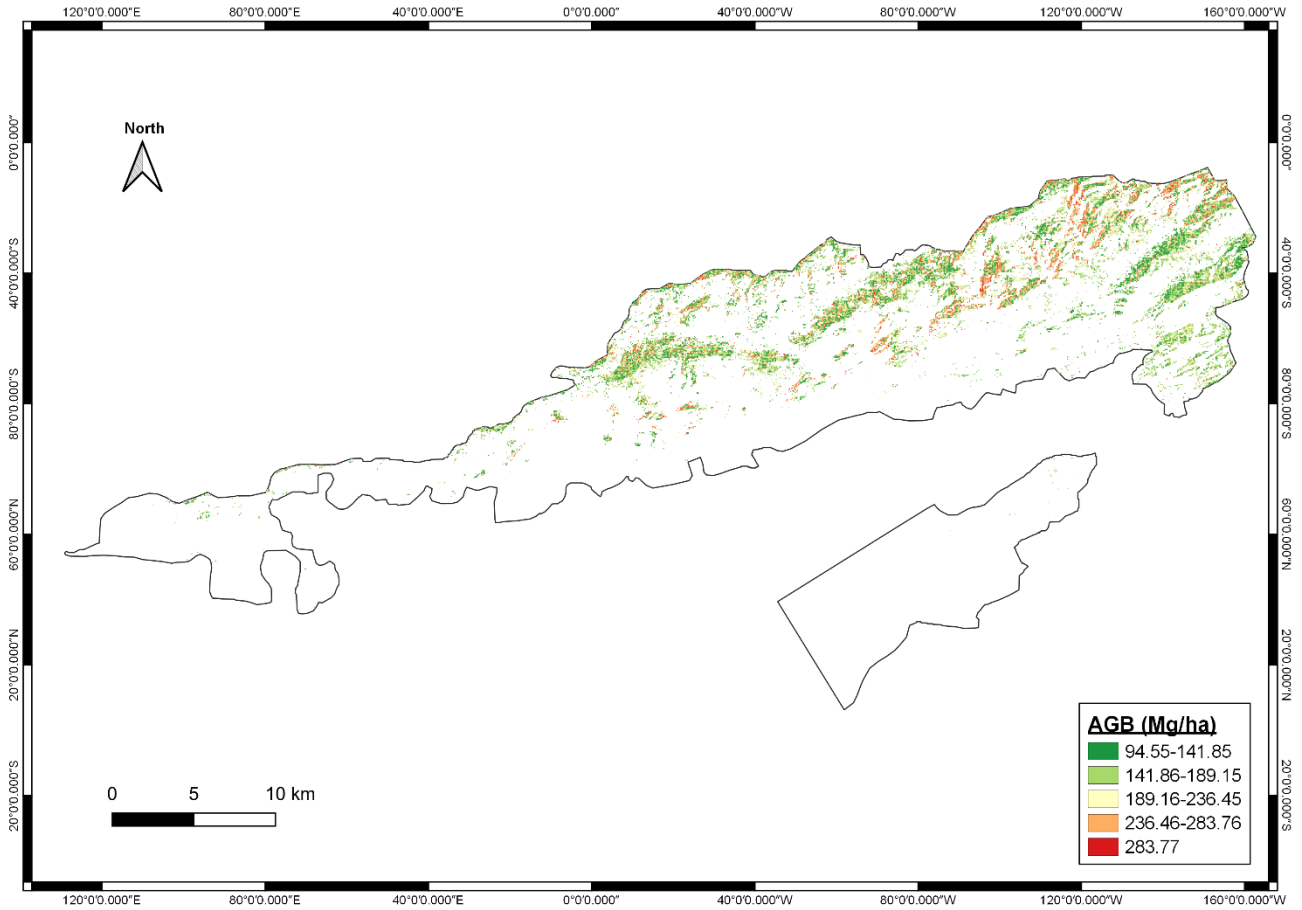
Fig. 44: AGB Map of SCPF

The predicted AGB by the final RF model was plotted against the observed AGB obtained through field inventorying (Fig. 45). A significant statistical association between the two variables (R^2 = 0.89) was obtained. This shows that the RF model has strongly predicted the AGB which is close to the observed AGB obtained through field inventorying. The same was also plotted for the SVM and the SR. The SVM showed a moderate association (R^2 = 0.66) and the SR showed a weak association (R^2 = 0.17) between the two variables.
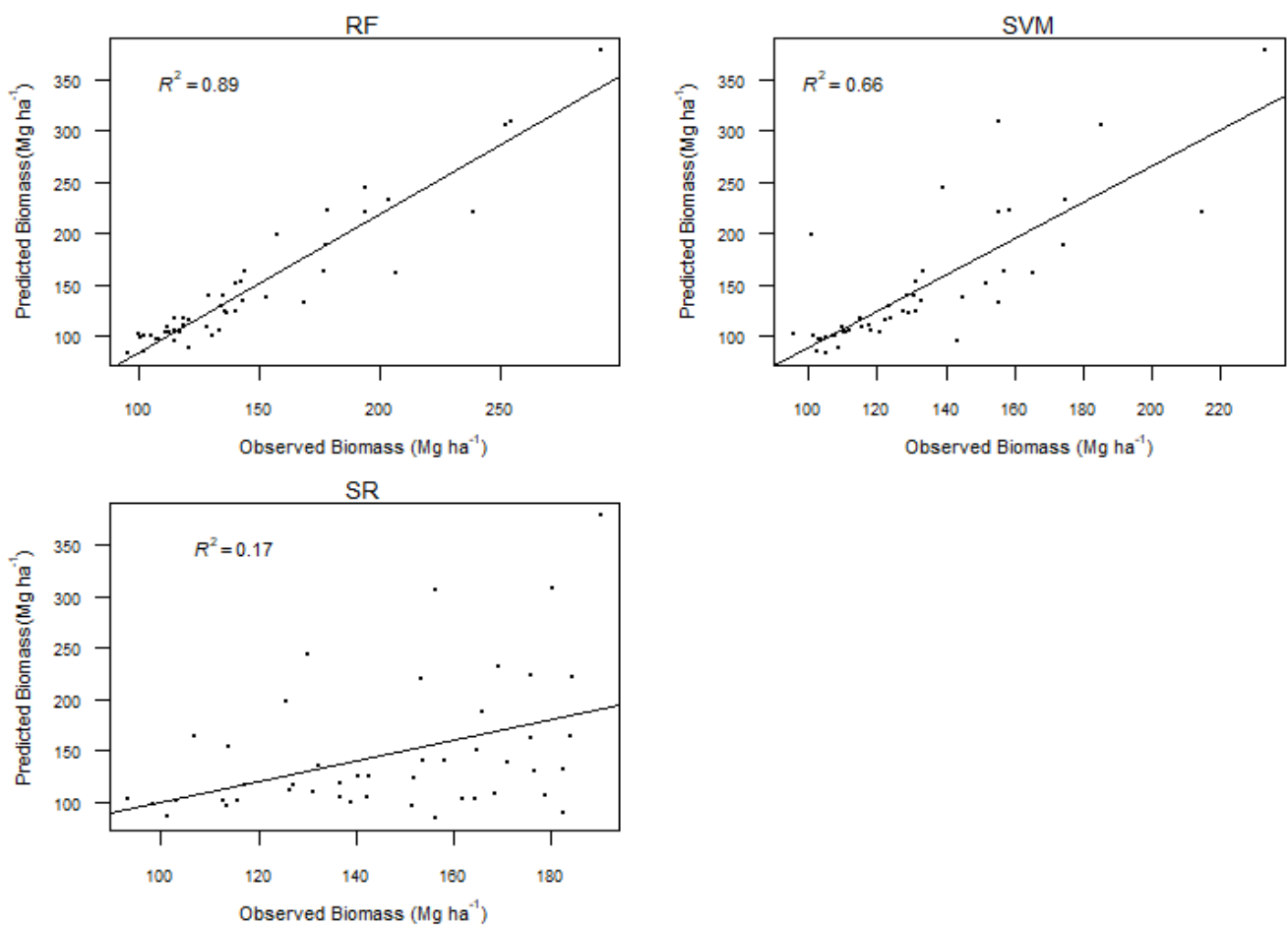
Fig. 45: Predicted vs Observed AGB of the SCPF

4.1.8. Correlations, Model Evaluations and AGB Mapping of the SBEF:

Fig. 46 shows the correlation of the 17 top remotely sensed parameters with the AGB of the SBEF. Spearman correlation coefficient was used for the correlation analysis. The following variables showed the highest moderate positive correlation with the AGB; S2_ent_max (r_s: 0.49; $p < 0.05$), S2_con_sd (r_s: 0.42; $p < 0.05$), S2_con_max (r_s: 0.4; $p < 0.05$), S2_con_avg (r_s: 0.4; $p < 0.05$), S2_con (r_s: 0.35; $p > 0.05$), S2_ent_avg (r_s: 0.32; $p > 0.05$). The rest of the variables recorded weak positive and negative correlations with the AGB of the SBEF.
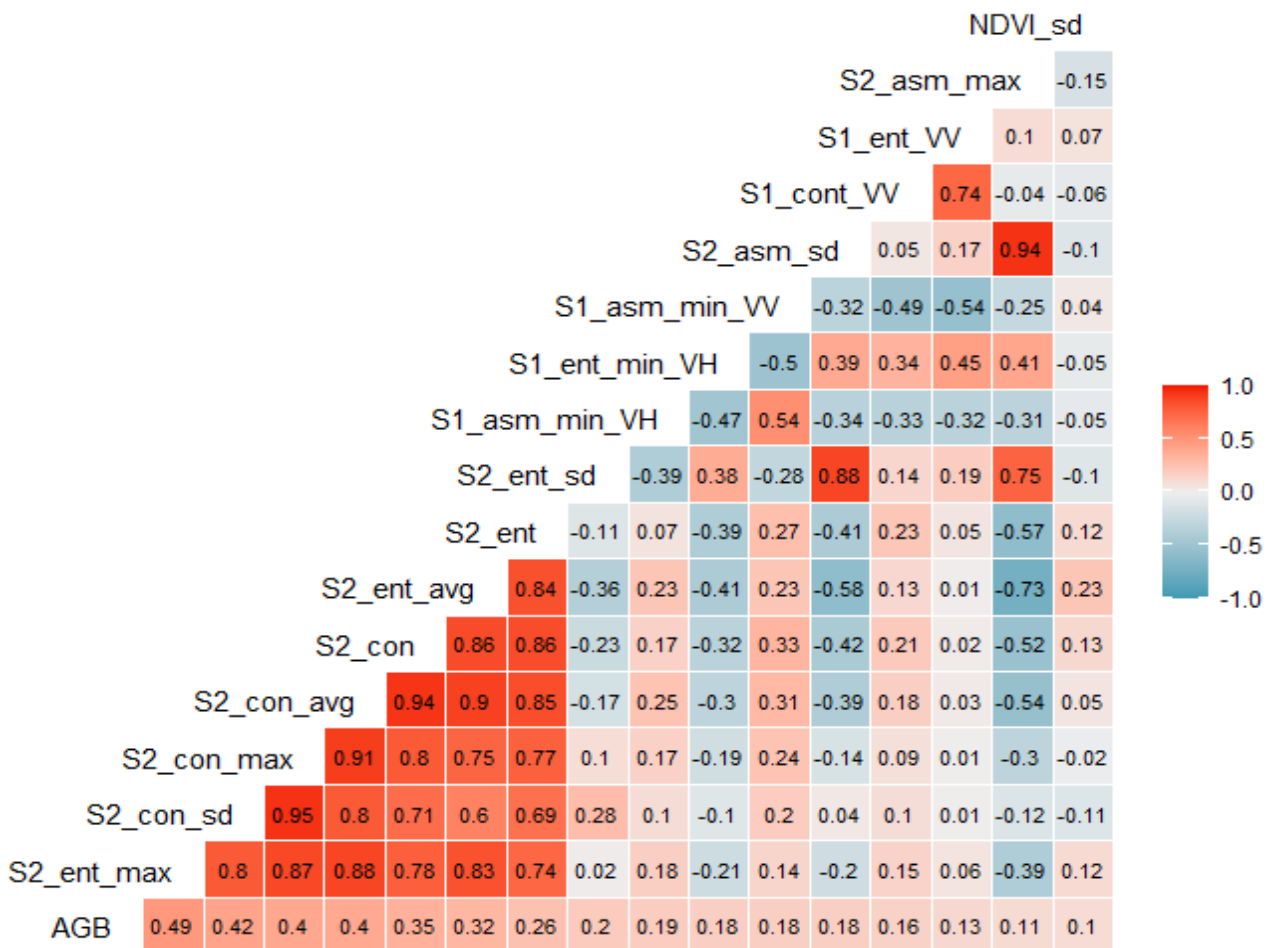
Fig. 46: Correlation between the remotely sensed variables and AGB of the SBEF

In the case of the model evaluations of the SBEF, the SVM produced the lowest RMSE for the predictor set 'S1 and S2 Texture' (Table 16). The RMSE recorded for this predictor set was 32.59 Mg ha^{-1} and the R^2 value was 0.21. The RMSE value for the same predictor set for the RF algorithm was 36.61 Mg ha^{-1} and the R^2 was 0.11. For the SR for the same predictor set, the RMSE was 43.05 Mg ha^{-1} and R^2 was 0.52. The range of RMSE for the SVM models for the SBEF was from 32.59 Mg ha^{-1} to 37.29 Mg ha^{-1}. The highest RMSE for the SR was recorded as 57.09 Mg ha^{-1} and the lowest was recorded as 41.85 Mg ha^{-1}.

Table 16: Model Evaluations of the SBEF

Predictor Variable Sets	RF		SVM		SR	
	RMSE (Mg ha^{-1})	R^2	RMSE (Mg ha^{-1})	R^2	RMSE (Mg ha^{-1})	R^2
Bands	39.11	0.32	34.21	0.28	43.58	0.35
Bands and S1	39.53	0.16	36.02	0.21	51.83	0.09
Bands and S1 Texture	43.33	0.27	34.19	0.09	54.99	0.45
Bands and S2 Texture	44.94	0.11	36.01	0.30	52.78	0.11
Bands and Vis	35.32	0.31	37.29	0.11	47.72	0.36
S1	38.32	0.23	36.08	0.03	52.86	0.21
S1 and S1 Texture	45.78	0.05	33.07	0.19	55.86	0.23
S1 and S2 Texture	36.61	0.11	32.59	0.21	43.05	0.52
S1 and Vis	40.07	0.08	33.96	0.13	56.17	0.28
S1 Texture	42.99	0.11	32.67	0.35	50.23	0.04
S1 Texture and S2 Texture	40.41	0.25	34.03	0.17	57.09	0.32
S1 Texture and Vis	36.11	0.31	33.73	0.42	41.85	0.17

S2 Texture	41.35	0.18	34.16	0.15	45.57	0.04
S2 Texture and Vis	35.19	0.32	33.72	0.31	52.67	0.23
Vis	35.51	0.32	35.78	0.05	49.61	0.12
All	37.44	0.14	35.21	0.05	52.96	0.09

The final model of SVM was selected from the predictor set 'S1 and S2 Texture'. The model initially had 25 total variables but after the iterative model evaluation process, only nine variables were left which produced the lowest RMSE of 32.59 Mg ha^{-1} and hence was selected as the final model for predicting the AGB for the SBEF of the MHNP. These nine variables (i.e., S1_VH, S1_VH_sd, S2_con_max, S2_con_sd, S2_con_avg, S2_ent_sd, S2_ent, S2_con, S2_asm_sd) were the top nine variables according to the scale of 0 to 100 amongst all the 25 variables of the predictor set 'S1 and S2 Texture' (Fig. 47). So, overall, 16 variables had to be removed until the lowest possible RMSE could finally be obtained in the respective predictor set.
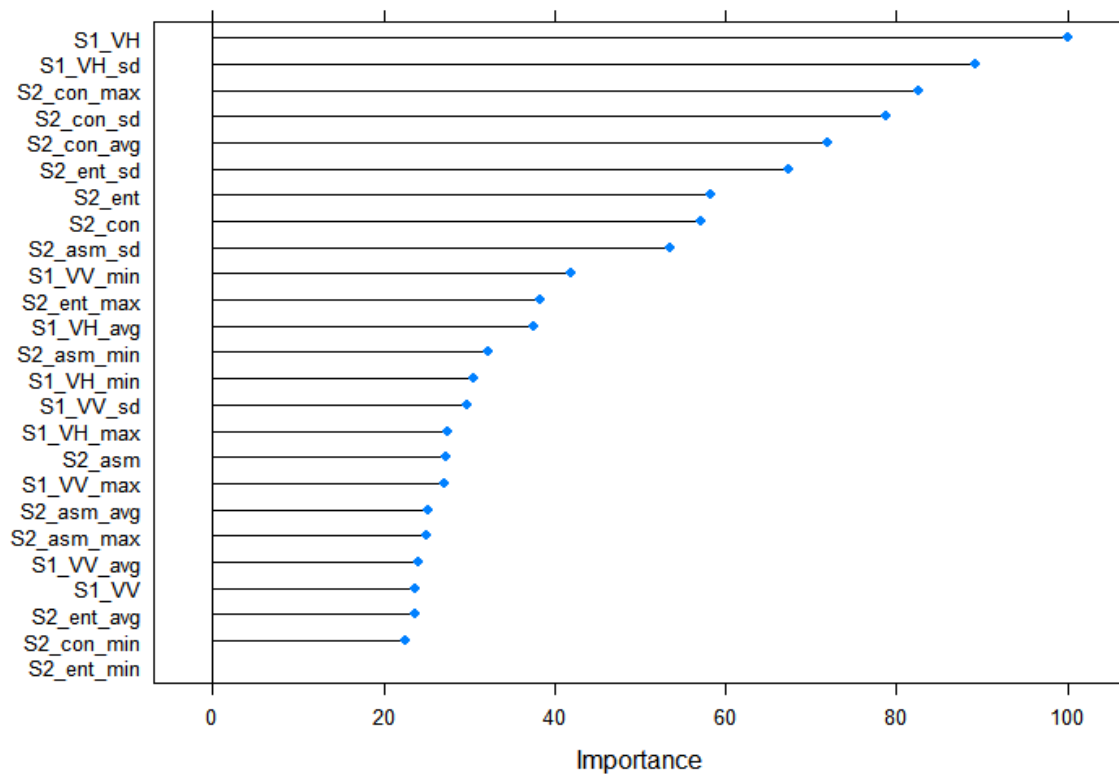
Fig. 47: Ranking of the Variables of the Predictor Set 'S1 and S2 Texture' using SVM algorithm

The AGB map of the SBEF was produced using the final SVM model from the predictor set of 'S1 and S2 Texture', using eventually nine variables. The AGB map, shown in Fig. 48, had the lowest AGB of 9.67 Mg ha^{-1} and the highest AGB of 30.92 Mg ha^{-1}. The mean AGB for the SBEF was recorded as 20.40 ± 3.70 Mg ha^{-1}.
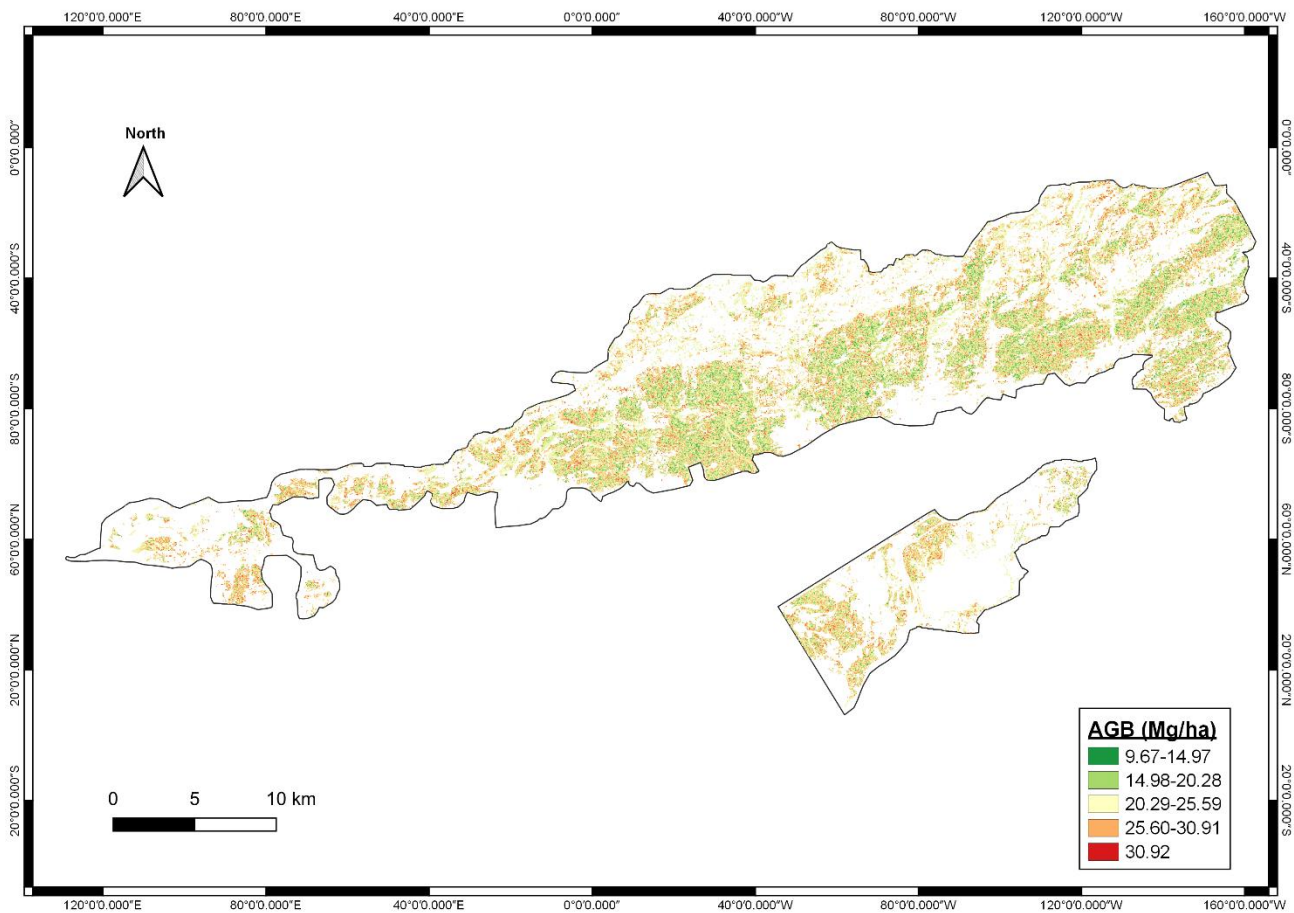
Fig. 48: AGB Map of the SBEF

The predicted AGB by the SVM final model did show only a moderate association (R^2 = 0.4) with the observed AGB from the SBEF (Fig. 49). The RF model from the same predictor category 'S1 and S2 Texture' showed a significant association between the predicted and observed AGB (R^2 = 0.85). The SR also showed a moderate association (R^2 = 0.31), for the same category, between the predicted and observed AGB of the SBEF.
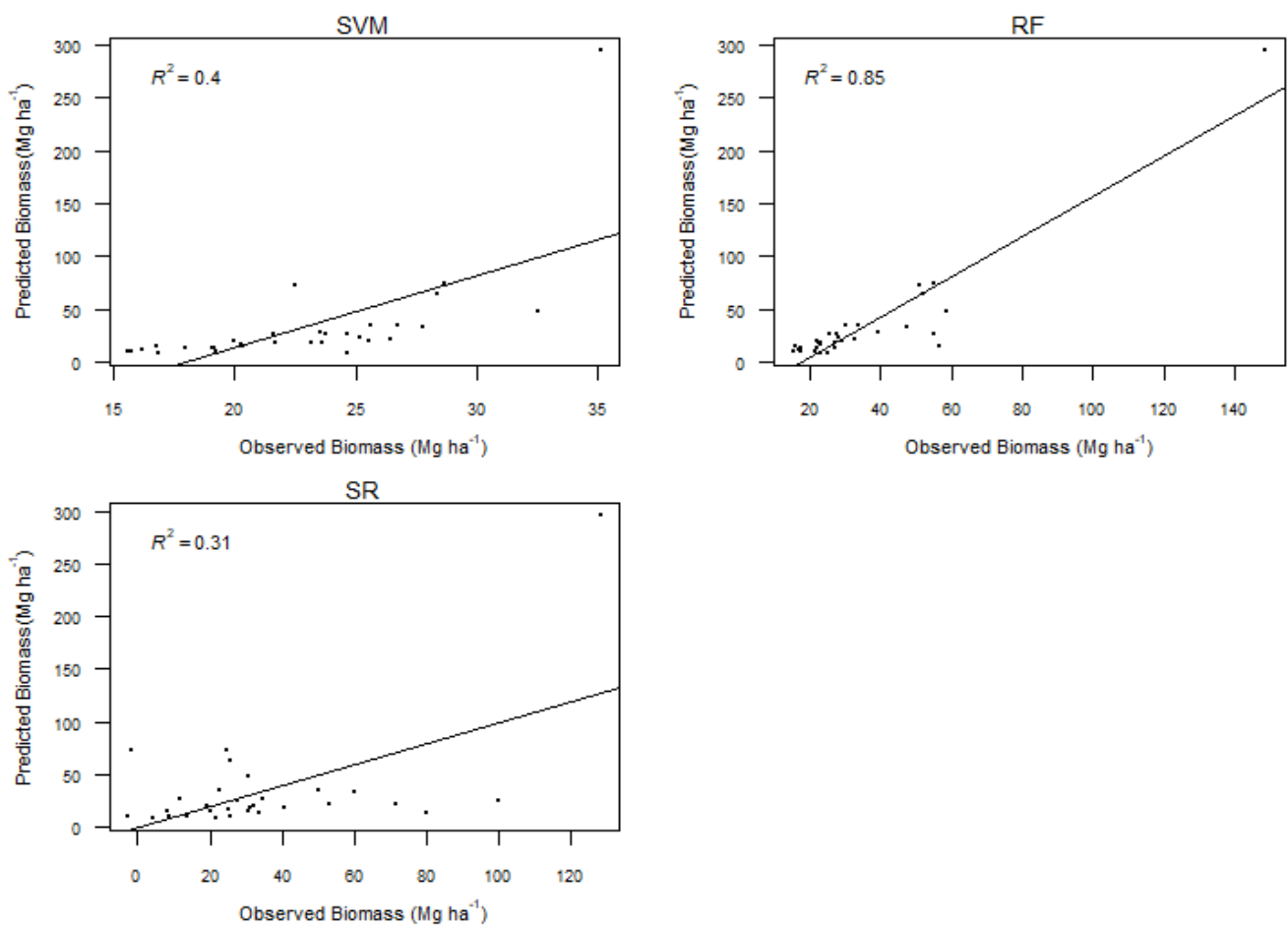
Fig. 49: Predicted vs Observed AGB of the SBEF

4.2. LC Classification and LCCD of MHNP for the time-period between 1999-2019:

4.2.1. RF Algorithm:

As was mentioned earlier that the RF depends on two important parameters *mtry* and *ntree*. The optimal *mtry*, with the lowest OOB error, was 4 for all the three RF models used for the land cover classification of three Landsat images (Fig. 50; Fig. 51; Fig. 52).

For the LC classes, a sharp decrease in OOB errors is observed, followed by the stabilization along with slight fluctuations, with the increase in *ntree* in all three figures (Fig. 53; Fig. 54; Fig. 55). For the RF model, which was used for the classification of Landsat 5 TM image for the year 1999 and the Landsat 7 ETM+ image for the year 2009, the grassland showed the lowest OOB errors. For the Landsat 8 OLI image for the year 2019, the water body showed the lowest OOB errors. Generally, the OOB errors decreased with the increasing number of trees (Rodriguez-Galiano et al., 2012). If for instance more number of trees are used, this will only result in increased time in the calculation without any sound improvement in the accuracy of the RF model (Feng et al., 2015).
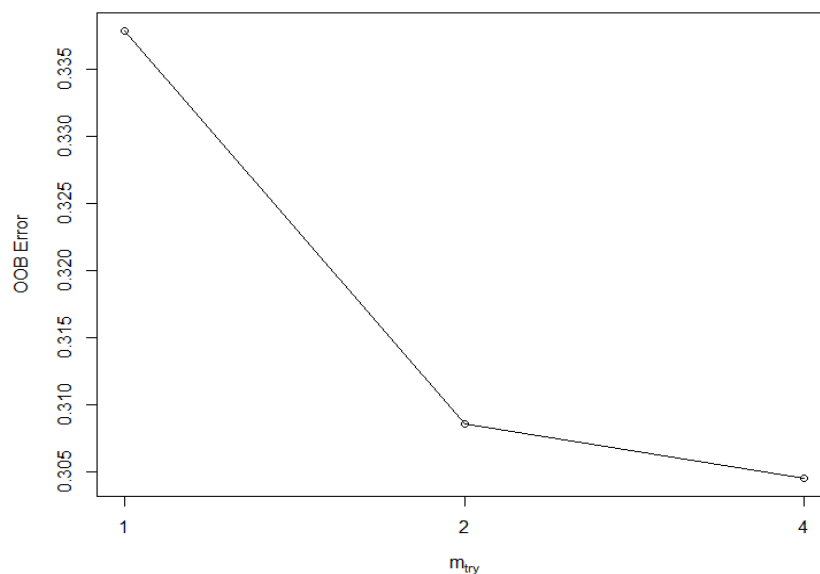
Fig. 50: Optimal *mtry* value for RF model of Landsat 7 ETM+ image for the year 1999
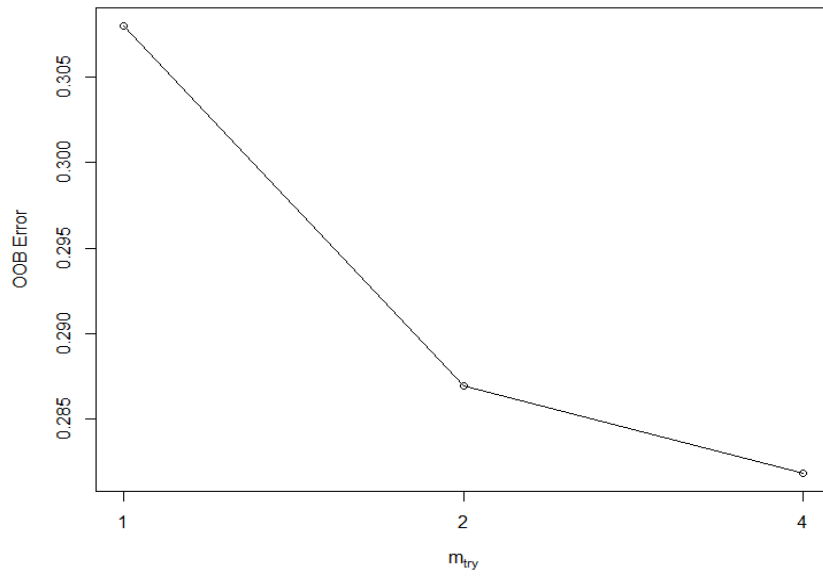
Fig. 51: Optimal *mtry* value for RF model of Landsat 5 TM image for the year 2009
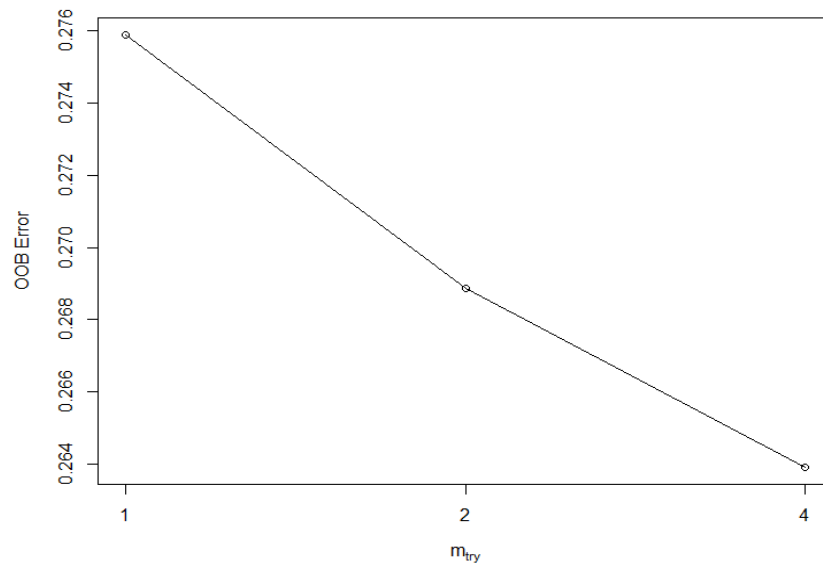
Fig. 52: Optimal *mtry* value for RF model of Landsat 8 OLI image for the year 2019

109
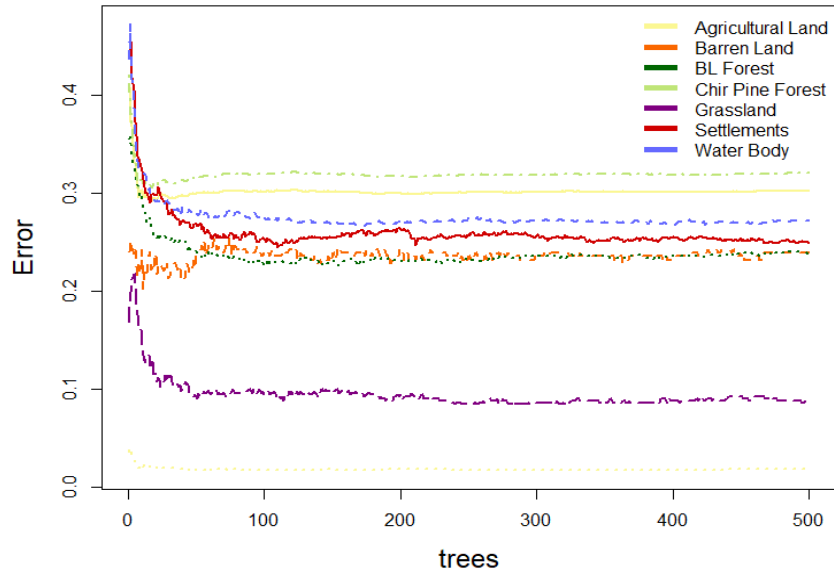
Fig. 53: The relationship between OOB error (used as Error in the graph) (*y*-axis) and *ntree* parameter (used as trees in the graph) (*x*-axis) of the RF model using Landsat 7 ETM+ image for the year 1999.
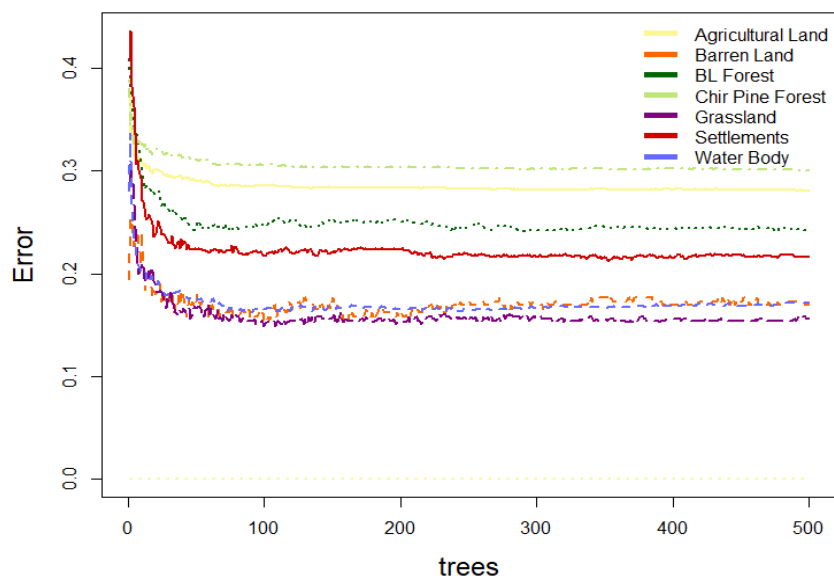
Fig. 54: The relationship between OOB error (used as Error in the graph) (*y*-axis) and *ntree* parameter (used as trees in the graph) (*x*-axis) of the RF model using Landsat 5 TM image for the year 2009.
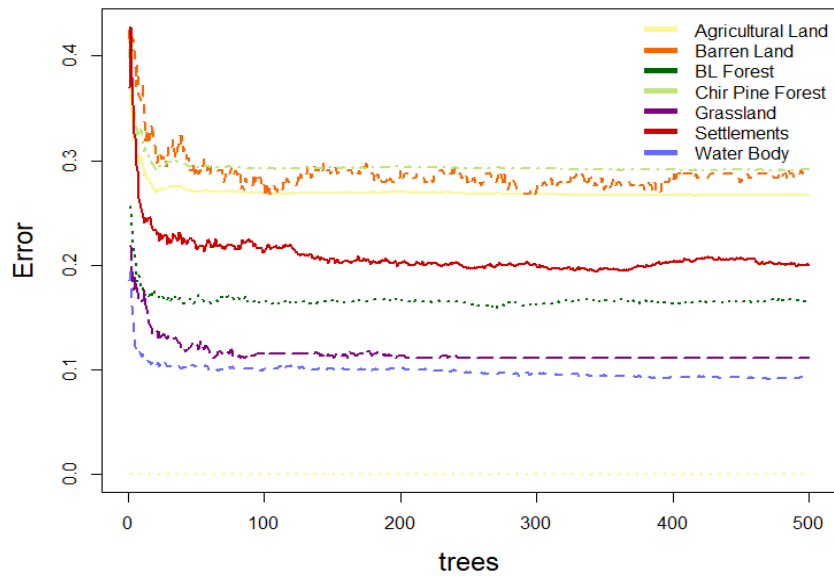
Fig. 55: The relationship between OOB error (used as Error in the graph) (*y*-axis) and *ntree* parameter (used as trees in the graph) (*x*-axis) of the RF model using Landsat 8 OLI image for the year 2019.

4.2.2. Importance of Variables:

The MDA shows that the band 4 (B4) is the most important variable in the RF model using the Landsat 7 ETM+ image for the year 1999 for the land cover classification of MHNP (Fig. 63). The MDG shows band 1 (B1) as the most important variable of the RF model (Fig. 56). The MDA generally expresses how much the model suffers in terms of accuracy if a variable is excluded from it and MDG shows how much a variable contributes to the homogeneity of the nodes and leaves in the RF model (Martinez-Taboada and Redondo, 2020). The higher their values, the higher will be the importance of the variables.

The RF model using Landsat 5 TM image for land cover classification of MHNP showed band 5 (B5) as the most important variable for MDA and band 1 (B1) as the most important variable for MDG (Fig. 57). The RF model using Landsat 8 OLI image had shown band 6 (B6) and band 2 (B2) as the most important variables for MDA and MDG respectively (Fig. 58).
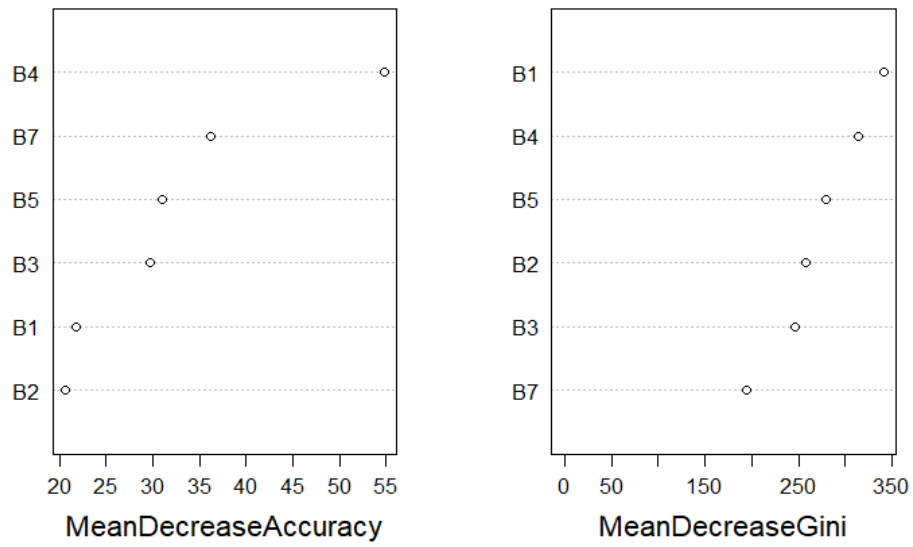
Fig. 56: Important Variables for the RF model using Landsat 7 ETM+ for the year 1999.
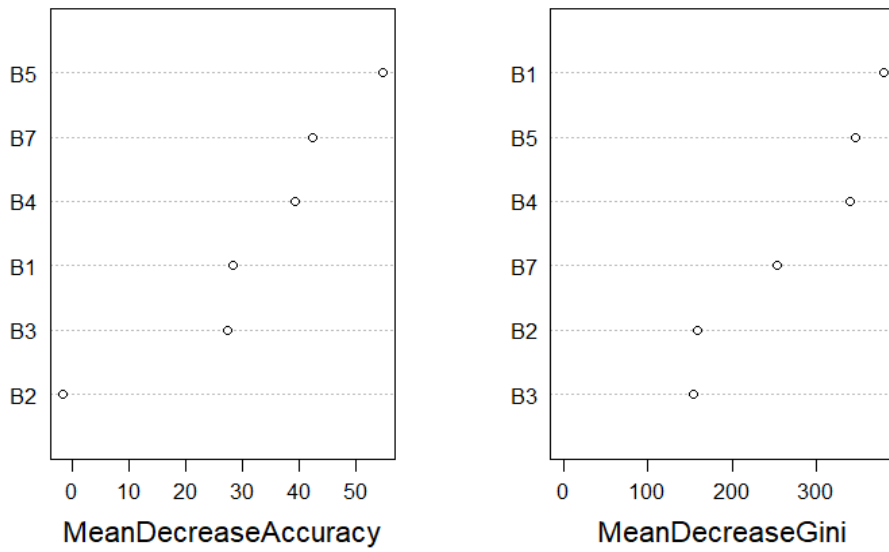
Fig. 57: Important Variables for the RF model using Landsat 5 TM for the year 2009.

112
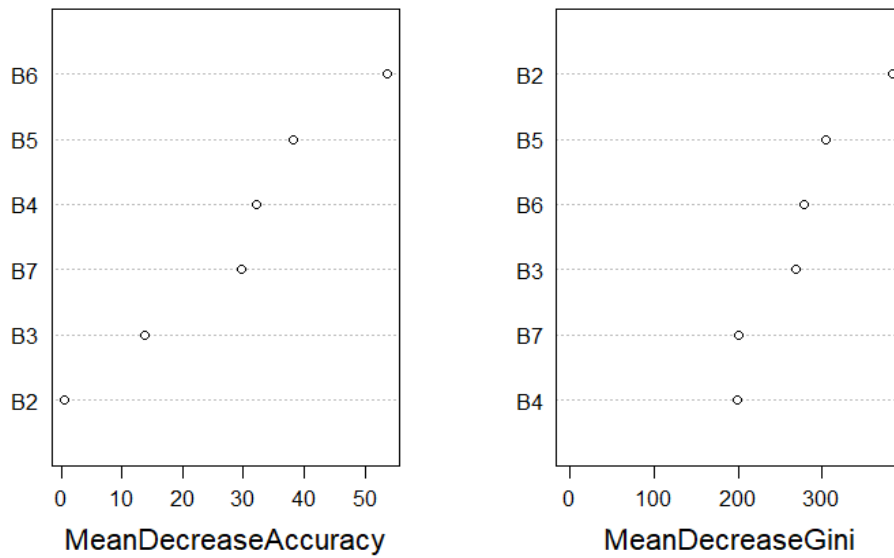
Fig. 58: Important Variables for the RF model using Landsat 8 OLI for the year 2019.

4.2.3. Spectral Reflection:

For Landsat 7 ETM+, SCPF and SBEF have shown the highest mean spectral reflectance for band 4 (B4) (Fig. 59). For Landsat 5 TM, Highest mean spectral reflectance for SCPF and SBEF was again recorded for band 4 (B4) (Fig. 60). However, band 5 (B5) recorded the highest mean spectral reflectance for SCPF and SBEF in case of Landsat 8 OLI (Fig. 61)

113
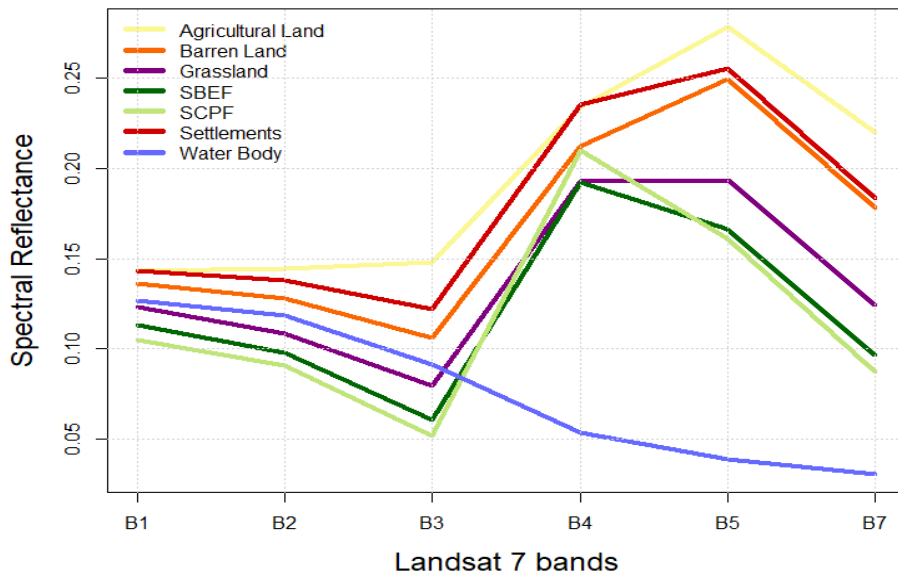
Fig. 59: Mean Spectral Reflectance of LC Classes for Landsat 7 ETM+ Image Bands.
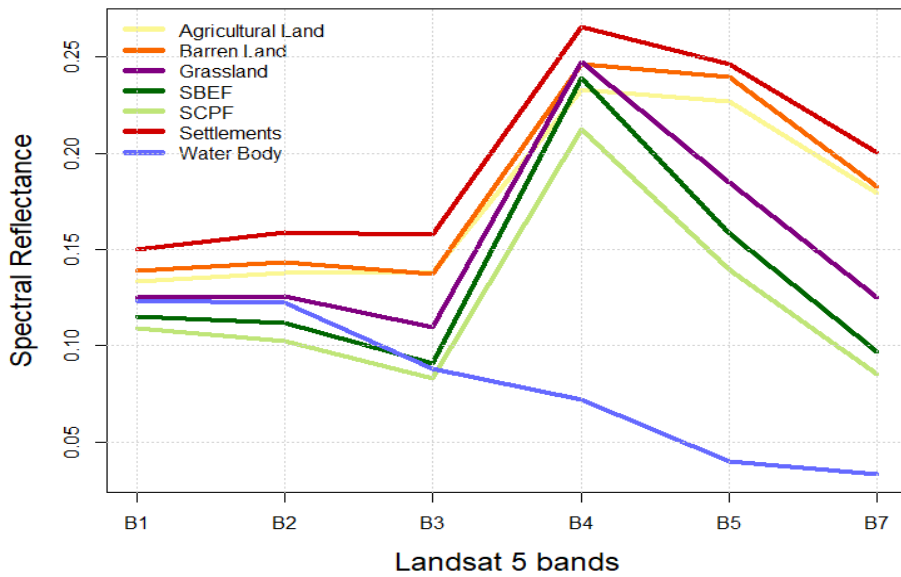
Fig. 60: Mean Spectral Reflectance of LC Classes for Landsat 5 TM Image Bands.

114
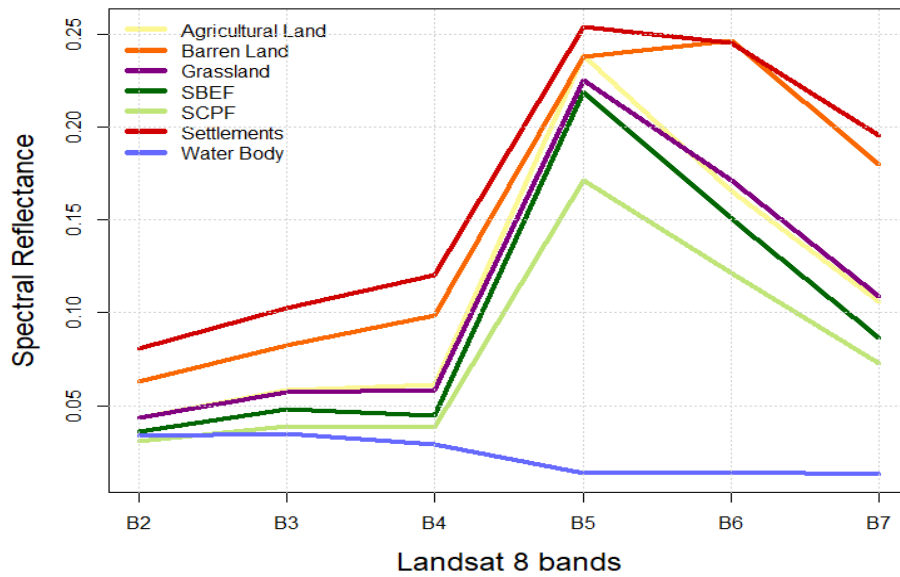
Fig. 61: Mean Spectral Reflectance of LC Classes for Landsat 8 ETM+Image Bands.

4.2.4. Analysis of LC Classifications:

Table 17 shows the extent of LC classes for MHNP for the years 1999, 2009, and 2019. For the year 1999, the SBEF formed the highest LC with 40.90%. The grassland formed the second highest with 17.68%. The other land cover types had the following coverage; SCPF (13.60%), Barren Land (11.56%), Settlements (10.64%), and Water Body (2.47%). For the year 2009, the SBEF formed the highest LC type with 40.11% of the total LC types. The SCPF formed the second highest LC type with 16.63%. The other LC types followed; Grassland (15.26%), Barren Land (11.90%), Settlements (7.49%), Agricultural Land (5.49%), and Water Body (3.10%). For the year 2019, SBEF again formed the highest LC with 43.21%. The grassland formed the second highest LC type with 14.23%. The other land cover types were; SCPF (14.14%), Barren Land (10.90%), Settlements (7.34%), Agricultural Land (7.17%), and Water Body (2.98%). Fig. 62 also shows the graphical representation of the extent of the LC types of the MHNP. Fig. 63 shows the LC map classification of the MHNP for the year 1999. Fig. 64 shows the LC map for the year 2009. Fig. 5 shows the LC map for the year 2019.

115

Table 17: Extents of Classified LC Classes of MHNP

Land Cover	1999		2009		2019	
	Area (ha)	% Area	Area (ha)	% Area	Area (ha)	% Area
Agricultural Land	536.4	3.11	946.71	5.49	1237.05	7.17
Barren Land	1994.49	11.56	2052.18	11.90	1880.01	10.90
SBEF	7052.49	40.90	6915.24	40.11	7449.48	43.21
SCPF	2345.76	13.60	2867.94	16.63	2437.92	14.14
Grassland	3048.39	17.68	2631.24	15.26	2453.4	14.23
Settlements	1835.64	10.64	1292.22	7.49	1266.93	7.34
Water Body	426.87	2.47	534.51	3.10	515.25	2.98
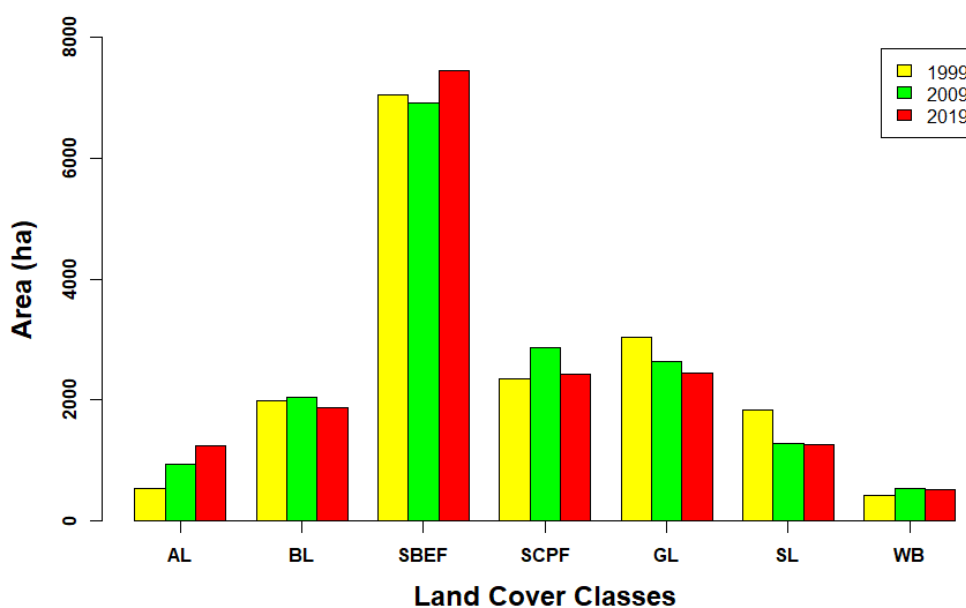
Fig. 62: Extents of Classified LC Classes for MHNP for the years of 1999, 2009 and 2019 in ha (AL= Agricultural Land, BL = Barren Land, GL = Grassland, SL = Settlements, WB = Water Body).

116
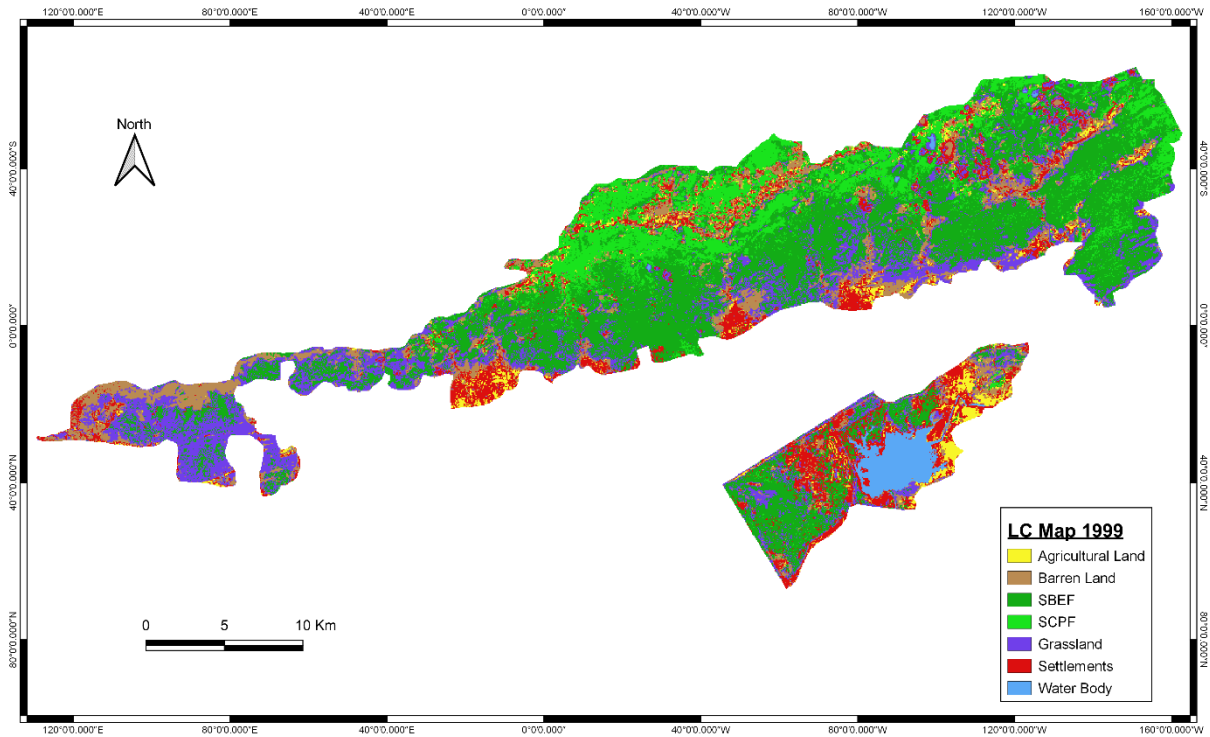
Fig. 63: LC Map for MHNP for the year 1999
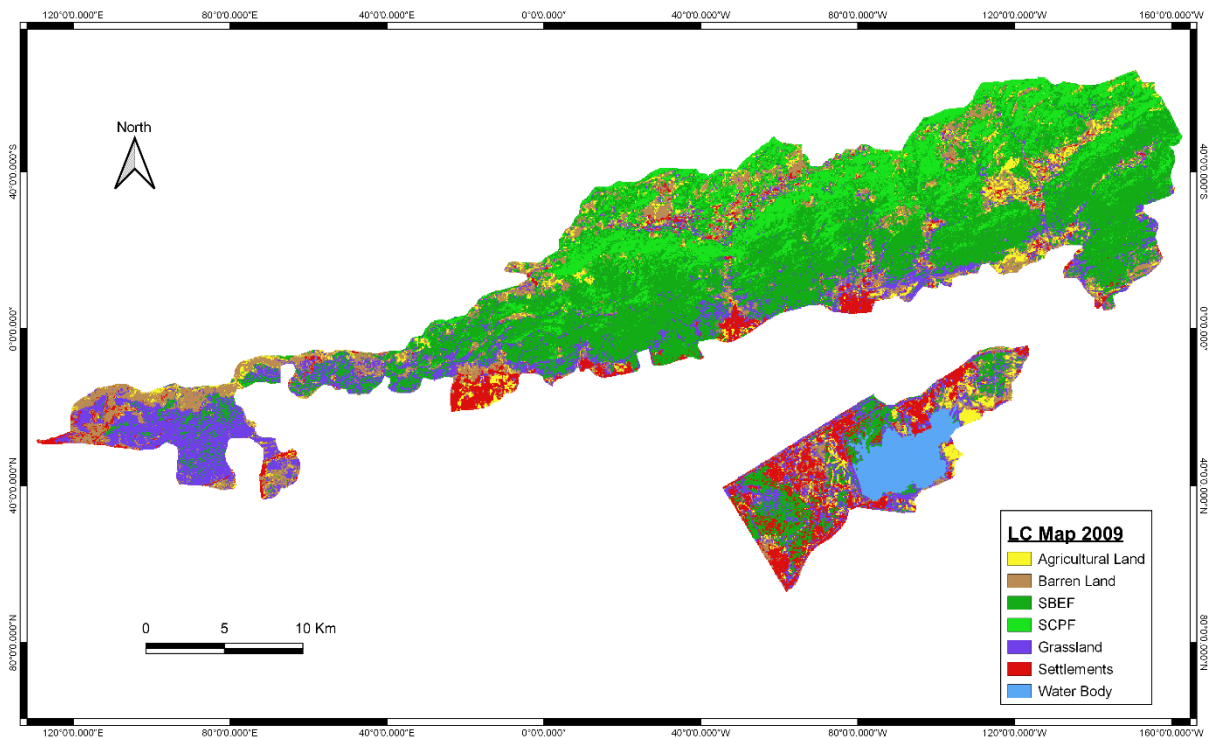
Fig. 64: LC Map for MHNP for the year 2009

117

4.2.5. Accuracy Assessment:

The accuracy assessments of the supervised LC classifications of the MHNP for the years 1999, 2009, and 2019 are documented in Table 18. For the year 1999, the highest user accuracy was recorded for agricultural land and water body with 100% each. The second highest was recorded for the barren land and SCPF with 97.91% each. The highest producer's accuracy was recorded for water body with 100% and the second highest was for grassland and settlements with 96% each. The overall accuracy for the year 1999 was recorded as 94.83%. The kappa coefficient was recorded as 0.93. For the year 2009, the highest user accuracy was recorded again for agricultural land and water body with 100% each, which was followed by the second highest grassland with 97.95%. The highest producer's accuracy was recorded for the water body with 100%, followed by the second highest for barren land, SCPF, and settlements with 98% each. The overall accuracy was recorded as 96.77% and the kappa coefficient was 0.96. For the year 2019, the highest user accuracy was recorded for agricultural land, barren land, and water body having 100% each. These classes were followed by the second highest grassland with 98.03%. The highest producer's accuracy was recorded for SCPF, grassland, and water body with 100% each. They were followed by the settlements with 98% as the second highest. The overall accuracy for the year 2019 was recorded as 97.09% and the kappa coefficient was recorded as 0.96.

The confusion matrices, with detailed information, for the land cover classifications of MHNP for the years 1999, 2009, and 2019 can be seen in Table 19, Table 20, and Table 21, respectively. The agricultural land showed the highest misrepresentation for all three years (Araya and Hergarten, 2008).

Table 18: Accuracy Assessment (in %) of LC Maps of MHNP for 1999, 2009 and 2019.

Land Cover Classes	1999		2009		2019	
	User's Accuracy	Producer's Accuracy	User's Accuracy	Producer's Accuracy	User's Accuracy	Producer's Accuracy
Agricultural Land	100	92	100	94	100	92
Barren Land	97.91	94	96.07	98	100	96
SBEF	92.59	100	96	96	92.30	96
SCPF	97.91	94	96.07	98	94.34	100
Grassland	88.88	96	97.95	96	98.03	100
Settlements	92.30	96	94.23	98	98	98
Water Body	100	80	100	100	100	100
Overall Accuracy	94.83		96.77		97.09	
Kappa Coefficient	0.93		0.96		0.96	

Table 19: Confusion Matrix for LC Classification of MHNP for 1999

		Reference Data							
		Agricultural Land	Barren Land	SBEF	SCPF	Grassland	Settlements	Water Body	Total
Classified Data	**Agricultural Land**	46	0	0	0	0	0	0	46
	Barren Land	0	47	0	0	1	0	0	48
	SBEF	0	0	50	3	1	0	0	54
	SCPF	1	0	0	47	0	0	0	48
	Grassland	1	3	0	0	48	2	0	54
	Settlements	2	0	0	0	0	48	2	52
	Water Body	0	0	0	0	0	0	8	8
	Total	50	50	50	50	50	50	10	310

Table 20: Confusion Matrix for LC Classification of MHNP for 2009

| | | Reference Data | | | | | | | |
		Agricultural Land	Barren Land	SBEF	SCPF	Grassland	Settlements	Water Body	Total
Classified Data	Agricultural Land	47	0	0	0	0	0	0	47
	Barren Land	0	49	0	0	2	0	0	51
	SBEF	1	0	48	1	0	0	0	50
	SCPF	0	0	2	49	0	0	0	51
	Grassland	0	0	0	0	48	1	0	49
	Settlements	2	1	0	0	0	49	0	52
	Water Body	0	0	0	0	0	0	10	10
	Total	50	50	50	50	50	50	10	310

Table 21: Confusion Matrix for LC Classification of MHNP for 2019

| | | Reference Data | | | | | | | |
		Agricultural Land	Barren Land	SBEF	SCPF	Grassland	Settlements	Water Body	Total
Classified Data	Agricultural Land	46	0	0	0	0	0	0	46
	Barren Land	0	48	0	0	0	0	0	48
	SBEF	2	1	48	0	0	1	0	52
	SCPF	1	0	2	50	0	0	0	53
	Grassland	0	1	0	0	50	0	0	51
	Settlements	1	0	0	0	0	49	0	50
	Water Body	0	0	0	0	0	0	10	10
	Total	50	50	50	50	50	50	10	310

4.2.6. LCC:

Table 22 highlights the percentage change, net change (ha), and ROC for the land covers of the MHNP for the three time periods of 1999 to 2009, 2009 to 2019, and 1999 to 2019. The agricultural land increased for all the three time periods, 1999-2009, 2009-2019, and 1999-2019 with 410.31 ha (76.49%), 290.34 ha (30.66%), and 700.65 ha (130.62%), respectively. The highest decrease occurred for the settlements with -543.42 ha (-29.60%) followed by the grassland at -417.15 ha (-

13.68%) for the time-period of 1999-2009. The highest decrease for the time-period 2009-2019 was recorded for SCPF with -430.02 ha (-14.99%).

The ROC showed that the SCPF increased by 52.21 ha/year for the time-period 1999-2009. For the same time-period, settlements had the highest decrease with -54.34 ha/year. SBEF showed the highest increase with 53.42 ha/year for the time-period 2009-2019. SCPF showed the highest decrease in ROC with -43.002ha/year for the same time-period. For the time-period 1999-2019, the highest increase in ROC was recorded for agricultural land with 35.03 ha/year. The highest decrease was recorded for grassland for the same time-period with -29.74 ha/year. Fig. 65 also shows the graphical representation of the LCC comparison of the MHNP.

Table 23, Table 24, and Table 25 provide a detailed description of land cover changes for the time-periods of 1999-2009, 2009-2019, and 1999-2019, respectively. According to Table 23, for the time-period 1999-2009, the highest change for agricultural land was to a barren land with 121.23 ha. The highest change for barren land was to grassland which was 369.81 ha. The highest change for SBEF was to SCPF with 1337.31 ha. The highest change for SCPF was to SBEF with 907.11 ha. The highest change for grassland was to SBEF with 1008.99 ha. The highest change for settlements was to a barren land with 354.6 ha. The highest change for the water body was to SCPF with 8.91 ha. According to Table 24, for the time-period 2009-2019, the highest change for agricultural land was to a barren land with 290.79 ha. The highest change for barren land was to grassland with 441.45 ha. The highest change for SBEF was to SCPF with 757.8 ha. The highest change for SCPF was to SBEF with 1150.11 ha. The highest change for grassland was to SBEF with 769.23 ha. The highest change for settlements was to a barren land with 177.3 ha. The highest change to the water body was to agricultural land with 7.65 ha. According to Table 25, for the time-period 1999-2019, the highest change for agricultural land was to settlements with136.35 ha. The highest change for barren land was to grassland with 444.06 ha. The highest change for SBEF was to SCPF with 1191.24 ha. The highest change for SCPF was to SBEF with 1103.94 ha. The highest change for grassland was to SBEF with 1082.07 ha. The highest change for settlements was to a barren land with 327.51 ha. The highest change for the water body was to SBEF

with 18.45 ha. Fig. 66, Fig. 67, and Fig. 68 show the LCC for 1999-2009, 2009-2019, and 1999-2019, respectively.

Table 22: Percentage change, net change, and rate of change occurring between the three time periods; 1999-2009, 2009-2019, 1999-2019 for the LC classes of MHNP.

Land Cover	Change (%)			Net Change (ha)			ROC (ha/year)		
	1999-2009	2009-2019	1999-2019	1999-2009	2009-2019	1999-2019	1999-2009	2009-2019	1999-2019
Agricultural Land	76.49	30.66	130.62	410.31	290.34	700.65	41.03	29.03	35.03
Barren Land	2.89	-8.38	-5.73	57.69	-172.17	-114.48	5.76	-17.21	-5.72
SBEF	-1.94	7.72	5.62	-137.25	534.24	396.99	-13.72	53.42	19.84
SCPF	22.26	-14.99	3.92	522.18	-430.02	92.16	52.21	-43.002	4.60
Grassland	-13.68	-6.75	-19.52	-417.15	-177.84	-594.99	-41.71	-17.78	-29.74
Settlements	-29.60	-1.95	-30.98	-543.42	-25.29	-568.71	-54.34	-2.52	-1.54
Water Body	25.21	-3.60	20.70	107.64	-19.26	88.38	10.76	-1.92	4.41

Note: - sign indicates the decrease in the LC
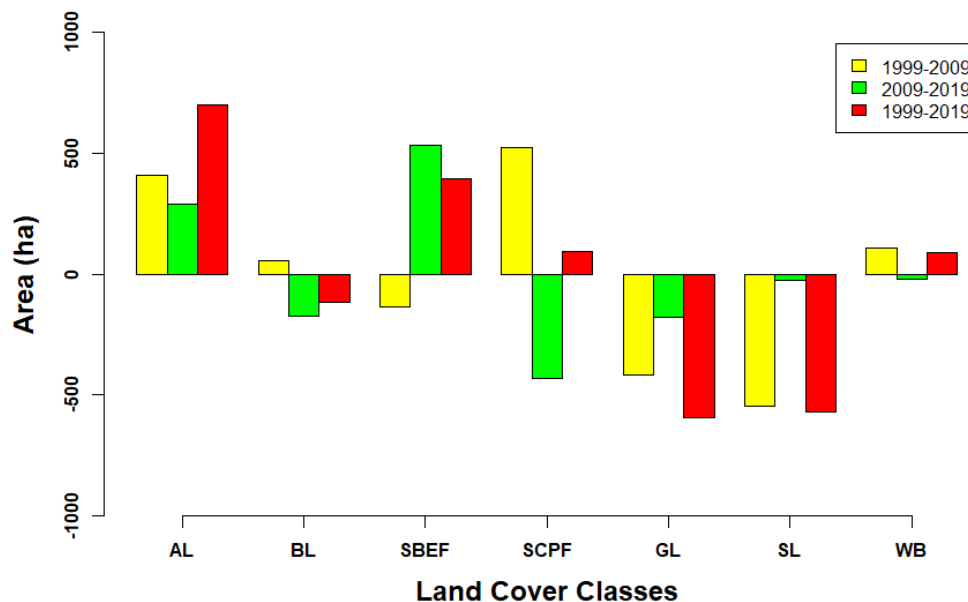
Fig. 65: LCC Comparison of MHNP (AL= Agricultural Land, BL = Barren Land, GL = Grassland, SL = Settlements, WB = Water Body)

Table 23: LCC matrix from 1999 to 2009 for MHNP

	Land Cover Classes	2009 Area (ha)						
		Agricultural Land	Barren Land	SBEF	SCPF	Grassland	Settlements	Water Body
1999 Area (ha)	Agricultural Land	**163.53**	121.23	41.13	16.11	58.14	111.24	25.02
	Barren Land	253.98	**853.47**	275.94	63.81	369.81	169.29	8.19
	SBEF	137.88	212.58	**4443.48**	1337.31	667.35	252.27	1.62
	SCPF	94.77	101.97	907.11	**1166.58**	17.37	0.18	402.21
	Grassland	137.61	402.21	1008.99	190.17	**1175.22**	127.08	7.11
	Settlements	158.22	354.6	231.93	85.05	298.17	**609.93**	97.74
	Water Body	0.72	6.12	6.66	8.91	4.77	5.04	**394.65**

Note: Bold figures within the table are an indication of no change.

Table 24: LCC matrix from 2009 to 2019 for MHNP

	Land Cover Classes	2019 Area (ha)						
		Agricultural Land	Barren Land	SBEF	SCPF	Grassland	Settlements	Water Body
2009 Area (ha)	Agricultural Land	**224.37**	290.79	126.81	63.27	139.14	102.33	0
	Barren Land	240.93	**886.68**	208.53	71.01	441.45	201.96	1.62
	SBEF	210.69	216.72	**5015.88**	757.8	678.24	33.75	2.16
	SCPF	75.6	64.08	1150.11	**1487.7**	86.85	3.6	0
	Grassland	346.5	242.73	769.23	57.96	**1031.31**	178.92	4.59
	Settlements	131.31	177.3	160.92	0.18	76.32	**746.19**	0
	Water Body	7.65	1.71	18	0	0.09	0.18	**506.88**

Note: Bold figures within the table are an indication of no change.

Table 25: LCC matrix from 1999 to 2019 for MHNP

	Land Cover Classes	2019 Area (ha)						
		Agricultural Land	Barren Land	SBEF	SCPF	Grassland	Settlements	Water Body
1999 Area (ha)	Agricultural Land	**141.03**	111.51	59.22	10.71	52.92	136.35	24.66
	Barren Land	222.57	**767.61**	244.53	78.48	444.06	229.77	7.47
	SBEF	259.65	232.65	**4621.95**	1191.24	613.17	132.75	1.08
	SCPF	86.58	135.54	1103.94	**875.52**	127.8	16.11	0.27
	Grassland	304.83	303.3	1082.07	215.19	**993.78**	143.82	5.4
	Settlements	216.81	327.51	319.32	61.2	220.86	**602.01**	87.93
	Water Body	5.58	1.89	18.45	5.58	0.81	6.12	**388.44**

Note: Bold figures within the table are an indication of no change.
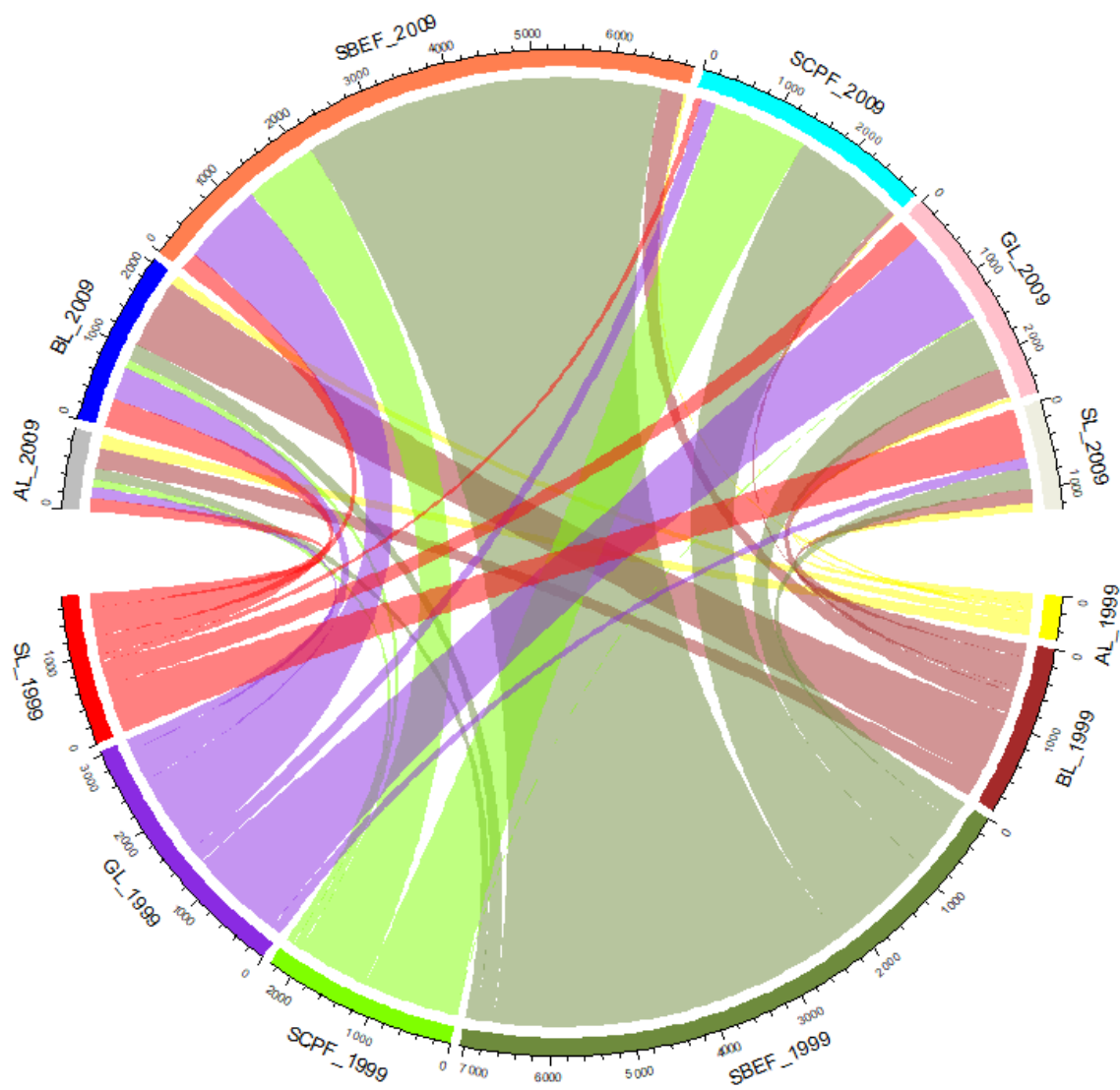
Fig. 66: Chord diagram representing LCC1999-2009 (in ha)

124
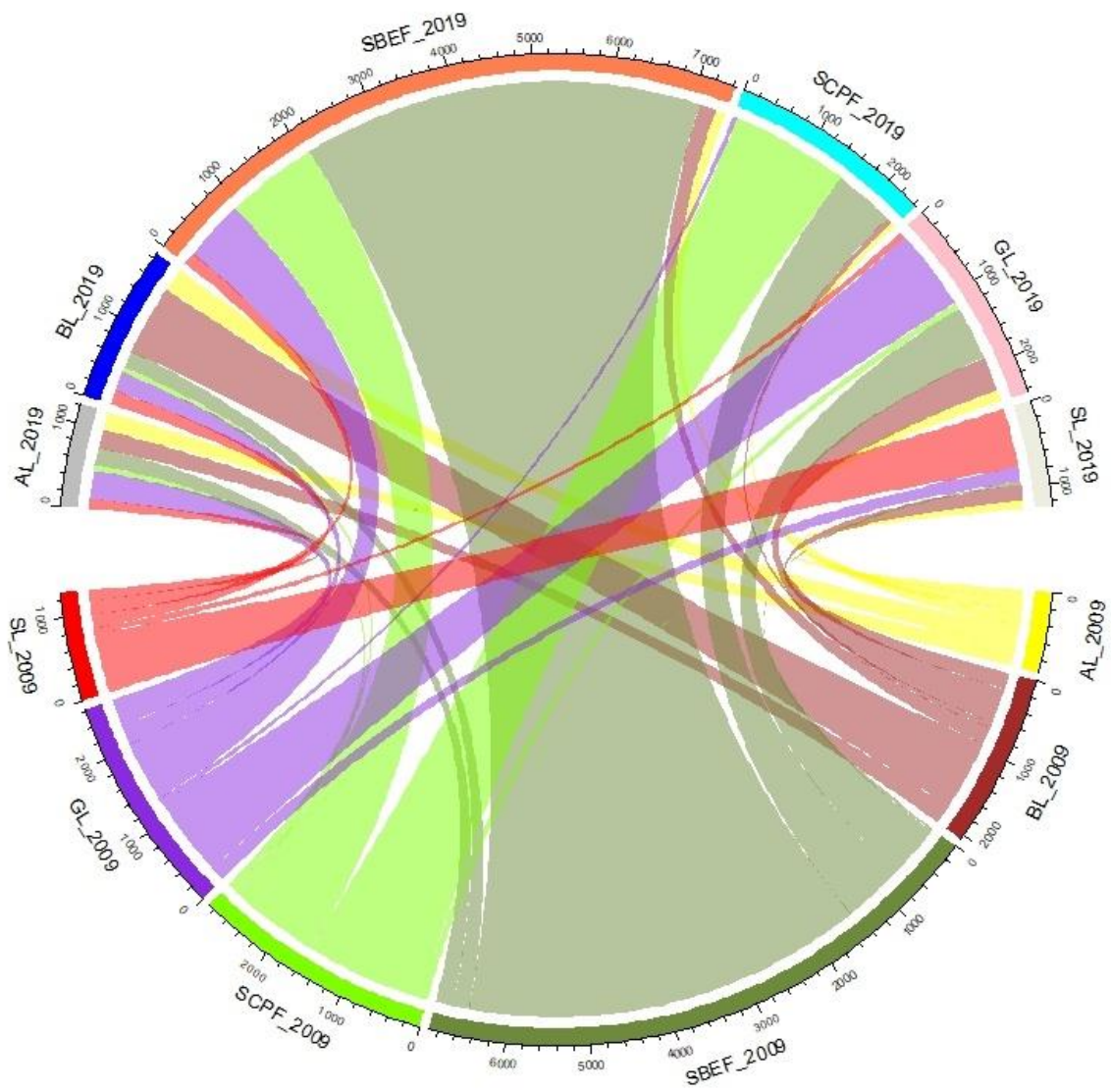
Fig. 67: Chord diagram representing LCC2009-2019 (in ha)
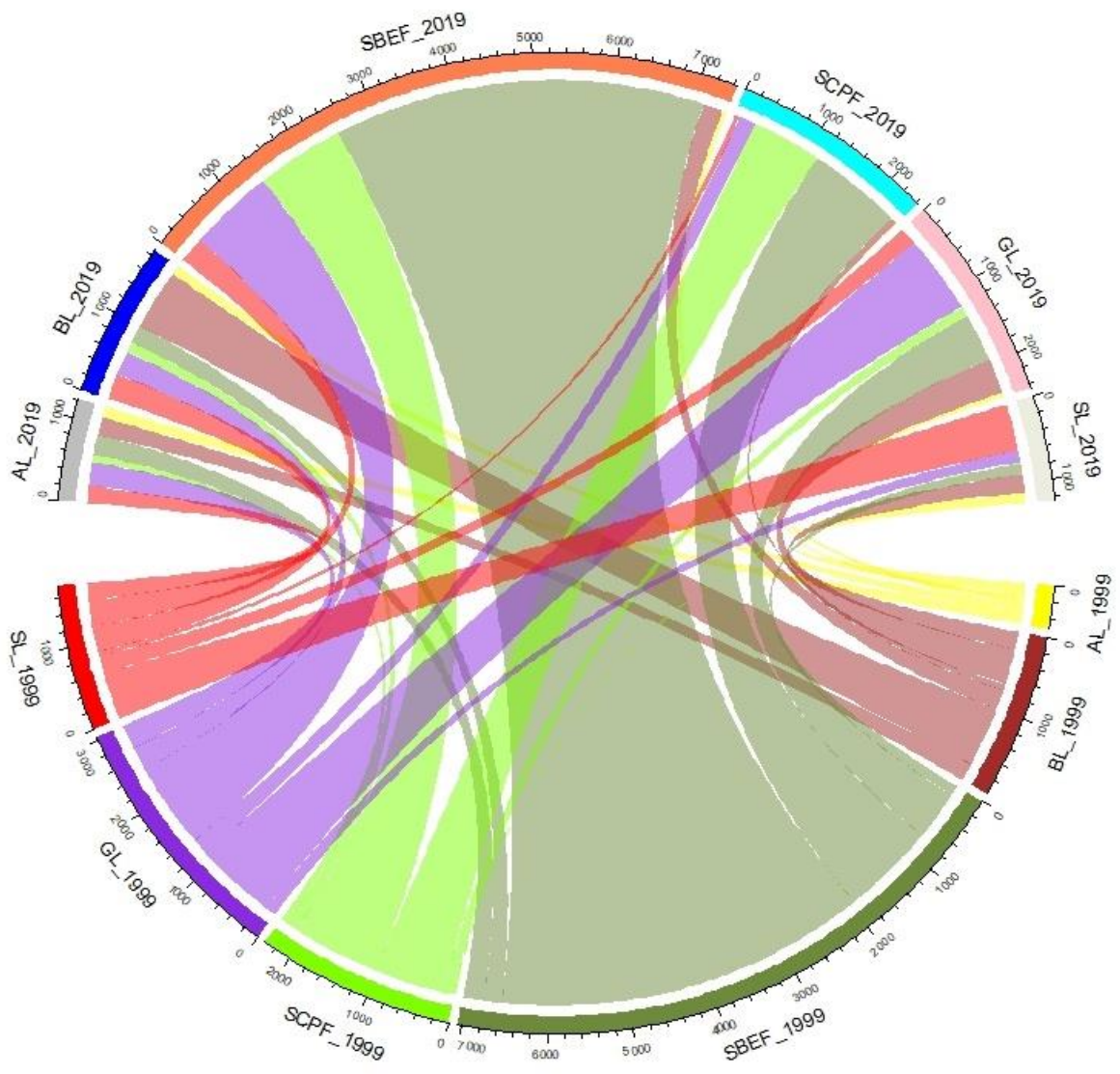
Fig. 68: Chord diagram representing LCC 1999-2019 (in ha)

5. Discussion:

5.1. Forest Biomass and Carbon Stock Assessment of MHNP:

5.1.1. AGB and AGC of the SCPF:

Table 26 shows the AGC estimations of the SCPF from different studies in Pakistan and Azad Jammu and Kashmir (AJK). The mean AGC estimated through this study, 73.36 ± 32.55 Mg C ha^{-1}, is higher than the mean AGC recorded by Amir et al. (2018) for SCPF which was 40 Mg C ha^{-1} at the Murre Hills, Pakistan, and from Ali et al. (2020b) who reported 24.77 Mg C ha^{-1} for the SCPF of the Khyber Pakhtunkhwa (KPK) Province. The other studies: (Nizami, 2012); (Shaheen et al., 2016); (Mannan et al., 2019a), have recorded higher mean AGC estimates compared to this study (Table 26). The other estimate provided by Amir et al. (2018), 264.5 Mg C ha^{-1}, for the SCPF at Murree Hills, Pakistan, is also higher than this study. In three of these studies i.e. (Amir et al., 2018); (Nizami, 2012); (Mannan et al., 2019a), the Belowground Carbon (BGC) was also included in the mean AGC. The BGC generally constitutes 20% of the AGC (Cairns et al., 1997). The result of this study is also in agreement with the estimates provided by Singh et al. (1985) who reported AGC of 35 to 75.2 Mg C ha^{-1} for the degraded forests of the Central Himalayan, India. The lower AGC for the SCPF can be attributed to the lower AGB yield of the study area (Segura and Kanninen, 2005). This low yield may also be ascribed to the anthropogenic activities and the natural disturbances occurring in the area (Bhadwal and Singh, 2002); (Rossi et al., 2007). The depletion in the AGC of the forest ecosystems is mainly attributed to forest degradation in developing countries (Pant and Tewari, 2014).

Table 26: Mean AGC of SCPF Reported by Different Studies

Sr. No.	Authors/Workers	Region/Study Area	Mean AGC (Mg C ha^{-1})
1	(Amir et al., 2018)	Murree Hills, Pakistan	40 to 264.5
2	(Nizami, 2012)	Ghoragali and Lehterar, Pakistan	119 and 92

3	(Shaheen et al., 2016)	Muzaffarabad District, AJK	154 and 264.5
4	(Mannan et al., 2019a)	Foothills of the Himalayan mountains, Pakistan	173.38
5	(Ali et al., 2020b)	KPK, Pakistan	24.77
6	This study	MHNP	73.36

The AGB estimation enables the quantification of the AGC, which forest stores (Naveenkumar et al., 2017). AGB estimation, therefore, is essential for the quantification of carbon budgets and for the national development planning for the overall forest management, which makes it also more important in view of the challenges posed by climate change (Devagiri et al., 2013). The mean AGB reported for this study, 146.73 ± 65.11 Mg ha^{-1}, is lower than the mean AGB reported for SCPF by Shaheen et al. (2016) which were 491.2 Mg ha^{-1} and 308 Mg ha^{-1} for the two sites of the Muzaffarabad District, AJK. The estimates for mean AGB (including BGB), 94.46 Mg ha^{-1}, and 112 Mg ha^{-1}, for the SCPF reported by Pant and Tewari (2014) for the two sites of the Kumaun Central Himalaya are also not in agreement with the estimate of this study. The estimate from this study is also not in agreement with the 113−283 Mgha^{-1} (including BGB) reported by Chaturvedi and Singh (1987) for the SCPF at the site areas of the Central Himalaya, India. The result for the mean AGB for the SCPF is also not in agreement with the estimate provided by Sharma et al. (2020) which was 167.7 Mg ha^{-1}for SCPF for a site area in Kathmandu, Nepal. Banday et al. (2018) reported a mean AGB of 194.19 Mg ha^{-1} for SCPF in Upper Himalayan, India, which is again higher than the estimate of this study.

5.1.2. Structural Characteristics of the SCPF:

The forest structure defines the arrangement and relationship between different tree components i.e. trunks, branches, and leaves (Ackermann, 2015). It consists of various attributes including type, size, shape, and spatial distribution of forest (McElhinny et al., 2005); (Pommerening, 2002). The mean basal area reported by

Nizami (2012) for the SCPF in Ghoragli and Lethrar, which were 30.38 m^2 $ha^{-1}$and 26.11 m^2 ha^{-1} respectively, are higher than the estimate of this study, 14.48 ± 4.80 m^2 ha^{-1}. The basal area is among the common variables such as DBH, total height, volume, and crown diameter, which are used for estimation of the AGB (Goodman et al., 2014). The result of this study is also not in agreement with Amir et al. (2018) who provided a mean basal area of 32.3 m^2 ha^{-1} for the SCPF of Murree Hills, Pakistan. Sharma et al. (2020) provided an estimate of 32.1 m^2 ha^{-1} for a plantation site of *Pinus roxburghii* in Kathmandu, Nepal, which is also not in agreement with this study. The estimate for this study however is higher than the minimum mean basal area provided by Kumar et al. (2019) which was 11.12 m^2 $ha^{-1}$for the SCPF of Garhwal Himalaya, India. The mean tree volume of 198.75 ± 87.76 m^3 ha^{-1} reported by this study is on the lower side compared to Nizami (2012) who reported 243 m^3 ha^{-1} for the SCPF of Ghoragli, but slightly higher than the 197 m^3 ha^{-1} for Lethrar area. The result for the mean tree volume for this study is more than the lower end of mean tree volume of 83 m^3 ha^{-1}, which was for the young stands of SCPF, reported by the Amir et al. (2018) for Murree Hills, Pakistan. The higher estimate of the study, 549.4 m^3 ha^{-1}, by Amir et al. (2018) for SCPF for Murree Hills, Pakistan, is higher than the estimate provided by this study. The mean tree volume estimate provided by Kumar et al. (2019) for SCPF of Garhwal Himalaya, India, which was 214.88m^3 ha^{-1}, is also higher than the result of this study. The mean tree density reported by Nizami (2012) for SCPF was 878 trees $ha^{-1}$for Ghoragali and 776 trees ha^{-1} for Lethrar. These estimates are on a higher side compared to the mean tree density of 139.13 ± 22.88 trees ha^{-1} for this study. The mean tree density estimate for this study is also lower than the estimate provided by Kumar et al. (2019) for SCPF, which was 244.34 trees ha^{-1} for Garhwal Himalaya, India. The tree density is also an indicator of deforestation pressures on the forest ecosystems since people are dependent on forests for their livelihood and this can further be aggregated by additional demands for construction and industrial demands (Shaheen et al., 2016); (Wani et al., 2010). In addition, lower tree densities may also portray lower forest carbon stock values (Kindermann et al., 2006). The mean tree density of this study is higher than the estimate provided by Khan et al. (2020) who reported 103-104 trees $ha^{-1}$for the SCPF of Murree Forests, Pakistan, and thereby have attributed their lower densities to the anthropogenic pressures such as lopping and high tourism.

The DBH distributions are an effective way for describing the tree populations and forest stands (de Lima et al., 2015). These can be used for valuing forests, planning harvest operations, and predicting forest growth (Burkhart and Tomé, 2012). DBH distributions can also be used for inferring past disturbances in the forest stands, the successional status of forests, and the AGB contained in the forests (Coomes and Allen, 2007). The DBH distribution for the SCPF has shown a hump-shaped (unimodal type) (Subedi et al., 2018), which shows that there is a lesser number of stems in the lower DBH classes, and the number of stems increases with the increasing DBH classes until the classes 25-30 cm and 35-40 cm and after which the number of stems starts to decrease again (Fig. 16). These two classes contained 16.72% and 17.81% of the total stems and were also the two highest classes in the DBH distribution. Pariyar et al. (2019) also reported similar results for the mixed *Pinus roxburghii* forest, of the Parbat District of Western Nepal, where most of the stems had 30 cm DBH compared to the pure stands of *Pinus roxburghii* which had higher representations from higher DBH classes. This type of distribution has also been observed elsewhere in different areas of the Himalayan region (Kunwar and Sharma, 2004); (Sharma et al., 2008); (Vetaas, 2000). This unimodal distribution is not a good sign for the forest ecosystem, since it is attributed to anthropogenic and natural disturbances (Wangda and Ohsawa, 2006); (Bin et al., 2012). Furthermore, looking at the classification of forest structure for *Pinus roxburghii* based on DBH; < 10 cm (sapling), 10-30 cm (young), 30-50 cm (middle-aged), 50-70 cm (mature), > 70 cm (overmature) (FRI, 2018), it was also found that highest percentage of the stems belonged to the young and middle-aged DBH classes with 39.84% and 52.18%, respectively. This distribution represents imbalance and poses further challenges towards the sustainable management of the forest (FRI, 2018).

The forest structure is a 3-dimensional phenomenon, which is represented by the horizontal and vertical components (Podlaski et al., 2019). The vertical structure of the forest plays an important role in ecological processes (Hao et al., 2007). The vertical structure of the forests is often represented by the height distribution (Podlaski et al., 2019). The height distribution for the SCPF is negatively skewed

(Fig. 17). The highest number of stems were found in two of the height classes i.e., 21-24 m and 24-27 m.

Regression analysis between DBH and height of the *Pinus roxburghii*, which was the dominant species of the SCPF, showed a significant association (R^2 = 0.74, p < 0.05) (Fig. 21). Tree heights are essential parameters for forest inventory variables and carbon budget models (Vanclay, 1994). Tree heights are difficult to collect in the forests and are also costlier compared to the DBH data collections (Peng et al., 2001). Mostly, height-DBH equations are developed for predicting the missing heights, which were skipped during field expeditions (Peng et al., 2001). In this study, all the heights for the tree stems for both forests were measured during the field expedition, 640 for the SCPF and 443 for SBEF. The highest height recorded for *Pinus roxburghii* was 41.7 m and the lowest was 13.9 m. *Pinus roxburghii* is a fast-growing pioneer species, which can reach up to the height of 51 m and DBH of 1 m (Jackson, 1994). Ghimire (2019) reported a maximum DBH of 84.41 cm and a maximum height of 37.50 m for *Pinus roxburghii*. FRI (2018) also reported a maximum DBH of 64.3 cm and a maximum height of 43.3 m for *Pinus roxburghii*. The linear regression relationship between DBH and height for the *Pinus roxburghii* from this study is in agreement with (Khan et al., 2016); (Nizami et al., 2009); (Subedi et al., 2018). Tree DBH and height can also directly influence biomass production, where lower DBH and heights can result in lower biomass and carbon stock values for the forests (Feldpausch et al., 2012).

The regression analysis between basal area and volume of the *Pinus roxburghii* has shown a significant linear association (R^2 = 0.96; p < 0.05) (Fig. 22). The result of the linear regression analysis is not in agreement with Amir et al. (2018) who have shown a polynomial relationship between the two variables. The result, however, is in agreement with Nizami et al. (2009). The regression analysis between DBH and AGB showed a significant non-linear relationship (R^2 = 0.98; p < 0.05) (Fig. 23). This is in agreement with Ali et al. (2020a) and Solomon et al. (2017), who also reported significant non-linear relationship between the two variables. Many studies have shown that DBH is a reliable predictor of AGB (Solomon et al., 2017); (Hasen-Yusuf et al., 2013); (Giday et al., 2013).

131

5.1.3. AGB and AGC of the SBEF:

The carbon stock assessment in the sub-tropical forests is of utmost importance because they have been poorly studied in comparison to the other forest types (Rosenfield and Souza, 2013). The estimate for AGC for the SBEF for this study is 16.88 ± 25.81 Mg C ha^{-1} (Table 8). The result is on the very low side compared to the study by Mannan et al. (2019a) who reported 73.81 Mg C ha^{-1} for the AGB of the SBEF which also included the BGC. The result for this study is also on the lower side compared to the mean AGC reported by Ali et al. (2019), for SBEF, which was 49.54 Mg C ha^{-1} for the sites in Swat, Dir Upper, Dir Lower, and Buner Districts in the KPK, Pakistan. The result of this study is also on the lower side compared to Ali et al. (2018) who reported a mean AGC of 39.02 Mg C ha^{-1} for SBEF at a site in Khanpur Range, KPK, Pakistan. The estimate for SBEF from this study is also lower than the estimates by Nizami (2012) who had reported mean AGC (including BGC) of 25.54 Mg C ha^{-1} and 20.23 Mg C ha^{-1} for SBEF at the sites of Kherimurat and Sohawa respectively. The result of this study is higher than the estimate reported by Ali et al. (2020b) which was 4.52 Mg C ha^{-1} for the SBEF for the entire KPK, Pakistan. All the above-mentioned comparisons can be found in Table 27.

Table 27: Mean AGC for SBEF from Different Studies

Sr. No.	Authors	Region/Study Area	Mean AGC (Mg C ha^{-1})
1	(Nizami, 2012)	Kherimurat and Sohawa, Pakistan	25.54 and 20.23
2	(Ali et al., 2020b)	KPK, Pakistan	4.52
3	(Mannan et al., 2019a)	Foothills of the Himalayan mountains, Pakistan	73.81
4	(Ali et al., 2019)	Swat, Dir Upper, Dir Lower, and Buner Districts, Pakistan	49.54
5	(Ali et al., 2018)	Khanpur Range, Khyber Pakhtunkhwa, Pakistan	39.02
6	This study	MHNP	16.88

The mean AGB reported by Nizami (2012) which was 50.93 Mg ha^{-1} and 40.43 Mg ha^{-1} (both estimates also included the BGB) for the SBEF for the sites of Kherimurat and Sohawa respectively are on the higher side comparing to this study, which is 33.77 ± 51.63 Mg ha^{-1}. The mean AGB reported by Ali et al. (2018) which was 83 Mg ha^{-1} for the SBEF for Khanpur Range, KPK, Pakistan, is higher than the estimate of this study. The estimate from this study is also on the lower side compared to the estimate provided by Mannan et al. (2019a) who reported a mean AGB (including BGB) of 147.62 Mg ha^{-1} for SBEF at the foothills of Murree. Mannan et al. (2019a) attributed their high AGB estimate to the high tree density observed in the SBEF in their study region. Ali et al. (2019) reported a mean AGB of 100.1 Mg ha^{-1} for SBEF in the Districts of Swat, Dir Upper, Dir Lower, and Buner of the Khyber Pakhtunkhwa Province of Pakistan; their estimate is also on the higher side comparing to the estimate of this study. Ali et al. (2019) attributed their high AGB to the presence of overmature trees, having DBH > 80 cm. Mannan et al. (2019b) reported a mean AGB of 70.80 Mg ha^{-1} for SBEF for the study sites of Margalla and Murree Forest Division, which is also on the higher side compared to the result of this study; they attributed their result to the high tree density of SBEF located at their study sites.

5.1.4. Structural Characteristics of the SBEF:

The mean tree volume recorded for the SBEF for this study, 37.82 ± 50.38 m^3 ha^{-1}, is on the higher side compared to the estimate provided by Nizami (2012) which was 12.86 m^3 ha^{-1} and 11.40 m^3 ha^{-1}for SBEF for the sites of Kherimurat and Sohawa, respectively. Mannan et al. (2019a) reported the mean tree volume for SBEF as 115.71 m^3 ha^{-1}, which is on the higher side compared to the mean tree volume estimate of this study. Ali et al. (2018) recorded a mean tree volume of 57.66 m^3 ha^{-1} for SBEF for Khanpur Range, KPK, Pakistan, which is also on the higher side compared to this study. The mean tree basal area for this study was recorded as 4.28 ± 3.43 m^2 ha^{-1}, which is slightly higher than the estimates of 3.06 m^2 ha^{-1} and 2.65 m^2 ha^{-1} reported by Nizami (2012) for SBEF for the sites of Kherimut and Sohawa, respectively. The estimate for this study is less than the estimate of 13.1 m^2 ha^{-1} reported by Mannan et al. (2019b) for SBEF for the sites at Margalla and Murree

Forest Division. The estimate reported from this study is also close to the estimate of 6.69 m^2 ha^{-1} reported by Ali et al. (2019). The mean tree density of 142.90 trees ha^{-1} were recorded for this study, which is lower than the mean densities of 197 trees ha^{-1} and 179 trees ha^{-1} reported by Nizami (2012) for SBEF for Kherimurat and Sohawa, respectively. The mean tree density of this study is also on the lower side compared to Mannan et al. (2019b) who reported a mean tree density of 761.18 trees ha^{-1} for SBEF. The tree densities and basal areas are important characteristics that have significant effects on the AGB (Gogoi et al., 2020).

Ideally, the DBH distribution of a forest should follow an inverse J shape (Shimano, 2000). The DBH distribution of the SBEF is positively skewed which means tree density increases till the DBH class is 10-50 cm and after which it starts to decrease. The DBH class 10-15 cm also contained the highest percentage of the stems, 37.70%. The highest number of stems in the lower DBH classes shows a good regeneration potential (Ballabha et al., 2013). It also highlights that a forest is in evolving stage (Campbell et al., 1992). But at the same time, the absence of the trees in the higher DBH classes suggests historical disturbances which must also be not neglected while undertaking the overall planning for management purposes (Nath et al., 2017). The height distribution of the SBEF also showed a positively skewed distribution, with most of the stems being present in the two classes, 6-9 m, and 9-12 m.

Two tree species were selected for performing the regression analysis from the SBEF based on the highest number of the sampled stems. The regression analysis between DBH and height of the *Bauhinia variegata* had shown a moderate linear association (R^2 = 0.36; p < 0.05) (Fig. 24). The DBH range recorded for *Bauhinia variegata* was 5.6-35 cm. The height range was 5.4-18.1 m. The regression analysis between basal area and tree volume of *Bauhinia variegata* had shown a significant linear association (R^2 = 0.92; p < 0.05) (Fig. 25). The mean basal area for *Bauhinia variegata* was recorded as 1.16 ± 0.77 m^2 ha^{-1} and the mean tree volume was recorded as 6.88 ± 4.77 m^3 ha^{-1}. Significant non-linear regression association was revealed between DBH and AGB of *Bauhinia variegate* (R^2 = 0.93; p < 0.05) (Fig. 26). The result of this study, a non-linear significant regression association between

DBH and AGB of *Bauhinia variegata*, is in agreement with the Kanwar (2019) who also recorded strong non-linear relationship between DBH and AGB. The mean AGB of *Bauhinia variegata*, 7.33 ± 5.02 Mg ha^{-1}, from this study, is not in agreement with Kumar and Sharma (2015) who reported a mean AGB of 25.82 ± 48.57 Mg ha^{-1} for the Balganga Range of the Garhwal Himalaya region, India.

The regression analysis between DBH and height of the *Grewia optiva* showed a moderate linear association (R^2 = 0.42; $p < 0.05$) (Fig. 27). The DBH for *Grewia optiva* ranged from 5.5 cm to 22 cm and the height ranged from 5 m to 15 m. The regression analysis between the basal area and volume of the *Grewia optiva* had shown a significant linear association (R^2 = 0.97; $p < 0.05$) (Fig. 28). The mean basal area and the mean tree volume were recorded as 0.83 ± 0.54 m^2 ha^{-1} and 4.75 ± 3.30 m^3 ha^{-1}, respectively. The regression analysis between DBH and AGB showed a moderate non-linear association (R^2 = 0.59; $p < 0.05$) (Fig. 29). The result for the moderate non-linear association of this study between the DBH and AGB of *Grewia optiva* is not in agreement with the Kanwar (2019) who had reported a strong non-linear association between the two variables at the Balganga Range of the Garhwal Himalaya region, India. The mean AGB for *Grewia optiva*, in this study, was recorded as 5.14 ± 3.57 Mg ha^{-1}. This means AGB for *Grewia optiva* is on the lower side compared to Rana et al. (2020) who reported a mean AGB of 35.9 Mg ha^{-1} for *Grewia optiva* in Garhwal Himalaya, India. The result, however, is slightly higher than the mean AGB estimate of 4.91 Mg ha^{-1} for *Grewia optiva* reported by Kumar et al. (2012) for Dungripanth Village, Srinagar. *Grewia optiva* is a very important agroforestry species, which can also provide fodder for livestock during the winter season (Verma et al., 2014). It is also a very good fuelwood species since it has a calorific value of 4920 k cal kg^{-1} (Joshi and Dhiman, 1992).

5.1.5. Comparison of AGC between SCPF and SBEF:

The SCPF recorded higher AGC compared to the SBEF (Fig. 20), which has also resulted in a significant statistical difference between the two (*W = 43, p < 0.05*). This can be attributed to the higher mean DBH and higher mean height recorded for the SCPF which were 36.37 ± 6.51 cm and 27.34 ± 3.67 respectively (Table 8). The

carbon storage in the forests is the function of size (girth), wood density, and height (Chave et al., 2014); (Chave et al., 2005); (Macías et al., 2017); (Moussa et al., 2019). The small-sized trees store less carbon compared to the large-sized trees (Nero et al., 2018); (Dimobe et al., 2019); (Portela et al., 2020); (Xu et al., 2018). Generally, therefore, the mature trees, which tend to have bigger and larger sizes such as DBHs, in a forest ecosystem store more carbon (Köhl et al., 2017); (Gandhi and Sundarapandian, 2017); (Clark and Clark, 2000); (Slik et al., 2013). In addition, larger trees have been reported to store more carbon despite lesser density and richness (Mensah et al., 2020); (Lutz et al., 2018); (Chiba, 1998). The SCPF recorded 7.81% of the trees in the mature category; DBH 50-70 cm (Fig. 33). At the same time, SCPF recorded 39.84% of the stems in the small-sized young aged DBH category < 30 cm. This category, therefore, can also be not neglected and hence can play a critical and important role in future carbon sequestration (Gandhi and Sundarapandian, 2017). Comparing all the plots, the SCPF had higher AGC in all the plots compared to SBEF (Fig. 37). The difference between the AGC of the two forests can therefore be attributed to the higher DBHs and heights recorded for the trees in the SCPF, as already mentioned above. The difference could also be attributed to the species composition since it is also considered an important factor in modulating forest carbon stocks (Reyes-Palomeque et al., 2021). Negi et al. (2003), for instance, reported that the maximum AGC was stored in the following order: pines > deciduous > evergreen > bamboos. A similar, pattern was also reported by Kaushal and Baishya (2021). The result of this study is in agreement with (Nizami, 2012); (Mannan et al., 2019b); (Sharma et al., 2010) who also reported higher AGC for the SCPF over the SBEF. Gogoi et al. (2020), however, had reported higher AGC in the SBEF in comparison to the Pine Forests which were 140.4 Mg C ha^{-1} and 133.6 Mg C ha^{-1} for SBEF against the 74.7 Mg C ha^{-1} and 63 Mg C ha^{-1} for Pine Forests of the Meghalaya District, India. They also attributed the higher carbon stocks to the presence of overmature trees, with DBH > 66 cm, and the relatively higher density of younger trees in the SBEF.

5.1.6. Species Wise AGB Contribution:

The *Pinus roxburghii* contained the highest AGC, with 98.85% of the total, for the SCPF (Table 11). The result is in agreement with Pariyar et al. (2019); Shaheen et al. (2016) showing higher contributions of AGC by the *Pinus roxburghii*. *Pinus roxburghii* is usually a dominant species and mostly grows in pure stands throughout Pakistan, India, Nepal, and Bhutan (Khan et al., 2014); (Gupta and Dass, 2007). The species is commonly known as 'Chir Pine' (Anwar et al., 2019). It is spread over Bhutan, China, India, Nepal, and Pakistan from 400 to 2300 m a.s.l. (Polunin and Stainton, 1984). It is native to the foothills of the Himalayan Hindu Kush Region (Aryal et al., 2018). The species provides various economical and ecological benefits, due to which nearby communities leaving in or around its zone rely on it for various purposes (Khan et al., 2014); (Gupta and Dass, 2007).

The *Eucalyptus spp.* is native to Australia (Afzal et al., 2018) and was introduced in Pakistan in the late 19s (Shah et al., 1991). Amongst the 40 spp. introduced in Pakistan, *Eucalyptus camaldulensis* has been the most widespread and adaptable (Bilal et al., 2014). It is a fast-growing species (Afzal et al., 2018), and is locally known as 'Sufeda' (Khan et al., 2017). The DBH and height for *Eucalyptus camaldulensis* in this study ranged between 38-86 cm and 22-35.5 m, respectively. The *Eucalyptus camaldulensis* recorded a total AGC of 176.14 Mg C ha^{-1} in this study, contributing 33.65% of the total AGC for the SBEF (Table 12). The result of this study is in agreement with (Arif et al., 2017) who reported the highest AGC contribution from the *Eucalyptus camaldulensis* towards the Chichawatni Plantation in Pakistan. Mandal et al. (2017) also recorded the highest AGC contribution by the *Eucalyptus camaldulensis* in a mixed plantation in the Mahottari District of Nepal.

The *Ficus palmata subsp. virgata* was the second species with the highest AGC contribution to the SBEF. It contributed AGC of 94.24 Mg C ha^{-1} which was 18% of the total AGC. The DBH ranged from 8.2 cm to 87 cm and the height of the *Ficus palmata subsp. virgata* for this study ranged from 6.2 m to 18.6 m. The geographical distribution of the *Ficus palmata subsp. virgata* includes; Afghanistan, Arabian Peninsula, Ethiopia, Egypt, Iran, Nepal, Pakistan, Somalia, Sudan, and India

(Chaudhary et al., 2012). The species is well known for its medicinal properties (Saqib et al., 2014); (Salehi et al., 2021). The result of this study is not in agreement with Shaheen et al. (2016) who reported other trees species with higher AGC concentrations than the *Ficus palmata subsp. virgata* in AJK. The study is also not in agreement with Ali et al. (2019) who reported lower AGC contribution from *Ficus palmata subsp. virgata*., compared to other species, in four districts of Buner, Dir Upper, Dir Lower, and Swat of Khyber Pakhtunkhwa, Pakistan.

5.1.7. AGC in Protected Areas:

Protected areas can play a major role in avoiding the carbon emissions arising from deforestation and forest degradation (Fearnside, 2008). Protected areas include National Parks and other forms of protection which avoids illegal extractive activities and other anthropogenic disturbances (Collins et al., 2017). Protected areas are important carbon reserves (Walker et al., 2014); (Dimobe et al., 2019); (Haq et al., 2020). It is estimated that protected areas store 3.12×10^5 Tg C globally, which accounts for 15% of the overall world's terrestrial carbon stock (UNEP-WCMC, 2014). Moreover, these protected areas continue to sequester carbon at 0.5 Pg C/year, which is about 20% of the terrestrial carbon stock globally (Melillo et al., 2009).

Carbon stocks held by the protected areas posed with lower risk of being emitted into the atmosphere compared to the areas which are outside the protected areas due to legal protection (Nogueira et al., 2018). The relative higher carbon stocks in the protected areas, however, also portray the effectiveness of the legal protection of the protected areas (Nolte et al., 2013). In addition, preventing carbon loss in the protected areas can serve as a measure of the effectiveness of the management of the protected areas (Nogueira et al., 2018).

The government-managed *Pinus roxburghii* forests such as protected areas have recorded higher carbon stocks compared to the community-managed forests (Pariyar et al., 2019); (Sharma et al., 2011). Lecina-Diaz et al. (2019) reported higher carbon stocks for the protected areas in comparison to the buffer areas in the

Catalonia region, Spain. Sharma et al. (2008) have also reported higher carbon stocks for the protected and reserved forests compared to other land uses for Western Himalayan Watershed in India. Higher carbon stocks have also been reported in the protected areas compared to the areas outside protected areas (Dayamba et al., 2016); (Dimobe et al., 2019); (Asner et al., 2018); (Bebber et al., 2017). The large amounts of carbon, however, can also be released back from the protected areas into the atmosphere due to the disturbances such as fires, etc., if in case vegetation and fuel load are not adequately managed (Lu et al., 2018).

5.1.8. VIs and AGB:

The NDVI for the study region ranged from -0.34 to 0.80 (Fig. 30). The similar result was reported by Mannan et al. (2018) for the same study region ranging from -0.26 to 0.85 for the year 1990, but for the year 2017 slight differences were noted, as the values were reported from -0.67 to 0.62. They used the LANDSAT 5TM data for 1990 and LANDSAT 8 OLI for 2017, where both have a spatial resolution of 30 m. They attributed their lower NDVI values for 2017 to the deforestation caused by the local people for fuelwood extraction, livestock grazing, and frequent forest fires. Slight differences were also noticed with Naeem et al. (2017) who reported NDVI values between -0.87 to 0.69 for the SCPF near Ghora Gali, Murree, Pakistan. They used the SPOT-5 data with 2.5 resolution from 2013. Almost similar results were obtained by Mannan et al. (2019a) who reported NDVI values for the foothills of the Himalayan mountains of northern Pakistan from -0.34 to 1 (1998), -0.14 to 0.89 (2008), and -0.52-0.83 (2018) using LANDSAT 5 TM for 1998 and 2008 and LANDSAT 8 OLI for 2018. Mallick et al. (2012) reported NDVI values, for 2004, ranging from 0.15 to 0.528 for the SBEF and SCPF located in the foothills of Himalayan in northern India. They used the satellite data from Indian Remote-Sensing Satellite (IRS)-P6 Linear Imaging Self-Scanning Sensor (LISS)-4. The NDVI values range between -1 to 1 where barren lands and residential built areas usually have values below 0.1 (Baniya et al., 2019). The water bodies such as lakes etc. have values below 0 or in the minus range, as such is the case in this study where the water body i.e. Rawal Lake had recorded the NDVI values in the minus range

(Askar et al., 2018); (Hussain et al., 2020). The values for the green vegetation typically range from 0.2 to 0.8 (Jensen and Lulla, 1987).

In this study, the NDVI had recorded a weak association with the AGB of the SCPF (R^2 = 0.009; p > 0.05) (Fig. 32) and similarly also recorded a weak association with the AGB of SBEF (R^2 = 0.13; p < 0.05) (Fig. 33). The association between the two variables, NDVI and AGB, was however slightly better in the case of SBEF. The weak association between the AGB and NDVI in this study is in agreement with Imran et al. (2020) who also claimed a relatively weak non-linear association between the two for a study site in Muzaffarabad District, AJK, Pakistan. Similarly, Alam et al. (2017) also reported a weak association of the NDVI and AGB (R^2 = 0.19), using S2 satellite data, for the invasive tree species, *Broussonetia papyrifera*, found in the MHNP. Ali et al. (2018), however, reported a significant non-linear association between the two variables (R^2 = 0.81), using S2 satellite data, for the Khanpur Range, Khyber Pakhtunkhwa, Pakistan. Naeem et al. (2017) also reported a significant linear association between AGB and NDVI (R^2 = 0.7), using SPOT-5 satellite data, for study sites in Murree and Abbottabad, Pakistan. Similarly, strong associations have also been reported between the two variables by the following researchers: (Riihimäki et al., 2017); (Motlagh et al., 2018); (Pandey et al., 2019b); (Joshi et al., 2019); (Wani et al., 2015). On the contrary, various researchers: (Gizachew et al., 2016); (Prawasi et al., 2019); (Bhardwaj et al., 2016); (Sader et al., 1989); (Khan et al., 2020) have also reported a weak association between the two variables.

Some of the drawbacks associated with NDVI also include saturation, which means that the increase in forest biomass is not gauged by the NDVI (Wang et al., 2018). The saturation can either be due to the maturity of the forest crop (Mutanga and Skidmore, 2004); (Wang et al., 2016) or because of the complex forest canopy structure (Lu et al., 2016); (Sinha et al., 2016); (Gómez et al., 2014). In the case of this study, the complex canopy structure along with the understorey vegetation seems to have played a significant role. In SBEF for instance, multi-layer spreading crowns were observed along with the profuse understorey vegetation i.e. shrubby growth, etc., which may have accounted for an increase in the vegetated area (Khan

et al., 2020); (Spanner et al., 1990). This would have resulted in an increase in the NDVI values since the light would have been reflected from these vegetated surfaces and would not have accounted for the heights and DBHs of the trees which are strongly correlated with the AGB (Mohd Zaki et al., 2018). This could be one of the reasons that increasing AGB may not have been reflected by the increasing NDVI. Nonetheless, the DBHs and heights of trees can also not be directly recorded by the optical satellite sensors (Alam et al., 2017). The SCPF had recorded a mean NDVI (per plot) of 0.64 ± 0.06 compared to the mean NDVI (per plot) of SBEF which was 0.71 ± 0.03. This also corroborates the presence of more vegetated areas in the sampled plots of the SBEF mainly due to the spreading crowns and the understorey vegetation in the form of shrubs etc. The understorey vegetation was not considered in carbon stock calculations because of its negligible contribution to the overall carbon stocks (Ming et al., 2014); (Gizachew et al., 2016); (Mannan et al., 2019a). Understorey vegetation was mostly absent in the SCPF, which again substantiates the reason for higher NDVI values in the SBEF (Nizami, 2012). The other reasons for the weak association between the NDVI and the AGB could be due to the shadow since the study area is a hilly region, and the mixed spectral response (Sader et al., 1989); (Gizachew et al., 2016). The satellite data were atmospherically corrected, but shadows still may have existed affecting the NDVI values (Alam et al., 2017); (Baniya et al., 2019). Mixed spectral response in a pixel, similarly, may have been recorded due to the combined effects of soil and shadow etc. (Alam et al., 2017); (Wani et al., 2015).

The EVI is considered an improved version of NDVI and was developed to optimize vegetation signals for improving sensitivity in high biomass regions and for improved vegetation monitoring by de-coupling of canopy background signals and attenuation of atmospheric effects (Huete et al., 2002); (Halos and Abed, 2019). The values for EVI also range from -1 to 1 (Halos and Abed, 2019); (Fraga et al., 2014); (Malhi et al., 2020). The EVI from this study ranged from -0.11 to 0.89 with a mean of 0.45 ± 0.16 (Fig. 34). The EVI (per plot) for SCPF ranged from 0.24-0.59 with a mean (per plot) of 0.41 ± 0.08 and the EVI (per plot) for SBEF ranged from 0.33-0.68 with a mean (per plot) of 0.55 ± 0.08. This study has shown a weak statistical association between the two variables, EVI and AGB, for both the forests (Fig. 36; Fig. 37).

Similar results were also shown by the following researchers: (Anaya et al., 2009); (Askar et al., 2018); (Khan et al., 2020); (Nugroho, 2006). Various other researchers, however, have recorded a significant association between the two (Pandapotan et al., 2016); (Nguyen and Kappas, 2020); (Pandey et al., 2019a). The EVI is more sensitive to topographic variations compared to NDVI, which could be one of the reasons for the weak association between the EVI and AGB (Matsushita et al., 2007); (Askar et al., 2018); (Matsushita et al., 2007); (Garroutte et al., 2016). The second reason could be related to the canopy structure, as EVI is also known to be sensitive to the canopy structures (Gao et al., 2000); (Huete et al., 2002).

5.1.9. C-Band SAR S1 Data and AGB:

The C-band SAR data for this study showed a weak association with the AGB of both the forests (Fig. 38; Fig. 39; Fig. 40; Fig. 41). The result is in agreement with the following researchers; (Debastiani et al., 2019); (Lucas et al., 2006); (Periasamy, 2018); (Huang et al.,2018); (Kellndorfer et al., 2003); (Nuthammachot et al., 2020); (Kumar et al., 2019). Few researchers have also reported a strong association between the AGB and C band SAR data (Castillo et al., 2017); (Kumar et al., 2012); (Sarker et al., 2013). The backscatter approach based on SAR data has been widely used for AGB mapping (Berninger et al., 2018), and SAR sensors have been utilized in this context of AGB and AGC estimation for over three decades (Thumaty et al., 2016); (Cougo et al., 2015); (Nuthammachot et al., 2020). The backscatter is the energy received by the sensor after the transmission which is subsequently related to the AGB measurements recorded during the field inventories (Debastiani et al., 2019). The backscattering coefficient, similarly, is the function of various systems and target parameters (Ackermann, 2015). Microwave remote sensing uses radar signals of various wavelengths (1mm – 1m) for illuminating the area of interest and measures the backscattering from the same targets (Periasamy, 2018). The C-band (3.8-7.5 cm wavelength) is sensitive to leaves and smaller branches of tree crowns (Dobson et al., 1992). The C-band signals can penetrate 1-2 m deep into the canopy (Solberg et al., 2010); (Nizalapur et al., 2010). Unlike the shorter wavelengths such as C-band and X-band (2.4-3.8 cm wavelength), the L-band (15-30 cm wavelength) and P-band (30-100 cm wavelength) penetrate deeper into the canopy and are

sensitive to bigger branches and stems, which store highest of the biomass (Rodríguez-Veiga et al., 2017); (Yu and Saatchi, 2016); (Hamdan et al., 2011). Fig. 69 shows how trees are seen by the longer wavelength microwave SAR sensors. The C-band saturates at a biomass level of 20 Mg ha^{-1} (Solberg et al., 2010); (Imhoff, 1995); (Santos et al., 2003). It is therefore favored for low biomass areas such as regeneration sites (Sinha et al., 2015); (Ghasemi et al., 2011). The L-band saturates, for biomass, between 150-200 Mg ha^{-1} (Wagner et al., 2003); (Mitchard et al., 2009). And, the P-band saturates at around 300 Mg ha^{-1} (Saatchi et al., 2011); (Le Toan et al., 2011); (Sandberg et al., 2011); (Hoekman and Quiñones, 2000); (Papathanassiou and Cloude, 2001). The working, however, with the longer wavelength SAR data is not always feasible due to higher costs and lesser availability of operational satellites (Ghosh and Behera, 2018). There is also no P-band SAR satellite currently available either (Huang et al., 2018).
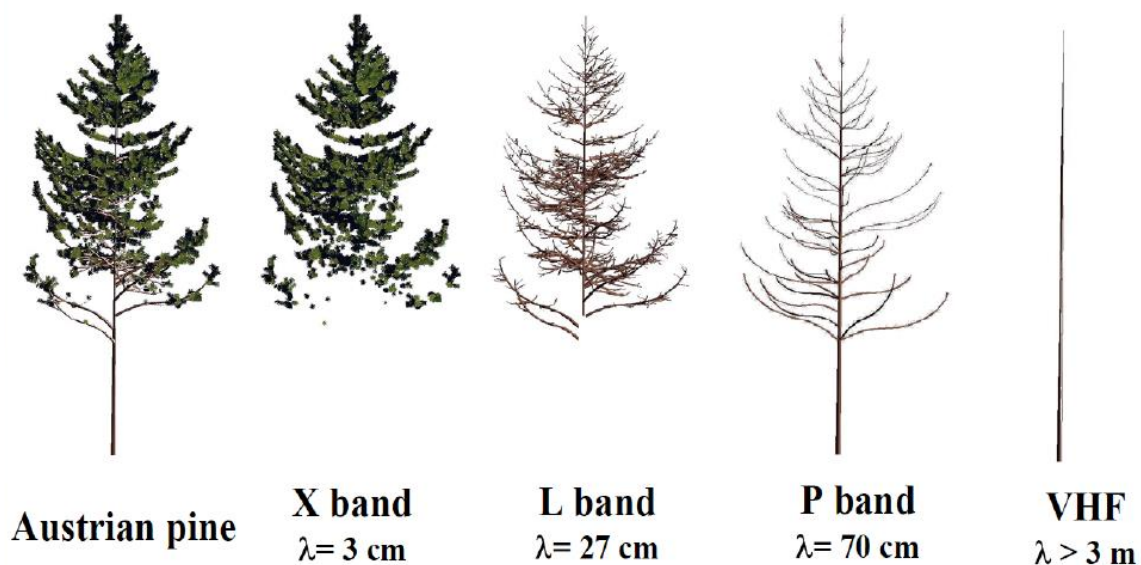
Fig. 69: Trees as seen by the longer wavelength microwave bands (Walker, 2000)

The BIOMASS mission, which is the seventh Earth Explorer mission by ESA, will be launched in 2023 (Gelas et al., 2021). This will be the first P-band space-borne mission aiming at AGB mapping (Quegan et al., 2019). Similarly, NASA -Indian Space Research Organization (ISRO) Synthetic Aperture Radar (NISAR) is a joint

mission planned for launch in 2022 which will also become the world's first SAR satellite operating in dual wavelengths of L-band and S-band (7.5-15 cm wavelength) (Silva et al., 2021); (Ghosh and Behera, 2018). The datasets from the NISAR satellite will also be freely available (Debastiani et al., 2019). The C-band SAR data by the ESA S1 mission is however freely available (Ghosh and Behera, 2018); (Huang et al., 2018). This can, nonetheless, serve as an opportunity for developing countries, where the requisite funding for satellite imageries is lacking, to regularly monitor their forest biomass potentials (Ghosh and Behera, 2018); (Castillo et al., 2017). In this study, therefore, the penetration level and saturation could be the reasons for the weak association between the C-band SAR data and the AGB of both the forests (Debastiani et al., 2019); (Imhoff, 1995); (Periasamy, 2018); (Huang et al., 2018); (Nuthammachot et al., 2020).

5.1.10. Machine Learning Algorithms for AGB:

The RF algorithm in this study performed better than the SVM and SR in estimating the AGB of the SCPF (Table 15). Debastiani et al. (2019) reported that the RF algorithm performed better compared to other algorithms, using S1, S2, and LiDAR data, in predicting the AGB in Brazilian tropical forests. Ghosh and Behera (2018) reported the better performance of the RF algorithm over the Stochastic Gradient Boosting (SGB) algorithm in predicting the AGB, by combining S1 and S2 datasets, for Katerniaghat Wildlife Sanctuary, India. Pandit et al. (2018) have reported that the RF algorithm performed better than the MLR model, using S2 data, in predicting AGB for the Parsa National Park, Nepal. Similarly, various researchers:(Dang et al., 2019);(Wu et al., 2016b); (Li et al., 2020); (Liu et al., 2019); (Pham and Brabyn, 2017) have also demonstrated better performance of RF algorithm in predicting the AGB using remote sensing data. Machine learning algorithms can help in establishing a complex non-linear relationship that exists between the predictor and outcome variables (Ghosh and Behera, 2018). The RF algorithm is not affected by dimensionality and therefore can handle a large set of variables which is why, in some instances, it performs better than the other algorithms (Biau, 2012); (Scornet et al., 2015). RF algorithm also offers other advantages such as high accuracy, high-speed computation, robustness, and its capacity for predicting important variables

(Belgiu and Drăguţ, 2016); (Cutler et al., 2007). As already mentioned, it also handles the non-linearity in a model effectively (Pandit et al., 2018).

The predictor set 'S1 and VIs' for the RF algorithm recorded the best RMSE of 52.46 Mg ha^{-1} and R^2 of 0.31 (Table 15). This predictor set at the onset had 20 variables but was left with six top predictor variables i.e. S1_VV_sd, S1_VV_min, S1_VH_avg, S1_VH_sd, S1_VV_avg, S1_VV_max, which provided the best result (Fig. 43). These top six variables mainly included the VV and VH polarizations of the C-band SAR data. The backscatter coefficients at these two polarizations have been therefore the most important variables in predicting AGB. The combination of predictor variables could yield better predictive results for AGB estimation (Ghosh and Behera, 2018). Similar results have also been reported by: (Pham et al., 2017); (Shao and Zhang, 2016); (Castillo et al., 2017); (Navarro et al., 2019); (Cougo et al., 2015); (Sivasankar et al., 2018). The two highest moderate correlations with the AGB for SCPF, using Spearman correlation coefficient, also included VV and VH polarizations; S1_VH_sd (r_s: 0.4; $p < 0.05$), S1_VV_sd (r_s: 0.38; $p < 0.05$) (Fig. 42).

The AGB map predicted by the RF algorithm for the SCPF ranged from 94.55 Mg ha^{-1} to 283.77 Mg ha^{-1}, with a mean of 163.57 ± 49.18 Mg ha^{-1} (Fig. 44). The AGB recorded at field plots, on the other hand, ranged between 83.91 Mg ha^{-1} and 378.03 Mg ha^{-1} with a mean of 146.73 ± 65.11 Mg ha^{-1}. The predicted AGB was higher at the lower end and lower on the higher end of the AGB recorded from the field. The mean of the predicted AGB was also higher than the mean of the AGB recorded at the field. Overall, a significant statistical association ($R^2 = 0.89$) was recorded between the observed AGB at the field plots and the estimated AGB from the RF algorithm (Fig. 45). According to the AGB map for SCPF, the highest AGB has displayed away from the human settlements mainly and the lower AGB is generally located near the settlements, which can also be corroborated by the field inventorying exercise. The higher AGB may therefore be attributed here to the lower disturbances due to the distant settlements (Caviglia-Harris and Harris, 2011); (Farias et al., 2018). The predicted AGB raster of the SCPF was clipped to the extent of the SCPF, obtained as an LC class, from the LC classification of the MHNP using Landsat 8 OLI image and RF algorithm. The LC classification of the Landsat 8 OLI

image, for the year 2019, recorded an overall accuracy of 97.09% (Table 18), which also validates the spatial distribution of the AGB of the SCPF in MHNP.

The SVM for the SBEF performed better than the RF algorithm and the SR (Table 16). Chen et al. (2018) reported the better performance of SVM over other algorithms such as RF and Artificial Neural Network (ANN), using S1 and S2 satellite data, for estimating AGB for the Jilin Province of North East China. Sivasankar et al. (2018) also demonstrated the better performance of SVM over linear regression analysis, using S1 and L-band ALOS-2/Phased-Array L-band Synthetic Aperture Radar – 2 (PALSAR-2), for Nongkhyllem Wildlife Sanctuary and Reserve Forest in Meghalaya State, India. Various researchers: (Navarro et al., 2019); (Pham et al., 2018); (Gleason and Im, 2012); (Wu et al., 2016a), similarly, also demonstrated better performance of SVM, using remote sensing data, for the estimation of AGB. The SVM is a popular machine learning algorithm because of its stability, easy tuning, and modeling precision (Deb et al., 2020); (Drake et al., 2006); (Adam et al., 2014). It is well known for outperforming various machine learning algorithms in estimating AGB (Jachowski et al., 2013). It also performs better with smaller datasets, which could be the reason why it was better in the case of SBEF (Wu et al., 2016a); (Diao et al., 2012); (Pal and Mather, 2005).

The predictor set 'S1 and S2 Texture' recorded the best RMSE of 32.59 Mg ha^{-1}and the R^2 of 0.21. The nine best variables out of the total 25 variables from this predictor set provided the most optimal RMSE result. These nine best variables were i.e., S1_VH, S1_VH_sd, S2_con_max, S2_con_sd, S2_con_avg, S2_ent_sd, S2_ent, S2_con, S2_asm_sd (Fig. 47). Image texture is considered as an important property that can assist in identifying spectrally different objects (Haralick et al., 1973). It is also an important source of information that shows potential for the identification of forest structural characteristics and AGB estimation (Champion et al., 2008); (Pandit et al., 2020). (Wang et al., 2014); (Pandit et al., 2020). Khan et al. (2020) also demonstrated that the inclusion of texture metrices improved the model accuracy for AGB estimation. Various other researchers: (Eckert, 2012); (Reddy et al., 2017); (Sarker and Nichol, 2011); (Schumacher et al., 2016); (Sibanda et al., 2017) have also used texture metrices for AGB estimation. Texture metrices perform better

146

under high local variance, which could also be the reason why they performed better in the SBEF because it consists of mixed broadleaved trees species (Pandit et al., 2020); (Woodcock and Strahler, 1987); (Ghosh and Behera, 2018). The texture metrices derived from S2 i.e., S2_ent_max (r_s: 0.49; $p< 0.05$), S2_con_sd (r_s: 0.42; $p< 0.05$), S2_con_max (r_s: 0.4; $p< 0.05$), S2_con_avg (r_s: 0.4; $p< 0.05$), also formed the highest moderate positive correlation, using Spearman correlation coefficient, with the AGB of the SBEF (Fig. 46). VH polarization of the C-band SAR data have been shown to be more efficient than the VV polarization for AGB estimation because it is less influenced by the soil moisture (Navarro et al., 2019); (Huang et al., 2018). This may be one of the reasons why VV polarization may not have played a significant role in AGB estimation in the case of SBEF. The higher backscatter from the VH polarization is also produced from the volume scattering coming from the tree crown, which could also be another reason for the VH being one of the important variables, for SBEF, in this study (Nuthammachot et al., 2020); (Laurin et al., 2018). The VV on the other hand is influenced more by the surface (Laurin et al., 2018). The result, regarding the VH being one of the most important variables in AGB estimation, is also consistent with (Castillo et al., 2017); (Navarro et al., 2019); (Cougo et al., 2015). SAR backscatter from the forest vegetation generally depends on the water content, size, density, and orientation of the leaves (Ghosh and Behera, 2018); (Castel et al., 2002).

The AGB estimated for SBEF using the final SVM algorithm ranged between 9.67 Mg ha^{-1} and 30.92 Mg ha^{-1} with the mean of 20.40 ± 3.70 Mg ha^{-1} (Fig. 48). The AGB recorded at the field plots ranged between 8.57 Mg ha^{-1} and 295.37 Mg ha^{-1} with the mean of 33.77 ± 51.63 Mg ha^{-1}. There was a slight difference at the lower end but a significant difference at the higher end between the two AGB estimates. The SBEF recorded mainly lower AGB compared to the SCPF. The highest AGB of 295.37 Mg ha^{-1} recorded for SBEF was only for one plot which included the *Eucalyptus camaldulensis*. The *Eucalyptus camaldulensis*is is known for its fast growth rate which results in higher AGB rates (Sheikh, 1993); (Smith et al., 2017). This significant difference could be the reason that the predicted AGB by the SVM final model recorded a moderate association ($R^2 = 0.4$) with the observed AGB (Fig. 49). The RF final model on the other hand recorded a significant association of ($R^2 =$

0.85) but the RMSE recorded by the RF, for the predictor set 'S1 and S2 texture', was 36.61 Mg ha^{-1}which was not better than the RMSE of SVM which was 32.59 Mg ha^{-1}. The sample size in this case may have played a role, since RF algorithm does not perform better in case of lower sample size (Fassnacht et al., 2014); (Latifi et al., 2012). The predicted AGB raster of the SBEF was clipped to the extent of the SBEF, obtained as an LC class, from the LC classification of MHNP using Landsat 8 OLI image and RF algorithm. As also mentioned earlier, the LC classification of the Landsat 8 OLI image, for the year 2019, recorded an overall accuracy of 97.09% (Table 18), which validates the spatial distribution of the AGB of the SBEF in MHNP.

5.2. LC Classification and LCCD of MHNP for the time-period between 1999 and 2019

5.2.1. RF for LC Classification:

The RF algorithm, used for the classification of remote sensing images, requires an optimal selection of *mtry* because it can affect the strength and correlation amongst the decision trees (Ming et al., 2016). Selection of all the variables at a split, in the case of *mtry*, can lead to the overfitting of the RF model, thus a portion of variables is selected instead of all the variables (Breiman, 2001b). A large *mtry* increases the interdependency of trees and may compromise the stability of the RF model (Zhang and Yang, 2020). A small *mtry*, however, may increase the biasness in the ranking of the variables (Strobl et al., 2008). The *ntree* on the other hand determines the votes as well as the accuracy. The increase in *ntree* converges the generalization error, thereby avoiding the overfitting of the RF model (Breiman, 1996). However, various studies have demonstrated that the addition of more trees does not improve the classification accuracy and also tends to increase the computational processing time required for running the RF algorithm (Menze et al., 2011); (Kühnlein et al., 2014). RF algorithm was used for LC classification for this study. The use of RF for land cover classification has also been demonstrated by various researchers with high accuracies. For instance, Talukdar et al. (2020a) reported high accuracy for RF (Kappa coefficient 0.89) compared to the SVM, ANN, Mahalanobis Distance(MD), Fuzzy Adaptive Resonance Theory-Supervised Predictive Mapping (Fuzzy

ARTMAP) and SAM using Landsat 8 OLI satellite data for the riparian landscape of the river Ganga from Rajmahal to Farakka barrage research site in India. Adam et al. (2014) reported a high accuracy for RF (Kappa coefficient 0.92) compared to the SVM using RapidEye image for the eastern coast of KwaZulu-Natal, South Africa. Pal (2005) reported that RF had slightly high accuracy (Kappa coefficient 0.86) than the SVM using Landsat 7 ETM+ for a study area near Littleport, Cambridgeshire, UK. Zhang et al. (2017) reported high accuracy for RF (Kappa coefficient 0.85) using Landsat 5 TM for the Wuhan urban agglomeration (WUA), located in the eastern portion of Hubei Province, China. Maxwell et al. (2018) have also reported high accuracies for RF classifier used for LC classifications.

5.2.2. Spectral Reflection:

The SBEF and SCPF showed the highest mean spectral reflection for band 4 (NIR) for Landsat 5 TM and Landsat 7 ETM+ images and band 5 (NIR) for Landsat 8 OLI image used in this research (Fig. 59; Fig. 60; Fig. 61), which is typical for the vegetation due to the internal structure of the leaves (Zhang and Zhu, 2011). The decrease, however, was noticed for the corresponding bands of SWIR1 (band 5 for Landsat 5 TM and Landsat 7 ETM+; band 6 for Landsat 8 OLI) and SWIR2 (band 7 for all three Landsat images i.e. Landsat 5 TM, Landsat 7 ETM+, Landsat 8 OLI), which may be due to the vibrational absorptions by the water content and other leaf components such as lignin and cellulose (Herold et al., 2004). The lowest mean spectral values for band 2 (Blue) and band 4 (Red) of the Landsat 8 OLI image of this study, for SBEF and SCPF, also corresponds with the results of Alba et al. (2017) and López-Serrano et al. (2016). The lower values can be associated with the absorption of electromagnetic radiation for photosynthesis by the vegetation (Feilhauer et al., 2015). The water body has also shown a typical highest mean spectral reflection for band 1 (Blue) for Landsat 5 TM and Landsat 7 ETM+ images and band 2 (Blue) for Landsat 8 OLI image and the lowest mean spectral reflectance for band 5 (SWIR 1) and band 7 (SWIR 2) for Landsat 5 TM and Landsat 7 ETM+ images and band 6 (SWIR 1) and band 7 (SWIR 2) for Landsat 8 OLI image (Zhang and Zhu, 2011). The settlements have shown the two highest mean spectral reflections for the band 4 (NIR) and band 5 (SWIR 1) for Landsat 5 TM and Landsat

7 ETM+ images and band 5 (NIR) and band 6 (SWIR 1) for Landsat 8 OLI image. Stathakis and Faraslis (2014) have stated that the spectral behavior for the settlements can be extracted from NIR and SWIR ranges. Iqbal et al. (2013) have also stated that the spectral curve for the settlements or man-built materials gradually increases from the visible to the NIR range, which was also the pattern in this study. The agricultural lands show high reflectivity in the NIR region and higher absorption in blue and red bands regions (Ayala-Silva and Beyl, 2005). This corresponds to the highest mean spectral values for agricultural land for band 4 (NIR) for Landsat 5 TM image and band 5 (NIR) for Landsat 8 OLI image in this study. Band 5 (SWIR 1) showed the highest mean spectral reflection for agricultural land in the case of the Landsat 7 ETM+ image in this study. The SWIR bands are known for showing specific reflections from vegetation and soil moisture contents (Swathandran and Aslam, 2019). Similarly, SWIR 1 had the highest mean spectral reflections in the case of bare lands as well, which is again due to the characteristic of SWIR bands to discriminate soil from vegetation (Kartika et al., 2019). Nguyen et al. (2021) have also recommended the use of modified bare soil index containing SWIR and NIR wavelengths derived from Landsat 8 OLI for bare soil detection, which emphasizes the importance of SWIR in the case of bare lands. The grasslands in this study have also shown the highest mean spectral reflection by NIR bands which again highlights the influence and presence of vegetation affecting these reflections.

5.2.3. Importance of Variables:

Although, only ranking of the variables was performed here and not the feature selection, otherwise Immitzer et al. (2012) demonstrated that the MDA criterion is very efficient for the feature selection, which is also supported by Nicodemus and Malley (2009) and Nicodemus (2011). Feature selection is mostly required for reducing the set of a large number of variables to an optimal size for enhancing the accuracies of the machine learning algorithms and optimizing the computational time required by the algorithms (Kursa and Rudnicki, 2010). The green band was noticed to be the lowest of all the variables on two occasions and the second lowest on one occasion in ranking concerning the MDA, which could be attributed to the similar

green color portrayed by the vegetation for different land cover classes i.e. SBEF, SCPF and grassland (Feng et al., 2015). The NIR (B4 - Landsat 7 ETM+ 1999)and SWIR 1 (B5 - Landsat 5 TM 2009; B6 - Landsat 8 OLI 2019) were highly ranked features in this study using MDA which is also consistent with the findings of Zhang and Yang (2020). This indicates that these two bands provide more useful information for the classification than the visible bands used in this study (Li and Chen, 2005). As already mentioned, SWIR bands are also sensitive to leaf and surface moisture contents, which assists the classification between land covers with high moisture differences (Ge et al., 2020).

5.2.4. LCC Pattern:

The highest increase was recorded for agricultural land which increased 76.49% from 1999 to 2009, 30.66% from 2009 to 2019, and an overall increase of 130.62% from 1999 to 2019 (Table 22). The ROC for agricultural land, for the period 1999-2019, was recorded in the form of an increase of 35.03 ha/year.

Results of this study are in agreement with Mannan et al. (2018) who have reported the highest increases in agricultural land for all three time periods i.e., 1990-2000, 2000-2010, and 2010-2017 for MHNP. They have reported, for agricultural land, an increase of 9.21% for 1990-2000, a 21.22% increase for 2000-2010, and a 15.69% increase for 2010-2017. They used Landsat 8 OIL, Landsat 5 TM, and Landsat 7 ETM images for classification and change detection. Their kappa coefficient, using MLC, were 0.90, 0.91, 0.87, and 0.91 for the years 1990, 2000, 2010, and 2017 respectively, which are close to the kappa coefficients estimated for this study. Mannan et al. (2018) have attributed this increase in agricultural land to the increasing population in the MHNP and its surroundings, especially the adjoining Islamabad city. Khalid et al. (2019) have reported one of the highest increases for the agricultural land in the MHNP with a 9% increase from 1992-2000 and a 4% increase from 2000-2011. They used Landsat 5 TM images for their study and recorded an overall accuracy, using a hybrid maximum likelihood approach, of 99.17% for the LC classification of 1992, 98.33% for the LC classification of 2000, and 98.33% for the LC classification of 2011, which are slightly higher than the

results for this study. Kappa coefficients were reported as 0.9843, 0.9627, and 0.9679 for the years 1992, 2000, and 2011 respectively, which are close to the results of this study. They have attributed this increase in agricultural lands to the increase in road networks and population. According to Ayaz (2005), 60% of the population of the MHNP depends on agriculture for subsistence. Khalid et al. (2015) reported the highest increasing trends for agricultural land for the MHNP with 9% for 1992-2000 and 4% for 2000-2011. They used Landsat 5 TM images with hybrid classification for their LC classification. They also attributed this increasing trend to the development of roads and population growth. For instance, there were 10 villages in the park in 1990, which have increased to 20 villages in 2017 (Khalid et al., 2015).

Mannan et al. (2019a) have found the highest increases to occur in agricultural lands in the foothills of the Himalayan mountains, of which the MHNP is also a part. They reported a 68.05% increase in agricultural lands from 2008-2018. They used Landsat 8 OLI and Landsat 5 images for the LC classification and reported kappa coefficients of 0.83, 0.82, and 0.84 for their classifications, using MLC, for the years 1998, 2008, and 2018, respectively. Their user's accuracies and producer's accuracies for agricultural land were recorded as 72.73% and 96% respectively for the years 1998 and 2008, 72.73% and 85.71% for the year 2018. The results for the user's accuracies and producer's accuracies are not in agreement with this research. Similarly, the kappa coefficients are also not in agreement, since the kappa coefficients for this study are 0.93, 0.96, and 0.96 for the years 1999, 2009, and 2019 respectively. Mannan et al. (2019a) have attributed the increase to the population expansion of Islamabad city.

Islamabad is the capital city of Pakistan and is adjoined by the MHNP. The population of the city had grown rapidly from 169,000 in 1979 to 1,095,000 in 2019 (Shah et al., 2021). This growth had resulted in the expansion of the city from 97.7 km^2 in 1979 to 474.8 km^2 in 2019 (Shah et al., 2021). The expansion has opened various opportunities such as increasing road networks for providing easy access for the farmers to the desirable markets thus encouraging them to practice agriculture (Khalid et al., 2015). This study has shown a decrease in settlements, however,

which is contrary to various studies: Zafar (2020); (Iqbal et al. 2013); (Khalid et al., 2019). The highest conversion for settlements, in this study, was to grasslands and bare lands (Table 23; Table 24; Table 25). The contrary results for this study for settlements could therefore be attributed to the similarity of spectral signatures between the three classes i.e., settlements, grasslands, and bare lands.

The SCPF had the highest decrease, amongst all the LC classes, of 14.99% for the period 2009-2019 in this study (Table 22). Khalid et al. (2019) reported a 53% decrease in SCPF in MHNP, the highest amongst other LC classes, for the period 1992-2000. They, however, reported a 27% increase in SCPF for the period 2000-2011. They have attributed the decrease to soaring temperatures, prolonged droughts, forest fires, overgrazing, fuelwood extraction by local communities, conversion to agricultural lands, and limestone extraction for cement industries. The improvement was attributed to the ban on cutting *Pinus roxburghii* for fuelwood and timber purposes and the plantation campaign of the *Pinus roxburghii* was also cited as a reason for the improvement in the forest. In this study, the highest conversion of SCPF was to the SBEF and the grassland, from 2009-2019 (Table 23), which could also be due to the abovementioned reasons cited by Khalid et al. (2019) that may have led to this conversion (Sudhakar Reddy et al., 2018); (Shafiq et al., 1997). The prolonged drought followed by continuous soaring temperatures of 45 °C results in wild and anthropogenic fires, which subsequently contribute to the deforestation and degradation of the SCPF (Khalid et al., 2015). The forest is already under threat due to climate change, which is expected to aggravate further in the future (Khalid et al., 2019). Similarly, Khalid et al. (2015) reported 320 forest fires from 2002 to 2012, which have affected approximately 8 km^2 of the area in the MHNP. These fires mostly affect the SCPF more than the SBEF in the MHNP (Mannan et al., 2018). Forest fires can also lead to the conversion of coniferous forests to broadleaved forests, shrublands, and grasslands, which may require decades to revert to their original environment (Li et al., 2021). According to Berenguer et al. (2014), the forest sites which were encountered by the forest fires, combined with the logging, revealed the reduction of 40% of carbon stocks compared to the undisturbed sites in the Amazon. According to Khalid et al. (2015), the MHNP faces the threat of overgrazing from 12,000 to 13,000 livestock. Similarly, there are over 700 stone

quarries found around the MHNP, which are involved in limestone extraction (Mannan et al., 2018). Margalla Hills have high-quality Limestone, including sandstone and shale, which is used for infrastructural development purposes (Nawaz and Fayaz, 2004). Iqbal et al. (2013) have reported an increase in limestone extraction area in MHNP from 0.35% to 5.72% from 1992 to 2009 respectively. Overgrazing can influence vegetation and soil carbon negatively and can transform the carbon sink into a considerable source (Liu et al., 2021). There is also a high dependency of local communities on fuelwood. Saleem et al. (2014), for instance, have reported that 75% of the population of Saidpur Village of MHNP depend on fuelwood.

In this study, the SBEF had the second highest decrease for the period 1999-2009, amongst all the LC classes, which was 1.94% (Table 22). The grassland was one of the highest conversions for the SBEF for the period 1999-2009 (Table 23). The results are in agreement with Saeed et al. (2011) who reported a decrease in SBEF and its conversion to the grassland for the Rawal watershed area in the Pothwar region of Pakistan. They have attributed this to the undue pressure on the forests, by the local communities, for the firewood due to the unavailability of alternate energy resources. Khalid et al. (2019) also reported a change in SBEF of -6% for the period 2000-2011 for the MHNP. They attributed this change to an increase in settlements, population expansion, conversion to agricultural fields, and illegal logging.

The grassland, in this study, has shown a decreasing trend. Zafar (2020) reported a decrease of 1.8% from 1997 to 2003 and 2.9% from 2003 to 2008 for the grassland in the MHNP. They have attributed this decrease to the construction of road networks and an increase in anthropogenic activities. Khalid et al. (2019) have reported a decrease of 22% from 1992 to 2000 and 6% from 2000 to 2011 in the grassland of MHNP. They have attributed this reduction to overgrazing, an increase in settlements, and forest fires. Grasslands are high biodiverse areas, spreading approximately over 20-30% of the world's surface, and are often understudied and least protected (Wilsey, 2021). In this study, the highest conversion of grassland was to SBEF and agricultural land for the overall period from 1999 to 2019. The

availability of favorable conditions such as water may have encouraged the conversion of grassland to SBEF (Sheikh, 1993).

The water body had shown fluctuations in this study where it increased for the first decade 1999-2009 by 25.21% but decreased in the second decade from 2009-2019 by 3.60% (Table 22). Similar fluctuations were also highlighted by Zafar (2020) who reported a decrease of 0.7% in the water body of the MHNP for the period 1997-2003 and an increase of 1.08% for the period 2003-2008. They have attributed this change to seasonal variations. On the contrary, Khalid et al. (2019), have reported a continuous decrease of 46% and 1.5% of the water body of MHNP for the periods of 1992-2000 and 2000-2011, respectively. They have attributed this change to deforestation, population expansion, and infrastructure development, which have severely affected ground infiltration capacities. Hassan et al. (2016) reported an increase of 11.5% in the water body of the Islamabad region, including the MHNP, from 1992 to 2012. They have attributed this increase to the monsoon's rainfall. Similarly, Iqbal et al. (2013) also reported fluctuating trends in the water body in MHNP and attributed the increase to the rainfall before the satellite data was obtained and the decrease to the overconsumption of the water. In the case of barren land, a similar fluctuating trend recorded in this study was also reported by Khalid et al. (2015) for MHNP. They attributed the decrease in barren lands to the increasing settlements.

Mannan et al. (2019a) have predicted an increase in agricultural lands and settlements for the years 2018 to 2028 in the region of the Himalayan foothills, which will put undue pressure on the forests of the region resulting in their decline. Similarly, Wang et al. (2020) have predicted a decrease in forests of Kathmandu, Nepal, by 14.43% due to an increase in urbanization and population expansion for the year 2030. Christensen and Jokar Arsanjani (2020) have predicted a decrease of 4.21%, by 2030, in the forest area of Virunga National Park, Democratic Republic of Congo, due to the urbanization and agricultural fields. Another study by Tadese et al. (2021) has predicted a decline of 77.8% in forests of Majang Forest Biosphere Reserve, Ethiopia, for the period 2032-2047, due to settlement and agricultural expansion. The population expansion, thus, poses a grave threat to the future of the

forest ecosystems too, as clearly highlighted by the abovementioned studies. It is, therefore, essential to formulate suitable strategies for safeguarding forests and tackling the challenges arising from the increasing population.

6. Conclusion:

6.1. Forest Biomass and Carbon Stock Assessment of MHNP.

In this study, it was found that SCPF had a higher mean AGB and mean AGC compared to the SBEF. The SCPF recorded mean AGB and mean AGC as 146.73 ± 65.11 Mg ha^{-1} and 73.36 ± 32.55 Mg C ha^{-1}, respectively. The mean AGB and mean AGC for the SBEF were 33.77 ± 51.63 Mg ha^{-1} and 16.88 ± 25.81 Mg C ha^{-1}, respectively. There were significant statistical differences recorded between the mean AGB ($W = 43, p < 0.05$) and mean AGC ($W = 43, p < 0.05$) of the two forests. The higher mean AGB and mean AGC of the SCPF in comparison to the SBEF can be attributed to the larger sizes of the trees in the former in the form of higher DBHs and heights. The difference may also be attributed to the species composition. *Pinus roxburghii* recorded higher AGC compared to other trees species in the SCPF. It recorded a total AGC of 3336.13 Mg C ha^{-1}, forming 98.85% of the total AGC of the SCPF. *Eucalyptus camaldulensis* recorded the highest AGC, amongst all the trees species, for the SBEF with 176.14 Mg C ha^{-1}, which was 33.65% of the total AGC. The unimodal DBH distribution of the two forests suggests they are experiencing deforestation and degradation. Further comparison with other similar forest types and protected areas, also hinted towards the lower AGB and AGC. The lower AGB and AGC in a forest ecosystem are mainly associated with human or natural disturbances (Lugo and Brown, 1992). Similarly, lower deforestation and forest degradation rates are generally encountered in protected areas, affecting forest biomass and carbon stocks, in comparison to the areas lying outside the protected areas (Leverington et al., 2010); (Nagendra, 2008). Adequate forest management, therefore, is necessary for conserving and enhancing not only the AGB and AGC but also for safeguarding the associated biodiversity and the local communities which depend upon the forestry resources for their sustenance (Feldpausch et al., 2005).

The NDVI and EVI for the Margalla Hills National Park were recorded as -0.34-0.80 and -0.11-0.89, respectively. The linear regression analysis between the AGB and the NDVI for the SCPF and SBEF showed weak statistical associations. Weak

statistical associations were also recorded for the EVI and AGB of the two forests. A similar pattern was also noticed with the linear regression analysis of the AGB with the VH and VV Polarizations obtained from the SCPF and SBEF, using C-band SAR data.

The best model was RF, for the SCPF, which was eventually used for the AGB mapping. And the best model for the SBEF was SVM. SR did not perform well in the case of both forests. The predictor set 'S1 and VIs' with six variables performed the best for the RF algorithm. The predictor set 'S1 and S2 Texture' finally with nine variables performed the best for the SVM algorithm. The AGB map for SCPF had the predicted AGB values ranging from 94.55 Mg ha^{-1} to 283.77 Mg ha^{-1}. Significant statistical association (R^2 = 0.89) was recorded between the predicted and observed AGB of the SCPF. The predicted AGB map for the SBEF ranged between 9.67 Mg ha^{-1} and 30.92 Mg ha^{-1}. A moderate linear association (R^2 = 0.4) was recorded between the predicted and observed AGB of the SBEF.

6.2. LC Classification and LCCD of MHNP for the time-period between 1999-2019.

The SBEF formed the highest LC, amongst all other LC classes, for the MHNP with 40.90%in 1999, 40.11% in 2009, and 43.21% in 2019. RF algorithm used for the LC classification produced an overall accuracy of 94.83%, 96.77%, and 97.09% for the years 1999, 2009, and 2019, respectively. Kappa coefficients were recorded as 0.93, 0.96, and 0.96 for the years 1999, 2009, and 2019, respectively. The highest decrease for the time-period 2009-2019 was recorded for the SCPF with 14.99%. The highest increase for the overall period 1999-2019 was recorded for the agricultural land with 130.62%.

Overall, it was found in this study that the mean AGB and AGC from the two forests of the MHNP are generally on the lower side based on the comparison with other studies. The LCCD in this study revealed a decrease of 14.99 % in the SCPF which was the highest amongst all the LC classes for the time-period 2009-2019. This, therefore, has affected the actual potential of the SCPF and which could be the

reason why the mean AGB and AGC have been on the lower side compared with other studies. The increasing areas of agricultural land recorded in this study further pose a danger to the forest ecosystems and the mean AGB and AGC of the MHNP for the future.

To the best of my knowledge, this has been the first time where AGB has been estimated using the machine learning algorithms i.e., RF and SVM, in combination with S1 and S2 data in Pakistan. The same is the case with the use of RF for the LC classification in this study, which has been again, to the best of my knowledge, the first time, it has been used in the same study area. Mostly, the MLC had been used in various studies for LC classifications for the same study area. The RF algorithm used in this study mostly showed higher overall accuracies and kappa coefficients for the LC classifications compared to other studies using MLC for the same site or the nearby regions. MLC delivers excellent results when using unimodal data but shows limitations against the multi-modal data because of assuming that the data have normal distributions (Liu et al., 2011). RF on the other hand does not have to assume that the distribution of the data is normal (Belgiu and Drăguţ, 2016). Therefore, the RF algorithm can also be adopted for future LC classification studies in the mountainous and other forested areas of Pakistan.

7. Recommendations:

Following are the recommendations based on the findings from the research objectives/sub-objectives of this study:

➢ The IWMB should formulate sustainable management plans for the MHNP, which should cater to the adequate management of the forests in combination with safeguarding the local communities depending on these forests for their subsistence. The findings from this study in this regard should be utilized and incorporated into these plans by the IWMB.

➢ The findings should also be used by the IWMB for the formulation of REDD+ projects with the help of international nature conservation organizations such as WWF-P and IUCN and regional forest department and the Ministry of Climate Change, Pakistan, etc. These REDD+ projects would be able to draw suitable and adequate funding required for the conservation and improvement of the forestry resources of the MHNP. Local communities must also be catered for in these projects since they rely on these forests for their sustenance.

➢ MHNP should also be included in the urban planning and management of Islamabad city for countering the negative consequences, that the MHNP is facing due to the increase in population and settlements in the city. Capital Development Authority (CDA), which is responsible for the overall management of Islamabad city should be approached by the IWMB and the inclusion of the MHNP in the urban management plan should be emphasized.

➢ The use of remotely sensed satellite imagery must be integrated into the research and monitoring activities of the IWMB. The Landsat imageries, S2 and S1 are freely available resources and have demonstrated their effectiveness in AGB and AGC assessment studies and monitoring of LC areas, and in detecting the spatial and temporal changes in the various LCs.

Necessary training and capacity-building programmes should be conducted for the responsible staff by the IWMB in this regard, which would make the integration and use of the remote sensing techniques and GIS tools easier in the research and monitoring framework of the MHNP.

➢ The RF algorithm had shown good potential for producing LC classifications. It offers certain advantages such as being easy to use, producing higher accuracies, being robust to noise and outliers, providing estimates of the important variables involved in the classification, etc. The use of RF algorithm with remotely sensed data has gained popularity because of the complex nature of the data involved (Belgiu and Drăguţ, 2016). It is suggested therefore that it should be used for the LC classification exercises in the future.

➢ The RF and SVM algorithms also have improved the performances of the models used for the estimation of the AGB. These are easy-to-use machine learning algorithms and therefore it is suggested that they should also be used, in combination with the remotely sensed data and the ground forest inventories, in future studies conducted by the IWMB for research and monitoring purposes.

➢ It is imperative that environmental laws are enforced in the MHNP, and stringent measures are adopted in this regard. The activities such as the construction of commercial properties and road expansion etc. must be prevented since MHNP is a national park and its essence and integrity, therefore, needs to be maintained.

➢ Afforestation programmes should be initiated to deal with the imbalances in the structures of the two forest types, which are noticed in this study. These afforestation programmes could also be based on the Assisted Natural Regeneration (ANR) technique, which has been considered a very useful technique involving local communities where active planting is combined with passive forest restoration. Passive forest restoration means the removal of

barriers and disturbances from the forests for allowing the natural succession of an ecosystem to occur. Local communities therefore can play a vital role in the implementation of ANR. Overall can help in contributing toward the Paris Climate Agreement, the Trillion Trees initiative, and the Bonn Challenge - which aims to restore 350 million ha of degraded and deforested areas by 2030.

➢ Mass awareness and media campaigns should be designed, which should highlight the importance of the MHNP concerning the challenges such as climate change.

➢ Ecotourism plans should be developed for reducing pressure on the MHNP and for creating livelihood opportunities for the local communities.

➢ Overhauling and up-gradation of the fire-fighting equipment and capacity building of the relevant staff should be carried out. Adequate fire-fighting strategies should be developed for dealing with the anthropogenic and natural forest fires occurring in the MHNP.

➢ Strategies should be developed for creating alternate fuel options for the local communities, which heavily rely on the fuelwood from the forests for energy production purposes.

➢ Local communities should be involved in various MHNP conservation and improvement-related strategies and plans. They should also be included in the research and monitoring teams for creating a sense of ownership in them.

➢ The site and species-specific allometric equations should be developed for future AGB and AGC studies in the park.

➢ The SAR microwave bands, with longer wavelengths, such as P-band (30-100 cm wavelength), L-band (15-30 cm wavelength) and S-band (7.5-15 cm wavelength) should also be utilized in the future for AGB estimation. These

data will be freely available in the future with the BIOMASS and NISAR missions.

8. References:

Abdou, B., Morin, D., Bonn, F., Huete, A., 1995. A review of vegetation indices. Remote Sens. Rev. 13, 95–120. https://doi.org/10.1080/02757259509532298

Abid, M., Schilling, J., Scheffran, J., Zulfiqar, F., 2016. Climate change vulnerability, adaptation and risk perceptions at farm level in Punjab, Pakistan. Sci. Total Environ. 547, 447–460. https://doi.org/10.1016/j.scitotenv.2015.11.125

Ackermann, N., 2015. Growing Stock Volume Estimation in Temperate Forested Areas Using a Fusion Approach with SAR Satellites Imagery, Springer Theses. Springer International Publishing. https://doi.org/10.1007/978-3-319-13138-2

Adam, E., Mutanga, O., Odindi, J., Abdel-Rahman, E.M., 2014. Land-use/cover classification in a heterogeneous coastal landscape using RapidEye imagery: evaluating the performance of random forest and support vector machines classifiers. Int. J. Remote Sens. 35, 3440–3458. https://doi.org/10.1080/01431161.2014.903435

Adams, V.M., Iacona, G.D., Possingham, H.P., 2019. Weighing the benefits of expanding protected areas versus managing existing ones. Nat. Sustain. 2, 404–411. https://doi.org/10.1038/s41893-019-0275-5

Aftab, E., Hickey, G., 2010. Forest administration challenges in Pakistan: the case of the Patriata reserved forest and the new Murree development. Int. For. Rev. 12, 97–105. https://doi.org/10.1505/ifor.12.1.97

Afzal, S., Nawaz, M.F., Siddiqui, M.T., Aslam, Z., 2018. Comparative study on water use efficiency between introduced species (Eucalyptus camaldulensis) and indigenous species (Tamarix aphylla) on marginal sandy lands of Noorpur Thal. Pak. J. Agric. Sci. 55, 127–135. https://doi.org/10.21162/PAKJAS/18.6626

Agapiou, A., Hadjimitsis, D., Alexakis, D., 2012. Evaluation of Broadband and Narrowband Vegetation Indices for the Identification of Archaeological Crop Marks. Remote Sens. 4, 3892–3919. https://doi.org/10.3390/rs4123892

Ahmad, M., 2001. Agricultural Productivity Growth Differential in Punjab, Pakistan: A District-level Analysis. Pak. Dev. Rev. 40, 1–25.

Akbar, S., 2012. A sociological study exploring influence of natural flora on livelihood strategies of rural communities (A Case Study of Margalla Hills) (MS). International Islamic University, Islamabad, Pakistan.

Alam, M., Zafar, S., Muhammad, W., 2017. Assessment of sentinel-2 vegetation indices for plot level tree AGB estimation, in: 2017 Fifth International Conference on Aerospace Science & Engineering (ICASE). Presented at the 2017 Fifth International Conference on Aerospace Science & Engineering (ICASE), IEEE, Islamabad, pp. 1–5. https://doi.org/10.1109/ICASE.2017.8374278

Alba, E., Mello, E.P., Marchesan, J., Silva, E.A., Tramontina, J., Pereira, R.S., 2017. Spectral characterization of forest plantations with Landsat 8/OLI images for forest

planning and management. Pesqui. Agropecuária Bras. 52, 1072–1079. https://doi.org/10.1590/S0100-204X2017001100013

Ali, A., Ashraf, I., Gulzar, S., Akmal, M., 2020a. Development of an Allometric Model for Biomass Estimation of Pinus roxburghii, Growing in Subtropical Pine Forests of Khyber Pakhtunkhwa, Pakistan. Sarhad J. Agric. 36, 236–244. https://doi.org/10.17582/journal.sja/2020/36.1.236.244

Ali, A., Ashraf, M.I., Gulzar, S., Akmal, M., 2020b. Estimation of forest carbon stocks in temperate and subtropical mountain systems of Pakistan: implications for REDD+ and climate change mitigation. Environ. Monit. Assess. 192, 198. https://doi.org/10.1007/s10661-020-8157-x

Ali, A., Ullah, S., Bushra, S., Ahmad, N., Ali, Asad, Khan, M.A., 2018. Quantifying forest carbon stocks by integrating satellite images and forest inventory data. Austrian J. For. Sci. 93–117.

Ali, F., Khan, N., Ahmad, A., Khan, A.A., 2019. Structure and biomass carbon of Olea ferruginea forests in the foot hills of Malakand division, Hindukush range mountains of Pakistan. Acta Ecol. Sin. 39, 261–266. https://doi.org/10.1016/j.chnaes.2019.05.011

Ali, G., Mustafa, G., Shah, S.Z., 2020. Performance of Agriculture Sector in Foreign Trade of Pakistan. Glob. Econ. Rev. 5, 12–23.

Ali, J., Benjaminsen, T.A., Hammad, A.A., Dick, Ø.B., 2005. The road to deforestation: An assessment of forest loss and its causes in Basho Valley, Northern Pakistan. Glob. Environ. Change 15, 370–380. https://doi.org/10.1016/j.gloenvcha.2005.06.004

Ali, N., Hu, X., Hussain, J., 2020. The dependency of rural livelihood on forest resources in Northern Pakistan's Chaprote Valley. Glob. Ecol. Conserv. 22, e01001. https://doi.org/10.1016/j.gecco.2020.e01001

Amir, M., Liu, X., Ahmad, A., Saeed, S., Mannan, A., Muneer, M.A., 2018. Patterns of Biomass and Carbon Allocation across Chronosequence of Chir Pine (Pinus roxburghii) Forest in Pakistan: Inventory-Based Estimate. Adv. Meteorol. e3095891. https://doi.org/10.1155/2018/3095891

Anaya, J.A., Chuvieco, E., Palacios-Orueta, A., 2009. Aboveground biomass assessment in Colombia: A remote sensing approach. For. Ecol. Manag. 257, 1237–1246. https://doi.org/10.1016/j.foreco.2008.11.016

Anwar, M., Chapman, J., 2000. Feeding habits and food of grey goral in the Margalla hills national park [Pakistan]. Pak. J. Agric. Res. Pak. 16, 28–32.

Anwar, T., Ilyas, N., Qureshi, R., Rahim, B., Qureshi, H., Kousar, R., Maqsood, M., Muhammad Ismail Bhatti, Panni, M., 2019. Allelopathic potential of Pinus Roxburghii needles against selected weeds of wheat crop. Appl. Ecol. Environ. Res. 17, 1717–1739. https://doi.org/10.15666/aeer/1702_17171739

Araya, Y., Hergarten, C., 2008. A comparison of pixel and object-based land cover classification: a case study of the Asmara region, Eritrea. WIT Trans. Built Environ. 100, 233–243.

Arekhi, M., Goksel, C., Balik Sanli, F., Senel, G., 2019. Comparative Evaluation of the Spectral and Spatial Consistency of Sentinel-2 and Landsat-8 OLI Data for Igneada Longos Forest. ISPRS Int. J. Geo-Inf. 8, 56. https://doi.org/10.3390/ijgi8020056

Arif, M., Shahzad, M., Elzaki, E., Hussain, A., Zhang, B., Yukun, C., 2017. Biomass and carbon stocks estimation in Chichawatni irrigated plantation in Pakistan. Int. J. Agric. Biol. 19, 1339–1349. https://doi.org/10.17957/IJAB/15.0410

Arjasakusuma, S., Kamal, M., Hafizt, M., Forestriko, H.F., 2018. Local-scale accuracy assessment of vegetation cover change maps derived from Global Forest Change data, ClasLite, and supervised classifications: case study at part of Riau Province, Indonesia. Appl. Geomat. 10, 205–217. https://doi.org/10.1007/s12518-018-0226-2

Aryal, S., Bhuju, D., Kharal, D., Gaire, N., Dyola, N., 2018. Climatic upshot using growth pattern of Pinus roxburghii from western Nepal. Pak. J. Bot. 50, 579–588.

Ashish, B.I., Kurtadikar, M.L., 2017. Microwave Dielectric Properties and Emissivity Estimation of Freshly Cut Banana Leaves at 5 GHz. Int. J. Adv. Remote Sens. GIS 5, 58–66.

Askar, N.N., Worradorn Phairuang, P.W., Sayektiningsih, T., 2018. Estimating Aboveground Biomass on Private Forest Using Sentinel-2 Imagery. J. Sens. 2018, 1–11. https://doi.org/10.1155/2018/6745629

Asner, G.P., Brodrick, P.G., Philipson, C., Vaughn, N.R., Martin, R.E., Knapp, D.E., Heckler, J., Evans, L.J., Jucker, T., Goossens, B., Stark, D.J., Reynolds, G., Ong, R., Renneboog, N., Kugan, F., Coomes, D.A., 2018. Mapped aboveground carbon stocks to advance forest conservation and recovery in Malaysian Borneo. Biol. Conserv. 217, 289–310. https://doi.org/10.1016/j.biocon.2017.10.020

Asrat, Z., Eid, T., Gobakken, T., Negash, M., 2020. Aboveground tree biomass prediction options for the Dry Afromontane forests in south-central Ethiopia. For. Ecol. Manag. 473, 118335. https://doi.org/10.1016/j.foreco.2020.118335

Awan, A.R., Chughtai, M.I., Ashraf, M.Y., Mahmood, K., Rizwan, M., Akhtar, M., Siddiqui, M.T., Khan, R.A., 2012. Comparison for physico-mechanical properties of farm-grown Eucalyptus camaldulensis Dehn. With conventional timbers. Pak. J. Bot. 44, 2067–2070.

Axelsson, C., Skidmore, A.K., Schlerf, M., Fauzi, A., Verhoef, W., 2013. Hyperspectral analysis of mangrove foliar chemistry using PLSR and support vector regression. Int. J. Remote Sens. 34, 1724–1743. https://doi.org/10.1080/01431161.2012.725958

Ayala-Silva, T., Beyl, C.A., 2005. Changes in spectral reflectance of wheat leaves in response to specific macronutrient deficiency. Adv. Space Res., Space Life Sciences: Ground-Based Iron-Ion Biology and Physics, Including Shielding 35, 305–317. https://doi.org/10.1016/j.asr.2004.09.008

Ayarkwa, J., Owusu, F.W., Appiah, J.K., 2011. Steam bending qualities of eight timber species of ghana. Ghana J. For. 27, 11–22.

Ayaz, S., 2005. Ecological Zonation and Identification of Core Biodiversity Zones in Margalla Hills National Park (MPhil Thesis). Quad-e-Azam University, Islamabad, Pakistan.

Aziz, T., 2021. Changes in land use and ecosystem services values in Pakistan, 1950–2050. Environ. Dev. 37, 100576. https://doi.org/10.1016/j.envdev.2020.100576

Ballabha, R., Tiwari, J., Tiwari, P., 2013. Regeneration of tree species in the sub-tropical forest of Alaknanda Valley, Garhwal Himalaya, India. For. Sci. Pract. 15, 89–97. https://doi.org/10.1007/s11632-013-0205-y

Banday, M., Bhardwaj, D.R., Pala, N.A., 2018. Variation of stem density and vegetation carbon pool in subtropical forests of Northwestern Himalaya. J. Sustain. For. 37, 389–402. https://doi.org/10.1080/10549811.2017.1416641

Baniya, B., Tang, Q., Pokhrel, Y., Xu, X., 2019. Vegetation dynamics and ecosystem service values changes at national and provincial scales in Nepal from 2000 to 2017. Environ. Dev. 32, 100464. https://doi.org/10.1016/j.envdev.2019.100464

Basuki, T.M., Skidmore, A.K., Hussin, Y.A., Duren, I.V., 2013. Estimating tropical forest biomass more accurately by integrating ALOS PALSAR and Landsat-7 ETM+ data. Int. J. Remote Sens. 34, 4871–4888. https://doi.org/10.1080/01431161.2013.777486

Beamish, A., Raynolds, M.K., Epstein, H., Frost, G.V., Macander, M.J., Bergstedt, H., Bartsch, A., Kruse, S., Miles, V., Tanis, C.M., Heim, B., Fuchs, M., Chabrillat, S., Shevtsova, I., Verdonen, M., Wagner, J., 2020. Recent trends and remaining challenges for optical remote sensing of Arctic tundra vegetation: A review and outlook. Remote Sens. Environ. 246, 111872. https://doi.org/10.1016/j.rse.2020.111872

Bebber, D.P., Butt, N., Butt, N., 2017. Tropical protected areas reduced deforestation carbon emissions by one third from 2000–2012. Sci. Rep. 7, 14005. https://doi.org/10.1038/s41598-017-14467-w

Belgiu, M., Drăguţ, L., 2016. Random forest in remote sensing: A review of applications and future directions. ISPRS J. Photogramm. Remote Sens. 114, 24–31. https://doi.org/10.1016/j.isprsjprs.2016.01.011

Berenguer, E., Ferreira, J., Gardner, T.A., Aragão, L.E.O.C., Camargo, P.B.D., Cerri, C.E., Durigan, M., Oliveira, R.C.D., Vieira, I.C.G., Barlow, J., 2014. A large-scale field assessment of carbon stocks in human-modified tropical forests. Glob. Change Biol. 20, 3713–3726. https://doi.org/10.1111/gcb.12627

Berninger, A., Lohberger, S., Stängel, M., Siegert, F., 2018. SAR-Based Estimation of Above-Ground Biomass and Its Changes in Tropical Forests of Kalimantan Using L- and C-Band. Remote Sens. 10, 831. https://doi.org/10.3390/rs10060831

Bhadwal, S., Singh, R., 2002. Carbon sequestration estimates for forestry options under different land-use scenarios in India. Curr. Sci. 83, 1380–1386.

Bhardwaj, D.R., Banday, M., Pala, N.A., Rajput, B.S., 2016. Variation of biomass and carbon pool with NDVI and altitude in sub-tropical forests of northwestern Himalaya. Environ. Monit. Assess. 188, 635. https://doi.org/10.1007/s10661-016-5626-3

Bi, H., Turner, J., Lambert, M.J., 2004. Additive biomass equations for native eucalypt forest trees of temperate Australia. Trees 18, 467–479.

Biau, G., 2012. Analysis of a Random Forests Model. J. Mach. Learn. Res. 13. http://arxiv.org/abs/1005.0208

Biau, G., Scornet, E., 2016. A random forest guided tour. Test 25, 197–227.

Bilal, H., Nisa, S., Ali, S.S., 2014. Effects of Exotic Eucalyptus Plantation on the Ground and Surface Water of District Malakand, Pakistan. Int. J. Innov. Sci. Res. 8, 299–304.

Bin, Y., Ye, W., Muller-Landau, H.C., Wu, L., Lian, J., Cao, H., 2012. Unimodal Tree Size Distributions Possibly Result from Relatively Strong Conservatism in Intermediate Size Classes. PLOS ONE 7, e52596. https://doi.org/10.1371/journal.pone.0052596

Bojinski, S., Verstraete, M., Peterson, T.C., Richter, C., Simmons, A., Zemp, M., 2014. The concept of essential climate variables in support of climate research, applications, and policy. Bull. Am. Meteorol. Soc. 95, 1431–1443.

Bortolot, Z.J., Wynne, R.H., 2005. Estimating forest biomass using small footprint LiDAR data: An individual tree-based approach that incorporates training data. ISPRS J. Photogramm. Remote Sens. 59, 342–360. https://doi.org/10.1016/j.isprsjprs.2005.07.001

Breiman, L., 2001a. Statistical modeling: The two cultures (with comments and a rejoinder by the author). Stat. Sci. 16, 199–231. https://doi.org/10.1214/ss/1009213726

Breiman, L., 2001b. Random Forests. Mach. Learn. 45, 5–32. https://doi.org/10.1023/A:1010933404324

Breiman, L., 1996. Bagging predictors. Mach. Learn. 24, 123–140. https://doi.org/10.1007/BF00058655

Breiman, L., 1995. Better Subset Regression Using the Nonnegative Garrote. Technometrics 37, 373–384. https://doi.org/10.1080/00401706.1995.10484371

Brockerhoff, E.G., Barbaro, L., Castagneyrol, B., Forrester, D.I., Gardiner, B., González-Olabarria, J.R., Lyver, P.O., Meurisse, N., Oxbrough, A., Taki, H., 2017. Forest biodiversity, ecosystem functioning and the provision of ecosystem services. Biodivers. Conserv. 26, 3005–3035. https://doi.org/10.1007/s10531-017-1453-2

Brown, S., 1997. Estimating Biomass and Biomass Change of Tropical Forests: A Primer, A forest resources assessment publication. Food and Agriculture Organization of the United Nations, Rome, Italy.

Brown, S.L., Schroeder, P., Kern, J.S., 1999. Spatial distribution of biomass in forests of the eastern USA. For. Ecol. Manag. 123, 81–90. https://doi.org/10.1016/S0378-1127(99)00017-1

Buchholz, T., Friedland, A.J., Hornig, C.E., Keeton, W.S., Zanchi, G., Nunery, J., 2014. Mineral soil carbon fluxes in forests and implications for carbon balance assessments. GCB Bioenergy 6, 305–311. https://doi.org/10.1111/gcbb.12044

Buchhorn, M., Raynolds, M.K., Walker, D.A., 2016. Influence of BRDF on NDVI and biomass estimations of Alaska Arctic tundra. Environ. Res. Lett. 11, 125002. https://doi.org/10.1088/1748-9326/11/12/125002

Burkhart, H.E., Tomé, M., 2012. Modeling Forest Trees and Stands. Springer, Dordrecht, New York.

Burt, P.J., Adelson, E.H., 1983. A multiresolution spline with application to image mosaics. ACM Trans. Graph. 2, 217–236. https://doi.org/10.1145/245.247

Butt, A., Shabbir, R., Ahmad, S.S., Aziz, N., Nawaz, M., Shah, M.T.A., 2015. Land cover classification and change detection analysis of Rawal watershed using remote sensing data. J. Biodivers. Environ. Sci. 6, 236–248.

Cairns, M.A., Brown, S., Helmer, E.H., Baumgardner, G.A., 1997. Root biomass allocation in the world's upland forests. Oecologia 111, 1–11. https://doi.org/10.1007/s004420050201

Calvão, T., Palmeirim, J.M., 2004. Mapping Mediterranean scrub with satellite imagery: biomass estimation and spectral behaviour. Int. J. Remote Sens. 25, 3113–3126. https://doi.org/10.1080/01431160310001654978

Campbell, B.M., 2009. Beyond Copenhagen: REDD plus, agriculture, adaptation strategies and poverty. Glob. Environ. Change 19, 397–399. https://doi.org/10.1016/j.gloenvcha.2009.07.010

Campbell, D.G., Stone, J.L., Rosas, A., 1992. A comparison of the phytosociology and dynamics of three floodplain (Várzea) forests of known ages, Rio Juruá, western Brazilian Amazon. Bot. J. Linn. Soc. 108, 213–237. https://doi.org/10.1111/j.1095-8339.1992.tb00240.x

Carreiras, J.M.B., Melo, J.B., Vasconcelos, M.J., 2013. Estimating the Above-Ground Biomass in Miombo Savanna Woodlands (Mozambique, East Africa) Using

L-Band Synthetic Aperture Radar Data. Remote Sens. 5, 1524–1548. https://doi.org/10.3390/rs5041524

Castel, T., Guerra, F., Caraglio, Y., Houllier, F., 2002. Retrieval biomass of a large Venezuelan pine plantation using JERS-1 SAR data. Analysis of forest structure impact on radar signature. Remote Sens. Environ. 79, 30–41. https://doi.org/10.1016/S0034-4257(01)00236-X

Castillo, J.A.A., Apan, A.A., Maraseni, T.N., Salmo, S.G., 2017. Estimation and mapping of above-ground biomass of mangrove forests and their replacement land uses in the Philippines using Sentinel imagery. ISPRS J. Photogramm. Remote Sens. 134, 70–85. https://doi.org/10.1016/j.isprsjprs.2017.10.016

Caviglia-Harris, J., Harris, D., 2011. The Impact of Settlement Design on Tropical Deforestation Rates and Resulting Land Cover Patterns. Agric. Resour. Econ. Rev. 40, 451–470. https://doi.org/10.1017/S1068280500002896

Champion, I., Dubois-Fernandez, P., Guyon, D., Cottrel, M., 2008. Radar Image Texture as a Function of Forest Stand Age. Int J Remote Sens 29, 1795–1800. https://doi.org/10.1080/01431160701730128

Chan, J.C.-W., Paelinckx, D., 2008. Evaluation of Random Forest and Adaboost tree-based ensemble classification and spectral band selection for ecotope mapping using airborne hyperspectral imagery. Remote Sens. Environ. 112, 2999–3011. https://doi.org/10.1016/j.rse.2008.02.011

Chan, Y.K., Koo, V.C., 2008. An Introduction to Synthetic Aperture Radar (SAR). Prog. Electromagn. Res. B 2, 27–60. https://doi.org/10.2528/PIERB07110101

Chandola, S., 2014. Polarimetric SAR Interferometry for Forest Aboveground Biomass Estimation (Master's Thesis). University of Twente, Enschede, the Netherlands.

Chang, J., Shoshany, M., 2016. Mediterranean shrublands biomass estimation using Sentinel-1 and Sentinel-2, in: 2016 IEEE International Geoscience and Remote Sensing Symposium (IGARSS). Presented at the 2016 IEEE International Geoscience and Remote Sensing Symposium (IGARSS), pp. 5300–5303. https://doi.org/10.1109/IGARSS.2016.7730380

Chaturvedi, O.P., Singh, J.S., 1987. The structure and function of pine forest in Central Himalaya. I. Dry matter dynamics. Ann. Bot. 60, 237–252.

Chaudhary, L.B., Sudhakar, J.V., Kumar, A., Bajpai, O., Tiwari, R., Murthy, V.S., 2012. Synopsis of the Genus Ficus L. (Moraceae) in India. Taiwania 57, 193–216.

Chave, J., Andalo, C., Brown, S., Cairns, M.A., Chambers, J.Q., Eamus, D., Fölster, H., Fromard, F., Higuchi, N., Kira, T., Lescure, J.-P., Nelson, B.W., Ogawa, H., Puig, H., Riéra, B., Yamakura, T., 2005. Tree allometry and improved estimation of carbon stocks and balance in tropical forests. Oecologia 145, 87–99. https://doi.org/10.1007/s00442-005-0100-x

Chave, J., Condit, R., Aguilar, S., Hernandez, A., Lao, S., Perez, R., 2004. Error propagation and scaling for tropical forest biomass estimates. Philos. Trans. R. Soc. Lond. B. Biol. Sci. 359, 409–420. https://doi.org/10.1098/rstb.2003.1425

Chave, J., Réjou-Méchain, M., Búrquez, A., Chidumayo, E., Colgan, M.S., Delitti, W.B.C., Duque, A., Eid, T., Fearnside, P.M., Goodman, R.C., Henry, M., Martínez-Yrízar, A., Mugasha, W.A., Muller-Landau, H.C., Mencuccini, M., Nelson, B.W., Ngomanda, A., Nogueira, E.M., Ortiz-Malavassi, E., Pélissier, R., Ploton, P., Ryan, C.M., Saldarriaga, J.G., Vieilledent, G., 2014. Improved allometric models to estimate the aboveground biomass of tropical trees. Glob. Change Biol. 20, 3177–3190. https://doi.org/10.1111/gcb.12629

Chavez, P.S., 1996. Image-Based Atmospheric Corrections - Revisited and Improved. Photogramm. Eng. Remote Sens. 62, 1025–1036.

Chen, D., Deng, X., Jin, G., Samie, A., Li, Z., 2017. Land-use-change induced dynamics of carbon stocks of the terrestrial ecosystem in Pakistan. Phys. Chem. Earth Parts ABC, Physics and Economics of Ecosystem Services Flows 101, 13–20. https://doi.org/10.1016/j.pce.2017.01.018

Chen, D., Stow, D., 2002. The effect of training strategies on supervised classification at different spatial resolutions. Photogramm. Eng. Remote Sens. 68, 1155–1162.

Chen, F., Lou, S., Fan, Q., Wang, Chenxing, Claverie, M., Wang, Cheng, Li, J., 2019. Normalized Difference Vegetation Index Continuity of the Landsat 4-5 MSS and TM: Investigations Based on Simulation. Remote Sens. 11, 1681. https://doi.org/10.3390/rs11141681

Chen, L., Ren, C., Zhang, B., Wang, Z., Xi, Y., 2018. Estimation of Forest Above-Ground Biomass by Geographically Weighted Regression and Machine Learning with Sentinel Imagery. Forests 9, 582. https://doi.org/10.3390/f9100582

Cheng, S.H., MacLeod, K., Ahlroth, S., Onder, S., Perge, E., Shyamsundar, P., Rana, P., Garside, R., Kristjanson, P., McKinnon, M.C., 2019. A systematic map of evidence on the contribution of forests to poverty alleviation. Environ. Evid. 8, 1–22.

Chiba, Y., 1998. Architectural analysis of relationship between biomass and basal area based on pipe model theory. Ecol. Model. 108, 219–225. https://doi.org/10.1016/S0304-3800(98)00030-1

Chin, W., 1998. The Partial Least Squares Approach to Structural Equation Modeling, in: Marcoulides, G.A. (Ed.), Modern Methods for Business Research. Lawrence Erlbaum Associates, New Jersey, London, pp. 295–358.

Christensen, M., Jokar Arsanjani, J., 2020. Stimulating Implementation of Sustainable Development Goals and Conservation Action: Predicting Future Land Use/Cover Change in Virunga National Park, Congo. Sustainability 12, 1570. https://doi.org/10.3390/su12041570

Chrysafis, I., Mallinis, G., Siachalou, S., Patias, P., 2017. Assessing the relationships between growing stock volume and Sentinel-2 imagery in a Mediterranean forest ecosystem. Remote Sens. Lett. 8, 508–517. https://doi.org/10.1080/2150704X.2017.1295479

Clark, D.A., Brown, S., Kicklighter, D.W., Chambers, J.Q., Thomlinson, J.R., Ni, J., Holland, E.A., 2001. Net primary production in tropical forests: an evaluation and synthesis of existing field data. Ecol. Appl. 11, 371–384. https://doi.org/10.1890/1051-0761(2001)011[0371:NPPITF]2.0.CO;2

Clark, D.B., Clark, D.A., 2000. Landscape-scale variation in forest structure and biomass in a tropical rain forest. For. Ecol. Manag. 137, 185–198. https://doi.org/10.1016/S0378-1127(99)00327-8

Clark, M.L., Aide, T.M., Riner, G., 2012. Land change for all municipalities in Latin America and the Caribbean assessed from 250-m MODIS imagery (2001–2010). Remote Sens. Environ. 126, 84–103. https://doi.org/10.1016/j.rse.2012.08.013

Clerici, N., Paracchini, M.L., Maes, J., 2014. Land-cover change dynamics and insights into ecosystem services in European stream riparian zones. Ecohydrol. Hydrobiol. 14, 107–120. https://doi.org/10.1016/j.ecohyd.2014.01.002

Clevers, J.G.P.W., van der Heijden, G., Verzakov, S., Schaepman, M.E., 2007. Estimating Grassland Biomass Using SVM Band Shaving of Hyperspectral Data. Photogramm. Eng. Remote Sens. 73 2007 10 73, 141–1148. https://doi.org/10.14358/PERS.73.10.1141

Collins, M.B., Mitchard, E.T.A., Mitchard, E.T.A., 2017. A small subset of protected areas are a highly significant source of carbon emissions. Sci. Rep. 7, 41902. https://doi.org/10.1038/srep41902

Congalton, R.G., 1991. A review of assessing the accuracy of classifications of remotely sensed data. Remote Sens. Environ. 37, 35–46. https://doi.org/10.1016/0034-4257(91)90048-B

Congedo, L., 2016. Semi-automatic classification plugin documentation (No. Release 4, no. 0.1).

Coomes, D.A., Allen, R.B., 2007. Mortality and tree-size distributions in natural mixed-age forests. J. Ecol. 95, 27–40. https://doi.org/10.1111/j.1365-2745.2006.01179.x

Corbane, C., Politis, P., Kempeneers, P., Simonetti, D., Soille, P., Burger, A., Pesaresi, M., Sabo, F., Syrris, V., Kemper, T., 2020. A global cloud free pixel- based image composite from Sentinel-2 data. Data Brief 31, 105737. https://doi.org/10.1016/j.dib.2020.105737

Costanza, R., d'Arge, R., De Groot, R., Farber, S., Grasso, M., Hannon, B., Limburg, K., Naeem, S., O'neill, R.V., Paruelo, J., 1998. The value of the world's ecosystem services and natural capital. Ecol. Econ. 25, 3–15.

Cougo, M.F., Souza-Filho, P.W.M., Silva, A.Q., Fernandes, M.E.B., Santos, J.R. dos, Abreu, M.R.S., Nascimento, W.R., Simard, M., 2015. Radarsat-2 Backscattering for the Modeling of Biophysical Parameters of Regenerating Mangrove Forests. Remote Sens. 7, 17097–17112. https://doi.org/10.3390/rs71215873

Crabbe, R.A., Lamb, D.W., Edwards, C., 2021. Investigating the potential of Sentinel-1 to detect varying spatial heterogeneity in pasture cover in grasslands. Int. J. Remote Sens. 42, 274–285. https://doi.org/10.1080/01431161.2020.1812129

Curlander, J.C., McDonough, R.N., 1991. Synthetic aperture radar. Wiley, New York.

Cutler, D.R., Edwards, T.C., Beard, K.H., Cutler, A., Hess, K.T., Gibson, J., Lawler, J.J., 2007. Random Forests for Classification in Ecology. Ecology 88, 2783–2792. https://doi.org/10.1890/07-0539.1

d'Annunzio, R., Sandker, M., Finegold, Y., Min, Z., 2015. Projecting global forest area towards 2030. For. Ecol. Manag., Changes in Global Forest Resources from 1990 to 2015 352, 124–133. https://doi.org/10.1016/j.foreco.2015.03.014

Dahinden, C., Guyon, I., 2011. An improved Random Forests approach with application to the performance prediction challenge datasets. Hands- Pattern Recognit. Chall. Mach. Learn. 1, 223–230.

Dang, A.T.N., Nandy, S., Srinet, R., Luong, N.V., Ghosh, S., Senthil Kumar, A., 2019. Forest aboveground biomass estimation using machine learning regression algorithm in Yok Don National Park, Vietnam. Ecol. Inform. 50, 24–32. https://doi.org/10.1016/j.ecoinf.2018.12.010

Dayamba, S.D., Djoudi, H., Zida, M., Sawadogo, L., Verchot, L., 2016. Biodiversity and carbon stocks in different land use types in the Sudanian Zone of Burkina Faso, West Africa. Agric. Ecosyst. Environ. 216, 61–72. https://doi.org/10.1016/j.agee.2015.09.023

de Lima, R.A.F., Batista, J.L.F., Prado, P.I., 2015. Modeling Tree Diameter Distributions in Natural Forests: An Evaluation of 10 Statistical Models. For. Sci. 61, 320–327. https://doi.org/10.5849/forsci.14-070

Deb, D., Deb, S., Chakraborty, D., Singh, J.P., Singh, A.K., Dutta, P., Choudhury, A., 2020. Aboveground biomass estimation of an agro-pastoral ecology in semi-arid Bundelkhand region of India from Landsat data: a comparison of support vector machine and traditional regression models. Geocarto Int. 1–16. https://doi.org/10.1080/10106049.2020.1756461

Debastiani, A.B., Sanquetta, C.R., Corte, A.P.D., Pinto, N.S., Rex, F.E., 2019. Evaluating SAR-optical sensor fusion for aboveground biomass estimation in a Brazilian tropical forest. Ann. For. Res. 62, 109–122. https://doi.org/10.15287/afr.2018.1267

Devagiri, G.M., Money, S., Singh, S., Dadhawal, V.K., Patil, P., Khaple, A., Devakumar, A.S., Hubballi, S., 2013. Assessment of above ground biomass and

carbon pool in different vegetation types of south western part of Karnataka, India using spectral modeling. Trop. Ecol. 54, 149–165.

Dhanda, P., Nandy, S., Kushwaha, S., Ghosh, S., Murthy, Y.K., Dadhwal, V., 2017. Optimizing spaceborne LiDAR and very high resolution optical sensor parameters for biomass estimation at ICESat/GLAS footprint level using regression algorithms. Prog. Phys. Geogr. Earth Environ. 41, 247–267. https://doi.org/10.1177/0309133317693443

Dhruv, B., Mittal, N., Modi, M., 2017. Analysis of different filters for noise reduction in images, in: 2017 Recent Developments in Control, Automation Power Engineering (RDCAPE). Presented at the 2017 Recent Developments in Control, Automation Power Engineering (RDCAPE), pp. 410–415. https://doi.org/10.1109/RDCAPE.2017.8358306

Diao, Y., Zhang, C., Liu, J., Liang, Y., Hou, X., Gong, X., 2012. Optimization Model to Estimate Mount Tai Forest Biomass Based on Remote Sensing, in: Li, D., Chen, Y. (Eds.), Computer and Computing Technologies in Agriculture V, IFIP Advances in Information and Communication Technology. Springer, Berlin, Heidelberg, pp. 453–459. https://doi.org/10.1007/978-3-642-27275-2_51

Dimobe, K., Kuyah, S., Dabré, Z., Ouédraogo, A., Thiombiano, A., 2019. Diversity-carbon stock relationship across vegetation types in W National park in Burkina Faso. For. Ecol. Manag. 438, 243–254. https://doi.org/10.1016/j.foreco.2019.02.027

Disperati, L., Virdis, S.G.P., 2015. Assessment of land-use and land-cover changes from 1965 to 2014 in Tam Giang-Cau Hai Lagoon, central Vietnam. Appl. Geogr. 58, 48–64. https://doi.org/10.1016/j.apgeog.2014.12.012

Dlugokencky, E., Tans, P., 2020. Trends in atmospheric carbon dioxide, National Oceanic and Atmospheric Administration, Earth System Research Laboratory (NOAA/ESRL) [WWW Document]. URL https://www.esrl.noaa.gov/gmd/ccgg/trends/global.html (accessed 11.16.20).

Dobson, M.C., Ulaby, F.T., LeToan, T., Beaudoin, A., Kasischke, E.S., Christensen, N., 1992. Dependence of radar backscatter on coniferous forest biomass. IEEE Trans. Geosci. Remote Sens. 30, 412–415. https://doi.org/10.1109/36.134090

Domingo, D., Lamelas-Gracia, M.T., Montealegre-Gracia, A.L., Riva-Fernández, J. de la, 2017. Comparison of regression models to estimate biomass losses and CO2 emissions using low-density airborne laser scanning data in a burnt Aleppo pine forest. Eur. J. Remote Sens. 50, 384–396. https://doi.org/10.1080/22797254.2017.1336067

Dong, J., Kaufmann, R.K., Myneni, R.B., Tucker, C.J., Kauppi, P.E., Liski, J., Buermann, W., Alexeyev, V., Hughes, M.K., 2003. Remote sensing estimates of boreal and temperate forest woody biomass: carbon pools, sources, and sinks. Remote Sens. Environ. 84, 393–410. https://doi.org/10.1016/S0034-4257(02)00130-X

Drake, J.M., Randin, C., Guisan, A., 2006. Modelling ecological niches with support vector machines. J. Appl. Ecol. 43, 424–432. https://doi.org/10.1111/j.1365-2664.2006.01141.x

Dubayah, R., Blair, J.B., Goetz, S., Fatoyinbo, L., Hansen, M., Healey, S., Hofton, M., Hurtt, G., Kellner, J., Luthcke, S., Armston, J., Tang, H., Duncanson, L., Hancock, S., Jantz, P., Marselis, S., Patterson, P.L., Qi, W., Silva, C., 2020. The Global Ecosystem Dynamics Investigation: High-resolution laser ranging of the Earth's forests and topography. Sci. Remote Sens. 1, 100002. https://doi.org/10.1016/j.srs.2020.100002

Dudley, N. (Ed.), 2008. Guidelines for applying protected area management categories. IUCN, Gland, Switzerland.

Dumitrașcu, M., Kucsicsa, G., Dumitrică, C., Popovici, E.-A., Vrînceanu, A., Mitrică, B., Mocanu, I., Șerban, P.-R., 2020. Estimation of Future Changes in Aboveground Forest Carbon Stock in Romania. A Prediction Based on Forest-Cover Pattern Scenario. Forests 11, 914. https://doi.org/10.3390/f11090914

Duncanson, L., Neuenschwander, A., Hancock, S., Thomas, N., Fatoyinbo, T., Simard, M., Silva, C.A., Armston, J., Luthcke, S.B., Hofton, M., Kellner, J.R., Dubayah, R., 2020. Biomass estimation from simulated GEDI, ICESat-2 and NISAR across environmental gradients in Sonoma County, California. Remote Sens. Environ. 242, 111779. https://doi.org/10.1016/j.rse.2020.111779

Dwyer, J.L., Roy, D.P., Sauer, B., Jenkerson, C.B., Zhang, H.K., Lymburner, L., 2018. Analysis Ready Data: Enabling Analysis of the Landsat Archive. Remote Sens. 10, 1363. https://doi.org/10.3390/rs10091363

Eckert, S., 2012. Improved Forest Biomass and Carbon Estimations Using Texture Measures from WorldView-2 Satellite Data. Remote Sens. 4, 810–829. https://doi.org/10.3390/rs4040810

Erb, K.-H., 2012. How a socio-ecological metabolism approach can help to advance our understanding of changes in land-use intensity. Ecol. Econ. 76–341, 8–14. https://doi.org/10.1016/j.ecolecon.2012.02.005

ESA, 2021. Sentinel-1 Toolbox: SAR Basics Tutorial.

Estévez, J., Vicent, J., Rivera-Caicedo, J.P., Morcillo-Pallarés, P., Vuolo, F., Sabater, N., Camps-Valls, G., Moreno, J., Verrelst, J., 2020. Gaussian processes retrieval of LAI from Sentinel-2 top-of-atmosphere radiance data. ISPRS J. Photogramm. Remote Sens. 167, 289–304. https://doi.org/10.1016/j.isprsjprs.2020.07.004

FAO, 2020a. Global Forest Resource Assessment 2020: Main Report. Food and Agriculture Organization of the United Nations (FAO), Rome, Italy.

FAO, 2020b. Global Forest Resources Assessment 2020: Key findings. FAO, Rome, Italy. https://doi.org/10.4060/ca8753enAlso Available in: Spanish French Russian

FAO, 2015. Knowledge reference for national forest assessments. Food and Agriculture Organization of the United Nations, Rome, Italy.

FAO, 2012. State of the world's forests, 2012. Food and Agriculture Organization of the United Nations, Rome.

FAO, 2010. Global Forest Resources Assessment 2010: Main Report. (No. FAO Forestry Paper 63). Food and Agriculture Organization of the United Nations (FAO), Rome, Italy.

Farias, M.H.C.S., Beltrão, N.E.S., Cordeiro, Y.E.M., Santos, C.A. dos, 2018. Impact of rural settlements on the deforestation of the Amazon. Mercator 17, 1–20. https://doi.org/10.4215/rm2018.e17009

Fassnacht, F.E., Hartig, F., Latifi, H., Berger, C., Hernández, J., Corvalán, P., Koch, B., 2014. Importance of sample size, data type and prediction method for remote sensing-based estimations of aboveground forest biomass. Remote Sens. Environ. 154, 102–114. https://doi.org/10.1016/j.rse.2014.07.028

Fawagreh, K., Gaber, M.M., Elyan, E., 2014. Random forests: from early developments to recent advancements. Syst. Sci. Control Eng. 2, 602–609. https://doi.org/10.1080/21642583.2014.956265

Fawzy, S., Osman, A.I., Doran, J., Rooney, D.W., 2020. Strategies for mitigation of climate change: a review. Environ. Chem. Lett. 1–26.

Fearnside, P.M., 2008. Amazon Forest maintenance as a source of environmental services. An. Acad. Bras. Ciênc. 80, 101–114. https://doi.org/10.1590/S0001-37652008000100006

Fearnside, P.M., 1997. Wood density for estimating forest biomass in Brazilian Amazonia. For. Ecol. Manag. 90, 59–87. https://doi.org/10.1016/S0378-1127(96)03840-6

Feilhauer, H., Asner, G.P., Martin, R.E., 2015. Multi-method ensemble selection of spectral bands related to leaf biochemistry. Remote Sens. Environ. 164, 57–65. https://doi.org/10.1016/j.rse.2015.03.033

Feldpausch, T.R., Jirka, S., Passos, C.A.M., Jasper, F., Riha, S.J., 2005. When big trees fall: Damage and carbon export by reduced impact logging in southern Amazonia. For. Ecol. Manag. 219, 199–215. https://doi.org/10.1016/j.foreco.2005.09.003

Feldpausch, T.R., Lloyd, J., Lewis, S.L., Brienen, R.J.W., Gloor, M., Monteagudo Mendoza, A., Lopez-Gonzalez, G., Banin, L., Abu Salim, K., Affum-Baffoe, K., Alexiades, M., Almeida, S., Amaral, I., Andrade, A., Aragão, L.E.O.C., Araujo Murakami, A., Arets, E.J.M.M., Arroyo, L., Aymard C., G.A., Baker, T.R., Bánki, O.S., Berry, N.J., Cardozo, N., Chave, J., Comiskey, J.A., Alvarez, E., de Oliveira, A., Di Fiore, A., Djagbletey, G., Domingues, T.F., Erwin, T.L., Fearnside, P.M., França, M.B., Freitas, M.A., Higuchi, N., E. Honorio C, Iida, Y., Jiménez, E., Kassim, A.R., Killeen, T.J., Laurance, W.F., Lovett, J.C., Malhi, Y., Marimon, B.S., Marimon-Junior,

B.H., Lenza, E., Marshall, A.R., Mendoza, C., Metcalfe, D.J., Mitchard, E.T.A., Neill, D.A., Nelson, B.W., Nilus, R., Nogueira, E.M., Parada, A., Peh, K.S.-H., Pena Cruz, A., Peñuela, M.C., Pitman, N.C.A., Prieto, A., Quesada, C.A., Ramírez, F., Ramírez-Angulo, H., Reitsma, J.M., Rudas, A., Saiz, G., Salomão, R.P., Schwarz, M., Silva, N., Silva-Espejo, J.E., Silveira, M., Sonké, B., Stropp, J., Taedoumg, H.E., Tan, S., ter Steege, H., Terborgh, J., Torello-Raventos, M., van der Heijden, G.M.F., Vásquez, R., Vilanova, E., Vos, V.A., White, L., Willcock, S., Woell, H., Phillips, O.L., 2012. Tree height integrated into pantropical forest biomass estimates. Biogeosciences 9, 3381–3403. https://doi.org/10.5194/bg-9-3381-2012

Feng, Q., Liu, J., Gong, J., 2015. UAV Remote Sensing for Urban Vegetation Mapping Using Random Forest and Texture Analysis. Remote Sens. 7, 1074–1094. https://doi.org/10.3390/rs70101074

Fernández-Landa, A., Algeet-Abarquero, N., Fernández-Moya, J., Guillén-Climent, M.L., Pedroni, L., García, F., Espejo, A., Villegas, J.F., Marchamalo, M., Bonatti, J., Escamochero, I., Rodríguez-Noriega, P., Papageorgiou, S., Fernandes, E., 2016. An Operational Framework for Land Cover Classification in the Context of REDD+ Mechanisms. A Case Study from Costa Rica. Remote Sens. 8, 593. https://doi.org/10.3390/rs8070593

Filipponi, F., 2019. Sentinel-1 GRD Preprocessing Workflow. Proceedings 18, 11. https://doi.org/10.3390/ECRS-3-06201

Flores-Anderson, A.I., Herndon, K.E., Thapa, R.B., Cherrington, E. (Eds.), 2019. The SAR Handbook: Comprehensive Methodologies for Forest Monitoring and Biomass Estimation.

Foley, J.A., DeFries, R., Asner, G.P., Barford, C., Bonan, G., Carpenter, S.R., Chapin, F.S., Coe, M.T., Daily, G.C., Gibbs, H.K., Helkowski, J.H., Holloway, T., Howard, E.A., Kucharik, C.J., Monfreda, C., Patz, J.A., Prentice, I.C., Ramankutty, N., Snyder, P.K., 2005. Global Consequences of Land Use. Science 309, 570–574. https://doi.org/10.1126/science.1111772

Folkesson, K., Smith-Jonforsen, G., Ulander, L.M.H., 2009. Model-Based Compensation of Topographic Effects for Improved Stem-Volume Retrieval From CARABAS-II VHF-Band SAR Images. IEEE Trans. Geosci. Remote Sens. 47, 1045–1055. https://doi.org/10.1109/TGRS.2008.2009531

Foody, G.M., 2002. Status of land cover classification accuracy assessment. Remote Sens. Environ. 80, 185–201. https://doi.org/10.1016/S0034-4257(01)00295-4

Foody, G.M., Boyd, D.S., Cutler, M.E.J., 2003. Predictive relations of tropical forest biomass from Landsat TM data and their transferability between regions. Remote Sens. Environ. 85, 463–474. https://doi.org/10.1016/S0034-4257(03)00039-7

Foody, G.M., Cutler, M.E., McMorrow, J., Pelz, D., Tangki, H., Boyd, D.S., Douglas, I., 2001. Mapping the biomass of Bornean tropical rain forest from remotely sensed data. Glob. Ecol. Biogeogr. 10, 379–387. https://doi.org/10.1046/j.1466-822X.2001.00248.x

Fraga, H., Amraoui, M., Malheiro, A.C., Moutinho-Pereira, J., Eiras-Dias, J., Silvestre, J., Santos, J.A., 2014. Examining the relationship between the Enhanced Vegetation Index and grapevine phenology. Eur. J. Remote Sens. 47, 753–771. https://doi.org/10.5721/EuJRS20144743

Freie Universität Berlin, 2020. Analyse [WWW Document]. URL https://blogs.fu-berlin.de/reseda/analyse/ (accessed 9.15.21).

FRI, 2018. Impact of Ban on Green Felling on Biophysical status of Forest (No. 8). Forest Research Institute (FRI), Dehradun, India.

Gaber, A., Amarah, B.A., Abdelfattah, M., Ali, S., 2017. Investigating the use of the dual-polarized and large incident angle of SAR data for mapping the fluvial and aeolian deposits. NRIAG J. Astron. Geophys. 6, 349–360. https://doi.org/10.1016/j.nrjag.2017.10.005

Gairola, S., Rawal, R., Todaria, N., 2008. Forest vegetation patterns along an altitudinal gradient in sub-alpine zone of west Himalaya, India. Afr. J. Plant Sci. 2, 042–048.

Galicia, L., García-Romero, A., 2007. Land Use and Land Cover Change in Highland Temperate Forests in the Izta-Popo National Park, Central Mexico. Mt. Res. Dev. 27, 48–57. https://doi.org/10.1659/0276-4741(2007)27[48:LUALCC]2.0.CO;2

Gandhi, D.S., Sundarapandian, S., 2017. Large-scale carbon stock assessment of woody vegetation in tropical dry deciduous forest of Sathanur reserve forest, Eastern Ghats, India. Environ. Monit. Assess. 189, 187. https://doi.org/10.1007/s10661-017-5899-1

Gao, Q., 2019. Estimation of water resources on continental surfaces by multi-sensor microwave remote sensing (Ph.D. Thesis). TDX Tesis Dr. En Xarxa. Universitat Ramon Llull, Barcelona, Spain.

Gao, X., Huete, A.R., Ni, W., Miura, T., 2000. Optical–Biophysical Relationships of Vegetation Spectra without Background Contamination. Remote Sens. Environ. 74, 609–620. https://doi.org/10.1016/S0034-4257(00)00150-4

Garai, D., Narayana, A.C., 2018. Land use/land cover changes in the mining area of Godavari coal fields of southern India. Egypt. J. Remote Sens. Space Sci. 21, 375–381. https://doi.org/10.1016/j.ejrs.2018.01.002

Garroutte, E.L., Hansen, A.J., Lawrence, R.L., 2016. Using NDVI and EVI to Map Spatiotemporal Variation in the Biomass and Quality of Forage for Migratory Elk in the Greater Yellowstone Ecosystem. Remote Sens. 8, 404. https://doi.org/10.3390/rs8050404

Gashaw, T., Tulu, T., Argaw, M., Worqlul, A.W., Tolessa, T., Kindu, M., 2018. Estimating the impacts of land use/land cover changes on Ecosystem Service Values: The case of the Andassa watershed in the Upper Blue Nile basin of Ethiopia. Ecosyst. Serv. 31, 219–228. https://doi.org/10.1016/j.ecoser.2018.05.001

Ge, G., Shi, Z., Zhu, Y., Yang, X., Hao, Y., 2020. Land use/cover classification in an arid desert-oasis mosaic landscape of China using remote sensed imagery: Performance assessment of four machine learning algorithms. Glob. Ecol. Conserv. 22, e00971. https://doi.org/10.1016/j.gecco.2020.e00971

Gedefaw, A.A., Atzberger, C., Bauer, T., Agegnehu, S.K., Mansberger, R., 2020. Analysis of Land Cover Change Detection in Gozamin District, Ethiopia: From Remote Sensing and DPSIR Perspectives. Sustainability 12, 4534. https://doi.org/10.3390/su12114534

Geist, H.J., Lambin, E.F., 2002. Proximate Causes and Underlying Driving Forces of Tropical Deforestation: Tropical forests are disappearing as the result of many pressures, both local and regional, acting in various combinations in different geographical locations. BioScience 52, 143–150. https://doi.org/10.1641/0006-3568(2002)052[0143:PCAUDF]2.0.CO;2

Gelas, C., Villard, L., Ferro-Famil, L., Polidori, L., Koleck, T., Daniel, S., 2021. Multi-Temporal Speckle Filtering of Polarimetric P-Band SAR Data over Dense Tropical Forests: Study Case in French Guiana for the BIOMASS Mission. Remote Sens. 13, 142. https://doi.org/10.3390/rs13010142

Geldmann, J., Barnes, M., Coad, L., Craigie, I.D., Hockings, M., Burgess, N.D., 2013. Effectiveness of terrestrial protected areas in reducing habitat loss and population declines. Biol. Conserv. 161, 230–238. https://doi.org/10.1016/j.biocon.2013.02.018

Gemusse, U., Lima, A., Teodoro, A., 2018. Pegmatite spectral behavior considering ASTER and Landsat 8 OLI data in Naipa and Muiane mines (Alto Ligonha, Mozambique), in: Earth Resources and Environmental Remote Sensing/GIS Applications IX. Presented at the Earth Resources and Environmental Remote Sensing/GIS Applications IX, International Society for Optics and Photonics, p. 107901L. https://doi.org/10.1117/12.2325555

Geudtner, D., Torres, R., Snoeij, P., Ostergaard, A., Navas-Traver, I., 2013. Sentinel-1 mission capabilities and SAR system calibration, in: 2013 IEEE Radar Conference (RadarCon13). Presented at the 2013 IEEE Radar Conference (RadarCon13), pp. 1–4. https://doi.org/10.1109/RADAR.2013.6586141

Ghasemi, N., Sahebi, M., Mohammadzadeh, A., 2011. A review on biomass estimation methods using synthetic aperture radar data. Int. J. Geomat. Geosci. 1, 776–778. https://doi.org/0976-4380

Ghimire, P., 2019. Carbon Sequestration Potentiality of *Pinus roxburghii* Forest in Makawanpur District of Nepal. J. Energy Environ. Chem. Eng. 4, 7. https://doi.org/10.11648/j.jeece.20190401.12

Ghosh, S.M., Behera, M.D., 2018. Aboveground biomass estimation using multi-sensor data synergy and machine learning algorithms in a dense tropical forest. Appl. Geogr. 96, 29–40. https://doi.org/10.1016/j.apgeog.2018.05.011

Gibbs, H.K., Brown, S., Niles, J.O., Foley, J.A., 2007. Monitoring and estimating tropical forest carbon stocks: making REDD a reality. Environ. Res. Lett. 2, 045023.

Giday, K., Eshete, G., Barklund, P., Aertsen, W., Muys, B., 2013. Wood biomass functions for Acacia abyssinica trees and shrubs and implications for provision of ecosystem services in a community managed exclosure in Tigray, Ethiopia. J. Arid Environ. 94, 80–86. https://doi.org/10.1016/j.jaridenv.2013.03.001

Gilani, H., Ahmad, S., Qazi, W.A., Abubakar, S.M., Khalid, M., 2020. Monitoring of Urban Landscape Ecology Dynamics of Islamabad Capital Territory (ICT), Pakistan, Over Four Decades (1976–2016). Land 9, 123. https://doi.org/10.3390/land9040123

Gizachew, B., Solberg, S., Næsset, E., Gobakken, T., Bollandsås, O.M., Breidenbach, J., Zahabu, E., Mauya, E.W., 2016. Mapping and estimating the total living biomass and carbon in low-biomass woodlands using Landsat 8 CDR data. Carbon Balance Manag. 11, 13. https://doi.org/10.1186/s13021-016-0055-8

Gleason, C.J., Im, J., 2012. Forest biomass estimation from airborne LiDAR data using machine learning approaches. Remote Sens. Environ. 125, 80–91. https://doi.org/10.1016/j.rse.2012.07.006

Goetz, S.J., Baccini, A., Laporte, N.T., Johns, T., Walker, W., Kellndorfer, J., Houghton, R.A., Sun, M., 2009. Mapping and monitoring carbon stocks with satellite observations: a comparison of methods. Carbon Balance Manag. 4, 2. https://doi.org/10.1186/1750-0680-4-2

GOFC-GOLD, 2016. A sourcebook of methods and procedures for monitoring and reporting anthropogenic greenhouse gas emissions and removals associated with deforestation, gains and losses of carbon stocks in forests remaining forests, and forestation. GOFC-GOLD, Wageningen.

Gogoi, R.R., Adhikari, D., Upadhaya, K., Barik, S.K., 2020. Tree diversity and carbon stock in a subtropical broadleaved forest are greater than a subtropical pine forest occurring in similar elevation of Meghalaya, north-eastern India. Trop. Ecol. 61, 142–149. https://doi.org/10.1007/s42965-020-00061-1

Golub, A.A., Fuss, S., Lubowski, R., Hiller, J., Khabarov, N., Koch, N., Krasovskii, A., Kraxner, F., Laing, T., Obersteiner, M., 2018. Escaping the climate policy uncertainty trap: options contracts for REDD+. Clim. Policy 18, 1227–1234.

Gómez, C., White, J.C., Wulder, M.A., 2016. Optical remotely sensed time series data for land cover classification: A review. ISPRS J. Photogramm. Remote Sens. 116, 55–72. https://doi.org/10.1016/j.isprsjprs.2016.03.008

Gómez, C., White, J.C., Wulder, M.A., Alejandro, P., 2014. Historical forest biomass dynamics modelled with Landsat spectral trajectories. ISPRS J. Photogramm. Remote Sens. 93, 14–28. https://doi.org/10.1016/j.isprsjprs.2014.03.008

Goodman, R.C., Phillips, O.L., Baker, T.R., 2014. The importance of crown dimensions to improve tropical tree biomass estimates. Ecol. Appl. 24, 680–698. https://doi.org/10.1890/13-0070.1

Goujon, A., Wazir, A., Gailey, N., 2020. Pakistan: A population giant falling behind in its demographic transition. Popul. Soc. No 576, 1–4.

Govaerts, Y.M., Verstraete, M.M., Pinty, B., Gobron, N., 1999. Designing optimal spectral indices: A feasibility and proof of concept study. Int. J. Remote Sens. 20, 1853–1873. https://doi.org/10.1080/014311699212524

Goward, S.N., Masek, J.G., Williams, D.L., Irons, J.R., Thompson, R.J., 2001. The Landsat 7 mission: Terrestrial research and applications for the 21st century. Remote Sens. Environ., Landsat 7 78, 3–12. https://doi.org/10.1016/S0034-4257(01)00262-0

Gower, S.T., 2003. Patterns and Mechanisms of the Forest Carbon Cycle. Annu. Rev. Environ. Resour. 28, 169–204. https://doi.org/10.1146/annurev.energy.28.050302.105515

GRASS Development Team, 2020. Geographic Resources Analysis Support System (GRASS) Software. Open Source Geospatial Foundation.

Gray, H.R., 1956. The form and taper of forest-tree stems (No. Institute Paper No. 32). Imperial Forestry Institute, University of Oxford, United Kingdom.

Gregorutti, B., Michel, B., Saint-Pierre, P., 2017. Correlation and variable importance in random forests. Stat. Comput. 27, 659–678. https://doi.org/10.1007/s11222-016-9646-1

Guerini Filho, M., Kuplich, T.M., Quadros, F.L.F.D., 2020. Estimating natural grassland biomass by vegetation indices using Sentinel 2 remote sensing data. Int. J. Remote Sens. 41, 2861–2876. https://doi.org/10.1080/01431161.2019.1697004

Guo, Y., Li, Z., Zhang, X., Chen, E., Bai, L., Tian, X., He, Q., Feng, Q., Li, W., 2012. Optimal Support Vector Machines for forest above-ground biomass estimation from multisource remote sensing data, in: 2012 IEEE International Geoscience and Remote Sensing Symposium. Presented at the 2012 IEEE International Geoscience and Remote Sensing Symposium, pp. 6388–6391. https://doi.org/10.1109/IGARSS.2012.6352721

Gupta, B., Dass, B., 2007. Composition of herbage in Pinus roxburghii Sargent stands: basal area and importance value index. Casp. J. Environ. Sci. 5, 93–98.

Gupta, P.K., Joshi, G., Rana, V., Rawat, J.S., Sharma, A., 2020. Utilization of Pine needles for preparation of Sheets for Application as Internal Packaging Material. Indian For. 146, 538–543.

Gutiérrez-Vélez, V.H., DeFries, R., Pinedo-Vásquez, M., Uriarte, M., Padoch, C., Baethgen, W., Fernandes, K., Lim, Y., 2011. High-yield oil palm expansion spares land at the expense of forests in the Peruvian Amazon. Environ. Res. Lett. 6, 044029. https://doi.org/10.1088/1748-9326/6/4/044029

Halos, S.H., Abed, F.G., 2019. Effect of spring vegetation indices NDVI & EVI on dust storms occurrence in Iraq. AIP Conf. Proc. 2144, 040015. https://doi.org/10.1063/1.5123116

Hamdan, O., Aziz, H.K., Rahman, K.A., 2011. Remotely sensed L-band SAR data for tropical forest biomass estimation. J. Trop. For. Sci. 23, 318–327.

Hamdan, O., Khali Aziz, H., Mohd Hasmadi, I., 2014. L-band ALOS PALSAR for biomass estimation of Matang Mangroves, Malaysia. Remote Sens. Environ. 155, 69–78. https://doi.org/10.1016/j.rse.2014.04.029

Han, H., Guo, X., Yu, H., 2016. Variable selection using Mean Decrease Accuracy and Mean Decrease Gini based on Random Forest, in: 2016 7th IEEE International Conference on Software Engineering and Service Science (ICSESS). Presented at the 2016 7th IEEE International Conference on Software Engineering and Service Science (ICSESS), pp. 219–224. https://doi.org/10.1109/ICSESS.2016.7883053

Hanes, J. (Ed.), 2014. Biophysical Applications of Satellite Remote Sensing, Springer Remote Sensing/Photogrammetry. Springer-Verlag, Berlin Heidelberg. https://doi.org/10.1007/978-3-642-25047-7

Hansen, M.C., Loveland, T.R., 2012. A review of large area monitoring of land cover change using Landsat data. Remote Sens. Environ., Landsat Legacy Special Issue 122, 66–74. https://doi.org/10.1016/j.rse.2011.08.024

Hansen, M.C., Potapov, P.V., Moore, R., Hancher, M., Turubanova, S.A., Tyukavina, A., Thau, D., Stehman, S.V., Goetz, S.J., Loveland, T.R., Kommareddy, A., Egorov, A., Chini, L., Justice, C.O., Townshend, J.R.G., 2013. High-Resolution Global Maps of 21st-Century Forest Cover Change. Science 342, 850–853. https://doi.org/10.1126/science.1244693

Hao, Z., Zhang, J., Song, B., Ye, J., Li, B., 2007. Vertical structure and spatial associations of dominant tree species in an old-growth temperate forest. For. Ecol. Manag. 252, 1–11. https://doi.org/10.1016/j.foreco.2007.06.026

Haq, S.M., Calixto, E.S., Kumar, M., 2020. Assessing Biodiversity and Productivity over a Small-scale Gradient in the Protected Forests of Indian Western Himalayas. J. Sustain. For. 1–20. https://doi.org/10.1080/10549811.2020.1803918

Haralick, R.M., Shanmugam, K., Dinstein, I., 1973. Textural Features for Image Classification. IEEE Trans. Syst. Man Cybern. SMC-3, 610–621. https://doi.org/10.1109/TSMC.1973.4309314

Haripriya, G.S., 2000. Estimates of biomass in Indian forests. Biomass Bioenergy 19, 245–258. https://doi.org/10.1016/S0961-9534(00)00040-4

Hasen-Yusuf, M., Treydte, A.C., Abule, E., Sauerborn, J., 2013. Predicting aboveground biomass of woody encroacher species in semi-arid rangelands, Ethiopia. J. Arid Environ. 96, 64–72. https://doi.org/10.1016/j.jaridenv.2013.04.007

Hassan, Z., Shabbir, R., Ahmad, S.S., Malik, A.H., Aziz, N., Butt, A., Erum, S., 2016. Dynamics of land use and land cover change (LULCC) using geospatial techniques: a case study of Islamabad Pakistan. SpringerPlus 5, 812. https://doi.org/10.1186/s40064-016-2414-z

He, H., Garcia, E.A., 2009. Learning from Imbalanced Data. IEEE Trans. Knowl. Data Eng. 21, 1263–1284. https://doi.org/10.1109/TKDE.2008.239

He, Q., Chen, E., An, R., Li, Y., 2013. Above-Ground Biomass and Biomass Components Estimation Using LiDAR Data in a Coniferous Forest. Forests 4, 984–1002. https://doi.org/10.3390/f4040984

Heiskanen, J., 2006. Estimating aboveground tree biomass and leaf area index in a mountain birch forest using ASTER satellite data. Int. J. Remote Sens. 27, 1135–1158. https://doi.org/10.1080/01431160500353858

Henchiri, M., Ali, S., Essifi, B., Kalisa, W., Zhang, S., Bai, Y., 2020. Monitoring land cover change detection with NOAA-AVHRR and MODIS remotely sensed data in the North and West of Africa from 1982 to 2015. Environ. Sci. Pollut. Res. 27, 5873–5889. https://doi.org/10.1007/s11356-019-07216-1

Hernández-Stefanoni, J.L., Castillo-Santiago, M.Á., Mas, J.F., Wheeler, C.E., Andres-Mauricio, J., Tun-Dzul, F., George-Chacón, S.P., Reyes-Palomeque, G., Castellanos-Basto, B., Vaca, R., Dupuy, J.M., 2020. Improving aboveground biomass maps of tropical dry forests by integrating LiDAR, ALOS PALSAR, climate and field data. Carbon Balance Manag. 15, 15. https://doi.org/10.1186/s13021-020-00151-6

Herold, M., Roberts, D.A., Gardner, M.E., Dennison, P.E., 2004. Spectrometry for urban area remote sensing—Development and analysis of a spectral library from 350 to 2400 nm. Remote Sens. Environ. 91, 304–319. https://doi.org/10.1016/j.rse.2004.02.013

Hijmans, R., J., Ettan, J. van, 2012. raster: Geographic analysis and modeling with raster data.

Hijmans, R.J., 2017. Introduction to the 'raster' package (version 2.6-7).

Hilbig, B.E., Zettler, I., Moshagen, M., Heydasch, T., 2013. Tracing the path from personality—via cooperativeness—to conservation. Eur. J. Personal. 27, 319–327.

Himalayan Wildlife Foundation, 2007. Margallah Hills National Park Ecological Baseline. (Draft Report No. D7BL1MHP:). Himalayan Wildlife Foundation and Capital Development Authority, Islamabad, Pakistan.

Hoekman, D.H., Quiñones, M.J., 2000. Land cover type and biomass classification using AirSAR data for evaluation of monitoring scenarios in the Colombian Amazon. IEEE Trans. Geosci. Remote Sens. 38, 685–696.

Horning, N., 2010. Random Forests : An algorithm for image classification and generation of continuous fields data sets, in: GeoInformatics for Spatial-Infrastructure

Development in Earth and Allied Sciences (GIS-IDEAS) 2010. Japan-Vietnam Geoinformatics Consortium (JVGC) and Hanoi University of Mining and Geology (HUMG), Hanoi, Vietnam, p. 6. https://doi.org/10/viewabstract.php?id=342

Hosonuma, N., Herold, M., Sy, V.D., Fries, R.S.D., Brockhaus, M., Verchot, L., Angelsen, A., Romijn, E., 2012. An assessment of deforestation and forest degradation drivers in developing countries. Environ. Res. Lett. 7, 044009. https://doi.org/10.1088/1748-9326/7/4/044009

Hossain, M., Siddique, M.R.H., Abdullah, S.M.R., Saha, C., Islam, S.M.Z., Iqbal, M.Z., Akhter, M., 2020. Development and Evaluation of Species-Specific Biomass Models for Most Common Timber and Fuelwood Species of Bangladesh. Open J. For. 10, 172. https://doi.org/10.4236/ojf.2020.101012

Hu, Y., Batunacun, Zhen, L., Zhuang, D., Batunacun, Zhen, L., Zhuang, D., 2019. Assessment of Land-Use and Land-Cover Change in Guangxi, China. Sci. Rep. 9, 2189. https://doi.org/10.1038/s41598-019-38487-w

Huang, X., Ziniti, B., Torbick, N., Ducey, M.J., 2018. Assessment of Forest above Ground Biomass Estimation Using Multi-Temporal C-band Sentinel-1 and Polarimetric L-band PALSAR-2 Data. Remote Sens. 10, 1424. https://doi.org/10.3390/rs10091424

Huete, A., Didan, K., Miura, T., Rodriguez, E.P., Gao, X., Ferreira, L.G., 2002. Overview of the radiometric and biophysical performance of the MODIS vegetation indices. Remote Sens. Environ., The Moderate Resolution Imaging Spectroradiometer (MODIS): a new generation of Land Surface Monitoring 83, 195–213. https://doi.org/10.1016/S0034-4257(02)00096-2

Hunter, M.O., Keller, M., Victoria, D., Morton, D.C., 2013. Tree height and tropical forest biomass estimation. Biogeosciences 10, 8385–8399. https://doi.org/10.5194/bg-10-8385-2013

Husch, B., Beers, T.W., Kershaw Jr, J.A., 2002. Forest mensuration. John Wiley & Sons.

Hussain, J., Zhou, K., Akbar, M., khan, M.Z., Raza, G., Ali, S., Hussain, A., Abbas, Q., Khan, G., Khan, M., Abbas, H., Iqbal, S., Ghulam, A., 2019. Dependence of rural livelihoods on forest resources in Naltar Valley, a dry temperate mountainous region, Pakistan. Glob. Ecol. Conserv. 20, e00765. https://doi.org/10.1016/j.gecco.2019.e00765

Hussain, M., Butt, A.R., Uzma, F., Ahmed, R., Irshad, S., Rehman, A., Yousaf, B., 2019a. A comprehensive review of climate change impacts, adaptation, and mitigation on environmental and natural calamities in Pakistan. Environ. Monit. Assess. 192, 48. https://doi.org/10.1007/s10661-019-7956-4

Hussain, M., Butt, A.R., Uzma, F., Ahmed, R., Rehman, A., Ali, M.U., Ullah, H., Yousaf, B., 2019b. Divisional disparities on climate change adaptation and mitigation in Punjab, Pakistan: local perceptions, vulnerabilities, and policy implications.

Environ. Sci. Pollut. Res. 26, 31491–31507. https://doi.org/10.1007/s11356-019-06262-z

Hussain, S., Mubeen, M., Ahmad, A., Akram, W., Hammad, H.M., Ali, M., Masood, N., Amin, A., Farid, H.U., Sultana, S.R., Fahad, S., Wang, D., Nasim, W., 2020. Using GIS tools to detect the land use/land cover changes during forty years in Lodhran District of Pakistan. Environ. Sci. Pollut. Res. 27, 39676–39692. https://doi.org/10.1007/s11356-019-06072-3

Huuva, I., Persson, H.J., Soja, M.J., Wallerman, J., Ulander, L.M.H., Fransson, J.E.S., 2020. Predictions of Biomass Change in a Hemi-Boreal Forest Based on Multi-Polarization L- and P-Band SAR Backscatter. Can. J. Remote Sens. 0, 1–20. https://doi.org/10.1080/07038992.2020.1838891

Hyde, P., Dubayah, R., Walker, W., Blair, J.B., Hofton, M., Hunsaker, C., 2006. Mapping forest structure for wildlife habitat analysis using multi-sensor (LiDAR, SAR/InSAR, ETM+, Quickbird) synergy. Remote Sens. Environ. 102, 63–73. https://doi.org/10.1016/j.rse.2006.01.021

Iles, K., Wilson, L.J., 1977. A Further Neglected Mean. Math. Teach. 70, 27–28. https://doi.org/10.5951/MT.70.1.0027

Imhoff, M.L., 1995. Radar backscatter and biomass saturation: ramifications for global biomass inventory. IEEE Trans. Geosci. Remote Sens. 33, 511–518. https://doi.org/10.1109/TGRS.1995.8746034

Immitzer, M., Atzberger, C., Koukal, T., 2012. Tree Species Classification with Random Forest Using Very High Spatial Resolution 8-Band WorldView-2 Satellite Data. Remote Sens. 4, 2661–2693. https://doi.org/10.3390/rs4092661

Imran, A.B., Khan, K., Ali, N., Ahmad, N., Ali, A., Shah, K., 2020. Narrow band based and broadband derived vegetation indices using Sentinel-2 Imagery to estimate vegetation biomass. Glob. J. Environ. Sci. Manag. 6, 97–108. https://doi.org/10.22034/GJESM.2020.01.08

Indirabai, I., Nair, M.H., Nair, J.R., Nidamanuri, R.R., 2019. Optical Remote Sensing for Biophysical Characterisation in Forests: A Review. Int. J. Appl. Eng. Res. 14, 344–354. https://dx.doi.org/10.37622/IJAER/14.2.2019.344-354

IPCC, 2019. Technical Summary, 2019. In: Climate Change and Land: an IPCC special report on climate change, desertification, land degradation, sustainable land management, food security, and greenhouse gas fluxes in terrestrial ecosystems. IPCC.

IPCC, 2014. Climate change 2014: synthesis report. Contribution of Working Groups I, II and III to the fifth assessment report of the Intergovernmental Panel on Climate Change. IPCC, Geneva, Switzerland.

IPCC, 2007a. Climate Change 2007: The Physical Science Basis. Contribution of Working Group I to the Fourth Assessment Report of the Intergovernmental Panel on Climate Change. Cambridge University Press, Cambridge, UK and New York, USA.

IPCC, 2007b. Technical Summary. In: Climate Change 2007, in: Mitigation. Contribution of Working Group III to the Fourth Assessment Report of the Intergovernmental Panel on Climate Change. Cambridge University Press Cambridge and New York, p. 93.

IPCC, 2003. Good practice guidance for land use, land-use change and forestry. Institute for Global Environmental Strategies, Kanagawa Prefecture, Japan.

Iqbal, M.F., Khan, M.R., Malik, A., 2013. Land use change detection in the limestone exploitation area of Margalla Hills National Park (MHNP), Islamabad, Pakistan using geo-spatial techniques. J. Himal. Earth Sci. 46, 89–98.

Islam, K., Jashimuddin, M., Nath, B., Nath, T.K., 2018. Land use classification and change detection by using multi-temporal remotely sensed imagery: The case of Chunati wildlife sanctuary, Bangladesh. Egypt. J. Remote Sens. Space Sci. 21, 37–47. https://doi.org/10.1016/j.ejrs.2016.12.005

Islam, K., Nath, T.K., Jashimuddin, M., Rahman, M.F., 2019. Forest dependency, co-management and improvement of peoples' livelihood capital: Evidence from Chunati Wildlife Sanctuary, Bangladesh. Environ. Dev. 32, 100456. https://doi.org/10.1016/j.envdev.2019.100456

Ismail, I., Muhammad, S., Hammad, G., Anwar, A., Kiramat, H., Kamran, H., Karky, B.S., Qamer, F.M., Waqas, Q., Ning, W., 2018. Forest inventory and analysis in Gilgit-Baltistan: a contribution towards developing a forest inventory for all Pakistan. Int. J. Clim. Change Strateg. Manag. 10, 616–631. https://doi.org/10.1108/ijccsm-05-2017-0100

Issa, S., Dahy, B., Ksiksi, T., Saleous, N., 2020. A Review of Terrestrial Carbon Assessment Methods Using Geo-Spatial Technologies with Emphasis on Arid Lands. Remote Sens. 12, 2008. https://doi.org/10.3390/rs12122008

Jachowski, N.R.A., Quak, M.S.Y., Friess, D.A., Duangnamon, D., Webb, E.L., Ziegler, A.D., 2013. Mangrove biomass estimation in Southwest Thailand using machine learning. Appl. Geogr. 45, 311–321. https://doi.org/10.1016/j.apgeog.2013.09.024

Jackson, J.K., 1994. Manual of afforestation in Nepal. Forest Research and Survey Centre, Ministry of Forests and Soil Conservation, Kathmandu, Nepal.

Jafari, E.K., Naghavi, H., Adeli, K., Latifi, H., 2020. A Nondestructive, Remote Sensing-Based Estimation of the Economic Value of Aboveground Temperate Forest Biomass (Case Study: Hyrcanian Forests, Nowshahr-Iran). J. Sustain. For. 39, 750–770. https://doi.org/10.1080/10549811.2020.1723645

James, G., Witten, D., Hastie, T., Tibshirani, R., 2013. An Introduction to Statistical Learning: with Applications in R, Springer Texts in Statistics. Springer-Verlag, New York. https://doi.org/10.1007/978-1-4614-7138-7

Janitza, S., Hornung, R., 2018. On the overestimation of random forest's out-of-bag error. PLOS ONE 13, e0201904. https://doi.org/10.1371/journal.pone.0201904

Jayaraman, K., 1999. A Statistical Manual for Forestry Research. FAO, Bangkok, Thailand.

Jensen, J.R., 2009. Remote sensing of the environment: An earth resource perspective, 2nd Edition. ed. Pearson Education Limited, London, UK.

Jensen, J.R., Lulla, D.K., 1987. Introductory digital image processing: A remote sensing perspective. Geocarto Int. 2, 65. https://doi.org/10.1080/10106048709354084

Jin, J., Yang, J., 2020. Effects of sampling approaches on quantifying urban forest structure. Landsc. Urban Plan. 195, 103722. https://doi.org/10.1016/j.landurbplan.2019.103722

Jin, Y., Liu, X., Chen, Y., Liang, X., 2018. Land-cover mapping using Random Forest classification and incorporating NDVI time-series and texture: a case study of central Shandong. Int. J. Remote Sens. 39, 8703–8723. https://doi.org/10.1080/01431161.2018.1490976

Jones, K.R., Venter, O., Fuller, R.A., Allan, J.R., Maxwell, S.L., Negret, P.J., Watson, J.E.M., 2018. One-third of global protected land is under intense human pressure. Science 360, 788–791. https://doi.org/10.1126/science.aap9565

Joos, F., Spahni, R., 2008. Rates of change in natural and anthropogenic radiative forcing over the past 20,000 years. Proc. Natl. Acad. Sci. 105, 1425–1430. https://doi.org/10.1073/pnas.0707386105

Joshi, A., Shahnawaz, S., Ranjit, B., 2019. Estimating above ground biomass of Pinus roxbhurghii using slope based vegetation index model. ISPRS Ann. Photogramm. Remote Sens. Spat. Inf. Sci. IV-5/W2, 35–42. https://doi.org/10.5194/isprs-annals-IV-5-W2-35-2019

Joshi, N.K., Dhiman, R.C., 1992. Lopping yield studies of Grewia optiva Drummond. Van Vigyan 30, 80–85.

Jothivel, S., 2016. Diversity of wood specific gravity among Forest Trees, Kolli hills, Southern Tamilnadu, India. Int. J. Environ. Biol. 6, 29–33.

Kajisa, T., Murakami, T., Mizoue, N., Top, N., Yoshida, S., 2009. Object-based forest biomass estimation using Landsat ETM+ in Kampong Thom Province, Cambodia. J. For. Res. 14, 203–211. https://doi.org/10.1007/s10310-009-0125-9

Kamusoko, C., 2019. Remote Sensing Image Classification in R, Springer Geography. Springer Singapore, Singapore.

Kantakumar, L.N., Neelamsetti, P., 2015. Multi-temporal land use classification using hybrid approach. Egypt. J. Remote Sens. Space Sci. 18, 289–295. https://doi.org/10.1016/j.ejrs.2015.09.003

Kanwar, A., 2019. Allometric estimation of biomass and carbon sequestration potential of some important agroforestry tree species of mid-hills of Himachal Pradesh (M.Sc Thesis). UHF, NAUNI, Himachal Pradesh, India.

Kartika, T., Arifin, S., Sari, I.L., Tosiani, A., Firmansyah, R., Kustiyo, Carolita, I., Adi, K., Daryanto, A.F., Said, Z., 2019. Analysis of Vegetation Indices Using Metric Landsat-8 Data to Identify Tree Cover Change in Riau Province. IOP Conf. Ser. Earth Environ. Sci. 280, 012013. https://doi.org/10.1088/1755-1315/280/1/012013

Kaushal, S., Baishya, R., 2021. Stand structure and species diversity regulate biomass carbon stock under major Central Himalayan forest types of India. Ecol. Process. 10, 14. https://doi.org/10.1186/s13717-021-00283-8

Kellndorfer, J.M., Dobson, M.C., Vona, J.D., Clutter, M., 2003. Toward Precision Forestry: Plot-Level Parameter Retrieval for Slash Pine Plantations With JPL AIRSAR. IEEE Trans. Geosci. REMOTE Sens. 41, 1571–1582.

Ketterings, Q.M., Coe, R., van Noordwijk, M., Palm, C.A., 2001. Reducing uncertainty in the use of allometric biomass equations for predicting above-ground tree biomass in mixed secondary forests. For. Ecol. Manag. 146, 199–209.

Khalid, N., Ahmad, S., Erum, S., Butt, A., 2015. Monitoring forest cover change of Margalla Hills over a period of two decades (1992-2011): A spatiotemporal perspective. J. Ecosyst. Ecography 6, 174–181. https://doi.org/10.4172/2157-7625.1000174

Khalid, N., Ullah, S., Ahmad, S.S., Ali, A., Chishtie, F., 2019. A remotely sensed tracking of forest cover and associated temperature change in Margalla hills. Int. J. Digit. Earth 12, 1133–1150. https://doi.org/10.1080/17538947.2018.1448008

Khan, A., Ahmed, M., Ahmed, F., Saeed, R., Siddiqui, F., 2020. Vegetation of highly disturbed conifer forests around Murree, Pakistan. Türk Biyoçeşitlilik Derg. 3, 43–53. https://doi.org/10.38059/biodiversity.708154

Khan, I., Lei, H., Khan, Ahmad, Muhammad, I., Javeed, T., Khan, Asif, Huo, X., 2021. Yield gap analysis of major food crops in Pakistan: prospects for food security. Environ. Sci. Pollut. Res. 28, 7994–8011. https://doi.org/10.1007/s11356-020-11166-4

Khan, I., Lei, H., Shah, I.A., Ali, I., Khan, Inayat, Muhammad, I., Huo, X., Javed, T., 2020. Farm households' risk perception, attitude and adaptation strategies in dealing with climate change: Promise and perils from rural Pakistan. Land Use Policy 91, 104395. https://doi.org/10.1016/j.landusepol.2019.104395

Khan, K., Iqbal, J., Ali, A., Khan, S.N., 2020. Assessment of Sentinel-2-Derived Vegetation Indices for The Estimation of Above-Ground Biomass/Carbon Stock, Temporal Deforestation and Carbon Emissions Estimation in The Moist Temperate Forests of Pakistan. Appl. Ecol. Environ. Res. 18, 783–815. https://doi.org/10.15666/aeer/1801_783815

Khan, M., Mahmood, H.Z., Abbas, G., Damalas, C.A., 2017. Agroforestry Systems as Alternative Land-Use Options in the Arid Zone of Thal, Pakistan. Small-Scale For. 16, 553–569. https://doi.org/10.1007/s11842-017-9372-3

Khan, M.R., Khan, I.A., Baig, M.H.A., Liu, Z., Ashraf, M.I., 2020. Exploring the potential of Sentinel-2A satellite data for aboveground biomass estimation in fragmented Himalayan subtropical pine forest. J. Mt. Sci. 17, 2880–2896. https://doi.org/10.1007/s11629-019-5968-8

Khan, M.S., Khan, S., Shah, W., Hussain, A., Masaud, S., 2016. Height growth, diameter increment and age relationship response to sustainable volume of subtropical Chir pine (Pinus roxburghii) forest of Karaker Barikot forest Muhammad Sadiq khan. Pure Appl. Biol. 5, 760–767. https://doi.org/10.19045/bspab.2016.50095

Khan, M.S., Ullah, S., Sun, T., Rehman, A.U., Chen, L., 2020. Land-Use/Land-Cover Changes and Its Contribution to Urban Heat Island: A Case Study of Islamabad, Pakistan. Sustainability 12, 3861. https://doi.org/10.3390/su12093861

Khan, N., Ali, K., Shaukat, S., 2014. Phytosociology, structure and dynamics of Pinus roxburghii associations from Northern Pakistan. J. For. Res. 25, 511–521. https://doi.org/10.1007/s11676-014-0490-x

Khan, Z.I., 2003. Protected areas in Pakistan: Management and Issues. J. Natl. Sci. Found. Sri Lanka 31, 239–248. https://doi.org/10.4038/jnsfsr.v31i1-2.3036

Kindermann, G.E., Obersteiner, M., Rametsteiner, E., McCallum, I., 2006. Predicting the deforestation-trend under different carbon-prices. Carbon Balance Manag. 1, 15. https://doi.org/10.1186/1750-0680-1-15

Kindu, M., Schneider, T., Teketay, D., Knoke, T., 2016. Changes of ecosystem service values in response to land use/land cover dynamics in Munessa–Shashemene landscape of the Ethiopian highlands. Sci. Total Environ. 547, 137–147. https://doi.org/10.1016/j.scitotenv.2015.12.127

Koch, B., 2010. Status and future of laser scanning, synthetic aperture radar and hyperspectral remote sensing data for forest biomass assessment. ISPRS J. Photogramm. Remote Sens. 65, 581–590.

Köhl, M., Ehrhart, H.-P., Knauf, M., Neupane, P.R., 2020a. A viable indicator approach for assessing sustainable forest management in terms of carbon emissions and removals. Ecol. Indic. 111, 106057. https://doi.org/10.1016/j.ecolind.2019.106057

Köhl, M., Magnussen, S., Marchetti, M., 2006. Sampling methods, remote sensing and GIS multiresource forest inventory, Tropical forestry. Springer, Berlin ; London.

Köhl, M., Neupane, P.R., Lotfiomran, N., 2017. The impact of tree age on biomass growth and carbon accumulation capacity: A retrospective analysis using tree ring data of three tropical tree species grown in natural forests of Suriname. PLOS ONE 12, e0181187. https://doi.org/10.1371/journal.pone.0181187

Köhl, M., Neupane, P.R., Mundhenk, P., 2020b. REDD+ measurement, reporting and verification – A cost trap? Implications for financing REDD+MRV costs by result-based payments. Ecol. Econ. 168, 106513. https://doi.org/10.1016/j.ecolecon.2019.106513

Konings, A.G., Rao, K., Steele-Dunne, S.C., 2019. Macro to micro: microwave remote sensing of plant water content for physiology and ecology. New Phytol. 223, 1166–1172. https://doi.org/10.1111/nph.15808

Kuhn, M., 2008. Building Predictive Models in R Using the caret Package. J. Stat. Softw. 28, 1–26. https://doi.org/10.18637/jss.v028.i05

Kühnlein, M., Appelhans, T., Thies, B., Nauss, T., 2014. Improving the accuracy of rainfall rates from optical satellite sensors with machine learning — A random forests-based approach applied to MSG SEVIRI. Remote Sens. Environ. 141, 129–143. https://doi.org/10.1016/j.rse.2013.10.026

Kumar, A., Kishore, B.S.P.C., Saikia, P., Deka, J., Bharali, S., Singha, L.B., Tripathi, O.P., Khan, M.L., 2019. Tree diversity assessment and above ground forests biomass estimation using SAR remote sensing: A case study of higher altitude vegetation of North-East Himalayas, India. Phys. Chem. Earth Parts ABC 111, 53–64. https://doi.org/10.1016/j.pce.2019.03.007

Kumar, A., Sharma, M.P., 2015. Estimation of carbon stocks of Balganga Reserved Forest, Uttarakhand, India. For. Sci. Technol. 11, 177–181. https://doi.org/10.1080/21580103.2014.990060

Kumar, L., Mutanga, O., 2017. Remote Sensing of Above-Ground Biomass. Remote Sens. 9, 935. https://doi.org/10.3390/rs9090935

Kumar, L., Sinha, P., Taylor, S., Alqurashi, A.F., 2015. Review of the use of remote sensing for biomass estimation to support renewable energy generation. J. Appl. Remote Sens. 9, 097696. https://doi.org/doi: 10.1117/1.JRS.9.097696

Kumar, M., Anemsh, K., Sheikh, M., Raj, A.J., 2012. Structure and carbon stock potential in traditional agro forestry system of Garhwal Himalaya. Int. J. Agric. Technol. 8, 2187–2200.

Kumar, M., Kumar, R., Konsam, B., Sheikh, M., Pandey, R., 2019. Above-And Below-Ground Biomass Production in Pinus roxburghii Forests along Altitudes in Garhwal Himalaya, India. Curr. Sci. 116. https://doi.org/10.18520/cs/v116/i9/1506-1514

Kumar, P., Sharma, L.K., Pandey, P.C., Sinha, S., Nathawat, M.S., 2013. Geospatial Strategy for Tropical Forest-Wildlife Reserve Biomass Estimation. IEEE J. Sel. Top. Appl. Earth Obs. Remote Sens. 6, 917–923. https://doi.org/10.1109/JSTARS.2012.2221123

Kumar, S., Pandey, U., Kushwaha, S.P., Chatterjee, R.S., Bijker, W., 2012. Aboveground biomass estimation of tropical forest from Envisat advanced synthetic aperture radar data using modeling approach. J. Appl. Remote Sens. 6, 063588.

Kunwar, R.M., Sharma, S.P., 2004. Quantitative analysis of tree species in two community forests of Dolpa district, mid-west Nepal. Himal. J. Sci. 2, 23–28. https://doi.org/10.3126/hjs.v2i3.226

Kuplich, T.M., Curran, P.J., Atkinson, P.M., 2003. Relating SAR image texture and backscatter to tropical forest biomass, in: IGARSS 2003. 2003 IEEE International Geoscience and Remote Sensing Symposium. Proceedings (IEEE Cat. No.03CH37477). Presented at the IGARSS 2003. 2003 IEEE International Geoscience and Remote Sensing Symposium. Proceedings (IEEE Cat. No.03CH37477), pp. 2872–2874 vol.4. https://doi.org/10.1109/IGARSS.2003.1294615

Kursa, M.B., Rudnicki, W.R., 2010. Feature Selection with the Boruta Package. J. Stat. Softw. 36, 1–13. https://doi.org/10.18637/jss.v036.i11

Laar, A. van, Akça, A., 2007. Forest mensuration, 2. ed., completely rev. and supplemented. ed, Managing forest ecosystems. Springer, Dordrecht.

Lal, R., 2008. Carbon sequestration. Philos. Trans. R. Soc. B Biol. Sci. 363, 815–830. https://doi.org/10.1098/rstb.2007.2185

Lambin, E.F., Geist, H.J., Lepers, E., 2003. Dynamics of Land-Use and Land-Cover Change in Tropical Regions. Annu. Rev. Environ. Resour. 28, 205–241. https://doi.org/10.1146/annurev.energy.28.050302.105459

Lambin, E.F., Turner, B.L., Geist, H.J., Agbola, S.B., Angelsen, A., Bruce, J.W., Coomes, O.T., Dirzo, R., Fischer, G., Folke, C., George, P.S., Homewood, K., Imbernon, J., Leemans, R., Li, X., Moran, E.F., Mortimore, M., Ramakrishnan, P.S., Richards, J.F., Skånes, H., Steffen, W., Stone, G.D., Svedin, U., Veldkamp, T.A., Vogel, C., Xu, J., 2001. The causes of land-use and land-cover change: moving beyond the myths. Glob. Environ. Change 11, 261–269. https://doi.org/10.1016/S0959-3780(01)00007-3

Lamquin, N., Woolliams, E., Bruniquel, V., Gascon, F., Gorroño, J., Govaerts, Y., Leroy, V., Lonjou, V., Alhammoud, B., Barsi, J.A., Czapla-Myers, J.S., McCorkel, J., Helder, D., Lafrance, B., Clerc, S., Holben, B.N., 2019. An inter-comparison exercise of Sentinel-2 radiometric validations assessed by independent expert groups. Remote Sens. Environ. 233, 111369. https://doi.org/10.1016/j.rse.2019.111369

Lanzas, M., Hermoso, V., de-Miguel, S., Bota, G., Brotons, L., 2019. Designing a network of green infrastructure to enhance the conservation value of protected areas and maintain ecosystem services. Sci. Total Environ. 651, 541–550. https://doi.org/10.1016/j.scitotenv.2018.09.164

Latifi, H., Fassnacht, F., Koch, B., 2012. Forest structure modeling with combined airborne hyperspectral and LiDAR data. Remote Sens. Environ. 121, 10–25. https://doi.org/10.1016/j.rse.2012.01.015

Laurin, G.V., Balling, J., Corona, P., Mattioli, W., Papale, D., Puletti, N., Rizzo, M., Truckenbrodt, J., Urban, M., 2018. Above-ground biomass prediction by Sentinel-1 multitemporal data in central Italy with integration of ALOS2 and Sentinel-2 data. J. Appl. Remote Sens. 12, 016008. https://doi.org/10.1117/1.JRS.12.016008

Le Toan, T., Quegan, S., Davidson, M., Balzter, H., Paillou, P., Papathanassiou, K., Plummer, S., Rocca, F., Saatchi, S., Shugart, H., 2011. The BIOMASS mission: Mapping global forest biomass to better understand the terrestrial carbon cycle. Remote Sens. Environ. 115, 2850–2860.

Lecina-Diaz, J., Alvarez, A., De Cáceres, M., Herrando, S., Vayreda, J., Retana, J., 2019. Are protected areas preserving ecosystem services and biodiversity? Insights from Mediterranean forests and shrublands. Landsc. Ecol. 34, 2307–2321. https://doi.org/10.1007/s10980-019-00887-8

Leverington, F., Costa, K.L., Pavese, H., Lisle, A., Hockings, M., 2010. A Global Analysis of Protected Area Management Effectiveness. Environ. Manage. 46, 685–698. https://doi.org/10.1007/s00267-010-9564-5

Lewis, E., MacSharry, B., Juffe-Bignoli, D., Harris, N., Burrows, G., Kingston, N., Burgess, N.D., 2019. Dynamics in the global protected-area estate since 2004. Conserv. Biol. 33, 570–579.

Li, C., Li, M., Li, Y., Qian, P., 2020. Estimating aboveground forest carbon density using Landsat 8 and field-based data: a comparison of modelling approaches. Int. J. Remote Sens. 41, 4269–4292. https://doi.org/10.1080/01431161.2020.1714782

Li, C., Li, Y., Li, M., 2019. Improving forest aboveground biomass (AGB) estimation by incorporating crown density and using landsat 8 OLI images of a subtropical forest in Western Hunan in Central China. Forests 10, 104. https://doi.org/10.3390/f10020104

Li, J., Chen, W., 2005. A rule-based method for mapping Canada's wetlands using optical, radar and DEM data. Int. J. Remote Sens. 26, 5051–5069. https://doi.org/10.1080/01431160500166516

Li, J., Wang, Z., Lai, C., Wu, X., Zeng, Z., Chen, X., Lian, Y., 2018. Response of net primary production to land use and land cover change in mainland China since the late 1980s. Sci. Total Environ. 639, 237–247. https://doi.org/10.1016/j.scitotenv.2018.05.155

Li, M., Tan, Y., Pan, J., Peng, S., 2008. Modeling forest aboveground biomass by combining spectrum, textures and topographic features. Front. For. China 3, 10–15. https://doi.org/10.1007/s11461-008-0013-z

Li, M., Zang, S., Zhang, B., Li, S., Wu, C., 2014. A Review of Remote Sensing Image Classification Techniques: the Role of Spatio-contextual Information. Eur. J. Remote Sens. 47, 389–411. https://doi.org/10.5721/EuJRS20144723

Li, S., Zhang, H., Zhou, X., Yu, H., Li, W., 2020. Enhancing protected areas for biodiversity and ecosystem services in the Qinghai–Tibet Plateau. Ecosyst. Serv. 43, 101090. https://doi.org/10.1016/j.ecoser.2020.101090

Li, W., Niu, Z., Shang, R., Qin, Y., Wang, L., Chen, H., 2020. High-resolution mapping of forest canopy height using machine learning by coupling ICESat-2

LiDAR with Sentinel-1, Sentinel-2 and Landsat-8 data. Int. J. Appl. Earth Obs. Geoinformation 92, 102163. https://doi.org/10.1016/j.jag.2020.102163

Li, X., Feng, R., Guan, X., Shen, H., Zhang, L., 2019. Remote Sensing Image Mosaicking: Achievements and Challenges. IEEE Geosci. Remote Sens. Mag. 7, 8–22. https://doi.org/10.1109/MGRS.2019.2921780

Li, X., Hui, N., Shen, H., Fu, Y., Zhang, L., 2015. A robust mosaicking procedure for high spatial resolution remote sensing images. ISPRS J. Photogramm. Remote Sens. 109, 108–125. https://doi.org/10.1016/j.isprsjprs.2015.09.009

Li, Xiao-Ying, Jin, H.-J., Wang, H.-W., Marchenko, S.S., Shan, W., Luo, D.-L., He, R.-X., Spektor, V., Huang, Y.-D., Li, Xin-Yu, Jia, N., 2021. Influences of forest fires on the permafrost environment: A review. Adv. Clim. Change Res., Including special topic on degrading permafrost and its impacts 12, 48–65. https://doi.org/10.1016/j.accre.2021.01.001

Li, Y., Andersen, H.-E., McGaughey, R., 2008. A Comparison of Statistical Methods for Estimating Forest Biomass from Light Detection and Ranging Data. West. J. Appl. For. 23, 223–231. https://doi.org/10.1093/wjaf/23.4.223

Li, Y., Li, M., Li, C., Liu, Z., Li, M., Li, C., Liu, Z., 2020. Forest aboveground biomass estimation using Landsat 8 and Sentinel-1A data with machine learning algorithms. Sci. Rep. 10, 9952. https://doi.org/10.1038/s41598-020-67024-3

Liaw, A., Wiener, M., 2002. Classification and Regression by RandomForest. R News 2, 18–22. https://CRAN.R-project.org/doc/Rnews/

Lillesand, T., Kiefer, R.W., Chipman, J., 2015. Remote Sensing and Image Interpretation, 7th ed. Wiley.

Lin, B., Ahmad, I., 2016. Energy substitution effect on transport sector of Pakistan based on trans-log production function. Renew. Sustain. Energy Rev. 56, 1182–1193. https://doi.org/10.1016/j.rser.2015.12.012

Lin, B., Raza, M.Y., 2019. Analysis of energy related CO2 emissions in Pakistan. J. Clean. Prod. 219, 981–993. https://doi.org/10.1016/j.jclepro.2019.02.112

Lindner, M., Maroschek, M., Netherer, S., Kremer, A., Barbati, A., Garcia-Gonzalo, J., Seidl, R., Delzon, S., Corona, P., Kolström, M., 2010. Climate change impacts, adaptive capacity, and vulnerability of European forest ecosystems. For. Ecol. Manag. 259, 698–709.

Liping, C., Yujun, S., Saeed, S., 2018. Monitoring and predicting land use and land cover changes using remote sensing and GIS techniques—A case study of a hilly area, Jiangle, China. PLOS ONE 13, e0200493. https://doi.org/10.1371/journal.pone.0200493

Liu, J., Dietz, T., Carpenter, S.R., Alberti, M., Folke, C., Moran, E., Pell, A.N., Deadman, P., Kratz, T., Lubchenco, J., 2007. Complexity of coupled human and natural systems. science 317, 1513–1516.

Liu, K., Shi, W., Zhang, H., 2011. A fuzzy topology-based maximum likelihood classification. ISPRS J. Photogramm. Remote Sens. 66, 103–114. https://doi.org/10.1016/j.isprsjprs.2010.09.007

Liu, K., Wang, J., Zeng, W., Song, J., 2017. Comparison and evaluation of three methods for estimating forest above ground biomass using TM and GLAS data. Remote Sens. 9, 341.

Liu, L., Lim, S., Shen, X., Yebra, M., 2020. Assessment of generalized allometric models for aboveground biomass estimation: A case study in Australia. Comput. Electron. Agric. 175, 105610. https://doi.org/10.1016/j.compag.2020.105610

Liu, M., Ouyang, S., Tian, Y., Wen, S., Zhao, Y., Li, X., Baoyin, T., Kuzyakov, Y., Xu, X., 2021. Effects of rotational and continuous overgrazing on newly assimilated C allocation. Biol. Fertil. Soils 57, 193–202. https://doi.org/10.1007/s00374-020-01516-2

Liu, Q., Trinder, J.C., Turner, I.L., 2017. Automatic super-resolution shoreline change monitoring using Landsat archival data: a case study at Narrabeen–Collaroy Beach, Australia. J. Appl. Remote Sens. 11, 016036. https://doi.org/10.1117/1.JRS.11.016036

Liu, Y., Gong, W., Xing, Y., Hu, X., Gong, J., 2019. Estimation of the forest stand mean height and aboveground biomass in Northeast China using SAR Sentinel-1B, multispectral Sentinel-2A, and DEM imagery. ISPRS J. Photogramm. Remote Sens. 151, 277–289. https://doi.org/10.1016/j.isprsjprs.2019.03.016

Lodhi, M.A., Echavarria, F.R., Keithley, C., 1998. Using remote sensing data to monitor land cover changes near Afghan refugee camps in northern Pakistan. Geocarto Int. 13, 33–39. https://doi.org/10.1080/10106049809354626

Lopes, A., Nezry, E., Touzi, R., Laur, H., 1993. Structure detection and statistical adaptive speckle filtering in SAR images. Int. J. Remote Sens. 14, 1735–1758. https://doi.org/10.1080/01431169308953999

López-Serrano, P.M., Cárdenas Domínguez, J.L., Corral-Rivas, J.J., Jiménez, E., López-Sánchez, C.A., Vega-Nieva, D.J., 2020. Modeling of aboveground biomass with Landsat 8 OLI and machine learning in temperate forests. Forests 11, 11. https://doi.org/10.3390/f11010011

López-Serrano, P.M., López Sánchez, C.A., Solís-Moreno, R., Corral-Rivas, J.J., 2016. Geospatial Estimation of above Ground Forest Biomass in the Sierra Madre Occidental in the State of Durango, Mexico. Forests 7, 70. https://doi.org/10.3390/f7030070

Lu, D., 2006. The potential and challenge of remote sensing-based biomass estimation. Int. J. Remote Sens. 27, 1297–1328. https://doi.org/10.1080/01431160500486732

Lu, D., Chen, Q., Wang, G., Liu, L., Li, G., Moran, E., 2016. A survey of remote sensing-based aboveground biomass estimation methods in forest ecosystems. Int. J. Digit. Earth 9, 63–105. https://doi.org/10.1080/17538947.2014.990526

Lu, D., Mausel, P., Brondízio, E., Moran, E., 2004. Change detection techniques. Int. J. Remote Sens. 25, 2365–2401. https://doi.org/10.1080/0143116031000139863

Lu, J., Wang, H., Qin, S., Cao, L., Pu, R., Li, G., Sun, J., 2020. Estimation of aboveground biomass of Robinia pseudoacacia forest in the Yellow River Delta based on UAV and Backpack LiDAR point clouds. Int. J. Appl. Earth Obs. Geoinformation 86, 102014. https://doi.org/10.1016/j.jag.2019.102014

Lu, X., Zhou, Y., Liu, Y., Page, Y.L., 2018. The role of protected areas in land use/land cover change and the carbon cycle in the conterminous United States. Glob. Change Biol. 24, 617–630. https://doi.org/10.1111/gcb.13816

Lucas, R.M., Cronin, N., Moghaddam, M., Lee, A., Armston, J., Bunting, P., Witte, C., 2006. Integration of radar and Landsat-derived foliage projected cover for woody regrowth mapping, Queensland, Australia. Remote Sens. Environ. 100, 388–406. https://doi.org/10.1016/j.rse.2005.09.020

Lugo, A.E., Brown, S., 1992. Tropical forests as sinks of atmospheric carbon. For. Ecol. Manag. 54, 239–255. https://doi.org/10.1016/0378-1127(92)90016-3

Lutz, J.A., Furniss, T.J., Johnson, D.J., Davies, S.J., Allen, D., Alonso, A., Anderson-Teixeira, K.J., Andrade, A., Baltzer, J., Becker, K.M.L., Blomdahl, E.M., Bourg, N.A., Bunyavejchewin, S., Burslem, D.F.R.P., Cansler, C.A., Cao, K., Cao, M., Cárdenas, D., Chang, L.-W., Chao, K.-J., Chao, W.-C., Chiang, J.-M., Chu, C., Chuyong, G.B., Clay, K., Condit, R., Cordell, S., Dattaraja, H.S., Duque, A., Ewango, C.E.N., Fischer, G.A., Fletcher, C., Freund, J.A., Giardina, C., Germain, S.J., Gilbert, G.S., Hao, Z., Hart, T., Hau, B.C.H., He, F., Hector, A., Howe, R.W., Hsieh, C.-F., Hu, Y.-H., Hubbell, S.P., Inman-Narahari, F.M., Itoh, A., Janík, D., Kassim, A.R., Kenfack, D., Korte, L., Král, K., Larson, A.J., Li, Y., Lin, Y., Liu, S., Lum, S., Ma, K., Makana, J.-R., Malhi, Y., McMahon, S.M., McShea, W.J., Memiaghe, H.R., Mi, X., Morecroft, M., Musili, P.M., Myers, J.A., Novotny, V., de Oliveira, A., Ong, P., Orwig, D.A., Ostertag, R., Parker, G.G., Patankar, R., Phillips, R.P., Reynolds, G., Sack, L., Song, G.-Z.M., Su, S.-H., Sukumar, R., Sun, I.-F., Suresh, H.S., Swanson, M.E., Tan, S., Thomas, D.W., Thompson, J., Uriarte, M., Valencia, R., Vicentini, A., Vrška, T., Wang, X., Weiblen, G.D., Wolf, A., Wu, S.-H., Xu, H., Yamakura, T., Yap, S., Zimmerman, J.K., 2018. Global importance of large-diameter trees. Glob. Ecol. Biogeogr. 27, 849–864. https://doi.org/10.1111/geb.12747

Lv, W., Wang, X., 2020. Overview of Hyperspectral Image Classification. J. Sens. 2020, e4817234. https://doi.org/10.1155/2020/4817234

Ma, L., Liu, Y., Zhang, X., Ye, Y., Yin, G., Johnson, B.A., 2019. Deep learning in remote sensing applications: A meta-analysis and review. ISPRS J. Photogramm. Remote Sens. 152, 166–177. https://doi.org/10.1016/j.isprsjprs.2019.04.015

Macías, C.A.S., Orihuela, J.C.A., Abad, S.I., 2017. Estimation of above-ground live biomass and carbon stocks in different plant formations and in the soil of dry forests of the Ecuadorian coast. Food Energy Secur. 6, e00115. https://doi.org/10.1002/fes3.115

Malhi, R.K.M., Anand, A., Mudaliar, A.N., Pandey, P.C., Srivastava, P.K., Sandhya Kiran, G., 2020. Synergetic use of in situ and hyperspectral data for mapping species diversity and above ground biomass in Shoolpaneshwar Wildlife Sanctuary, Gujarat. Trop. Ecol. 61, 106–115. https://doi.org/10.1007/s42965-020-00068-8

Malik, R.N., Husain, S.Z., 2007. Broussonetia papyrifera (L.) L'Hér. Ex Vent.: An environmental constraint on the Himalayan foothills vegetation. Pak. J. Bot. 39, 1045–1053.

Mallick, J., Hoa, P., Hang, H., Rahman, A., 2012. Satellite Based Assessment of Biomass and Carbon Stock for a Mountainous Watershed Using Geoinformatics Technique. J. Remote Sens. GIS 3, 33–50.

Maltamo, M., Naesset, E., Vauhkonen, J. (Eds.), 2014. Forestry Applications of Airborne Laser Scanning: Concepts and Case Studies, Managing Forest Ecosystems. Springer Netherlands. https://doi.org/10.1007/978-94-017-8663-8

Mandal, R.A., Dutta, I.C., Jha, P.K., 2017. Comparing Carbon Stock and Increment Estimation using Destructive Sampling and Inventory Guideline of Acacia Catechu, Dalbergia Sissoo, Eucalyptus Camaldulensis and Pylunthus emblica Plantations, Mahottary Nepal. Int. J. Chem. Math. Phys. 1, 48–54.

Mannan, A., Feng, Z., Ahmad, A., Liu, J., Saeed, S., Mukete, B., 2018. Carbon dynamic shifts with land use change in Margallah hills national park, Islamabad (Pakistan) from 1990 to 2017. Appl. Ecol. Environ. Res. 16, 3197–3214.

Mannan, A., Liu, J., Zhongke, F., Khan, T.U., Saeed, S., Mukete, B., ChaoYong, S., Yongxiang, F., Ahmad, A., Amir, M., Ahmad, S., Shah, S., 2019a. Application of land-use/land cover changes in monitoring and projecting forest biomass carbon loss in Pakistan. Glob. Ecol. Conserv. 17, e00535. https://doi.org/10.1016/j.gecco.2019.e00535

Mannan, A., Zhongke, F., Khan, T.U., Khan, M.A., Tariq, M., 2019b. Variation in tree biomass and carbon stocks with respect to altitudinal gradient in the Himalayan forests of Northern Pakistan. J. Pure Appl. Agric. 4, 21–28.

Maraseni, T.N., Neupane, P.R., Lopez-Casero, F., Cadman, T., 2014. An assessment of the impacts of the REDD+ pilot project on community forests user groups (CFUGs) and their community forests in Nepal. J. Environ. Manage. 136, 37–46. https://doi.org/10.1016/j.jenvman.2014.01.011

Martinez-Taboada, F., Redondo, J.I., 2020. The SIESTA (SEAAV Integrated evaluation sedation tool for anaesthesia) project: Initial development of a multifactorial sedation assessment tool for dogs. PLOS ONE 15, e0230799. https://doi.org/10.1371/journal.pone.0230799

Mather, P., Tso, B., 2016. Classification methods for remotely sensed data, Second. ed. CRC press, Boca Raton, Florida, USA.

Matsushita, B., Yang, W., Chen, J., Onda, Y., Qiu, G., 2007. Sensitivity of the Enhanced Vegetation Index (EVI) and Normalized Difference Vegetation Index (NDVI) to Topographic Effects: A Case Study in High-density Cypress Forest. Sensors 7, 2636–2651. https://doi.org/10.3390/s7112636

Maxwell, A.E., Warner, T.A., Fang, F., 2018. Implementation of machine-learning classification in remote sensing: an applied review. Int. J. Remote Sens. 39, 2784–2817. https://doi.org/10.1080/01431161.2018.1433343

Mazhar, F., Fadia, F., 2019. A Time Series Analysis of Satellite Imageries for Land Use & Land Cover (LULC) Change Detection of Gujranwala City, Pakistan from 1999–2019. Indian J. Sci. Technol. 12, 1–9. https://doi.org/10.17485/ijst/2019/v12i46/148606

McDonald, K.C., Zimmermann, R., Kimball, J.S., 2002. Diurnal and spatial variation of xylem dielectric constant in Norway Spruce (Picea abies [L.] Karst.) as related to microclimate, xylem sap flow, and xylem chemistry. IEEE Trans. Geosci. Remote Sens. 40, 2063–2082. https://doi.org/10.1109/TGRS.2002.803737

McElhinny, C., Gibbons, P., Brack, C., Bauhus, J., 2005. Forest and woodland stand structural complexity: Its definition and measurement. For. Ecol. Manag. 218, 1–24. https://doi.org/10.1016/j.foreco.2005.08.034

Means, J.E., Acker, S.A., Harding, D.J., Blair, J.B., Lefsky, M.A., Cohen, W.B., Harmon, M.E., McKee, W.A., 1999. Use of Large-Footprint Scanning Airborne Lidar To Estimate Forest Stand Characteristics in the Western Cascades of Oregon. Remote Sens. Environ. 67, 298–308. https://doi.org/10.1016/S0034-4257(98)00091-1

Mei, A., Manzo, C., Fontinovo, G., Bassani, C., Allegrini, A., Petracchini, F., 2016. Assessment of land cover changes in Lampedusa Island (Italy) using Landsat TM and OLI data. J. Afr. Earth Sci., Contributions to the Global Earth Sciences Integration 122, 15–24. https://doi.org/10.1016/j.jafrearsci.2015.05.014

Meli Fokeng, R., Gadinga Forje, W., Meli Meli, V., Nyuyki Bodzemo, B., 2020. Multi-temporal forest cover change detection in the Metchie-Ngoum Protection Forest Reserve, West Region of Cameroon. Egypt. J. Remote Sens. Space Sci. 23, 113–124. https://doi.org/10.1016/j.ejrs.2018.12.002

Melillo, J.M., Reilly, J.M., Kicklighter, D.W., Gurgel, A.C., Cronin, T.W., Paltsev, S., Felzer, B.S., Wang, X., Sokolov, A.P., Schlosser, C.A., 2009. Indirect Emissions from Biofuels: How Important? Science 326, 1397–1399. https://doi.org/10.1126/science.1180251

Mellor, A., Boukir, S., Haywood, A., Jones, S., 2015. Exploring issues of training data imbalance and mislabelling on random forest performance for large area land cover

classification using the ensemble margin. ISPRS J. Photogramm. Remote Sens. 105, 155–168. https://doi.org/10.1016/j.isprsjprs.2015.03.014

Mensah, S., Noulèkoun, F., Ago, E.E., 2020. Aboveground tree carbon stocks in West African semi-arid ecosystems: Dominance patterns, size class allocation and structural drivers. Glob. Ecol. Conserv. 24, e01331. https://doi.org/10.1016/j.gecco.2020.e01331

Menze, B.H., Kelm, B.M., Splitthoff, D.N., Koethe, U., Hamprecht, F.A., 2011. On Oblique Random Forests, in: Gunopulos, D., Hofmann, T., Malerba, D., Vazirgiannis, M. (Eds.), Machine Learning and Knowledge Discovery in Databases, Lecture Notes in Computer Science. Springer, Berlin, Heidelberg, pp. 453–469. https://doi.org/10.1007/978-3-642-23783-6_29

Meyer, D., Wien, F.T., 2017. Support vector machines. R News 1, 23–26.

Millard, K., Richardson, M., 2015. On the Importance of Training Data Sample Selection in Random Forest Image Classification: A Case Study in Peatland Ecosystem Mapping. Remote Sens. 7, 8489–8515. https://doi.org/10.3390/rs70708489

Ming, A., Jia, H., Zhao, J., Tao, Y., Li, Y., 2014. Above- and Below-Ground Carbon Stocks in an Indigenous Tree (Mytilaria laosensis) Plantation Chronosequence in Subtropical China. PLoS ONE 9, e109730. https://doi.org/10.1371/journal.pone.0109730

Ming, D., Zhou, T., Wang, M., Tan, T., 2016. Land cover classification using random forest with genetic algorithm-based parameter optimization. J. Appl. Remote Sens. 10, 035021. https://doi.org/10.1117/1.JRS.10.035021

Mishra, P.K., Rai, A., Rai, S.C., 2020. Land use and land cover change detection using geospatial techniques in the Sikkim Himalaya, India. Egypt. J. Remote Sens. Space Sci. 23, 133–143. https://doi.org/10.1016/j.ejrs.2019.02.001

Mitchard, E.T., Saatchi, S.S., Woodhouse, I.H., Nangendo, G., Ribeiro, N., Williams, M., Ryan, C.M., Lewis, S.L., Feldpausch, T., Meir, P., 2009. Using satellite radar backscatter to predict above-ground woody biomass: A consistent relationship across four different African landscapes. Geophys. Res. Lett. 36.

Mohajane, M., Essahlaoui, A., Oudija, F., Hafyani, M.E., Hmaidi, A.E., Ouali, A.E., Randazzo, G., Teodoro, A.C., 2018. Land Use/Land Cover (LULC) Using Landsat Data Series (MSS, TM, ETM+ and OLI) in Azrou Forest, in the Central Middle Atlas of Morocco. Environments 5, 131. https://doi.org/10.3390/environments5120131

MohanRajan, S.N., Loganathan, A., Manoharan, P., 2020. Survey on Land Use/Land Cover (LU/LC) change analysis in remote sensing and GIS environment: Techniques and Challenges. Environ. Sci. Pollut. Res. 27, 29900–29926. https://doi.org/10.1007/s11356-020-09091-7

Mohd Zaki, N.A., Latif, Z.A., Suratman, M.N., 2018. Modelling above-ground live trees biomass and carbon stock estimation of tropical lowland Dipterocarp forest:

integration of field-based and remotely sensed estimates. Int. J. Remote Sens. 39, 2312–2340. https://doi.org/10.1080/01431161.2017.1421793

Monserud, R.A., Leemans, R., 1992. Comparing global vegetation maps with the Kappa statistic. Ecol. Model. 62, 275–293. https://doi.org/10.1016/0304-3800(92)90003-W

Motlagh, M.G., Kafaky, S.B., Mataji, A., Akhavan, R., 2018. Estimating and mapping forest biomass using regression models and Spot-6 images (case study: Hyrcanian forests of north of Iran). Environ. Monit. Assess. 190, 352. https://doi.org/10.1007/s10661-018-6725-0

Moussa, S., Kyereh, B., Tougiani, A., Kuyah, S., Saadou, M., 2019. West African Sahelian cities as source of carbon stocks: Evidence from Niger. Sustain. Cities Soc. 50, 101653. https://doi.org/10.1016/j.scs.2019.101653

Mukul, S.A., Halim, Md.A., Herbohn, J., 2020. Forest Carbon Stock and Fluxes: Distribution, Biogeochemical Cycles, and Measurement Techniques, in: Leal Filho, W., Azul, A.M., Brandli, L., Lange Salvia, A., Wall, T. (Eds.), Life on Land. Springer International Publishing, Cham, pp. 1–16. https://doi.org/10.1007/978-3-319-71065-5_23-1

Mukul, S.A., Rashid, A.M., Uddin, M.B., Khan, N.A., 2016. Role of non-timber forest products in sustaining forest-based livelihoods and rural households' resilience capacity in and around protected area: a Bangladesh study. J. Environ. Plan. Manag. 59, 628–642. https://doi.org/10.1080/09640568.2015.1035774

Mura, M., Bottalico, F., Giannetti, F., Bertani, R., Giannini, R., Mancini, M., Orlandini, S., Travaglini, D., Chirici, G., 2018. Exploiting the capabilities of the Sentinel-2 multi spectral instrument for predicting growing stock volume in forest ecosystems. Int. J. Appl. Earth Obs. Geoinformation 66, 126–134. https://doi.org/10.1016/j.jag.2017.11.013

Mutanga, O., Adam, E., Cho, M.A., 2012. High density biomass estimation for wetland vegetation using WorldView-2 imagery and random forest regression algorithm. Int. J. Appl. Earth Obs. Geoinformation 18, 399–406. https://doi.org/10.1016/j.jag.2012.03.012

Mutanga, O., Skidmore, A.K., 2004. Hyperspectral band depth analysis for a better estimation of grass biomass (Cenchrus ciliaris) measured under controlled laboratory conditions. Int. J. Appl. Earth Obs. Geoinformation 5, 87–96. https://doi.org/10.1016/j.jag.2004.01.001

Muukkonen, P., Heiskanen, J., 2005. Estimating biomass for boreal forests using ASTER satellite data combined with standwise forest inventory data. Remote Sens. Environ. 99, 434–447. https://doi.org/10.1016/j.rse.2005.09.011

Naeem, S., Ghauri, B., Shahzad, A., Shaukat, S.S., 2017. Estimation of aboveground forest biomass using geospatial techniques in Murree and Abbottabad areas, Pakistan. Int. J. Biol. Biotechnol. 14, 203–213.

Næsset, E., Økland, T., 2002. Estimating tree height and tree crown properties using airborne scanning laser in a boreal nature reserve. Remote Sens. Environ. 79, 105–115. https://doi.org/10.1016/S0034-4257(01)00243-7

Nagendra, H., 2008. Do Parks Work? Impact of Protected Areas on Land Cover Clearing. AMBIO J. Hum. Environ. 37, 330–337. https://doi.org/10.1579/06-R-184.1

Nagler, P.L., Glenn, E.P., Lewis Thompson, T., Huete, A., 2004. Leaf area index and normalized difference vegetation index as predictors of canopy characteristics and light interception by riparian species on the Lower Colorado River. Agric. For. Meteorol. 125, 1–17. https://doi.org/10.1016/j.agrformet.2004.03.008

Natasha, M.S., Khalid, S., Murtaza, B., Anwar, H., Shah, A.H., Sardar, A., Shabbir, Z., Niazi, N.K., 2020. A critical analysis of wastewater use in agriculture and associated health risks in Pakistan. Environ. Geochem. Health. https://doi.org/10.1007/s10653-020-00702-3

Nath, S., Nath, A.J., Sileshi, G.W., Das, A.K., 2017. Biomass stocks and carbon storage in Barringtonia acutangula floodplain forests in North East India. Biomass Bioenergy 98, 37–42. https://doi.org/10.1016/j.biombioe.2017.01.014

Navarro, J.A., Algeet, N., Fernández-Landa, A., Esteban, J., Rodríguez-Noriega, P., Guillén-Climent, M.L., 2019. Integration of UAV, Sentinel-1, and Sentinel-2 Data for Mangrove Plantation Aboveground Biomass Monitoring in Senegal. Remote Sens. 11, 77. https://doi.org/10.3390/rs11010077

Naveenkumar, J., Arunkumar, K.S., Sundarapandian, Sm., 2017. Biomass and carbon stocks of a tropical dry forest of the Javadi Hills, Eastern Ghats, India. Carbon Manag. 8, 351–361. https://doi.org/10.1080/17583004.2017.1362946

Nawaz, F., Fayaz, A., 2004. The Effect of Mining On Geomorphology (Detection of Changes By Using Remote Sensing Techniques), in: Proceedings of ISPRS Congress Commission VII. Presented at the Geo-Imagery Briding Continents July 12-23, ISPRS, Istanbul, Turkey, pp. 1301–1305.

Negassa, M.D., Mallie, D.T., Gemeda, D.O., 2020. Forest cover change detection using Geographic Information Systems and remote sensing techniques: a spatio-temporal study on Komto Protected forest priority area, East Wollega Zone, Ethiopia. Environ. Syst. Res. 9, 1. https://doi.org/10.1186/s40068-020-0163-z

Negi, J.D.S., Manhas, R.K., Chauhan, P.S., 2003. Carbon allocation in different components of some tree species of India: A new approach for carbon estimation. Curr. Sci. 85, 1528–1531.

Nelson, R.F., Hyde, P., Johnson, P., Emessiene, B., Imhoff, M.L., Campbell, R., Edwards, W., 2007. Investigating RaDAR–LiDAR synergy in a North Carolina pine forest. Remote Sens. Environ. 110, 98–108. https://doi.org/10.1016/j.rse.2007.02.006

Nepstad, D.C., Stickler, C.M., Filho, B.S.-, Merry, F., 2008. Interactions among Amazon land use, forests and climate: prospects for a near-term forest tipping point.

Philos. Trans. R. Soc. B Biol. Sci. 363, 1737–1746. https://doi.org/10.1098/rstb.2007.0036

Nero, B.F., Callo-Concha, D., Denich, M., 2018. Structure, Diversity, and Carbon Stocks of the Tree Community of Kumasi, Ghana. Forests 9, 519. https://doi.org/10.3390/f9090519

Nguyen, C.T., Chidthaisong, A., Kieu Diem, P., Huo, L.-Z., 2021. A Modified Bare Soil Index to Identify Bare Land Features during Agricultural Fallow-Period in Southeast Asia Using Landsat 8. Land 10, 231. https://doi.org/10.3390/land10030231

Nguyen, T.D., Kappas, M., 2020. Estimating the Aboveground Biomass of an Evergreen Broadleaf Forest in Xuan Lien Nature Reserve, Thanh Hoa, Vietnam, Using SPOT-6 Data and the Random Forest Algorithm. Int. J. For. Res. 2020, 1–13. https://doi.org/10.1155/2020/4216160

Nicodemus, K.K., 2011. Letter to the Editor: On the stability and ranking of predictors from random forest variable importance measures. Brief. Bioinform. 12, 369–373. https://doi.org/10.1093/bib/bbr016

Nicodemus, K.K., Malley, J.D., 2009. Predictor correlation impacts machine learning algorithms: implications for genomic studies. Bioinformatics 25, 1884–1890. https://doi.org/10.1093/bioinformatics/btp331

Nizalapur, V., Jha, C.S., Madugundu, R., 2010. Estimation of above ground biomass in Indian tropical forested area using multi-frequency DLR-ESAR data 1, 167–178.

Nizami, S.M., 2012. The inventory of the carbon stocks in sub tropical forests of Pakistan for reporting under Kyoto Protocol. J. For. Res. 23, 377–384. https://doi.org/10.1007/s11676-012-0273-1

Nizami, S.M., 2010. Estimation of carbon stocks in subtropical managed and unmanaged forests of Pakistan (PhD Thesis). Arid Agriculture University Rawalpindi Pakistan, Rawalpindi, Pakistan.

Nizami, S.M., Mirza, S.N., Livesley, S., Arndt, S., Fox, J.C., Khan, I.A., Mahmood, T., 2009. Estimating carbon stocks in sub-tropical pine (Pinus roxburghii). Pak. J. Agric. Sci. 46, 266–270.

Njana, M.A., 2017. Indirect methods of tree biomass estimation and their uncertainties. South. For. J. For. Sci. 79, 41–49. https://doi.org/10.2989/20702620.2016.1233753

Nogueira, E.M., Yanai, A.M., de Vasconcelos, S.S., de Alencastro Graça, P.M.L., Fearnside, P.M., 2018. Carbon stocks and losses to deforestation in protected areas in Brazilian Amazonia. Reg. Environ. Change 18, 261–270. https://doi.org/10.1007/s10113-017-1198-1

Nolte, C., Agrawal, A., Silvius, K.M., Soares-Filho, B.S., 2013. Governance regime and location influence avoided deforestation success of protected areas in the

Brazilian Amazon. Proc. Natl. Acad. Sci. 110, 4956–4961. https://doi.org/10.1073/pnas.1214786110

Nugroho, N., 2006. Estimating Carbon Sequestration In Tropical Rainforest Using Integrated Remote Sensing and Ecosystem Productivity Modelling: A Case Study In Labanan Concession Area, East Kalimantan, Indonesia (Master's Thesis). ITC, Enschede, the Netherlands.

Nüsser, M., 2000. Change and Persistence: Contemporary Landscape Transformation in the Nanga Parbat Region, Northern Pakistan. Mt. Res. Dev. 20, 348–355. https://doi.org/10.1659/0276-4741(2000)020[0348:CAPCLT]2.0.CO;2

Nuthammachot, N., Askar, A., Stratoulias, D., Wicaksono, P., 2020. Combined use of Sentinel-1 and Sentinel-2 data for improving above-ground biomass estimation. Geocarto Int. 0, 1–11. https://doi.org/10.1080/10106049.2020.1726507

Omar, H., Misman, M.A., Kassim, A.R., 2017. Synergetic of PALSAR-2 and Sentinel-1A SAR polarimetry for retrieving aboveground biomass in dipterocarp forest of Malaysia. Appl. Sci. 7, 675.

Opelele, O., Yu, Y., Fan, W., Chen, C., Kachaka, S., 2021. Biomass estimation based on multilinear regression and machine learning algorithms in the Mayombe tropical forest, in the Democratic Republic of Congo. Appl. Ecol. Environ. Res. 19, 359–377. https://doi.org/10.15666/aeer/1901_359377

Ouma, Y.O., Tateishi, R., 2015. Optimization of Second-Order Grey-Level Texture in High-Resolution Imagery for Statistical Estimation of Above-Ground Biomass. J. Environ. Inform. 8, 70–85.

Pal, M., 2005. Random forest classifier for remote sensing classification. Int. J. Remote Sens. 26, 217–222. https://doi.org/10.1080/01431160412331269698

Pal, M., Foody, G.M., 2012. Evaluation of SVM, RVM and SMLR for Accurate Image Classification With Limited Ground Data. IEEE J. Sel. Top. Appl. Earth Obs. Remote Sens. 5, 1344–1355. https://doi.org/10.1109/JSTARS.2012.2215310

Pal, M., Mather, P.M., 2005. Support vector machines for classification in remote sensing. Int. J. Remote Sens. 26, 1007–1011. https://doi.org/10.1080/01431160512331314083

Pancel, L., Köhl, M. (Eds.), 2016. Tropical Forestry Handbook, 2nd ed. Springer Berlin Heidelberg, Berlin, Heidelberg. https://doi.org/10.1007/978-3-642-54601-3

Pandapotan, J., Sugianto, S., Darusman, D., 2016. Estimation of Carbon Stock Stands using EVI and NDVI Vegetation Index in Production Forest of Lembah Seulawah Sub-District, Aceh Indonesia. Aceh Int. J. Sci. Technol. 5, 126–139. https://doi.org/10.13170/aijst.5.3.5836

Pandey, P.C., Anand, A., Srivastava, P.K., 2019a. Spatial distribution of mangrove forest species and biomass assessment using field inventory and earth observation

hyperspectral data. Biodivers. Conserv. 28, 2143–2162. https://doi.org/10.1007/s10531-019-01698-8

Pandey, P.C., Srivastava, P.K., Chetri, T., Choudhary, B.K., Kumar, P., 2019b. Forest biomass estimation using remote sensing and field inventory: a case study of Tripura, India. Environ. Monit. Assess. 191, 593. https://doi.org/10.1007/s10661-019-7730-7

Pandit, S., Tsuyuki, S., Dube, T., 2020. Exploring the inclusion of Sentinel-2 MSI texture metrics in above-ground biomass estimation in the community forest of Nepal. Geocarto Int. 35, 1832–1849. https://doi.org/10.1080/10106049.2019.1588390

Pandit, S., Tsuyuki, S., Dube, T., 2018. Estimating Above-Ground Biomass in Sub-Tropical Buffer Zone Community Forests, Nepal, Using Sentinel 2 Data. Remote Sens. 10, 601. https://doi.org/10.3390/rs10040601

Pandžic, M., Mihajlovic, D., Pandžic, J., Pfeifer, N., 2016. Assessment of the geometric quality of Sentinel-2 data. ISPRS - Int. Arch. Photogramm. Remote Sens. Spat. Inf. Sci. XLI-B1, 489–494. https://doi.org/10.5194/isprs-archives-XLI-B1-489-2016

Pant, H., Tewari, A., 2014. Carbon sequestration in Chir-Pine (Pinus roxburghii Sarg.) forests under various disturbance levels in Kumaun Central Himalaya. J. For. Res. 25, 401–405. https://doi.org/10.1007/s11676-013-0424-z

Papathanassiou, K.P., Cloude, S.R., 2001. Single-baseline polarimetric SAR interferometry. IEEE Trans. Geosci. Remote Sens. 39, 2352–2363.

Pariyar, S., Mandal, R.A., 2019. Comparative tree height measurement using different instrument. Int. J. Ecol. Environ. Sci. 1, 12–17.

Pariyar, S., Volkova, L., Sharma, R.P., Sunam, R., Weston, C.J., 2019. Aboveground carbon of community-managed Chirpine (Pinus roxburghii Sarg.) forests of Nepal based on stand types and geographic aspects. PeerJ 7, e6494. https://doi.org/10.7717/peerj.6494

Pearson, T., Walker, S., Brown, S., 2005. Sourcebook for Land Use, Land-Use Change and Forestry Projects. Winrock International, Virginia, USA.

Peng, C., Zhang, L., Liu, J., 2001. Developing and Validating Nonlinear Height–Diameter Models for Major Tree Species of Ontario's Boreal Forests. North. J. Appl. For. 18, 87–94. https://doi.org/10.1093/njaf/18.3.87

Periasamy, S., 2018. Significance of dual polarimetric synthetic aperture radar in biomass retrieval: An attempt on Sentinel-1. Remote Sens. Environ. 217, 537–549.

Pham, L.T.H., Brabyn, L., 2017. Monitoring mangrove biomass change in Vietnam using SPOT images and an object-based approach combined with machine learning algorithms. ISPRS J. Photogramm. Remote Sens. 128, 86–97. https://doi.org/10.1016/j.isprsjprs.2017.03.013

Pham, M.H., Do, T.H., Pham, V.-M., Bui, Q.-T., 2020. Mangrove forest classification and aboveground biomass estimation using an atom search algorithm and adaptive neuro-fuzzy inference system. PLOS ONE 15, e0233110. https://doi.org/10.1371/journal.pone.0233110

Pham, T.D., Yoshino, K., Bui, D.T., 2017. Biomass estimation of Sonneratia caseolaris (l.) Engler at a coastal area of Hai Phong city (Vietnam) using ALOS-2 PALSAR imagery and GIS-based multi-layer perceptron neural networks. GIScience Remote Sens. 54, 329–353. https://doi.org/10.1080/15481603.2016.1269869

Pham, T.D., Yoshino, K., Le, N.N., Bui, D.T., 2018. Estimating aboveground biomass of a mangrove plantation on the Northern coast of Vietnam using machine learning techniques with an integration of ALOS-2 PALSAR-2 and Sentinel-2A data. Int. J. Remote Sens. 39, 7761–7788. https://doi.org/10.1080/01431161.2018.1471544

Pham, T.D., Yokoya, N., Xia, J., Ha, N.T., Le, N.N., Nguyen, T.T.T., Dao, T.H., Vu, T.T.P., Pham, Tien Duc, Takeuchi, W., 2020. Comparison of Machine Learning Methods for Estimating Mangrove Above-Ground Biomass Using Multiple Source Remote Sensing Data in the Red River Delta Biosphere Reserve, Vietnam. Remote Sens. 12, 1334. https://doi.org/10.3390/rs12081334

Phan, T.N., Kuch, V., Lehnert, L.W., 2020. Land Cover Classification using Google Earth Engine and Random Forest Classifier—The Role of Image Composition. Remote Sens. 12, 2411. https://doi.org/10.3390/rs12152411

Philip, M.S., 1994. Measuring trees and forests, 2nd ed. CAB International, Wallingford, England.

Pielke, R.A., Pitman, A., Niyogi, D., Mahmood, R., McAlpine, C., Hossain, F., Goldewijk, K.K., Nair, U., Betts, R., Fall, S., Reichstein, M., Kabat, P., Noblet, N. de, 2011. Land use/land cover changes and climate: modeling analysis and observational evidence. WIREs Clim. Change 2, 828–850. https://doi.org/10.1002/wcc.144

Podlaski, R., Sobala, T., Kocurek, M., 2019. Patterns of tree diameter distributions in managed and unmanaged Abies alba Mill. and Fagus sylvatica L. forest patches. For. Ecol. Manag. 435, 97–105. https://doi.org/10.1016/j.foreco.2018.12.046

Pokhriyal, P., Uniyal, P., Chauhan, D., Todaria, N., 2010. Regeneration status of tree species in forest of Phakot and Pathri Rao watersheds in Garhwal Himalaya. Curr. Sci. 98, 171–175.

Polunin, O., Stainton, A., 1984. Flowers of the Himalaya. Oxford University Press, Delhi, India.

Pommerening, A., 2002. Approaches to quantifying forest structures. For. Int. J. For. Res. 75, 305–324. https://doi.org/10.1093/forestry/75.3.305

Portela, M.G.T., de Espindola, G.M., Valladares, G.S., Amorim, J.V.A., Frota, J.C.O., 2020. Vegetation biomass and carbon stocks in the Parnaíba River Delta, NE Brazil. Wetl. Ecol. Manag. 28, 607–622. https://doi.org/10.1007/s11273-020-09735-y

Poškus, M.S., Žukauskienė, R., 2017. Predicting adolescents' recycling behavior among different big five personality types. J. Environ. Psychol. 54, 57–64.

Pouliot, D., Latifovic, R., Zabcic, N., Guindon, L., Olthof, I., 2014. Development and assessment of a 250m spatial resolution MODIS annual land cover time series (2000–2011) for the forest region of Canada derived from change-based updating. Remote Sens. Environ. 140, 731–743. https://doi.org/10.1016/j.rse.2013.10.004

Prasad, A.M., Iverson, L.R., Liaw, A., 2006. Newer Classification and Regression Tree Techniques: Bagging and Random Forests for Ecological Prediction. Ecosystems 9, 181–199. https://doi.org/10.1007/s10021-005-0054-1

Prawasi, R., Sharma, M.P., Pal, O., 2019. Biomass Estimation through Vegetation Structure Analysis and Ecological Trails of Almora District, Uttarakhand using Geospatial Technology. E-J. Earth Sci. India 12, 136–145. https://doi.org/10.31870/ESI.12.3.2019.10

Purohit, S., Aggarwal, S.P., Patel, N.R., 2021. Estimation of forest aboveground biomass using combination of Landsat 8 and Sentinel-1A data with random forest regression algorithm in Himalayan Foothills. Trop. Ecol. 62, 288–300. https://doi.org/10.1007/s42965-021-00140-x

Qamer, F.M., Abbas, S., Saleem, R., Shehzad, K., Ali, H., Gilani, H., 2012. Forest cover change assessment in conflict-affected areas of northwest Pakistan: the case of swat and shangla districts. J. Mt. Sci. 9, 297–306. https://doi.org/10.1007/s11629-009-2319-1

Qasim, M., Hubacek, K., Termansen, M., Khan, A., 2011. Spatial and temporal dynamics of land use pattern in District Swat, Hindu Kush Himalayan region of Pakistan. Appl. Geogr. 31, 820–828. https://doi.org/10.1016/j.apgeog.2010.08.008

QGIS Development Team, 2020. QGIS Geographic Information System (Open Source Geospatial Foundation Project).

Qiu, A., Yang, Y., Wang, D., Xu, S., Wang, X., 2020. Exploring parameter selection for carbon monitoring based on Landsat-8 imagery of the aboveground forest biomass on Mount Tai. Eur. J. Remote Sens. 53, 4–15. https://doi.org/10.1080/22797254.2019.1686717

Quegan, S., Le Toan, T., Chave, J., Dall, J., Exbrayat, J.-F., Minh, D.H.T., Lomas, M., d'Alessandro, M.M., Paillou, P., Papathanassiou, K., 2019. The European Space Agency BIOMASS mission: Measuring forest above-ground biomass from space. Remote Sens. Environ. 227, 44–60. https://doi.org/10.1016/j.rse.2019.03.032

Qureshi, A., Pariva, Badola, R., Hussain, S.A., 2012. A review of protocols used for assessment of carbon stock in forested landscapes. Environ. Sci. Policy 16, 81–89. https://doi.org/10.1016/j.envsci.2011.11.001

R Core Team, 2020. R: A Language and Environment for Statistical Computing. R Foundation for Statistical Computing, Vienna, Austria.

Rahman, M.M., Csaplovics, E., Koch, B., 2005. An efficient regression strategy for extracting forest biomass information from satellite sensor data. Int. J. Remote Sens. 26, 1511–1519. https://doi.org/10.1080/01431160500044705

Rana, K., Kumar, M., Kumar, A., 2020. Assessment of Annual Shoot Biomass and Carbon Storage Potential of Grewia optiva: an Approach to Combat Climate Change in Garhwal Himalaya. Water. Air. Soil Pollut. 231, 450. https://doi.org/10.1007/s11270-020-04825-2

Ranot, M., Sharma, D.P., 2013. Carbon Storage Potential of Selected Trees in Sub-Tropical Zone of Himachal Pradesh. J. Tree Sci. 32, 28–33.

Ratner, B., 2009. The correlation coefficient: Its values range between +1/−1, or do they? J. Target. Meas. Anal. Mark. 17, 139–142. https://doi.org/10.1057/jt.2009.5

Reddy, R.S., Rajashekar, G., Jha, C., Dadhwal, V., Pelissier, R., Couteron, P., 2017. Estimation of above ground biomass using texture metrics derived from IRS Cartosat-1 panchromatic data in evergreen forests of Western Ghats, India. J. Indian Soc. Remote Sens. 45, 657–665.

Rees, G., 1999. The Remote Sensing Data Book. Cambridge University Press.

Rehman Zia, U.U., Rashid, T. ur, Awan, W.N., Hussain, A., Ali, M., 2020. Quantification and technological assessment of bioenergy generation through agricultural residues in Punjab (Pakistan). Biomass Bioenergy 139, 105612. https://doi.org/10.1016/j.biombioe.2020.105612

Reichstein, M., Bahn, M., Ciais, P., Frank, D., Mahecha, M.D., Seneviratne, S.I., Zscheischler, J., Beer, C., Buchmann, N., Frank, D.C., 2013. Climate extremes and the carbon cycle. Nature 500, 287–295.

Reyes-Palomeque, G., Dupuy, J.M., Portillo-Quintero, C.A., Andrade, J.L., Tun-Dzul, F.J., Hernández-Stefanoni, J.L., 2021. Mapping forest age and characterizing vegetation structure and species composition in tropical dry forests. Ecol. Indic. 120, 106955. https://doi.org/10.1016/j.ecolind.2020.106955

Richards, J.A., Jia, X., 2006. Remote Sensing Digital Image Analysis: An Introduction, 4th ed. Springer-Verlag, Berlin Heidelberg. https://doi.org/10.1007/3-540-29711-1

Richardson, H.J., Hill, D.J., Denesiuk, D.R., Fraser, L.H., 2017. A comparison of geographic datasets and field measurements to model soil carbon using random forests and stepwise regressions (British Columbia, Canada). GIScience Remote Sens. 54, 573–591. https://doi.org/10.1080/15481603.2017.1302181

Riihimäki, H., Heiskanen, J., Luoto, M., 2017. The effect of topography on arctic-alpine aboveground biomass and NDVI patterns. Int. J. Appl. Earth Obs. Geoinformation 56, 44–53. https://doi.org/10.1016/j.jag.2016.11.005

Rodriguez-Galiano, V.F., Ghimire, B., Rogan, J., Chica-Olmo, M., Rigol-Sanchez, J.P., 2012. An assessment of the effectiveness of a random forest classifier for land-

cover classification. ISPRS J. Photogramm. Remote Sens. 67, 93–104. https://doi.org/10.1016/j.isprsjprs.2011.11.002

Rodríguez-Veiga, P., Carreiras, J., Smallman, T.L., Exbrayat, J.-F., Ndambiri, J., Mutwiri, F., Nyasaka, D., Quegan, S., Williams, M., Balzter, H., 2020. Carbon Stocks and Fluxes in Kenyan Forests and Wooded Grasslands Derived from Earth Observation and Model-Data Fusion. Remote Sens. 12, 2380. https://doi.org/10.3390/rs12152380

Rodríguez-Veiga, P., Wheeler, J., Louis, V., Tansey, K., Balzter, H., 2017. Quantifying Forest Biomass Carbon Stocks From Space. Curr. For. Rep. 3, 1–18. https://doi.org/10.1007/s40725-017-0052-5

Rojas Montaño, R.A.N., Roberto Sanquetta, C., Wojciechowski, J., Mattar, E., Dalla Corte, A.P., Todt, E., 2017. Artificial Intelligence Models to Estimate Biomass of Tropical Forest Trees. Polibits 56, 29–37.

Rosenfield, M.F., Souza, A.F., 2013. Biomass and carbon in subtropical forests: Overview of determinants, quantification methods and estimates. Neotropical Biol. Conserv. 8, 103–110. https://doi.org/10.4013/nbc.2013.82.06

Rossi, S., Deslauriers, A., Anfodillo, T., Carraro, V., 2007. Evidence of threshold temperatures for xylogenesis in conifers at high altitudes. Oecologia 152, 1–12. https://doi.org/10.1007/s00442-006-0625-7

Roy, D.P., Wulder, M.A., Loveland, T.R., C.e., W., Allen, R.G., Anderson, M.C., Helder, D., Irons, J.R., Johnson, D.M., Kennedy, R., Scambos, T.A., Schaaf, C.B., Schott, J.R., Sheng, Y., Vermote, E.F., Belward, A.S., Bindschadler, R., Cohen, W.B., Gao, F., Hipple, J.D., Hostert, P., Huntington, J., Justice, C.O., Kilic, A., Kovalskyy, V., Lee, Z.P., Lymburner, L., Masek, J.G., McCorkel, J., Shuai, Y., Trezza, R., Vogelmann, J., Wynne, R.H., Zhu, Z., 2014. Landsat-8: Science and product vision for terrestrial global change research. Remote Sens. Environ. 145, 154–172. https://doi.org/10.1016/j.rse.2014.02.001

RStudio Team, 2020. RStudio: Integrated Development Environment for R. RStudio, PBC, Boston, MA.

Saarela, S., Wästlund, A., Holmström, E., Mensah, A.A., Holm, S., Nilsson, M., Fridman, J., Ståhl, G., 2020. Mapping aboveground biomass and its prediction uncertainty using LiDAR and field data, accounting for tree-level allometric and LiDAR model errors. For. Ecosyst. 7, 43. https://doi.org/10.1186/s40663-020-00245-0

Saatchi, S.S., Harris, N.L., Brown, S., Lefsky, M., Mitchard, E.T., Salas, W., Zutta, B.R., Buermann, W., Lewis, S.L., Hagen, S., 2011. Benchmark map of forest carbon stocks in tropical regions across three continents. Proc. Natl. Acad. Sci. 108, 9899–9904.

Sader, S.A., Waide, R.B., Lawrence, W.T., Joyce, A.T., 1989. Tropical forest biomass and successional age class relationships to a vegetation index derived from

landsat TM data. Remote Sens. Environ. 28, 143–198. https://doi.org/10.1016/0034-4257(89)90112-0

Saeed, M.A., Ashraf, A., Ahmed, B., Shahid, M., 2011. Monitoring deforestation and urbanization growth in rawal watershed area using remote sensing and gis techniques. Sci. Vis. 16–17, 93–104.

Sajid, M.J., 2020. Inter-sectoral carbon ties and final demand in a high climate risk country: The case of Pakistan. J. Clean. Prod. 269, 122254. https://doi.org/10.1016/j.jclepro.2020.122254

Saleem, A.R., Rashid, F., Rashid, A., Mahmood, T., Nisa, W., 2014. Impact of population dynamics on Margalla Hills Ecosystem: a community-level case study. Chin. J. Popul. Resour. Environ. 12, 345–353. https://doi.org/10.1080/10042857.2014.969363

Salehi, B., Mishra, A.P., Nigam, M., Karazhan, N., Shukla, I., Kiełtyka-Dadasiewicz, A., Sawicka, B., Głowacka, A., Abu-Darwish, M.S., Tarawneh, A.H., Gadetskaya, A.V., Cabral, C., Salgueiro, L., Victoriano, M., Martorell, M., Docea, A.O., Abdolshahi, A., Calina, D., Sharifi-Rad, J., 2021. Ficus plants: State of the art from a phytochemical, pharmacological, and toxicological perspective. Phytother. Res. 35, 1187–1217. https://doi.org/10.1002/ptr.6884

Salum, R.B., Souza-Filho, P.W.M., Simard, M., Silva, C.A., Fernandes, M.E.B., Cougo, M.F., do Nascimento, W., Rogers, K., 2020. Improving mangrove above-ground biomass estimates using LiDAR. Estuar. Coast. Shelf Sci. 236, 106585. https://doi.org/10.1016/j.ecss.2020.106585

Samie, A., Deng, X., Jia, S., Chen, D., 2017. Scenario-Based Simulation on Dynamics of Land-Use-Land-Cover Change in Punjab Province, Pakistan. Sustainability 9, 1285. https://doi.org/10.3390/su9081285

Sandberg, G., Ulander, L.M.H., Fransson, J.E.S., Holmgren, J., Toan, T.L., 2011. L- and P-band backscatter intensity for biomass retrieval in hemiboreal forest. Remote Sens. Environ. 115, 2874–2886. https://doi.org/10.1016/j.rse.2010.03.018

Santos, J.R., Freitas, C.C., Araujo, L.S., Dutra, L.V., Mura, J.C., Gama, F.F., Soler, L.S., Sant'Anna, S.J.S., 2003. Airborne P-band SAR applied to the aboveground biomass studies in the Brazilian tropical rainforest. Remote Sens. Environ. 87, 482–493. https://doi.org/10.1016/j.rse.2002.12.001

Saqib, Z., Mahmood, Adeel, Naseem Malik, R., Mahmood, Aqeel, Hussian Syed, J., Ahmad, T., 2014. Indigenous knowledge of medicinal plants in Kotli Sattian, Rawalpindi district, Pakistan. J. Ethnopharmacol. 151, 820–828. https://doi.org/10.1016/j.jep.2013.11.034

Sarker, L.R., Nichol, J., Iz, H.B., Ahmad, B.B., Rahman, A.A., 2013. Forest Biomass Estimation Using Texture Measurements of High-Resolution Dual-Polarization C-Band SAR Data. IEEE Trans. Geosci. REMOTE Sens. 51, 3371–3384. https://doi.org/10.1109/TGRS.2012.2219872

Sarker, L.R., Nichol, J.E., 2011. Improved forest biomass estimates using ALOS AVNIR-2 texture indices. Remote Sens. Environ. 115, 968–977.

Schepaschenko, D., Moltchanova, E., Shvidenko, A., Blyshchyk, V., Dmitriev, E., Martynenko, O., See, L., Kraxner, F., 2018. Improved Estimates of Biomass Expansion Factors for Russian Forests. Forests 9, 312. https://doi.org/10.3390/f9060312

Schlund, M., Davidson, M.W.J., 2018. Aboveground Forest Biomass Estimation Combining L- and P-Band SAR Acquisitions. Remote Sens. 10, 1151. https://doi.org/10.3390/rs10071151

Schneider, A., 2012. Monitoring land cover change in urban and peri-urban areas using dense time stacks of Landsat satellite data and a data mining approach. Remote Sens. Environ. 124, 689–704. https://doi.org/10.1016/j.rse.2012.06.006

Schuh, M., Favarin, J.A.S., Marchesan, J., Alba, E., Berra, E.F., Pereira, R.S., 2020. Machine learning and generalized linear model techniques to predict aboveground biomass in Amazon rainforest using LiDAR data. J. Appl. Remote Sens. 14, 034518. https://doi.org/10.1117/1.JRS.14.034518

Schumacher, P., Mislimshoeva, B., Brenning, A., Zandler, H., Brandt, M., Samimi, C., Koellner, T., 2016. Do red edge and texture attributes from high-resolution satellite data improve wood volume estimation in a semi-arid mountainous region? Remote Sens. 8, 540.

Scornet, E., Biau, G., Vert, J.-P., 2015. Consistency of random forests. Ann. Stat. 43, 1716–1741. https://doi.org/10.1214/15-AOS1321

Segura, M., Kanninen, M., 2005. Allometric Models for Tree Volume and Total Aboveground Biomass in a Tropical Humid Forest in Costa Rica1. Biotropica 37, 2–8. https://doi.org/10.1111/j.1744-7429.2005.02027.x

Shafiq, M., Ahmad, S., Nasir, A., Ikram, M., Aslam, M., Khan, M., 1997. Surface runoff from degraded scrub forest watershed under high rainfall zone. J. Eng. Appl. Sci. 16, 7–12.

Shah, A., Ali, K., Nizami, S.M., 2021. Spatio-temporal analysis of urban sprawl in Islamabad, Pakistan during 1979–2019, using remote sensing. GeoJournal. https://doi.org/10.1007/s10708-021-10413-6

Shah, H., Bakhsh, M.I., Amjad, M., 1991. Tree growth on farmlands of NWFP. Pak. J. For. 41, 74–81.

Shahbaz, B., Ali, T., Suleri, A.Q., 2007. A critical analysis of forest policies of Pakistan: implications for sustainable livelihoods. Mitig. Adapt. Strateg. Glob. Change 12, 441–453.

Shaheen, H., Khan, R.W.A., Hussain, K., Ullah, T.S., Nasir, M., Mehmood, A., 2016. Carbon stocks assessment in subtropical forest types of Kashmir Himalayas. Pak. J. Bot. 48, 2351–2357.

Shan, J., Toth, C.K. (Eds.), 2008. Topographic laser ranging and scanning: principles and processing. CRC press.

Shao, Z., Zhang, L., 2016. Estimating Forest Aboveground Biomass by Combining Optical and SAR Data: A Case Study in Genhe, Inner Mongolia, China. Sensors 16, 834. https://doi.org/10.3390/s16060834

Sharma, C.M., Baduni, N.P., Gairola, S., Ghildiyal, S.K., Suyal, S., 2010. Tree diversity and carbon stocks of some major forest types of Garhwal Himalaya, India. For. Ecol. Manag. 260, 2170–2179. https://doi.org/10.1016/j.foreco.2010.09.014

Sharma, C.M., Gairola, S., Baduni, N.P., Ghildiyal, S.K., Suyal, S., 2011. Variation in carbon stocks on different slope aspects in seven major forest types of temperate region of Garhwal Himalaya, India. J. Biosci. 36, 701–708. https://doi.org/10.1007/s12038-011-9103-4

Sharma, K., Bhatta, S., Khatri, G., Pajiyar, A., Joshi, D., 2020. Estimation of Carbon Stock in the Chir Pine (Pinus roxburghii Sarg.) Plantation Forest of Kathmandu Valley, Central Nepal. J. For. Environ. Sci. 36, 37–46. https://doi.org/10.7747/JFES.2020.36.1.37

Sharma, R.K., Sankhayan, P.L., Hofstad, O., 2008. Forest biomass density, utilization and production dynamics in a western Himalayan watershed. J. For. Res. 19, 171. https://doi.org/10.1007/s11676-008-0032-5

Shehzad, K., Qamer, F.M., Murthy, M.S.R., Abbas, S., Bhatta, L.D., 2014. Deforestation trends and spatial modelling of its drivers in the dry temperate forests of northern Pakistan — A case study of Chitral. J. Mt. Sci. 11, 1192–1207. https://doi.org/10.1007/s11629-013-2932-x

Sheikh, M.A., Kumar, M., Bhat, J.A., 2011. Wood specific gravity of some tree species in the Garhwal Himalayas, India. For. Sudies China 13, 225–230. https://doi.org/10.1007/s11632-011-0310-8

Sheikh, M.A., Kumar, M., Bussmann, R.W., 2009. Altitudinal variation in soil organic carbon stock in coniferous subtropical and broadleaf temperate forests in Garhwal Himalaya. Carbon Balance Manag. 4, 6. https://doi.org/10.1186/1750-0680-4-6

Sheikh, M.I., 1993. Trees of Pakistan. GOP-USAID Forestry Planning and Development Project, Islamabad, Pakistan.

Shih, H., Stow, D.A., Tsai, Y.H., 2019. Guidance on and comparison of machine learning classifiers for Landsat-based land cover and land use mapping. Int. J. Remote Sens. 40, 1248–1274. https://doi.org/10.1080/01431161.2018.1524179

Shimano, K., 2000. A power function for forest structure and regeneration pattern of pioneer and climax species in patch mosaic forests. Plant Ecol. 146, 205–218. https://doi.org/10.1023/A:1009867302660

Sibanda, M., Mutanga, O., Rouget, M., Kumar, L., 2017. Estimating biomass of native grass grown under complex management treatments using worldview-3 spectral derivatives. Remote Sens. 9, 55.

Silva, C.A., Duncanson, L., Hancock, S., Neuenschwander, A., Thomas, N., Hofton, M., Fatoyinbo, L., Simard, M., Marshak, C.Z., Armston, J., Lutchke, S., Dubayah, R., 2021. Fusing simulated GEDI, ICESat-2 and NISAR data for regional aboveground biomass mapping. Remote Sens. Environ. 253, 112234. https://doi.org/10.1016/j.rse.2020.112234

Silvia, L., Alexander, T., Anna, K., Polina, K., 2019. Assessment of carbon dynamics in Ecuadorian forests through the Mathematical Spatial Model of Global Carbon Cycle and the Normalized Differential Vegetation Index (NDVI). E3S Web Conf. 96, 02002. https://doi.org/10.1051/e3sconf/20199602002

Singh, A., 1989. Review Article Digital change detection techniques using remotely-sensed data. Int. J. Remote Sens. 10, 989–1003. https://doi.org/10.1080/01431168908903939

Singh, J.S., Tiwari, A.K., Saxena, A.K., 1985. Himalayan Forests: A Net Source of Carbon for the Atmosphere. Environ. Conserv. 12, 67–69. https://doi.org/10.1017/S0376892900015174

Sinha, S., Jeganathan, C., Sharma, L.K., Nathawat, M.S., 2015. A review of radar remote sensing for biomass estimation. Int. J. Environ. Sci. Technol. 12, 1779–1792. https://doi.org/10.1007/s13762-015-0750-0

Sinha, S., Jeganathan, C., Sharma, L.K., Nathawat, M.S., Das, A.K., Mohan, S., 2016. Developing synergy regression models with space-borne ALOS PALSAR and Landsat TM sensors for retrieving tropical forest biomass. J. Earth Syst. Sci. 125, 725–735. https://doi.org/10.1007/s12040-016-0692-z

Sivasankar, T., Lone, J., Sarma, K.K., Qadir, A., Raju, P., 2018. The potential of multi-frequency multipolarized ALOS-2/PALSAR-2 and Sentinel-1 SAR data for aboveground forest biomass estimation. Int. J. Eng. Technol. 10, 797–802. https://doi.org/10.21817/ijet/2018/v10i3/181003095

Skowronski, N.S., Clark, K.L., Gallagher, M., Birdsey, R.A., Hom, J.L., 2014. Airborne laser scanner-assisted estimation of aboveground biomass change in a temperate oak–pine forest. Remote Sens. Environ., Special Issue on 2012 ForestSAT 151, 166–174. https://doi.org/10.1016/j.rse.2013.12.015

Slik, J.W.F., Paoli, G., McGuire, K., Amaral, I., Barroso, J., Bastian, M., Blanc, L., Bongers, F., Boundja, P., Clark, C., Collins, M., Dauby, G., Ding, Y., Doucet, J.-L., Eler, E., Ferreira, L., Forshed, O., Fredriksson, G., Gillet, J.-F., Harris, D., Leal, M., Laumonier, Y., Malhi, Y., Mansor, A., Martin, E., Miyamoto, K., Araujo-Murakami, A., Nagamasu, H., Nilus, R., Nurtjahya, E., Oliveira, Á., Onrizal, O., Parada-Gutierrez, A., Permana, A., Poorter, L., Poulsen, J., Ramirez-Angulo, H., Reitsma, J., Rovero, F., Rozak, A., Sheil, D., Silva-Espejo, J., Silveira, M., Spironelo, W., Steege, H. ter, Stevart, T., Navarro-Aguilar, G.E., Sunderland, T., Suzuki, E., Tang, J., Theilade, I.,

Heijden, G. van der, Valkenburg, J. van, Do, T.V., Vilanova, E., Vos, V., Wich, S., Wöll, H., Yoneda, T., Zang, R., Zhang, M.-G., Zweifel, N., 2013. Large trees drive forest aboveground biomass variation in moist lowland forests across the tropics. Glob. Ecol. Biogeogr. 22, 1261–1271. https://doi.org/10.1111/geb.12092

Small, D., 2011. Flattening Gamma: Radiometric Terrain Correction for SAR Imagery. IEEE Trans. Geosci. Remote Sens. 49, 3081–3093. https://doi.org/10.1109/TGRS.2011.2120616

Smit, B., Skinner, M.W., 2002. Adaptation options in agriculture to climate change: a typology. Mitig. Adapt. Strateg. Glob. Change 7, 85–114. https://doi.org/10.1023/A:1015862228270

Smith, R., Renton, M., Reid, N., 2017. Growth and carbon sequestration by remnant Eucalyptus camaldulensis woodlands in semi-arid Australia during La Niña conditions. Agric. For. Meteorol. 232, 704–710. https://doi.org/10.1016/j.agrformet.2016.10.014

SNAP, 2020. Sentinels Application Platform software. European Space Agency.

Soares, J.V., Rennó, C.D., Formaggio, A.R., da Costa Freitas Yanasse, C., Frery, A.C., 1997. An investigation of the selection of texture features for crop discrimination using SAR imagery. Remote Sens. Environ., Spaceborne Imaging Radar Mission 59, 234–247. https://doi.org/10.1016/S0034-4257(96)00156-3

Soares, M.L.G., Schaeffer-Novelli, Y., 2005. Above-ground biomass of mangrove species. I. Analysis of models. Estuar. Coast. Shelf Sci. 65, 1–18. https://doi.org/10.1016/j.ecss.2005.05.001

Solberg, S., Astrup, R., Gobakken, T., Næsset, E., Weydahl, D.J., 2010. Estimating spruce and pine biomass with interferometric X-band SAR. Remote Sens. Environ. 114, 2353–2360. https://doi.org/10.1016/j.rse.2010.05.011

Solomon, N., Birhane, E., Tadesse, T., Treydte, A.C., Meles, K., 2017. Carbon stocks and sequestration potential of dry forests under community management in Tigray, Ethiopia. Ecol. Process. 6, 20. https://doi.org/10.1186/s13717-017-0088-2

Song, C., 2013. Optical remote sensing of forest leaf area index and biomass. Prog. Phys. Geogr. 37, 98–113. https://doi.org/10.1177/0309133312471367

Soutter, A.R.B., Mõttus, R., 2020. "Global warming" versus "climate change": A replication on the association between political self-identification, question wording, and environmental beliefs. J. Environ. Psychol. 69, 101413. https://doi.org/10.1016/j.jenvp.2020.101413

Spanner, M.A., Pierce, L.L., Peterson, D.L., Running, S.W., 1990. Remote sensing of temperate coniferous forest leaf area index The influence of canopy closure, understory vegetation and background reflectance. Int. J. Remote Sens. 11, 95–111. https://doi.org/10.1080/01431169008955002

Spracklen, B.D., Kalamandeen, M., Galbraith, D., Gloor, E., Spracklen, D.V., 2015. A Global Analysis of Deforestation in Moist Tropical Forest Protected Areas. PLOS ONE 10, e0143886. https://doi.org/10.1371/journal.pone.0143886

Stathakis, D., Faraslis, I., 2014. Monitoring urban sprawl using simulated PROBA-V data. Int. J. Remote Sens. 35, 2731–2743. https://doi.org/10.1080/01431161.2014.883089

Steven, M.D., Malthus, T.J., Baret, F., Xu, H., Chopping, M.J., 2003. Intercalibration of vegetation indices from different sensor systems. Remote Sens. Environ. 88, 412–422. https://doi.org/10.1016/j.rse.2003.08.010

Story, M., Congalton, R.G., 1986. Accuracy assessment: a user's perspective. Photogramm. Eng. Remote Sens. 52, 397–399.

Strobl, C., Boulesteix, A.-L., Kneib, T., Augustin, T., Zeileis, A., 2008. Conditional variable importance for random forests. BMC Bioinformatics 9, 307. https://doi.org/10.1186/1471-2105-9-307

Su, Y., Guo, Q., Xue, B., Hu, T., Alvarez, O., Tao, S., Fang, J., 2016. Spatial distribution of forest aboveground biomass in China: Estimation through combination of spaceborne lidar, optical imagery, and forest inventory data. Remote Sens. Environ. 173, 187–199. https://doi.org/10.1016/j.rse.2015.12.002

Subedi, C.K., Gurung, J., Ghimire, S.K., Chettri, N., Pasakhala, B., Bhandari, P., Chaudhary, R.P., 2018. Variation in structure and composition of two pine forests in Kailash Sacred Landscape, Nepal. Banko Janakari 28, 26–36. https://doi.org/10.3126/banko.v28i1.21453

Sudhakar Reddy, C., Vazeed Pasha, S., Satish, K.V., Saranya, K.R.L., Jha, C.S., Krishna Murthy, Y.V.N., 2018. Quantifying nationwide land cover and historical changes in forests of Nepal (1930–2014): implications on forest fragmentation. Biodivers. Conserv. 27, 91–107. https://doi.org/10.1007/s10531-017-1423-8

Sun, G., Ranson, K.J., Kharuk, V.I., 2002. Radiometric slope correction for forest biomass estimation from SAR data in the Western Sayani Mountains, Siberia. Remote Sens. Environ., Recent Advances in Remote Sensing of Biophysical Variables 79, 279–287. https://doi.org/10.1016/S0034-4257(01)00279-6

Sun, L., Wang, M., Fan, X., 2020. Spatial pattern and driving factors of biomass carbon density for natural and planted coniferous forests in mountainous terrain, eastern Loess Plateau of China. For. Ecosyst. 7, 9. https://doi.org/10.1186/s40663-020-0218-7

Sun, W., Liu, X., 2019. Review on carbon storage estimation of forest ecosystem and applications in China. For. Ecosyst. 7, 4. https://doi.org/10.1186/s40663-019-0210-2

Sun, Y., Kamel, M.S., Wong, A.K.C., Wang, Y., 2007. Cost-sensitive boosting for classification of imbalanced data. Pattern Recognit. 40, 3358–3378. https://doi.org/10.1016/j.patcog.2007.04.009

Swathandran, S., Aslam, M.A.M., 2019. Assessing the role of SWIR band in detecting agricultural crop stress: a case study of Raichur district, Karnataka, India. Environ. Monit. Assess. 191, 442. https://doi.org/10.1007/s10661-019-7566-1

Szantoi, Z., Strobl, P., 2019. Copernicus Sentinel-2 Calibration and Validation. Eur. J. Remote Sens. 52, 253–255. https://doi.org/10.1080/22797254.2019.1582840

Taddeo, S., Dronova, I., Depsky, N., 2019. Spectral vegetation indices of wetland greenness: Responses to vegetation structure, composition, and spatial distribution. Remote Sens. Environ. 234, 111467. https://doi.org/10.1016/j.rse.2019.111467

Tadese, S., Soromessa, T., Bekele, T., 2021. Analysis of the Current and Future Prediction of Land Use/Land Cover Change Using Remote Sensing and the CA-Markov Model in Majang Forest Biosphere Reserves of Gambella, Southwestern Ethiopia. Sci. World J. 2021, e6685045. https://doi.org/10.1155/2021/6685045

Talukdar, S., Singha, P., Mahato, S., Shahfahad, Pal, S., Liou, Y.-A., Rahman, A., 2020a. Land-Use Land-Cover Classification by Machine Learning Classifiers for Satellite Observations—A Review. Remote Sens. 12, 1135. https://doi.org/10.3390/rs12071135

Talukdar, S., Singha, P., Shahfahad, Mahato, S., Praveen, B., Rahman, A., 2020b. Dynamics of ecosystem services (ESs) in response to land use land cover (LU/LC) changes in the lower Gangetic plain of India. Ecol. Indic. 112, 106121. https://doi.org/10.1016/j.ecolind.2020.106121

Tariq, A., Shu, H., Siddiqui, S., Imran, M., Farhan, M., 2021. Monitoring Land Use And Land Cover Changes Using Geospatial Techniques, A Case Study Of Fateh Jang, Attock, Pakistan. Geogr. Environ. Sustain. 14, 41–52. https://doi.org/10.24057/2071-9388-2020-117

Teluguntla, P., Thenkabail, P.S., Oliphant, A., Xiong, J., Gumma, M.K., Congalton, R.G., Yadav, K., Huete, A., 2018. A 30-m landsat-derived cropland extent product of Australia and China using random forest machine learning algorithm on Google Earth Engine cloud computing platform. ISPRS J. Photogramm. Remote Sens. 144, 325–340. https://doi.org/10.1016/j.isprsjprs.2018.07.017

Tetemke, B.A., Birhane, E., Rannestad, M.M., Eid, T., 2019. Allometric Models for Predicting Aboveground Biomass of Trees in the Dry Afromontane Forests of Northern Ethiopia. Forests 10, 1114. https://doi.org/10.3390/f10121114

Thakare, V.S., Patil, N.N., 2014. Classification of Texture Using Gray Level Co-occurrence Matrix and Self-Organizing Map, in: 2014 International Conference on Electronic Systems, Signal Processing and Computing Technologies. Presented at the 2014 International Conference on Electronic Systems, Signal Processing and Computing Technologies, pp. 350–355. https://doi.org/10.1109/ICESC.2014.66

Thanh Noi, P., Kappas, M., 2018. Comparison of Random Forest, k-Nearest Neighbor, and Support Vector Machine Classifiers for Land Cover Classification Using Sentinel-2 Imagery. Sensors 18, 18. https://doi.org/10.3390/s18010018

Thenkabail, P.S., Stucky, N., Griscom, B.W., Ashton, M.S., Diels, J., Meer, B. van der, Enclona, E., 2004. Biomass estimations and carbon stock calculations in the oil palm plantations of African derived savannas using IKONOS data. Int. J. Remote Sens. 25, 5447–5472. https://doi.org/10.1080/01431160412331291279

Thomas, V., Treitz, P., McCaughey, J., Morrison, I., 2006. Mapping stand-level forest biophysical variables for a mixedwood boreal forest using lidar: an examination of scanning density. Can. J. For. Res. 36, 34–47. https://doi.org/10.1139/x05-230

Thomlinson, J.R., Bolstad, P.V., Cohen, W.B., 1999. Coordinating Methodologies for Scaling Landcover Classifications from Site-Specific to Global: Steps toward Validating Global Map Products. Remote Sens. Environ. 70, 16–28. https://doi.org/10.1016/S0034-4257(99)00055-3

Thumaty, K.C., Fararoda, R., Middinti, S., Gopalakrishnan, R., Jha, C.S., Dadhwal, V.K., 2016. Estimation of Above Ground Biomass for Central Indian Deciduous Forests Using ALOS PALSAR L-Band Data. J. Indian Soc. Remote Sens. 44, 31–39. https://doi.org/10.1007/s12524-015-0462-4

Tilahun, M., Birner, R., Ilukor, J., 2017. Household-level preferences for mitigation of Prosopis juliflora invasion in the Afar region of Ethiopia: a contingent valuation. J. Environ. Plan. Manag. 60, 282–308. https://doi.org/10.1080/09640568.2016.1152955

Torres, B., Vasseur, L., López, R., Lozano, P., García, Y., Arteaga, Y., Bravo, C., Barba, C., García, A., 2020. Structure and above ground biomass along an elevation small-scale gradient: case study in an Evergreen Andean Amazon forest, Ecuador. Agrofor. Syst. 94, 1235–1245. https://doi.org/10.1007/s10457-018-00342-8

Tsutsumida, N., Comber, A.J., 2015. Measures of spatio-temporal accuracy for time series land cover data. Int. J. Appl. Earth Obs. Geoinformation 41, 46–55. https://doi.org/10.1016/j.jag.2015.04.018

Tucker, C.J., 1979. Red and Photographic Infrared l,lnear Combinations for Monitoring Vegetation. Remote Sens. Environ. 127–150.

Twisa, S., Buchroithner, M.F., 2019. Land-Use and Land-Cover (LULC) Change Detection in Wami River Basin, Tanzania. Land 8, 136. https://doi.org/10.3390/land8090136

Ullah, S., Abid, A., Aslam, W., Noor, R.S., Waqas, M.M., Gang, T., 2021. Predicting Behavioral Intention of Rural Inhabitants toward Economic Incentive for Deforestation in Gilgit-Baltistan, Pakistan. Sustainability 13, 617. https://doi.org/10.3390/su13020617

UN, 2015. The World Population Prospects: 2015 Revision (Report). Department of Economic and Social Affairs, Population Division, New York, USA.

UNEP-WCMC, 2014. Global statistics from the World Database on Protected Areas (WDPA), August 2014. Cambridge: UNEP-WCMC.

USGS, 2019. Landsat 8 (L8) Data Users Handbook.

Vafaei, S., Soosani, J., Adeli, K., Fadaei, H., Naghavi, H., Pham, T.D., Tien Bui, D., 2018. Improving Accuracy Estimation of Forest Aboveground Biomass Based on Incorporation of ALOS-2 PALSAR-2 and Sentinel-2A Imagery and Machine Learning: A Case Study of the Hyrcanian Forest Area (Iran). Remote Sens. 10, 172. https://doi.org/10.3390/rs10020172

Vanclay, J.K., 1994. Modelling Forest Growth and Yield: Applications to Mixed Tropical Forests. CAB International, Wallingford, UK.

Vapnik, V., 2000. The Nature of Statistical Learning Theory, 2nd ed, Information Science and Statistics. Springer-Verlag, New York. https://doi.org/10.1007/978-1-4757-3264-1

Vashum, K.T., Jayakumar, S., 2012. Methods to estimate above-ground biomass and carbon stock in natural forests-a review. J Ecosyst Ecogr 2, 1–7.

Vedeld, P., Angelsen, A., Bojö, J., Sjaastad, E., Berg, G.K., 2007. Forest environmental incomes and the rural poor. For. Policy Econ. 9, 869–879. https://doi.org/10.1016/j.forpol.2006.05.008

Velázquez-Martí, B., Sajdak, M., López-Cortés, I., 2013. Available residual biomass obtained from pruning Morus alba L. trees cultivated in urban forest. Renew. Energy 60, 27–33. https://doi.org/10.1016/j.renene.2013.04.001

Verburg, P.H., van de Steeg, J., Veldkamp, A., Willemen, L., 2009. From land cover change to land function dynamics: A major challenge to improve land characterization. J. Environ. Manage. 90, 1327–1335. https://doi.org/10.1016/j.jenvman.2008.08.005

Verma, A., Kaushal, R., Alam, N.M., Mehta, H., Chaturvedi, O.P., Mandal, D., Tomar, J.M.S., Rathore, A.C., Singh, C., 2014. Predictive models for biomass and carbon stocks estimation in Grewiaoptiva on degraded lands in western Himalaya. Agrofor. Syst. 88, 895–905. https://doi.org/10.1007/s10457-014-9734-1

Verma, P., Raghubanshi, A., Srivastava, P.K., Raghubanshi, A.S., 2020. Appraisal of kappa-based metrics and disagreement indices of accuracy assessment for parametric and nonparametric techniques used in LULC classification and change detection. Model. Earth Syst. Environ. 6, 1045–1059. https://doi.org/10.1007/s40808-020-00740-x

Vetaas, O.R., 2000. The Effect of Environmental Factors on the Regeneration of Quercus semecarpifolia Sm. in Central Himalaya, Nepal. Plant Ecol. 146, 137–144.

Vicharnakorn, P., Shrestha, R.P., Nagai, M., Salam, A.P., Kiratiprayoon, S., 2014. Carbon stock assessment using remote sensing and forest inventory data in Savannakhet, Lao PDR. Remote Sens. 6, 5452–5479.

Viña, A., Gitelson, A.A., Nguy-Robertson, A.L., Peng, Y., 2011. Comparison of different vegetation indices for the remote assessment of green leaf area index of crops. Remote Sens. Environ. 115, 3468–3478. https://doi.org/10.1016/j.rse.2011.08.010

Vosselman, G., Maas, H.-G. (Eds.), 2010. Airborne and terrestrial laser scanning. CRC press.

Vries, P.G. de, 1986. Sampling theory for forest inventory; a teach-yourself course. Springer-Verlag Berlin Heidelberg, Berlin and Heidelberg, Germany.

Wagner, W., Luckman, A., Vietmeier, J., Tansey, K., Balzter, H., Schmullius, C., Davidson, M., Gaveau, D., Gluck, M., Le Toan, T., Quegan, S., Shvidenko, A., Wiesmann, A., Yu, J.J., 2003. Large-scale mapping of boreal forest in SIBERIA using ERS tandem coherence and JERS backscatter data. Remote Sens. Environ. 85, 125–144. https://doi.org/10.1016/S0034-4257(02)00198-0

Walker, W., 2000. Introduction to RADAR Remote Sensing for Vegetation Mapping and Monitoring.

Walker, W., Baccini, A., Schwartzman, S., Ríos, S., Oliveira-Miranda, M.A., Augusto, C., Ruiz, M.R., Arrasco, C.S., Ricardo, B., Smith, R., Meyer, C., Jintiach, J.C., Campos, E.V., 2014. Forest carbon in Amazonia: the unrecognized contribution of indigenous territories and protected natural areas. Carbon Manag. 5, 479–485. https://doi.org/10.1080/17583004.2014.990680

Wang, B., Wang, H.-J., Qi, H., 2010. Wood recognition based on grey-level co-occurrence matrix, in: 2010 International Conference on Computer Application and System Modeling (ICCASM 2010). Presented at the 2010 International Conference on Computer Application and System Modeling (ICCASM 2010), pp. V1-269-V1-272. https://doi.org/10.1109/ICCASM.2010.5619388

Wang, C., Feng, M.-C., Yang, W.-D., Ding, G.-W., Sun, H., Liang, Z.-Y., Xie, Y.-K., Qiao, X.-X., 2016. Impact of spectral saturation on leaf area index and aboveground biomass estimation of winter wheat. Spectrosc. Lett. 49, 241–248. https://doi.org/10.1080/00387010.2015.1133652

Wang, J., Xiao, X., Bajgain, R., Starks, P., Steiner, J., Doughty, R.B., Chang, Q., 2019. Estimating leaf area index and aboveground biomass of grazing pastures using Sentinel-1, Sentinel-2 and Landsat images. ISPRS J. Photogramm. Remote Sens. 154, 189–201. https://doi.org/10.1016/j.isprsjprs.2019.06.007

Wang, M., Wright, J., Brownlee, A., Buswell, R., 2016. A comparison of approaches to stepwise regression on variables sensitivies in building simulation and analysis. Energy Build. 127, 313–326. https://doi.org/10.1016/j.enbuild.2016.05.065

Wang, Q., Blackburn, G.A., Onojeghuo, A.O., Dash, J., Zhou, L., Zhang, Y., Atkinson, P.M., 2017. Fusion of Landsat 8 OLI and Sentinel-2 MSI Data. IEEE Trans. Geosci. Remote Sens. 55, 3885–3899. https://doi.org/10.1109/TGRS.2017.2683444

Wang, S.W., Gebru, B.M., Lamchin, M., Kayastha, R.B., Lee, W.-K., 2020. Land Use and Land Cover Change Detection and Prediction in the Kathmandu District of Nepal Using Remote Sensing and GIS. Sustainability 12, 3925. https://doi.org/10.3390/su12093925

Wang, X., Pang, Y., Zhang, Z., Yuan, Y., 2014. Forest aboveground biomass estimation using SPOT-5 texture indices and spectral derivatives. Presented at the 2014 IEEE Geoscience and Remote Sensing Symposium, IEEE, pp. 2830–2833.

Wang, X., Wang, S., Dai, L., 2018. Estimating and mapping forest biomass in northeast China using joint forest resources inventory and remote sensing data. J. For. Res. 29, 797–811. https://doi.org/10.1007/s11676-017-0504-6

Wang, Y., Lehtomäki, M., Liang, X., Pyörälä, J., Kukko, A., Jaakkola, A., Liu, J., Feng, Z., Chen, R., Hyyppä, J., 2019. Is field-measured tree height as reliable as believed – A comparison study of tree height estimates from field measurement, airborne laser scanning and terrestrial laser scanning in a boreal forest. ISPRS J. Photogramm. Remote Sens. 147, 132–145. https://doi.org/10.1016/j.isprsjprs.2018.11.008

Wangda, P., Ohsawa, M., 2006. Structure and regeneration dynamics of dominant tree species along altitudinal gradient in a dry valley slopes of the Bhutan Himalaya. For. Ecol. Manag. 230, 136–150. https://doi.org/10.1016/j.foreco.2006.04.027

Wani, A.A., Joshi, P.K., Singh, O., 2015. Estimating biomass and carbon mitigation of temperate coniferous forests using spectral modeling and field inventory data. Ecol. Inform. 25, 63–70. https://doi.org/10.1016/j.ecoinf.2014.12.003

Wani, N., Velmurugan, A., Dadhwal, V.K., 2010. Assessment of agricultural crop and soil carbon pools in Madhya Pradesh, India. Trop. Ecol. 51, 11–19.

Wessel, M., Brandmeier, M., Tiede, D., 2018. Evaluation of Different Machine Learning Algorithms for Scalable Classification of Tree Types and Tree Species Based on Sentinel-2 Data. Remote Sens. 10, 1419. https://doi.org/10.3390/rs10091419

West, P.W., 2009. Tree and Forest Measurement, 2nd ed. Springer Berlin Heidelberg, Berlin, Heidelberg. https://doi.org/10.1007/978-3-540-95966-3

Wijaya, A., 2009. Evaluation of ALOS-PALSAR mosaic data for estimating stem volume and biomass: A case study from tropical rainforest of central Indonesia. J. Geogr. 2, 14–21.

Wilkes, P., Disney, M., Vicari, M.B., Calders, K., Burt, A., 2018. Estimating urban above ground biomass with multi-scale LiDAR. Carbon Balance Manag. 13, 1–20.

Williams, D.R., Clark, M., Buchanan, G.M., Ficetola, G.F., Rondinini, C., Tilman, D., Clark, M., Buchanan, G.M., Ficetola, G.F., Rondinini, C., Tilman, D., 2021. Proactive conservation to prevent habitat losses to agricultural expansion. Nat. Sustain. 4, 314–322. https://doi.org/10.1038/s41893-020-00656-5

Wilsey, B., 2021. Restoration in the face of changing climate: importance of persistence, priority effects, and species diversity. Restor. Ecol. 29, e13132. https://doi.org/10.1111/rec.13132

Wongpakaran, N., Wongpakaran, T., Wedding, D., Gwet, K.L., 2013. A comparison of Cohen's Kappa and Gwet's AC1 when calculating inter-rater reliability coefficients: a study conducted with personality disorder samples. BMC Med. Res. Methodol. 13, 61. https://doi.org/10.1186/1471-2288-13-61

Woodcock, C.E., Strahler, A.H., 1987. The factor of scale in remote sensing. Remote Sens. Environ. 21, 311–332.

Woodhouse, I.H., 2006. Introduction to microwave remote sensing, 1st Edition. ed. CRC press, Boca Raton, Florida, USA.

Wu, C., Shen, H., Shen, A., Deng, J., Gan, M., Zhu, J., Xu, H., Wang, K., 2016a. Comparison of machine-learning methods for above-ground biomass estimation based on Landsat imagery. J. Appl. Remote Sens. 10, 035010. https://doi.org/10.1117/1.JRS.10.035010

Wu, C., Shen, H., Wang, K., Shen, A., Deng, J., Gan, M., 2016b. Landsat Imagery-Based Above Ground Biomass Estimation and Change Investigation Related to Human Activities. Sustainability 8, 159. https://doi.org/10.3390/su8020159

Wulder, M.A., Loveland, T.R., Roy, D.P., Crawford, C.J., Masek, J.G., Woodcock, C.E., Allen, R.G., Anderson, M.C., Belward, A.S., Cohen, W.B., Dwyer, J., Erb, A., Gao, F., Griffiths, P., Helder, D., Hermosilla, T., Hipple, J.D., Hostert, P., Hughes, M.J., Huntington, J., Johnson, D.M., Kennedy, R., Kilic, A., Li, Z., Lymburner, L., McCorkel, J., Pahlevan, N., Scambos, T.A., Schaaf, C., Schott, J.R., Sheng, Y., Storey, J., Vermote, E., Vogelmann, J., White, J.C., Wynne, R.H., Zhu, Z., 2019. Current status of Landsat program, science, and applications. Remote Sens. Environ. 225, 127–147. https://doi.org/10.1016/j.rse.2019.02.015

Wulder, M.A., Masek, J.G., Cohen, W.B., Loveland, T.R., Woodcock, C.E., 2012. Opening the archive: How free data has enabled the science and monitoring promise of Landsat. Remote Sens. Environ., Landsat Legacy Special Issue 122, 2–10. https://doi.org/10.1016/j.rse.2012.01.010

Wulder, M.A., White, J.C., Loveland, T.R., Woodcock, C.E., Belward, A.S., Cohen, W.B., Fosnight, E.A., Shaw, J., Masek, J.G., Roy, D.P., 2016. The global Landsat archive: Status, consolidation, and direction. Remote Sens. Environ., Landsat 8 Science Results 185, 271–283. https://doi.org/10.1016/j.rse.2015.11.032

WWF-Pakistan, 2009. Boundary Deliniation of Margallah Hills National Park (Pakistan). WWF-Pakistan, Islamabad, Pakistan.

Xi-Liu, Y., Qing-Xian, G., 2018. Contributions of natural systems and human activity to greenhouse gas emissions. Adv. Clim. Change Res. 9, 243–252.

Xu, L., Shi, Y., Fang, H., Zhou, G., Xu, X., Zhou, Y., Tao, J., Ji, B., Xu, J., Li, C., Chen, L., 2018. Vegetation carbon stocks driven by canopy density and forest age in subtropical forest ecosystems. Sci. Total Environ. 631–632, 619–626. https://doi.org/10.1016/j.scitotenv.2018.03.080

Xue, B., 2015. Lidar and Machine Learning Estimation of Hardwood Forest Biomass in Mountainous and Bottomland Environments (Master). University of Akansas, USA.

Yadav, S., Padalia, H., Sinha, S.K., Srinet, R., Chauhan, P., 2021. Above-ground biomass estimation of Indian tropical forests using X band Pol-InSAR and Random Forest. Remote Sens. Appl. Soc. Environ. 21, 100462. https://doi.org/10.1016/j.rsase.2020.100462

Yin, H., Pflugmacher, D., Li, A., Li, Z., Hostert, P., 2018. Land use and land cover change in Inner Mongolia - understanding the effects of China's re-vegetation programs. Remote Sens. Environ. 204, 918–930. https://doi.org/10.1016/j.rse.2017.08.030

Young, N.E., Anderson, R.S., Chignell, S.M., Vorster, A.G., Lawrence, R., Evangelista, P.H., 2017. A survival guide to Landsat preprocessing. Ecology 98, 920–932. https://doi.org/10.1002/ecy.1730

Youssef, A.M., Pourghasemi, H.R., Pourtaghi, Z.S., Al-Katheeri, M.M., 2016. Landslide susceptibility mapping using random forest, boosted regression tree, classification and regression tree, and general linear models and comparison of their performance at Wadi Tayyah Basin, Asir Region, Saudi Arabia. Landslides 13, 839–856. https://doi.org/10.1007/s10346-015-0614-1

Yu, Y., Saatchi, S., 2016. Sensitivity of L-Band SAR Backscatter to Aboveground Biomass of Global Forests. Remote Sens. 8. https://doi.org/10.3390/rs8060522

Zafar, S.M., 2020. Spatio-Temporal Analysis of Land Cover/Land Use Changes Using Geoinformatics (A Case Study of Margallah Hills National Park). Indian J. Sci. Technol. 7, 1832–1841. https://doi.org/10.17485/ijst/2014/v7i11.23

Zeferino, L.B., Souza, L.F.T. de, Amaral, C.H. do, Fernandes Filho, E.I., Oliveira, T.S. de, 2020. Does environmental data increase the accuracy of land use and land cover classification? Int. J. Appl. Earth Obs. Geoinformation 91, 102128. https://doi.org/10.1016/j.jag.2020.102128

Zhang, C., Sargent, I., Pan, X., Li, H., Gardiner, A., Hare, J., Atkinson, P.M., 2019. Joint Deep Learning for land cover and land use classification. Remote Sens. Environ. 221, 173–187. https://doi.org/10.1016/j.rse.2018.11.014

Zhang, F., Yang, X., 2020. Improving land cover classification in an urbanized coastal area by random forests: The role of variable selection. Remote Sens. Environ. 251, 112105. https://doi.org/10.1016/j.rse.2020.112105

Zhang, H.K., Roy, D.P., 2016. Landsat 5 Thematic Mapper reflectance and NDVI 27-year time series inconsistencies due to satellite orbit change. Remote Sens. Environ. 186, 217–233. https://doi.org/10.1016/j.rse.2016.08.022

Zhang, J., Tian, H., Wang, D., Li, H., Mouazen, A.M., 2020. A Novel Approach for Estimation of Above-Ground Biomass of Sugar Beet Based on Wavelength Selection and Optimized Support Vector Machine. Remote Sens. 12, 620. https://doi.org/10.3390/rs12040620

Zhang, R., Zhu, D., 2011. Study of land cover classification based on knowledge rules using high-resolution remote sensing images. Expert Syst. Appl. 38, 3647–3652. https://doi.org/10.1016/j.eswa.2010.09.019

Zhang, X.M., He, G.J., Zhang, Z.M., Peng, Y., Long, T.F., 2017. Spectral-spatial multi-feature classification of remote sensing big data based on a random forest classifier for land cover mapping. Clust. Comput. 20, 2311–2321. https://doi.org/10.1007/s10586-017-0950-0

Zhao, M., Yang, J., Zhao, N., Liu, Y., Wang, Y., Wilson, J.P., Yue, T., 2019. Estimation of China's forest stand biomass carbon sequestration based on the continuous biomass expansion factor model and seven forest inventories from 1977 to 2013. For. Ecol. Manag. 448, 528–534. https://doi.org/10.1016/j.foreco.2019.06.036

Zhao, P., Lu, D., Wang, G., Wu, C., Huang, Y., Yu, S., 2016. Examining spectral reflectance saturation in Landsat imagery and corresponding solutions to improve forest aboveground biomass estimation. Remote Sens. 8, 469. https://doi.org/10.3390/rs8060469

Zheng, D., Rademacher, J., Chen, J., Crow, T., Bresee, M., Le Moine, J., Ryu, S.-R., 2004. Estimating aboveground biomass using Landsat 7 ETM+ data across a managed landscape in northern Wisconsin, USA. Remote Sens. Environ. 93, 402–411. https://doi.org/10.1016/j.rse.2004.08.008

Zheng, J., Wang, Y., Nihan, N.L., 2005. Quantitative evaluation of GPS performance under forest canopies, in: Proceedings. 2005 IEEE Networking, Sensing and Control, 2005. Presented at the Proceedings. 2005 IEEE Networking, Sensing and Control, 2005., pp. 777–782. https://doi.org/10.1109/ICNSC.2005.1461289

Zhu, X., Liu, D., 2015. Improving forest aboveground biomass estimation using seasonal Landsat NDVI time-series. ISPRS J. Photogramm. Remote Sens. 102, 222–231. https://doi.org/10.1016/j.isprsjprs.2014.08.014

Zhu, Z., Wulder, M.A., Roy, D.P., Woodcock, C.E., Hansen, M.C., Radeloff, V.C., Healey, S.P., Schaaf, C., Hostert, P., Strobl, P., Pekel, J.-F., Lymburner, L., Pahlevan, N., Scambos, T.A., 2019. Benefits of the free and open Landsat data policy. Remote Sens. Environ. 224, 382–385. https://doi.org/10.1016/j.rse.2019.02.016

Zobel, B.J., Jett, J.B., 1995. The Importance of Wood Density (Specific Gravity) and Its Component Parts, in: Genetics of Wood Production, Springer Series in Wood Science. Springer, Berlin, Heidelberg, pp. 78–97. https://doi.org/10.1007/978-3-642-79514-5_4
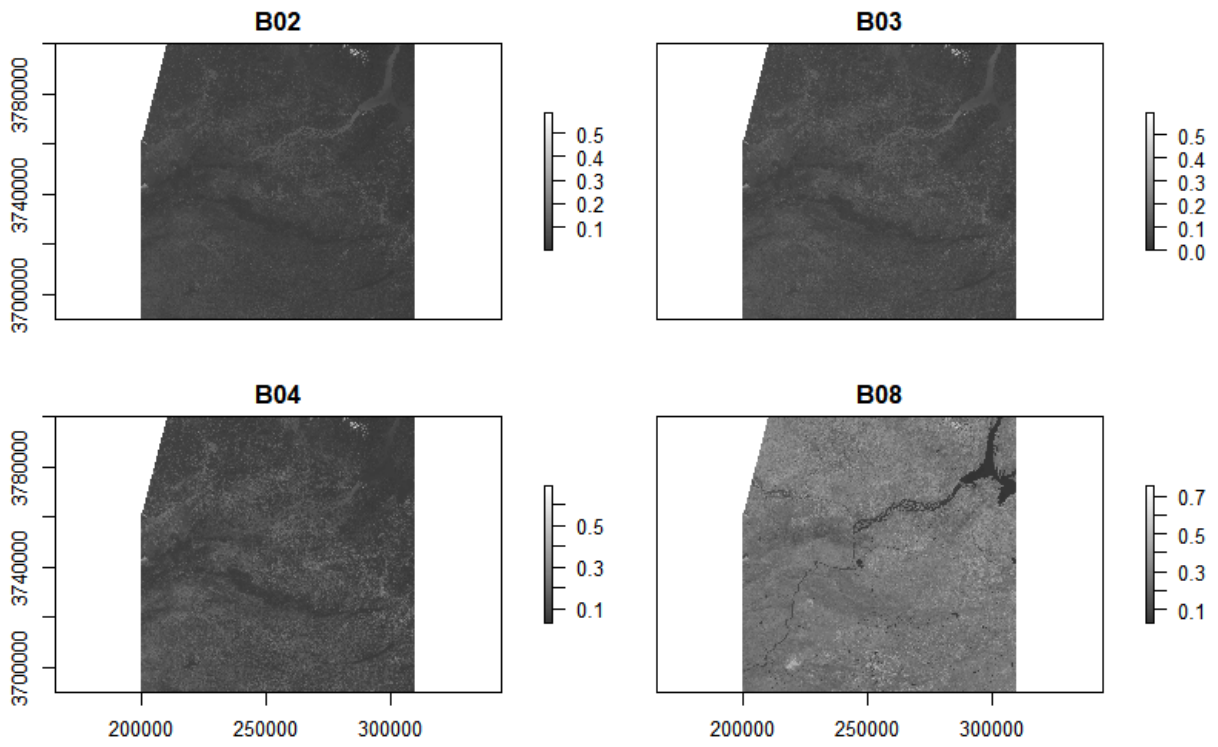
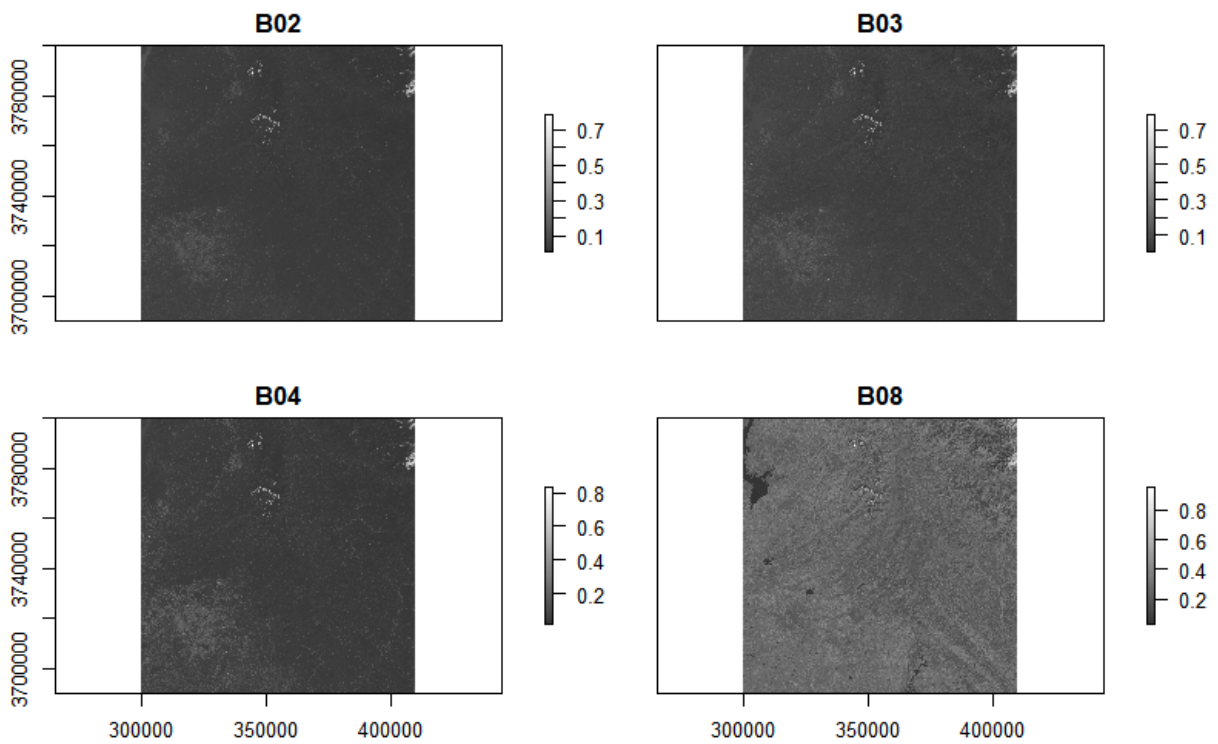**Annexure 1:** Satellite Imageries

Fig. 70: S2 First Image
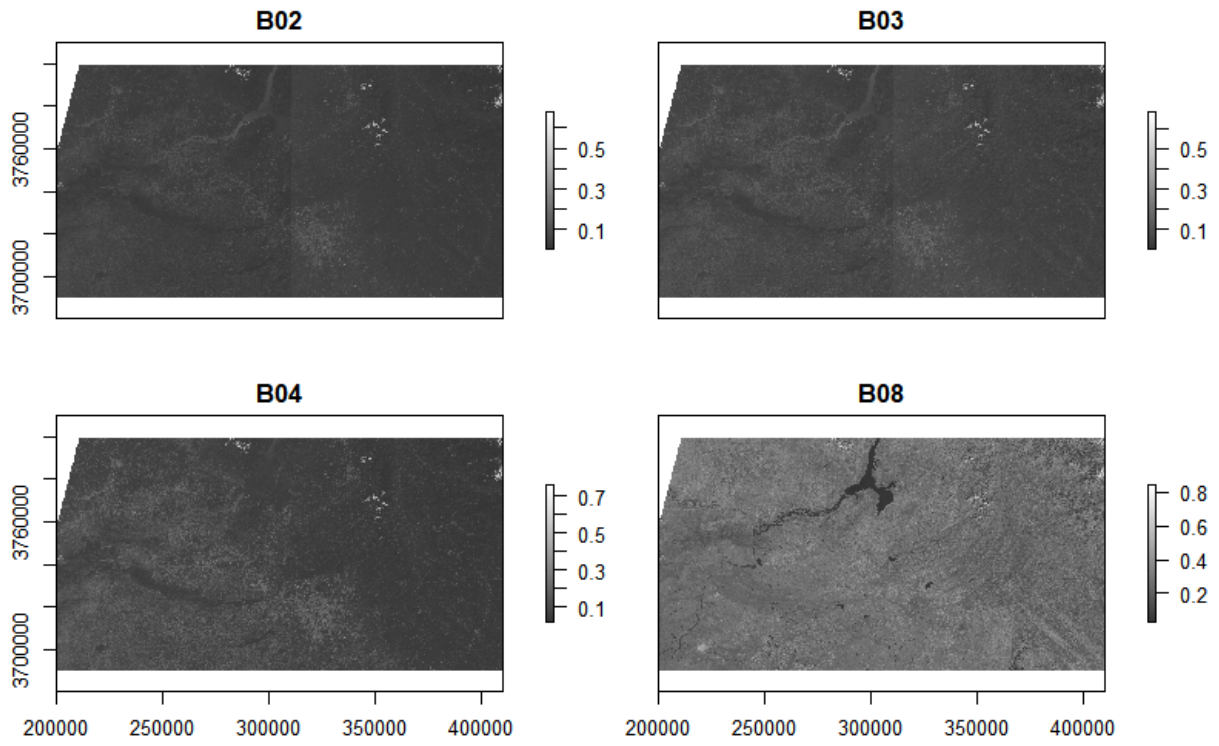

Fig. 71: S2 Second Image
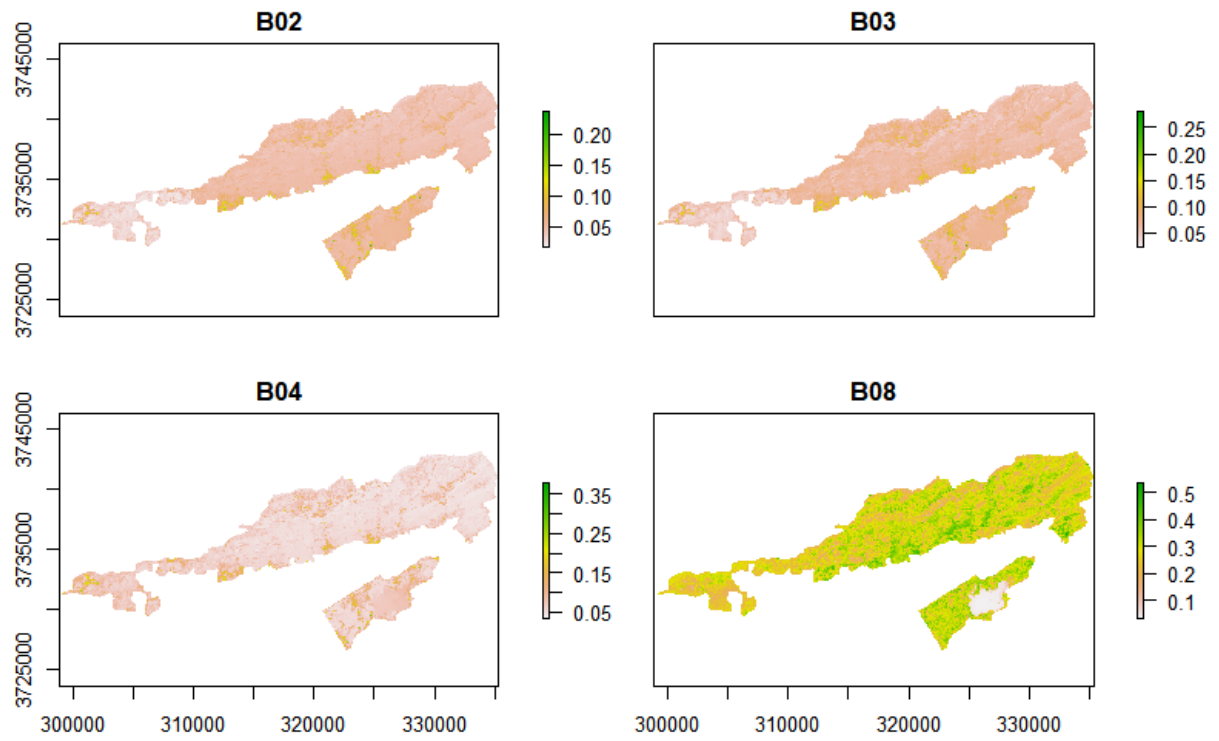
Fig. 72: Merged S2 Image

Fig. 73: Clipped S2 Image

223

Fig. 74: Natural Colour Composite of S2 Image of the Study Area

(Band combination 4,3,2)

Fig. 75: NIR Composite of S2 Image of the Study Area (Band combination 8,4,3)
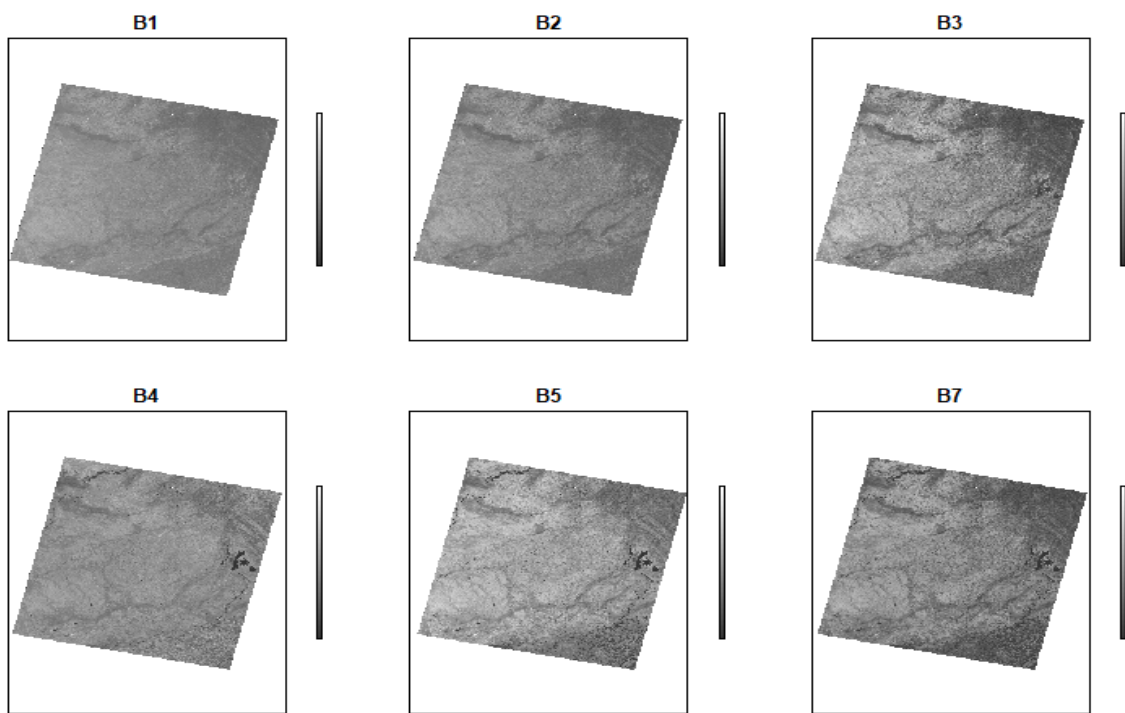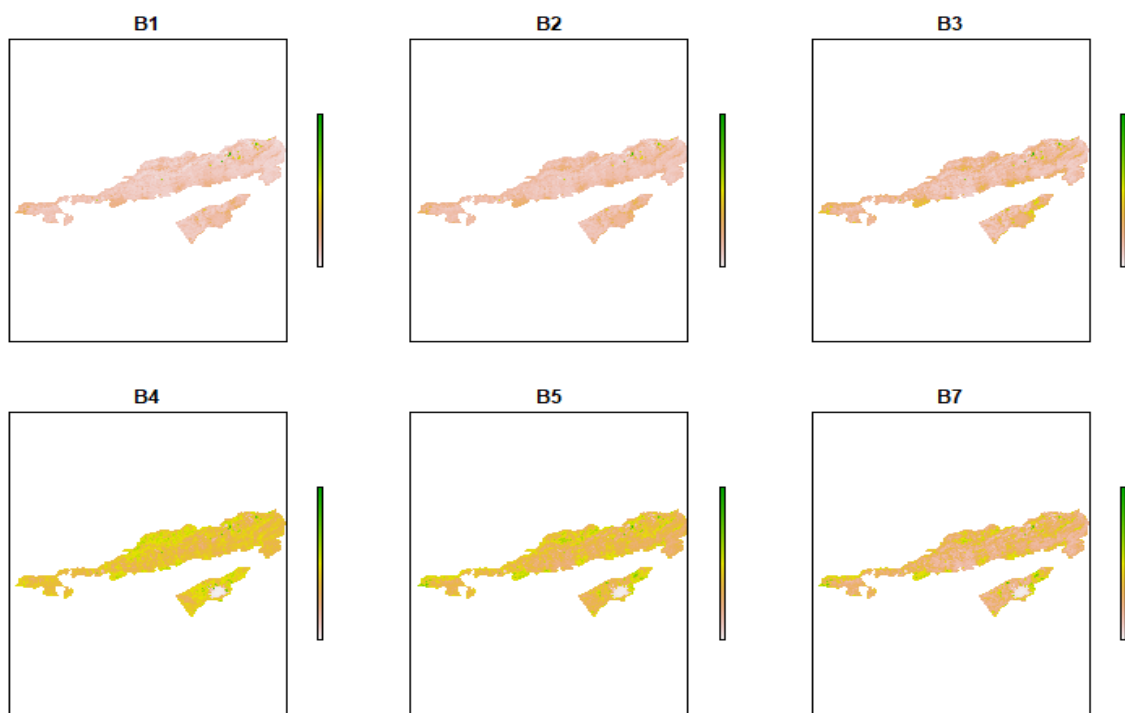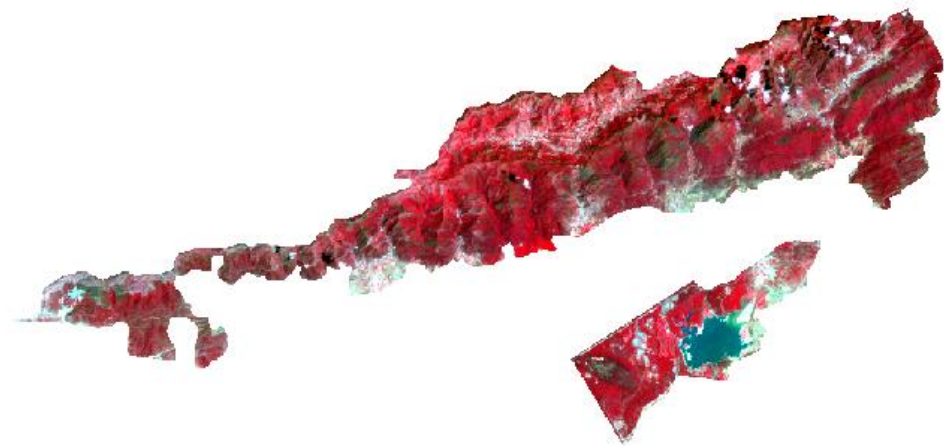
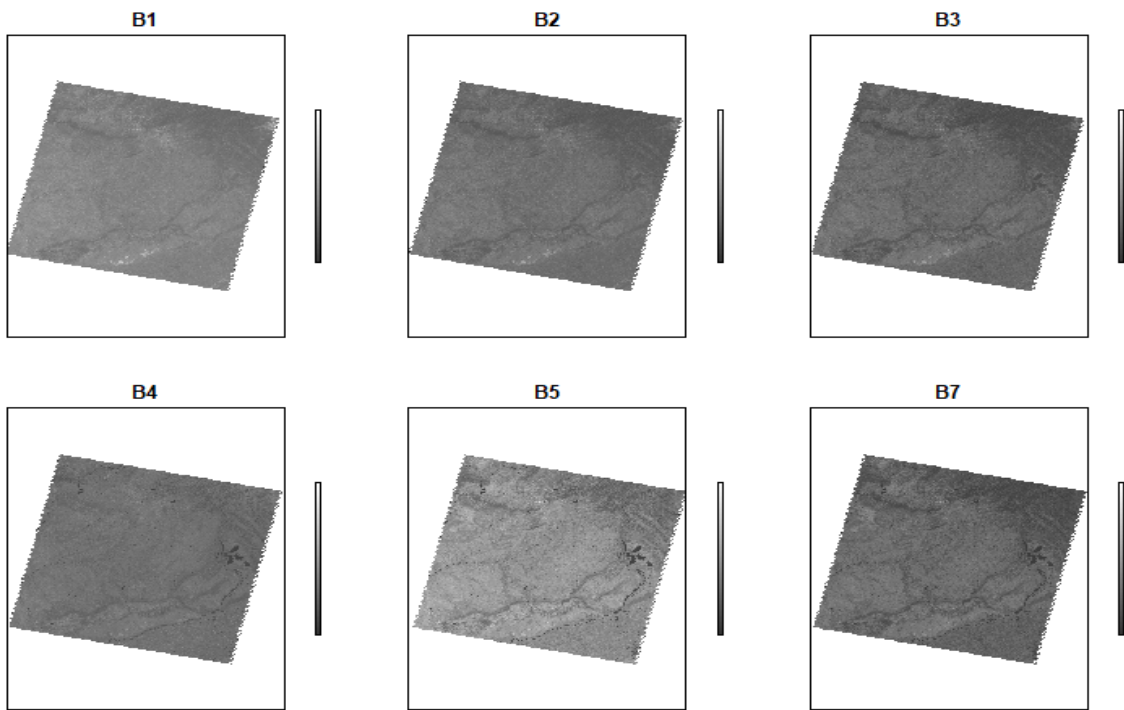**Fig. 76:** Bands Used for Landsat 7 ETM+ images
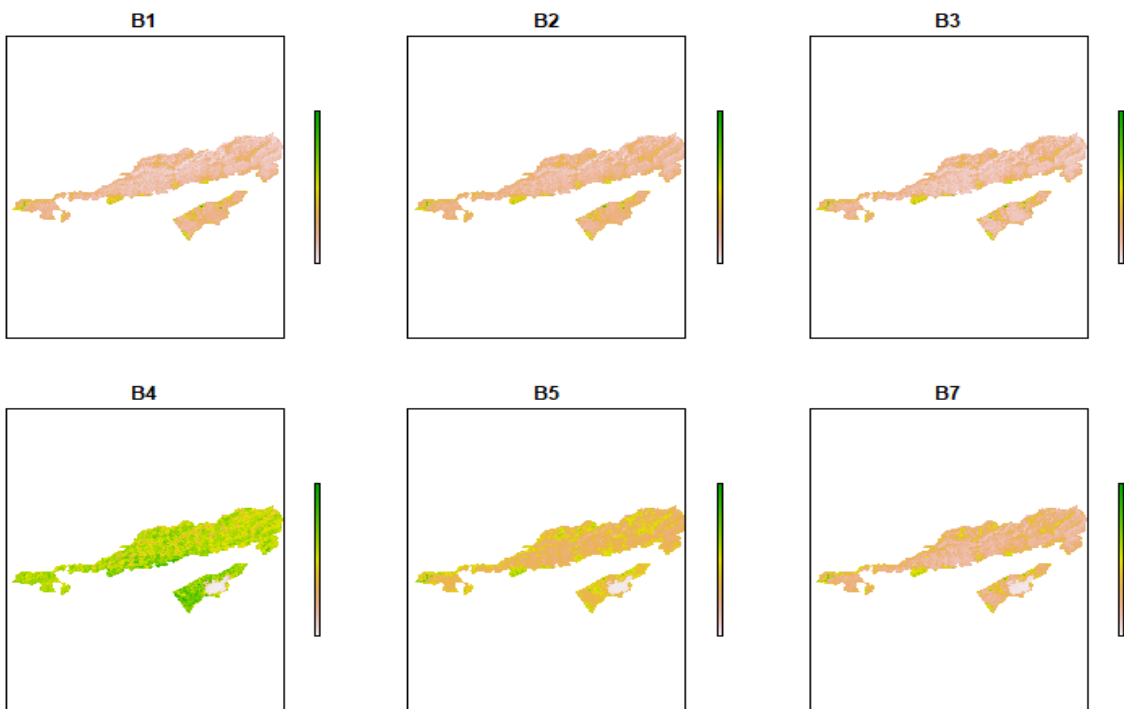

Fig. 77: Landsat 7 ETM+ Images of the Site Area with Respective Bands

Fig. 78: Natural Colour Composite of Landsat 7 ETM+ image of the Study Area
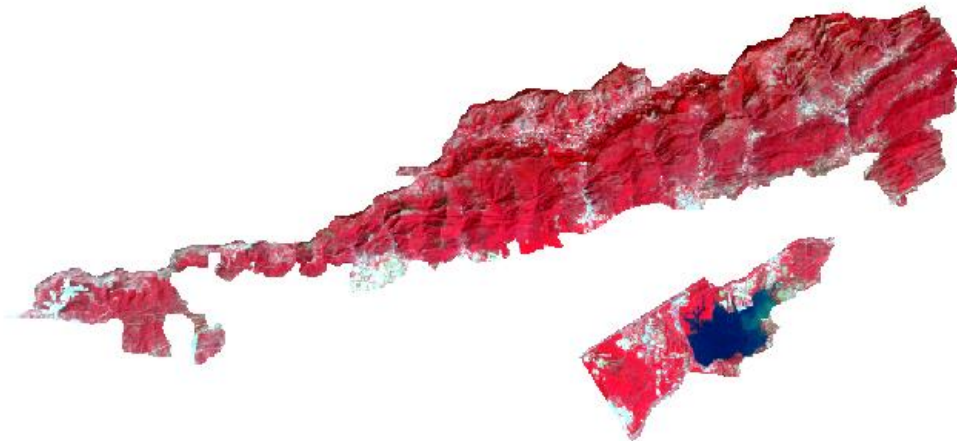
(Band combination 3,2,1)

Fig. 79: NIR Composite of Landsat 7 ETM+ Image of the Study Area
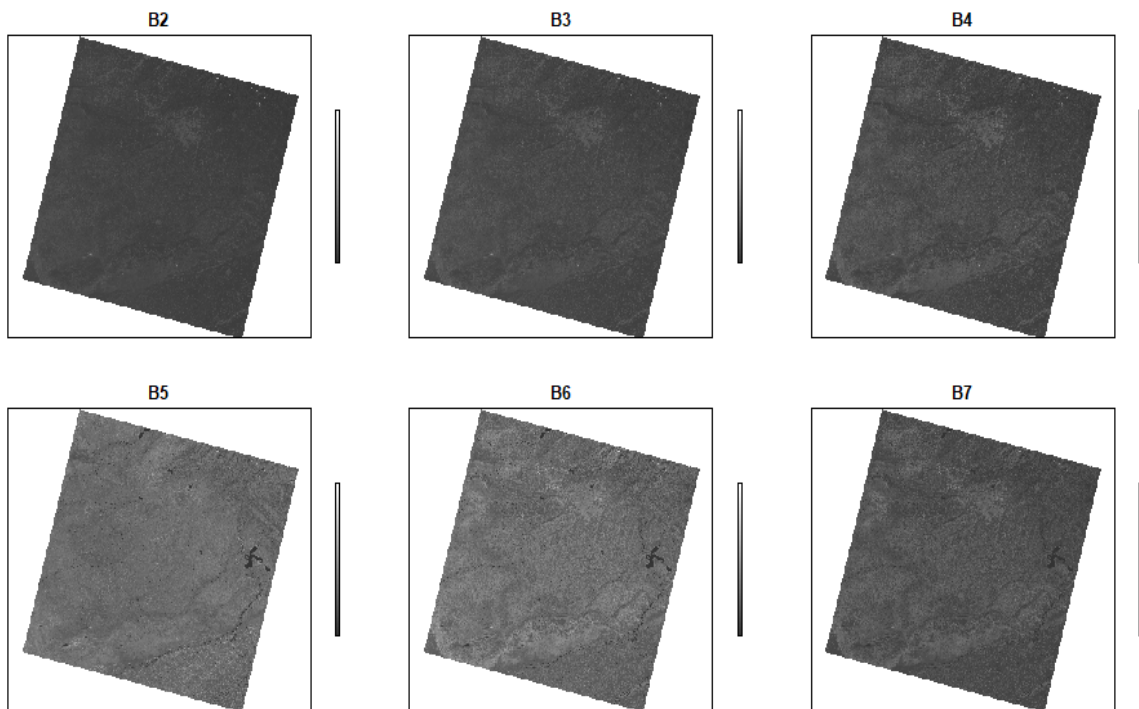
(Band combination 4,3,2)
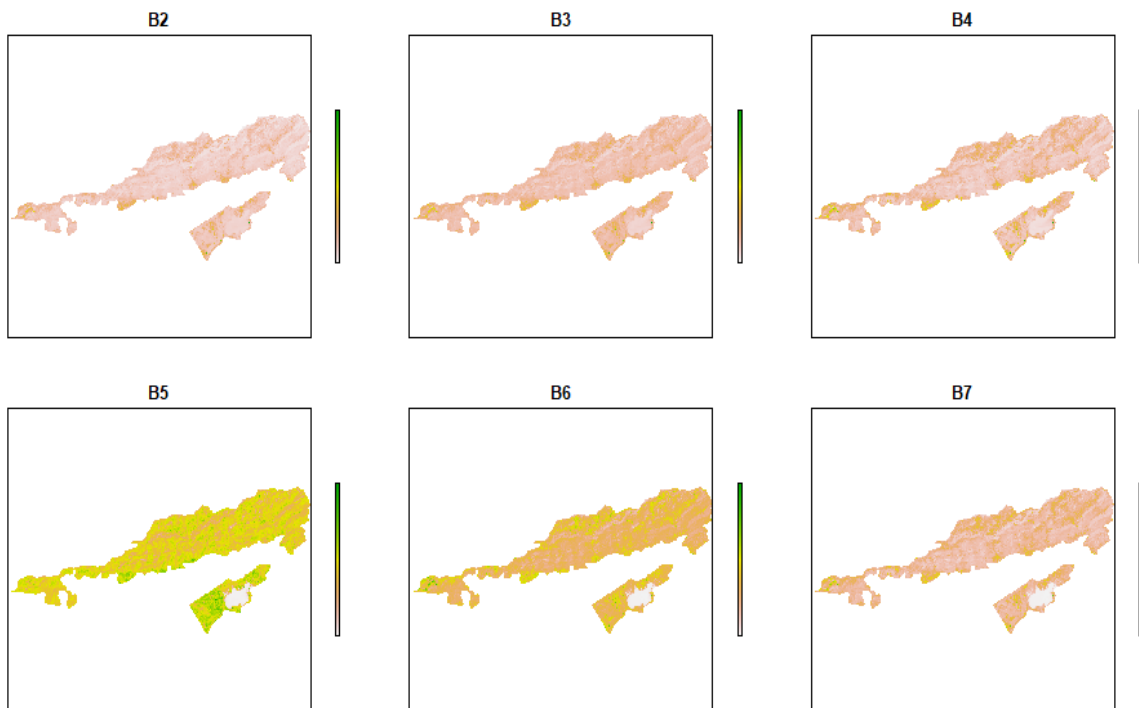
Fig. 80: Bands Used for Landsat 5 TM images

Fig. 81: Landsat 5 TM Images of the Site Area with Respective Bands

Fig. 82: Natural Colour Composite of Landsat 5 TM image of the Study Area
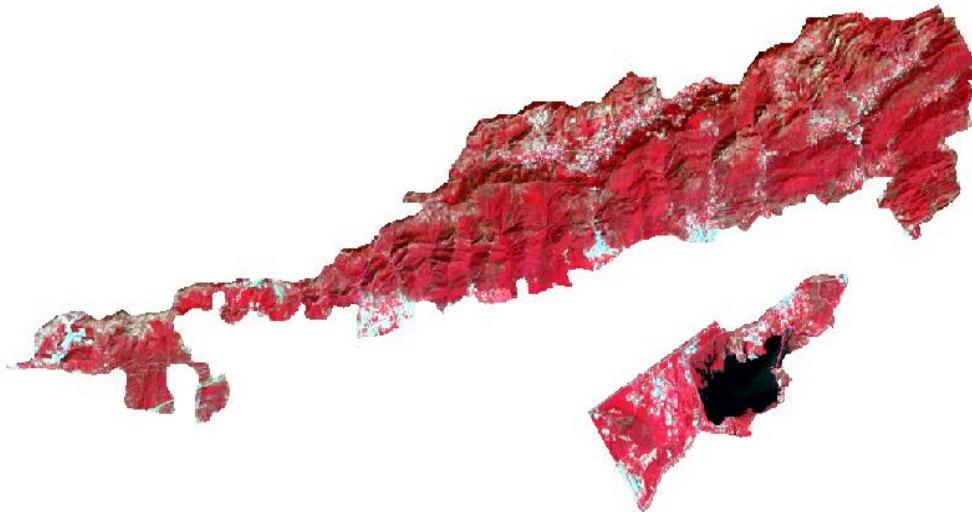
(Band combination 3,2,1)

Fig. 83: NIR Composite of Landsat 5 TM image of the Study Area

(Band combination 4,3,2)

Fig. 84: Bands Used for Landsat 8 OLI images

Fig. 85: Landsat 8 OLI Images of the Site Area with Respective Bands

229

Fig. 86: Natural Colour Composite of Landsat 8 OLI image of the Study Area

(Band combination 4,3,2)

Fig. 87: NIR Composite of Landsat 8 OLI Image of the Study Area

(Band combination 5,4,3)

Annexure 2: Data Collection Form

Plot No.	Name of the Place	GIS Coordinates	Slope	Elevation (m)	Aspect	Forest Type	Tree (Scientific Name)	Tree (Local Name)	DBH of Tree (cm)	Height of Tree (m)

231

Annexure 3: Pictures from MHNP

Fig. 88: View of MHNP (Photo Credit: IWMB)

Fig. 89: View of MHNP (Photo Credit: IWMB)
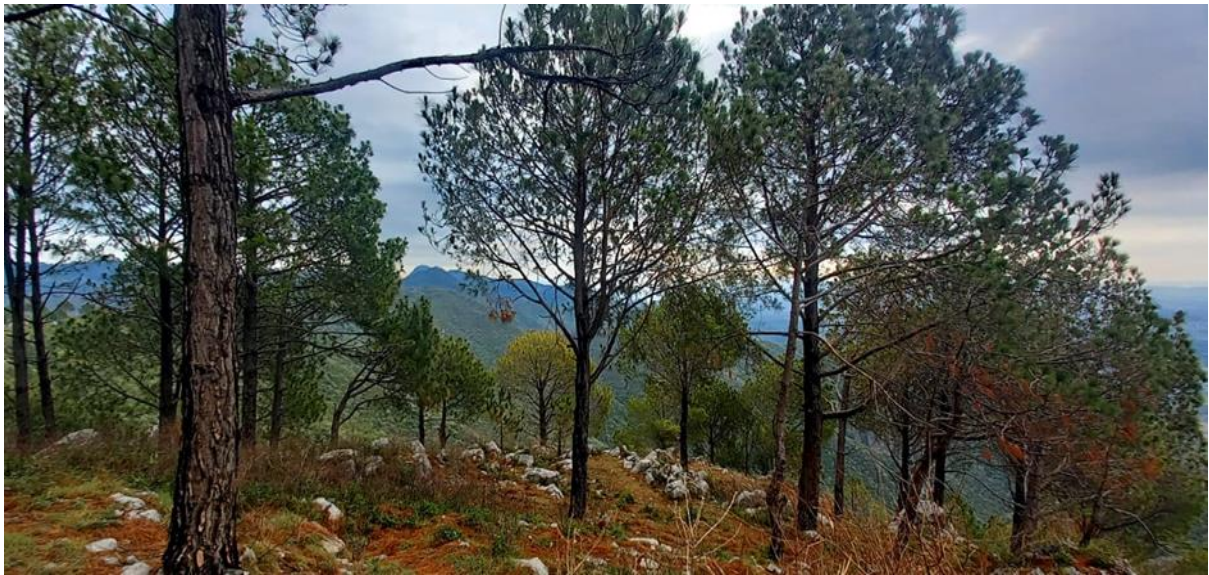
Fig. 90: SCPF Site in MHNP (Photo Credit: IWMB)

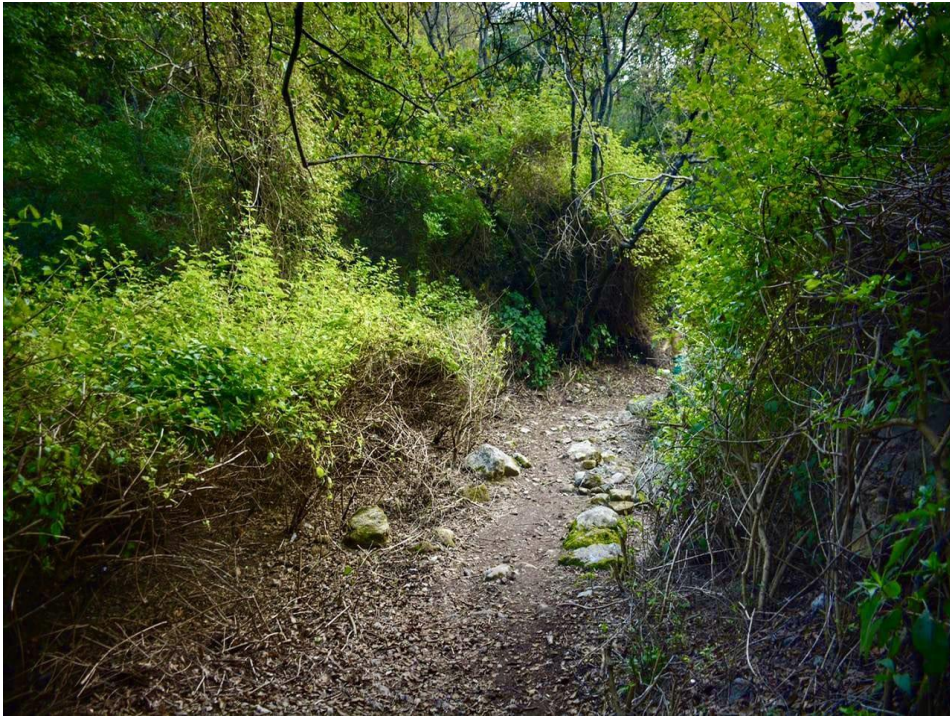**Fig. 91:** SCPF Site in MHNP (Photo Credit: IWMB)
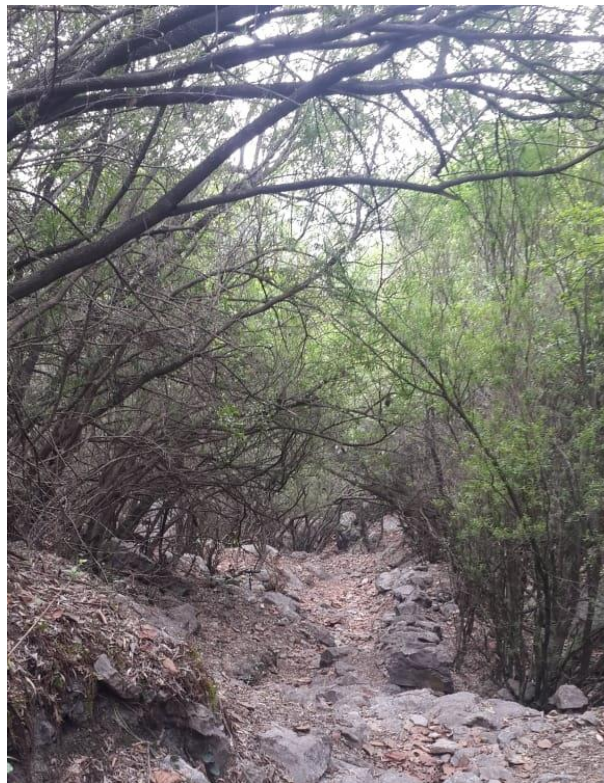
Fig. 92: SBEF Site in MHNP (Photo Credit: IWMB)

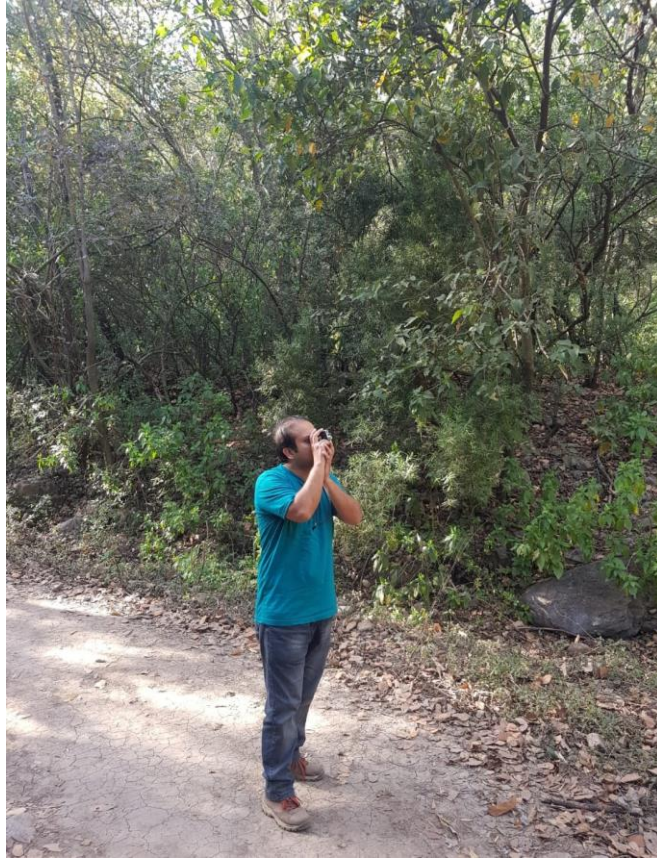**Fig. 93:** SBEF Site in MHNP (Photo Credit: IWMB)

Fig. 94: Field Inventorying Exercise in MHNP

Fig. 95: Field Inventorying Exercise in MHNP

Fig. 96: View of a Village in MHNP (Settlement)

Fig. 97: Grassland Site in MHNP (Photo Credit: IWMB)

Fig. 98: Agricultural Land in MHNP (Photo Credit: IWMB)

Fig. 99: View of Islamabad City and Rawal Lake from MHNP (Photo Credit: IWMB)